Additively manufactured lattice structures for vibration attenuation

Waiel Elmadih

Thesis submitted to University of Nottingham for the degree of Doctor of Philosophy

October 2019

Abstract

Advancements in additive manufacturing technology have allowed the realisation of geometrically complex structures with enhanced capabilities in comparison to solid structures. One of these capabilities is vibration attenuation which is of paramount importance for the precision and accuracy of metrology and machining instruments. In this project, new additively manufactured lattice structures are proposed for achieving vibration attenuation. The ability of these lattices to provide vibration attenuation at frequencies greater than their natural frequency was studied first. This is referred to as vibration isolation. For the vibration isolation study, a combination of finite element modelling and an experimental setup comprising a dynamic shaker and laser vibrometer was used. The natural frequencies obtained from the experimental results were 93 % in agreement with the simulated results. However, vibration attenuation was demonstrated only along one dimension and vibration waves were allowed to propagate, meaning the transmissibility was allowed to be greater than 0 dB. To achieve lower transmissibility, the project demonstrated that lattice structures can develop Bragg-scattering and internal resonance bandgaps. The bandgaps were identified from the lattices' dispersion curves calculated using a finite element based wave propagation modelling technique. Triply periodic minimal surface lattices and strut-based lattices developed Bragg-scattering bandgaps with a normalised bandgap frequency (wavelength divided by cell size) of ~ 0.2. The bandgap of the tested lattices was demonstrated to be tunable with the volume fraction of the lattice unit cell, thus, providing a tool to design lattice structures with bandgaps at required frequencies. An internal resonance mechanism in the form of a solid cube or sphere with struts was designed into the inner core of the unit cell of strut-based lattices. These new internal resonance lattices can provide (a) lower frequency bandgaps than Bragg-scattering lattices within the same design volume, and/or (b) comparable bandgaps frequencies with reduced unit cell dimensions. In comparison to lattices of higher normalised bandgap frequencies, lattices with lower normalised bandgap frequencies have

cell sizes that are more suitable for manufacturing with the current additive manufacturing technologies and have higher periodicity within a constrained design volume, resulting in higher attenuation within the bandgaps and more homogenous structures. Similar to the Bragg-scattering lattices, the bandgaps of the internal resonance lattices were demonstrated to be tunable through modification of the geometry of the lattice unit cell. The internal resonance lattice experimentally demonstrated a bandgap of normalised frequency between 0.039 to 0.067 and an attenuation of up to -77 dB. These results are essential for engineering vibration attenuation capabilities within the macro-scale of materials for complete elimination of all mechanical vibration waves at tailorable frequencies. Future work will include further reduction of the bandgap frequencies and increasing the bandgap width by exploring new unit cell designs and new materials for additive manufacturing.

Contents

Table of figures

VIII

X

XI

XII

XIII

Table of tables

Declaration

I, Waiel Elmadih, hereby declare that this thesis titled "Additively manufactured lattice structures for vibration attenuation" is my own work from the time of my PhD at University of Nottingham under supervision of Professor Richard Leach, Dr Syam Wahyudin and Dr Ian Maskery, and that it has never been previously submitted for the award of any degree, diploma or any similar type of recognition.

Acknowledgement

First and foremost, I would like to thank Professor Richard Leach for giving me the opportunity to do my PhD within the Manufacturing Metrology Team at University of Nottingham. I would like to express my deepest gratitude to my PhD supervisors Professor Richard Leach, Dr Wahyudin Syam and Dr Ian Maskery for their continuous support, patience, motivation and immense knowledge. I am very grateful for the support I have received from my supervisors through my time of research and writing of this thesis. Many thanks to my internal assessor Dr Simon Lawes for his constructive comments and valuable feedback. My appreciation also extends to Dr Dimitrios Chronopoulos, and the staff, technicians, and fellow postgraduate research students at the Advanced Manufacturing Technology Research Group at University of Nottingham for all of their help and support during my PhD research. I am deeply grateful to my amazing family (my dad Adil, my mom Wisal, and my two lovely sisters Fatima and Aiya) for the love, support and constant encouragement I have received from them over the years for I would not be the man I am today without them. Although they were geographically in a completely different continent for most of the time of my PhD, they have been in my heart all the time. I would also like to thank all my friends in Nottingham and Sudan who have been very supportive during my PhD research.

Terms definition

These terms are used throughout the thesis:

- Vibration attenuation: is the reduction of vibration transmissibility between two structures.

- Vibration damping: is a method for vibration attenuation by operating at frequencies lower than the first natural frequency of the structure.

- Vibration isolation: is a method for vibration attenuation by operating at frequencies higher than the natural frequency of the structure.

- Bandgap engineering: is a method for vibration attenuation with which wave propagation is prohibited at certain frequencies.

Chapter 1

Introduction

Additive manufacturing (AM) allows the manufacturing of periodic cellular structures (lattices structures) of enhanced properties when compared to solid structures. The aim of the project was to study the use of lattice structures for vibration attenuation purposes by providing the required design tools, modelling tools, and suitable lattice structures and vibration attenuation techniques.

When vibration propagates through the support/metrology frame of an instrument, it causes displacement of the end effector, for example, optical head in a measuring instrument or cutting tool in a precision machine, relative to the workpiece. Such displacement leads to machining and measuring errors. The main motivation behind the project was to enhance the performance of precision manufacturing and measuring instruments by attenuating vibration using lattice structures to machine better parts or perform better measurements. Enhancing the performance of these machines and instruments can be done by constructing them from lattice structures that have vibration attenuation capabilities. For constructing precision machines and measuring instruments, the required lattice geometries, structural properties and capabilities were studied and outlined to allow for later use in precision and metrology applications. The study of the capabilities of lattice structures included development of suitable wave modelling techniques, testing the vibration attenuation capabilities of various types of pre-existing

lattices and creating new types of lattices with superior vibration attenuation capabilities in comparison to solid structures.

1.1 Research questions

This research answered these questions:

- Can lattices be used for vibration attenuation?
- How can wave propagation be eliminated in lattices to achieve vibration attenuation below 0 dB?
- How can the vibrational performance of lattices be tailored to meet different vibrational needs (i.e. different vibration frequencies and directions)?

1.2 Vibration attenuation structures

Vibration attenuation structures are used to suppress vibration waves propagating from one structure to another. Vibration causes damage to structures and leads to machining and measuring errors. Vibration arises from different sources in different engineering fields. In construction engineering, vibration sources include machines such as compressors, ventilation systems and elevators [1]. In metrology and precision engineering, vibration sources include moving stages, camera shutters, contact between tool and workpiece, rotary components, for example, spindles, cutting tools, electronic fans and nearby traffic.

1.3 Manufacturing and materials

The ability of lattice structures to provide vibration attenuation was investigated. Lattice structures are a type of cellular structures with tailored geometrical features identified by a repeating unit cell [2]. The characteristics of these lattices include high strength to weight ratio, high surface area to volume ratios and high energy absorption properties. The solid geometries of lattices reflect the travelling waves which can destructively

interfere with each other (see Figure 1.1). The destructive interference of waves leads to the creation of frequencies of no wave propagation and results in high magnitudes of vibration attenuation (below 0 dB). The range of frequencies of no wave propagation is called a bandgap. In contrast, conventional solid structures lack the ability to destruct vibration waves and consequently allow propagation of waves which is associated with low magnitudes of vibration attenuation ($\geq$ 0 dB).
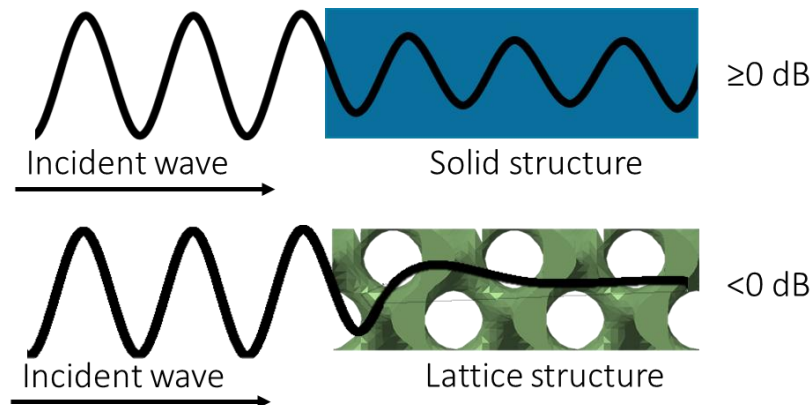
Figure 1.1. Vibration wave travelling within a conventional solid structure (top) and a lattice structure (bottom). Only low magnitudes of vibration attenuation are achievable with the use of solid structures, while lattice structure that is low in mass can provide high magnitudes of vibration attenuation when the wave frequency matches that of the bandgap.

The literature explored different types of lattices and their mechanical and structural capabilities have been studied for use in aerospace, automobile, mining and manufacturing sectors [3–5]. An opportunity exists to design lattice structures that have reduced response to vibration in comparison to solid structures (see Figure 1.2). In Figure 1.2, an example of a conventionally manufactured machine frame, shown on the left, is used to support the optical head of a measuring instrument. The optical head should be kept stable to avoid any measurements errors which are caused by the vibration of a measuring instrument. Since the metrology frame is a solid conventionally manufactured structure, then only vibration transmissibility $\geq$ 0 dB is achievable (see Section 3.3 for detailed description of vibration transmissibility). Lattice structures can be used in the design of

metrology/machine frames to achieve vibrational responses below 0 dB. This project provided lattice structures of enhanced vibration performance. These lattices can, later on, be used for manufacturing structural and metrology frames of enhanced vibration response and, thus, improved measurement and machining performance.
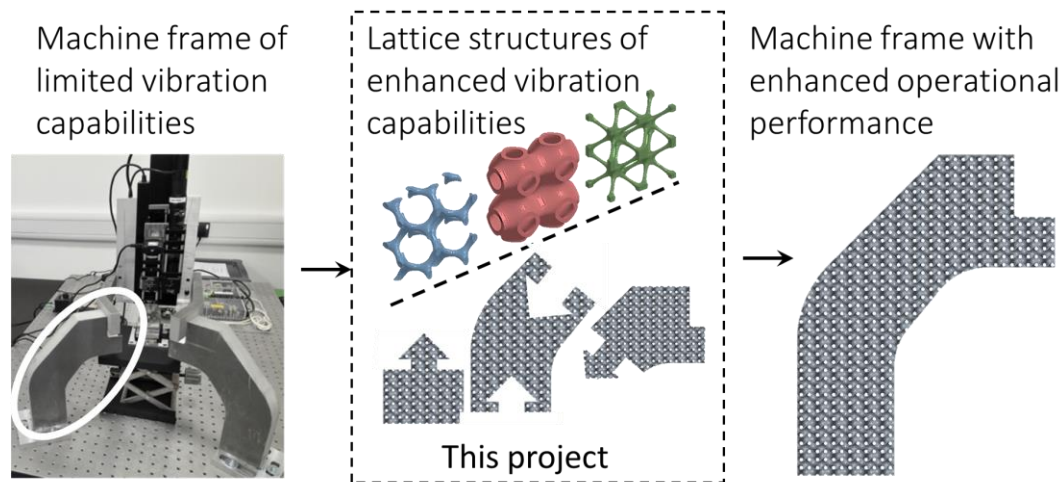
Figure 1.2. Illustration of the available opportunity to obtain machine frames with lattice structures of enhanced vibration attenuation capabilities.

Manufacturing of lattice structures with complex geometries is feasible and made easy with AM. AM is a manufacturing process that builds three-dimensional (3D) parts from a computer-aided design (CAD) file, usually by successively adding material layer by layer, as opposed to conventional manufacturing where materials are subtracted or formed to obtain the final part [6] (see Section 2.1.1 for more description of AM). AM provides an opportunity to realise complex lightweight structures of enhanced strength to weight ratio and superior vibration and thermal isolation capabilities in comparison to conventionally manufactured solid structures. In addition, AM parts can be tailored to meet the requirements of certain applications, for example, the strength, ductility, and thermal and vibration isolation capabilities of an AM part can be tuned by adjusting the density and sizes of geometrical features [7]; this eliminates the need for expensive tooling that is part-specific, for example, moulds in injection moulding and jigs and fixtures in machining.

1.4   Publications list

This thesis resulted in one book chapter, four conference papers and three peer-reviewed journal papers, all of which are published.

Book chapter:

- Elmadih, W.; Nefzi, M.; Bruice, E. Environmental isolation. In Basics of Precision Engineering; Leach, R. K., Smith, S., Eds.; 2018; pp. 565–600

Conference proceeding papers:

- Elmadih, W.; Syam, W.; Maskery, I.; Leach, R. K. Additively manufactured lattice structures for precision engineering applications. In: Proceedings of the 32nd Annual Meeting of American Society for Precision Engineering 29th October to 3rd November, Charlotte; 2017; pp. 164–169.

- Elmadih, W.; Syam, W.; Maskery, I.; Leach, R. K. Designing low-frequency bandgaps in additively manufactured parts using internal resonators. In: Proceedings of the 33rd Annual Meeting of American Society for Precision Engineering 4th to 8th November, Las Vegas; 2018; pp. 162-167.

- Elmadih, W.; Syam, W.; Maskery, I.; Leach, R. K. Control of elastic wave propagation in three-dimensional metamaterials. In: the American Society of Mechanical Engineers: 43rd Mechanisms and Robotics conference from 18th to 21st August 2019; 2019.

- Leach, R. K.; Elmadih, W.; Piano, S.; Senin, N.; Sims-Waterhouse, D.; Syam, W.; Su, R.; Thomas, M. Enriching micro-scale metrology with an all-optical dimensional measuring system. In Proceedings of the Proc. euspen Micro/Nano Manufacturing Workshop 8th to 9th November, Strathclyde; 2017.

Journal papers:

- Elmadih, W.; Wahyudin, S.; Maskery, I.; Meng, H.; Chornopolous, D.; Leach, R. K. Three-dimensional resonating metamaterials for low-frequency vibration attenuation. *Sci. Reps.* 2019, 9, 11503.

- Elmadih, W.; Wahyudin, S.; Maskery, I.; Chornopolous, D.; Leach, R. K. Mechanical vibration bandgaps in surface-based lattices. *Addit. Manuf.* 2019, 25, 421–429.

- Elmadih, W.; Syam, W.P.; Maskery, I.; Chronopoulos, D.; Leach, R. K. Multidimensional phononic bandgaps in three-dimensional lattices for additive manufacturing. *Mater. (Basel, Switzerland)* 2019, 12, 1878.

Part of the work here contributed in the following peer-reviewed journal papers:

- Meng, H.; Chronopoulos, D.; Fabro, A. T.; Elmadih, W.; Maskery, I. Rainbow metamaterials for broadband multi-frequency vibration attenuation: numerical analysis and experimental validation. *J Sound* Vib. 2019, (In-press).

- Syam, W.P.; Jianwei, W.; Zhao, B.; Maskery, I.; Elmadih, W.; Leach, R. K. Design and analysis of strut-based lattice structures for vibration isolation. *Precis. Eng.* 2017, *52*, 494–506.

Chapter 2

Lattice structures

Lattice structures are a set of interconnected networks of solid struts or plates that form a unit cell which is tessellated in space with no gaps between the cells [2].
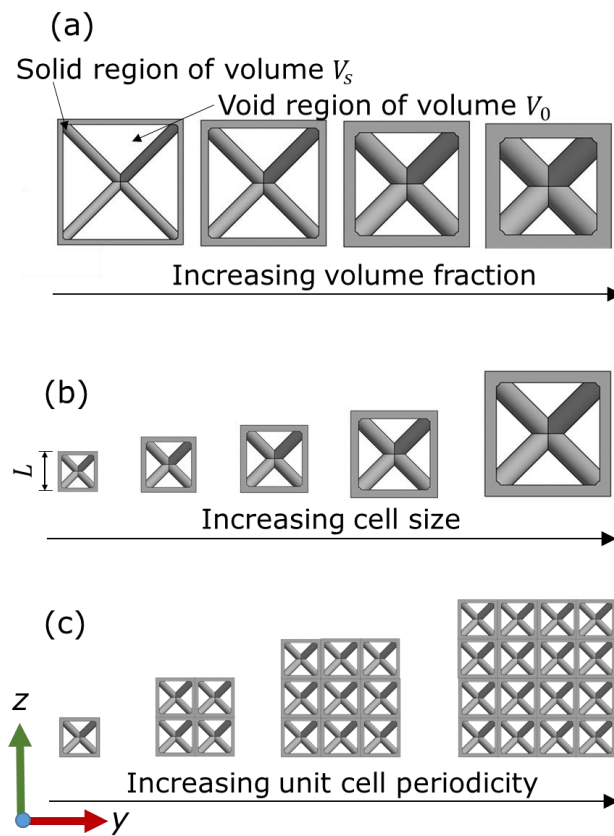
Figure 2.1. Examples of single unit cells of lattice structures at various (a) volume fractions, (b) cell sizes and (c) spatial periodicity.

The parameters of lattice structures include material, shape, volume fraction, unit cell size and spatial periodicity. The volume fraction (or relative density) ρ^* of a lattice unit cell is expressed as

$$\rho^* = \frac{V_s}{(V_s + V_0)} \, , \qquad\qquad 2.1$$

where V_s is the volume of the solid region of the lattice and V_0 is the volume of the void region as shown in Figure 2.1.a. The spatial periodicity of a lattice is defined as tessellation of the single unit cell of size L along certain directions in space (see Figure 2.1.b and Figure 2.1.c). Lattice structures generally have a high strength to weight ratio, high surface area to volume ratio, good energy absorption characteristics, and good thermal and acoustic insulation properties [8,9]. Research in lattice structures is motivated by the desire to design and manufacture structures of multifunctional properties; structures that are not only light in mass and stiff but also possess intrinsic vibrational attenuation and thermal isolation capabilities.
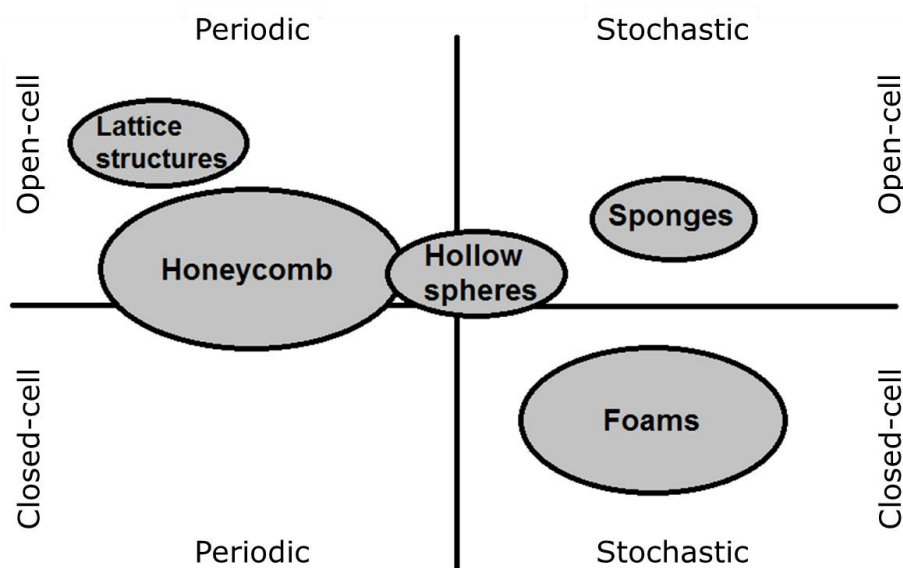
Figure 2.2. Lattice structures featured in the classification of cellular structures of Rehme et al. [10].

Rehme [10] classified cellular structures, depending on the type of porosity, into open-cell structures and closed-cell structures (see Figure 2.2) [10]; lattices are classified as

periodic open-cell structures as opposed to foam structures which are classified as closed-cell stochastic structures. According to Luxner et al. [11], who studied both periodic (regular) and stochastic (disordered) structures of simple cubic struts, periodic lattices have higher strength than stochastic ones (see Figure 2.3) due to the loads being evenly distributed among the unit cells. Stochastic structures cannot be identified by a repeating unit cell, but rather by a representative volume element (RVE) that contains the main microstructural features of the lattice (see elsewhere for more details on RVE [12]). Luxner et al. [11] found periodic lattices to be prone to strain localisation causing local damage at certain orientations.
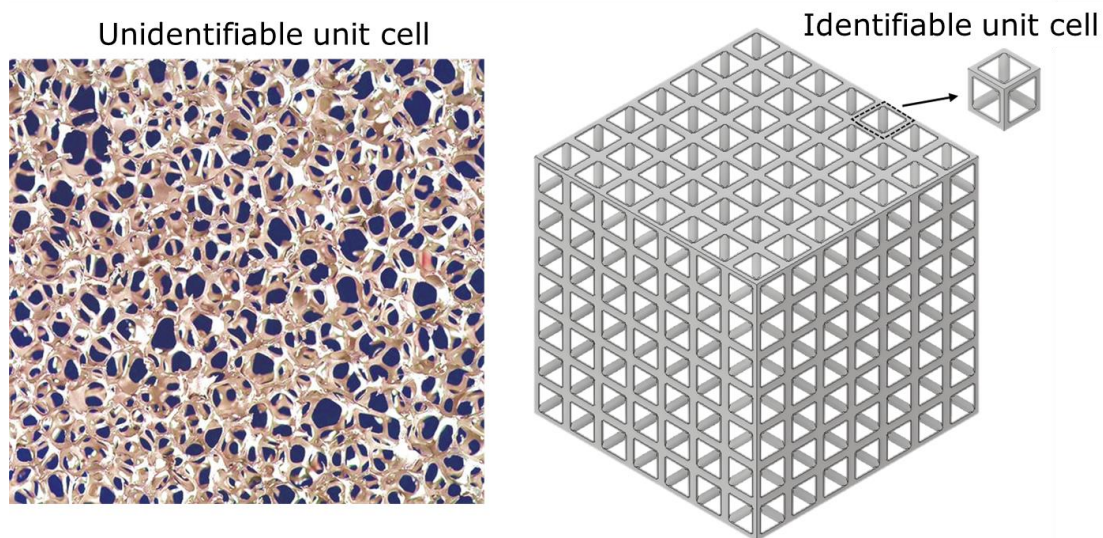
Figure 2.3. Example of a stochastic structure (left – photo adopted from [13]) and a periodic deterministic lattice structure (right).

In a contradicting study to that of Luxner et al. [11], Mullen et al. [14] highlighted that stochastic structures possess higher mechanical strengths than periodic structures, arguing that stochastic structures do not have the planes of natural fault which can be found in periodic structures. Mullen et al. [14] used L-PBF (an AM process which is discussed in Section 2.1.1). This is because L-PBF possesses the ability to manufacture the metallic and polymer lattice structures that Mullen et al. used in their study.

2.1 Lattice structure fabrication methods

In this section, the methods for manufacturing lattices are reviewed. Lattice structures can theoretically be manufactured in many ways, for example, fusion deposition modelling, stereolithography, material jetting, powder bed fusion, electron beam melting and metal forming [15]. However, only laser powder bed fusion, electron beam melting, investment casting and deformation forming will be discussed here as they are the most suitable methods for fabrication of lattice structures [4,16]. Description of other usable manufacturing methods, for example, material jetting and stereolithography, can be found elsewhere [17].

2.1.1 Additive manufacturing

- Laser powder bed fusion

L-PBF is an AM technique used for making solid parts from 3D CAD files by fusing selective regions of a powder bed using thermal energy [18]. The fundamental fabrication method of L-PBF relies on applying material powder in thin layers on a building platform and fusing specific areas using a laser beam of suitable thermal energy for consolidation of the powder [10]. The consolidation area depends on the data read from the 3D file and the required part resolution. The consolidation energy depends mainly on the material used which determines the exact L-PBF processing parameters, for example, thermal source energy, slicing of the part, scanning speed, scan line spacing (hatching), scanning strategy, atmosphere and powder bed temperature. The laser beam scans in a pattern obtained from CAD data. The laser beam melts the desired regions in the powder bed for consolidation [19,20]. During the building of metallic parts, supports are used to attach the parts to a base plate, while for plastic parts, the unfused powder acts as a support structure in most cases. A blade/wiper spreads another layer of unsolidified powder as the building platform indexes downwards. The platform is usually connected to a piston, as shown in Figure 2.4 which shows a schematic of L-PBF process [21].

10
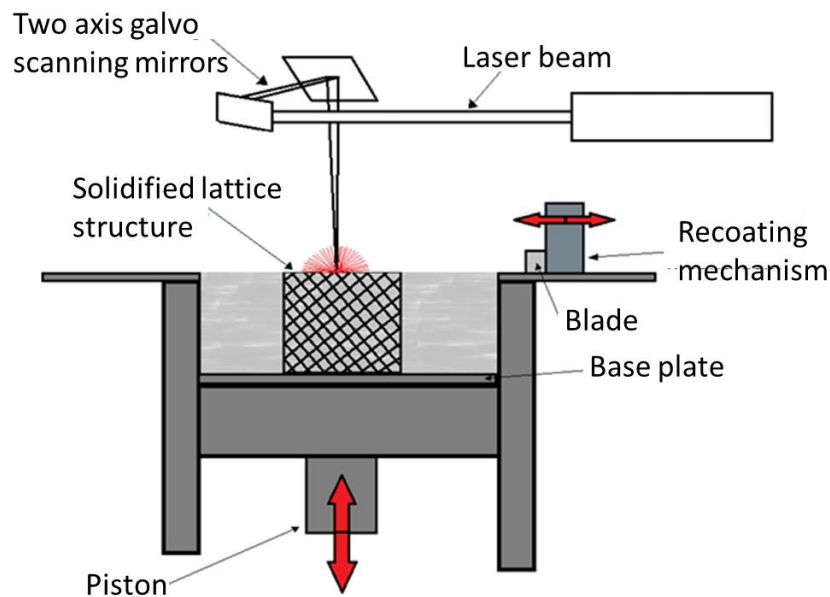
Figure 2.4. Schematic of L-PBF process adopted from [22].

A recent study by Tasch et al. [23] showed that L-PBF can manufacture features of sizes equal to or greater than 0.8 mm with minimal loss in mechanical capabilities, for example, ultimate tensile strength and Young's modulus, when compared to smaller features of sizes less than 0.8 mm. The smaller features either failed to manufacture or manufactured with considerable loss in mechanical capabilities when compared to the results of larger samples of no defects [23].

A problematic feature of L-PBF is the existence of porous regions (i.e. regions of unsolidified powder in the build) which occur due to, for example, entrapped gas between powder particles or incomplete melt of powder. To reduce porosity in L-PBF, the process parameters, for example, scanning speed and index amount, were studied and optimised based on their effect on porosity [24,25]. As a result, parts with near 100 % density were demonstrated to be achievable [22].

Generally, L-PBF can manufacture geometrically complex metallic and polymer components, and without the need, in some cases, for post-processing. Post-processing includes hot isostatic pressing, infiltration, removal of powder, and support, sintering and finishing. However, L-PBF is a costly process, because it requires expensive powder, especially metal powder, of spherical morphology and small size. The process is also time-consuming because it takes a longer time than conventional processes to build small metal parts [26] and is less energy efficient than milling, turning and drilling processes [27].

- Electron beam melting

Electron beam melting is a layer by layer process used to produce 3D parts. It is a similar process to L-PBF, except for that it uses an electron beam instead of a laser for melting metal powder layers of up to 50 μm in a near vacuum chamber at around 2×10^{-1} Pa [28,29]. The powder and the base plate require preheating [5]. The process, as Cansizoglu et al. [30] describe, starts with heating a tungsten filament for generating the electron beam. An acceleration voltage of 60 kilovolts is then imposed on the electrons to accelerate them towards the building table where the powder is placed. To control the electrons' deflection and focus, electromagnetic coils are used. Cansizoglu et al. [31] also studied the effect of electron beam angle in contact with the build material during the manufacturing of a Ti-6Al-4V lattice structure. As shown in Figure 2.5, the study of Cansizoglu et al. [31] concluded that small building angles affect the structural stiffness, as layers built at small angels have relatively smaller cross-sections than those built at wider angles. Syam et al. [32] presented an estimation of the accuracy and cost of EBM of Ti6Al4V parts. Despite being a cost-efficient and fast process, electron beam melting suffers from rougher surface finish compared to L-PBF process and investment casting methods (i.e. uneven surfaces) [33].
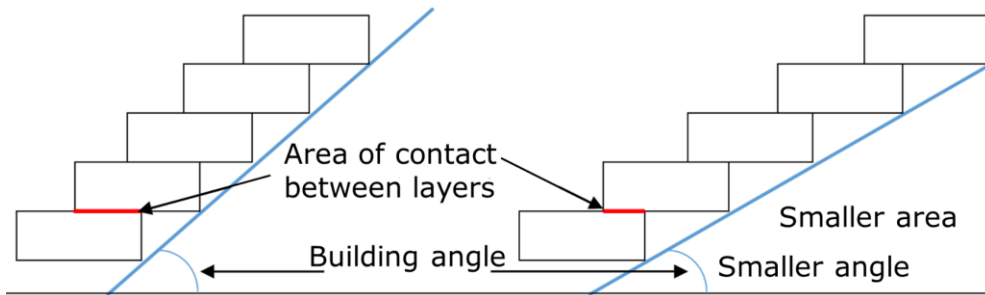
Figure 2.5. Effect of beam angle on the cross-section area in EBM, adopted from [30].

2.1.2 Investment casting

Investment casting is a traditional manufacturing method for manufacturing lattice structures by injecting material into disposable truss patterns connected to sheets which are made from a polymer or volatile wax, for example, polyurethane. A ceramic casting slurry covers the pattern and is allowed to cool down using a gating and risers cooling system. The wax or polymer is then vaporized or melted, from inside the ceramic casting, to form the cavity which the molten metal fills. Investment casting can produce different types of unit cells, for example tetrahedral, 3D kagome and octet-truss lattice (see Figure 2.6) [34,35]. Manufacturing of complex lattice geometries is possible with investment casting, however, cores of near-optimal shapes and very low volume fractions are challenging to obtain due to conventional manufacturing difficulties (i.e. stress concentration, liquid flowing issues, etc.).

The minimum achievable core density with investment casting is 2 % [36]. Only materials of low viscosity can be used, which narrows the variety of usable materials [34]. Investment casting produces parts of high porosity which is not favourable in some applications [36] and is not optimum for the manufacturing of lattice structures. Deshpande et al. [16] managed to manufacture octet-truss lattice structures (shown in Figure 2.6b) from aluminium alloys using investment casting with injection moulded polystyrene pre-forms. Sacrificial investment casting patterns were reported to be

13

manufacturable from Cu-Be alloy (see Figure 2.7a) using Acrylonitrile Butadiene Styrene (ABS - common thermoplastic polymer) by Wang et al. [37] and Wadley et al. [34].
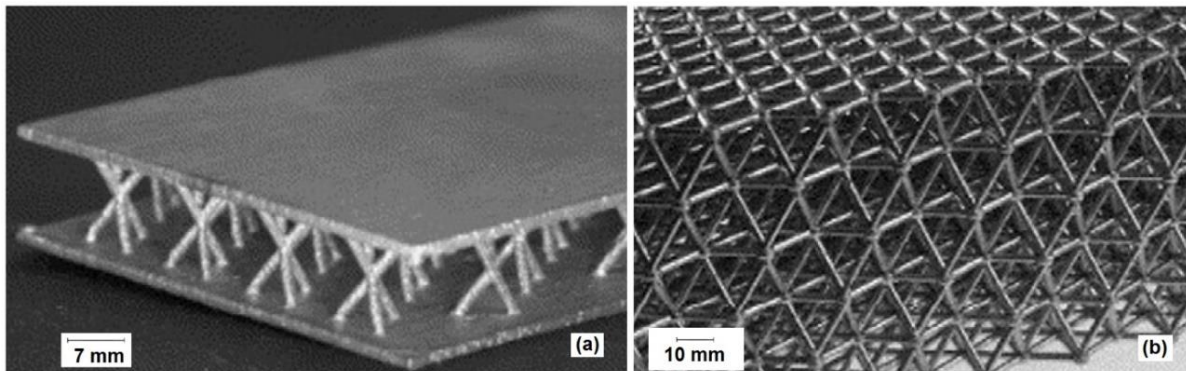
Figure 2.6. Investment casting: (a) 3D kagome lattice made from Cu - 1.8 % Be alloy [34], (b) octet-truss lattice structure made from aluminium alloy [16].

2.1.3 Deformation forming

Deformation forming is another way of producing lattice structures with the utilisation of shaping and perforation techniques. The process can produce cells of sizes ranging from millimetres up to several centimetres [34,38]. As illustrated in Figure 2.7, the process starts with the rolling of metal sheet to a perforator for producing holes of diamond or hexagonal shapes. Then, the produced sheets with the shaped holes are punched at predefined regions to turn the sheets into pyramidal or tetrahedron structures. As required by most of the deformation processes, the produced structures require annealing, to soften the material and take it towards its equilibrium state, and suffer from inefficient use of materials. Lattice structures produced by deformation forming are reported to have better ductility than those produced with investment casting [34]. Kooistra et al. [39] argued that deformation forming can produce structures with volume fractions between 1.7 % and 8 % by changing the sheet thickness and the hole dimensions.

14
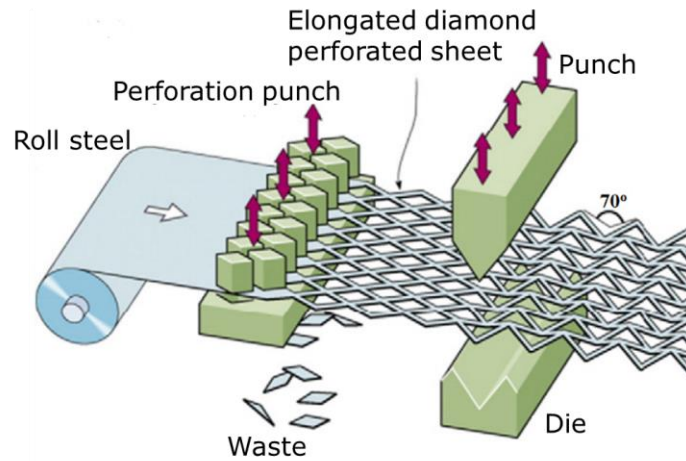
Figure 2.7. Illustration of the deformation forming process for producing lattice structures [40].

2.2   Classification of lattice structures

Lattice structures for engineering applications can be classified based on their unit cell design into three main categories: Strut-based lattices, triply periodic minimal surface (TPMS) lattices and topology optimised lattices. Topology optimised lattices are designed by introducing changes to the base design of the unit cell of strut-based and TPMS lattices. Thus, it can be argued that strut-based and TPMS lattices are the two main categories of lattice structures. Strut-based lattices, as shown in Figure 2.8., are characterised by having struts of certain cross-section, for example, circular, rectangular or square cross-section. The struts form the inner geometry and outer scaffold of the lattice unit cell. A strut-based lattice can have a different number of struts at different orientations. Identification of the struts (and their numbers) in a strut-based lattice is made based on the connection between the lattice nodes. For example, a simple cubic (SC) lattice has twelve struts forming the outer scaffold of the lattice unit cell, as can be seen in Figure 2.8. The body-centred cubic lattice (BCC) with reinforcement struts in x-, y- and z-directions (BCC$_{xyz}$) possesses twelve struts forming the outer scaffold, similar to the SC, and extra eight struts forming the inner geometry of the unit cell as can be seen in Figure 2.8. A SC

lattice has eight lattice nodes, all located at the corners. A BCC lattice has nine lattice nodes, eight of which are located in the corners and one is in the centre of the cubic lattice as in Figure 2.8.
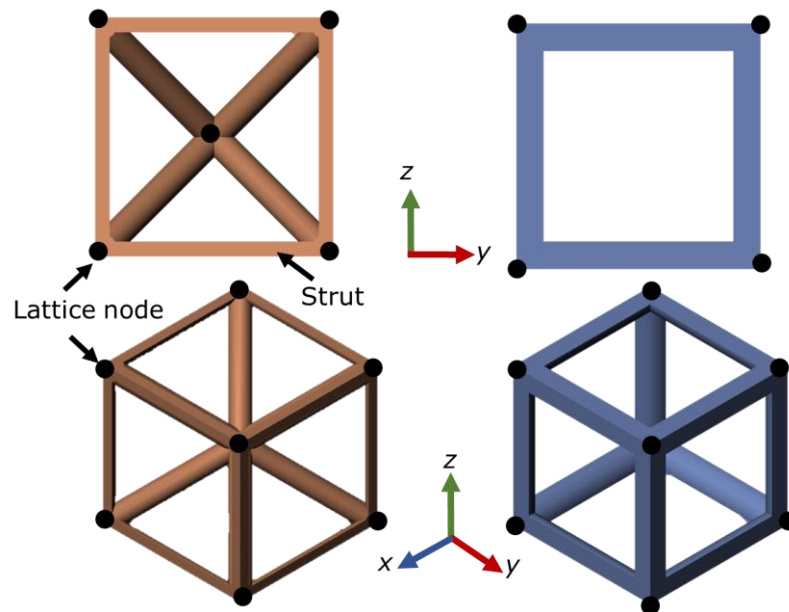
Figure 2.8. Illustrative examples of BCC_{xyz} (left) and SC (right) strut-based lattice with circular strut cross-section.

The other type of lattice structures is triply periodic minimal surface (TPMS) lattices which have complex morphologies making their fabrication by conventional manufacturing methods challenging, if not impossible [41]. Two categories of TPMS lattices exist: network phase TPMS and matrix phase TPMS. The unit cell of network phase TPMS have one void region and one solid region, both of which retain their connectivity in every part of the structure [42]. Matrix phase lattices have two non-connected void regions separated everywhere by a solid wall or sheet. Examples of network phase TPMS lattices and matrix phase TPMS lattices can be seen in Figure 2.9. At constant volume fraction, the thickness of material varies in network phase TPMS lattices, while it is constant in matrix phase TPMS's. In addition, matrix phase lattices are known to have higher specific stiffness than their network phase equivalents [43].
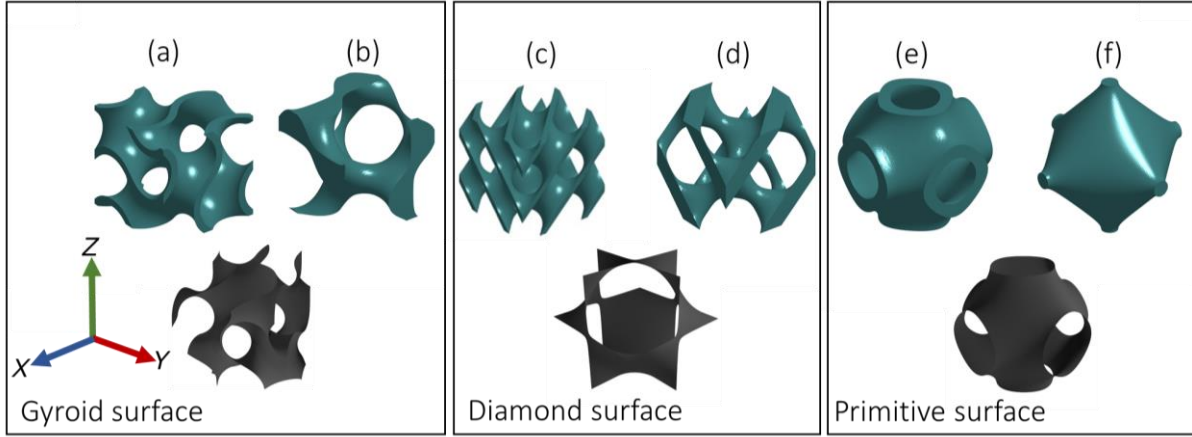
Figure 2.9. Illustrative examples of TPMS lattices: (a) Matrix gyroid, (b) network gyroid, (c) matrix diamond, (d) network diamond, (e) matrix primitive and (f) network primitive.

TPMS are identified by TPMS equations that describe 3D surfaces. For example, matrix gyroid lattice at certain volume fraction and number of tessellations can be generated by solving for the $U = 0$ isosurface of the function [41]

$$U = \cos(\mu_x x) \sin(\mu_y y) + \cos(\mu_y y) \sin(\mu_z z) + \cos(\mu_z z) \sin(\mu_x x) - t, \qquad 2.2$$

where μ_i are the tessellations of the TPMS function, defined as

$$\mu_i = 2\pi \frac{n_i}{L_i}, \qquad 2.3$$

where i denotes x-, y- and z-directions, n_i are the number of tessellation of the unit cell in a certain direction, L_i is the size of the single unit cell along a certain direction, and t is a variable to control the volume fraction of the lattice. Primitive TPMS lattices can be obtained by solving for the $U = 0$ isosurface of the function

$$U = \cos(\mu_x x) + \cos(\mu_y y) + \cos(\mu_z z) - t, \qquad 2.4$$

and, similarly, diamond TPMS lattice can be obtained by solving for the $U = 0$ isosurface of the function [44]

17

$$U = \sin(\mu_x x)\sin(\mu_y y)\sin(\mu_z z) + \sin(\mu_x x)\cos(\mu_y y)\cos(\mu_z z)$$

$$+ \cos(\mu_x x)\sin(\mu_y y)\cos(\mu_z z) + \cos(\mu_x x)\cos(\mu_y y)\sin(\mu_z z) \qquad 2.5$$

$$- t\,.$$

Many studies to date have focussed mainly on the load-bearing capabilities of TPMS lattices [4,41,45]. There is a wide range of TPMS lattice cell types, for example, gyroid, diamond and primitive [4,41,42]. TPMS lattices provide high stiffness when compared to strut-based lattices [42,46], are easier to manufacture with AM (i.e. can be manufactured with a fewer number of defects) than other strut-based lattices due to the self-supporting nature of TPMS lattices [46,47]. TPMS lattices also provide higher structural stiffness than strut-based lattices for use in different applications [43].

2.3 Geometrical modelling of lattice structures

Different methods are available for creating CAD files of lattice structures. For example, Brooks et al. [48] developed computer software that can create lattice structure CAD files using a combination of three different elements. These elements include: pillars, diagonals and octahedral, as shown in Figure 2.10. The software was reported to be able to produce metallic lattice structures of unit cell sizes ranging from 0.8 mm to 5.0 mm which were then manufactured with strut diameter ranging from 100 µm to 500 µm from stainless steel 316L using a L-PBF system [48].

Pillar elements   Diagonal elements   Octahedral elements

Figure 2.10. Types of elements that can be produced by the software of Brooks et al. [48]

TPMS lattices can be designed using a lattice generation software developed at University of Nottingham - called FLatt Pack [49]. FLatt Pack uses the TPMS surface equations introduced in Section 2.2 to design various TPMS lattice types of different sizes, periodicities and volume fractions, for the purpose of numerical modelling (finite element meshes) or printing (in .stl format). Maskery et al. [41] designed network phase gyroid, primitive and diamond TPMS lattices with dimensions (40×40×40) mm, and volume fraction of 30 %, using FLatt Pack, and successfully manufactured them using L-PBF. Santorinaios et al. [50] produced three types of simple geometry open-cell lattice structures of vertical pillars and cross-bracing L-PBF with the aim of testing their manufacturability. The cells were of sizes 1.25 mm, 2.5 mm and 5 mm. The 5 mm cell showed fabrication difficulties as the pillars tended to 'sag' during the melting process. McKown [51] was able to manufacture metallic lattice structures with octahedral and pillar-octahedral unit cells, both of sizes 1.5 mm and 2.5 mm, using L-PBF, and examined their blast loading and compression behaviour. The study of Yan et al. [52] used x-ray computed tomography (XCT) [53] to measure the internal structures of the cells and revealed that various gyroid lattices can be manufactured with unit cell sizes ranging from 2 mm up to 8 mm with no geometrical defects and without the need for support structures. As in the work of Syam et al. [54], strut-based lattices can be designed in CAD using estimates of the volume fraction relative to the strut thickness and cell sizes. The use of CAD provides suitable design freedom to alter lattice designs easily, for example adding or removing specific features and struts. This is essential for the development, and later on for the investigation of properties, of novel lattices, rather than relying on predefined lattice types. An estimate of the volume fractions of lattices is usually done by neglecting the intersection volume between the struts, which could be considerably large depending on the strut thickness and unit cell size. For example, for a strut-based lattice with struts of circular cross-section (see Figure 2.11), the volume of the solid region V_s is calculated as

$$V_s = \frac{\pi}{4} n d^2 L_t \ , \qquad\qquad 2.6$$

where d is the diameter of the strut, L_t is the length of the single strut and n is the number of struts in the lattice.
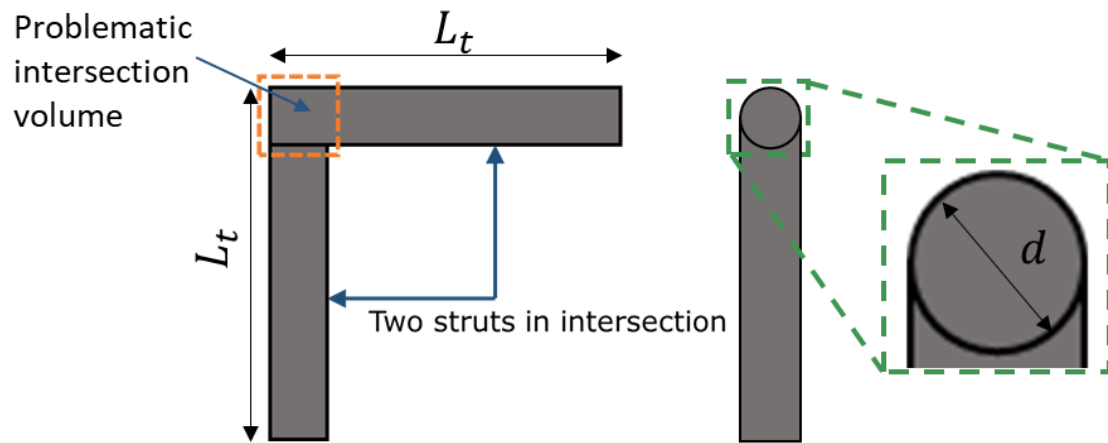
Figure 2.11. Illustration of two struts in an intersection.

For depicting the change in a lattice property with the change in volume fraction, an estimate of volume fractions can be used, but it is not effective when structures are to be designed and tailored for a specific use. Thus, there is a need for establishing the relationship between the volume fraction, cell size and strut thickness in strut-based lattices while taking into account the intersection volume.

2.4 Identification of lattice structures

Lattice structures represent the dominant type of open-cell structures which all fit under the umbrella of cellular materials. Unlike solid structures, lattice structure properties are not solely dependent on the material; they also depend on the cell size, cell configuration, structure periodicity and the connectivity between cell members or struts [10]. Gibson and Ashby used the relative elastic modulus E^* for relating the geometrical characteristics of lattice structures to their physical properties. The relative elastic modulus E^* is calculated as

$$E^* = \frac{E_{latt}}{E_{sol}} \; , \qquad\qquad 2.7$$

where E_{sol} is Young's modulus of the lattice material and E_{latt} is Young's modulus of the

lattice structure calculated as

$$E_{latt} = \frac{FL}{AU} \; , \qquad\qquad 2.8$$

where A is the surface area of the lattice, L is the size of the lattice and U is the

displacement of the lattice structure under a compression force (see Figure 2.12).
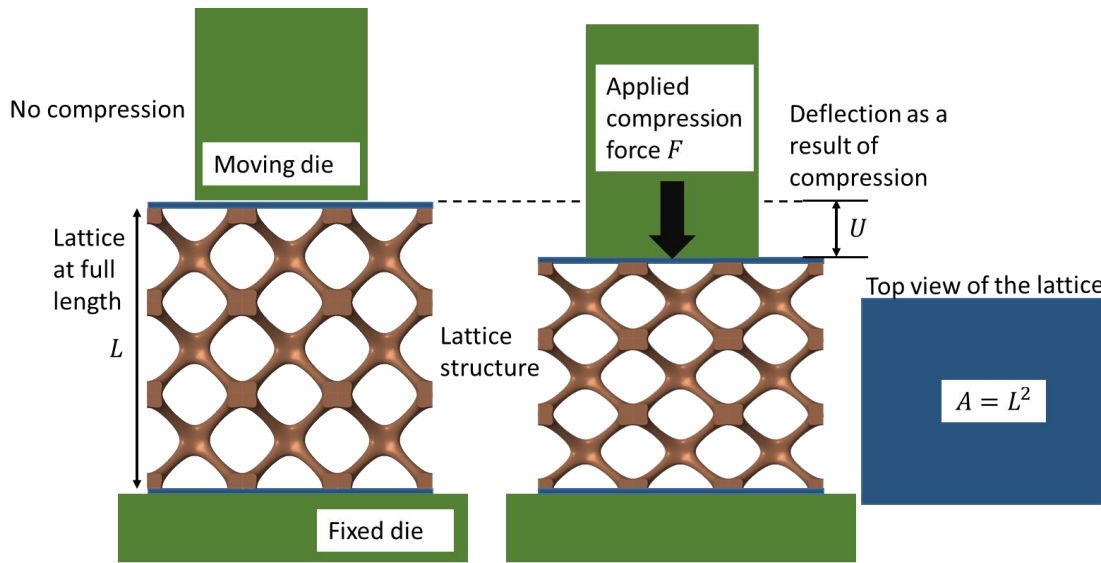
Figure 2.12. An illustrative example of a compression test carried on a lattice structure.

When the number of unit cells in a lattice is increased, the lattice can be approximated as

a homogenous porous structure. This is because smaller proportions of the unit cells are

located at the edges when a lattice has a higher number of unit cells. In comparison to

lower homogeneity structures, structures of higher homogeneity have uniform stress

distribution across the unit cells and, thus, less stress concentration at the edges. As a

result, the individual contribution of the single unit cell towards the overall stiffness of the

structures is reduced. It is expected that the relative elastic modulus of a lattice (as can

be calculated by Equation 2.7) will be increased with the increase in the number of unit

cells in the lattice. The convergence of the relative elastic modulus with the number of unit cells is expected to occur when the lattice has a sufficient number of unit cells. As shown by Maskery et al. [55], the relative modulus of lattice structures might be underestimated by up to 15 % from its converged value with respect to the number of unit cells in the lattice. Thus, in this project, the convergence of the number of unit cells in a lattice with respect to the relative elastic modulus is ensured to guarantee accurate estimation of the vibration and physical properties of lattice structures.

2.5   Summary

Lattice structures are a type of cellular structures which have a set of features interconnected through the edges and faces. Lattice structures are identified by a unit cell of certain geometry that repeats in space. Lattice structures generally have a high strength to weight ratio, high surface area to volume ratio, good energy absorption characteristics and good acoustic insulation properties. Depending on the geometry of the unit cell, a lattice can be classified into a strut-based lattice (inter-connected struts of defined cross-section, number and angles) and a TPMS lattice (intricate surfaces generated from mathematical equations and then given a certain thickness). Complex TPMS lattices can be designed for manufacturing or modelling, for example, using the Flatt Pack software, while strut-based lattices can be designed in general CAD software after establishing the relationship between the size of the features, cell sizes and the number of struts. Strut-based lattices can be manufactured using many techniques including L-PBF, electron beam melting, investment casting and deformation forming. The latter two are only accessible for simple lattice designs (i.e. designs with no intricate features) and suffer from conventional manufacturing issues (fluid flow issues in investment casting, inefficient use of materials in deformation forming and, generally, limited customisation ability). The literature has shown that AM and especially L-PBF is the more favourable for manufacturing of complex lattices (both strut-based and TPMS lattices). L-PBF has the

ability to produce strong, lightweight and complex metallic and polymer components, and to manufacture parts of full-density with no need for post-processing in some cases. All of these benefits show that additively manufactured lattice structures are well-suited for use as support structures in precision engineering and metrology applications.

Chapter 3

Vibration attenuation

In this chapter, the basic concepts of vibration and wave propagation are discussed. The various methods for vibration attenuation are reviewed in Section 3.3 and are published in this book chapter [56]. The major contribution of this project is on bandgap structures, thus, the concept of bandgaps is detailed in Section 3.5. The methods for investigation of bandgaps are available in Section 3.6 and the recent work on the topic is reviewed in Section 3.7.

Vibration is any repeating motion that occurs in a medium due to an initial or continuous cyclic disturbance. Vibration can be expressed mathematically with waves which can be classified into elastic waves that propagate through a solid medium, and acoustic waves which propagate through fluids. When disturbances occur in the parallel direction to the direction of travel of the waves, the waves are called longitudinal (primary) waves. When disturbances occur in the perpendicular direction to that of travel, the waves are called transverse (shear) waves [57] (see Figure 3.1).
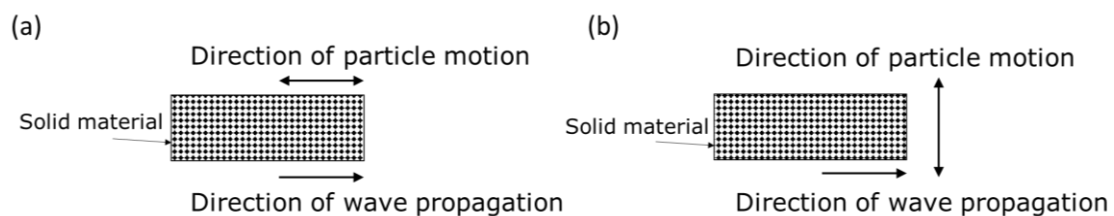
Figure 3.1. The direction of particle motion relative to the direction of propagation of (a) longitudinal waves, and (b) transverse waves.

Every structure/system has a frequency at which it vibrates in the absence of any driving force; this frequency is called the natural frequency and is described as a function of the stiffness of the structure k and the mass of the structure m. For a simple mass and spring system like that shown in Figure 3.2, the first natural frequency f_n is calculated using [58]

$$f_n = \sqrt{\frac{k}{m}}.$$ 3.1
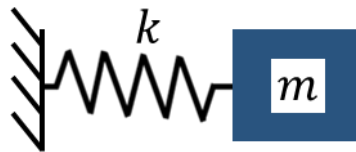
Figure 3.2. Illustration of a simple mass and spring system.

In precision engineering and metrology, vibration displaces the effective end of the instrument or machine relative to the workpiece; causing loss of accuracy and precision. In some cases, vibration damages the structural components of a system when the frequency of vibration coincides with the natural frequency of the system (see an example of precision and measuring instruments in Figure 3.3). Examples of end effectors include tools in conventional manufacturing machines and optics in optical scanning instruments. It is important to assess the design of instruments and machines to get knowledge of the achievable precision and limiting components within the assembled mechanism. Assessing of a design can be done by considering the structural loop, metrology loop and thermal loop of the assembled mechanism. A structural loop is an assembly of mechanical components that maintain relative position between specified objects. A metrology loop is a structural loop of all elements from the end effector to the workpiece for which dimensional changes would not be detected by the measurement process, thus, leading to measurement errors. A thermal loop includes components that will cause measurement errors if they undergo thermal expansion (see Bosmans and Reynarts [59] for further details). Of interest to this project are the components that form part of the metrology

and structural loop, for example, the metrology/rigid frame shown in Figure 3.3. This is because any disturbances due to vibration in these components would transfer into relative displacement between the workpiece and the end effector, resulting in loss of both precision and accuracy. This is usually in the hertz to low kilohertz frequency range [60].
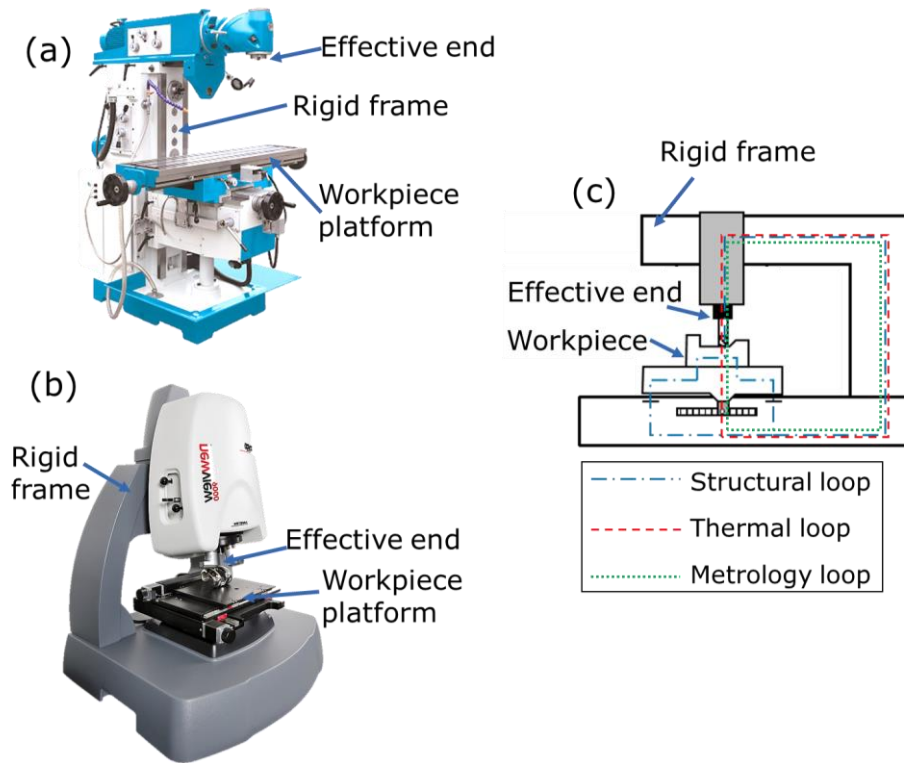
Figure 3.3. Example of (a) conventional manufacturing machines and (b) optical scanning instrument with (c) schematic of the main components.

Figure 3.4 shows a mechanical wave of wavelength λ and amplitude A which can be expressed by

$$q(x,t) = A \sin\left(\frac{2\pi}{\lambda}(x - vt)\right) , \qquad\qquad 3.2$$

where q is the amplitude of the wave at time t and position x, and v is the speed of the wave.
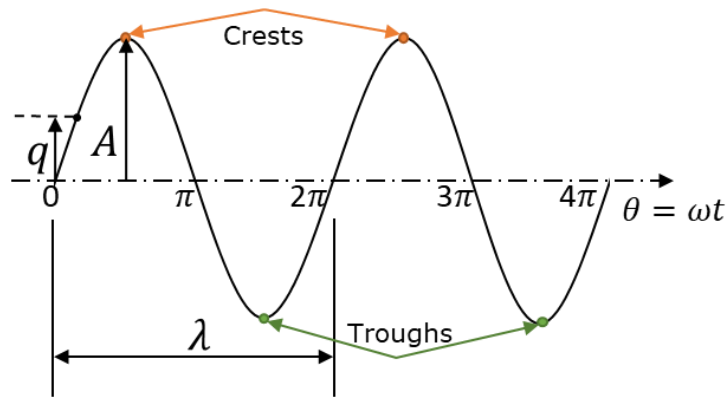
Figure 3.4. Illustration of wave motion.

Each type of elastic wave has a different propagation speed. For example, for longitudinal elastic waves (see Figure 3.1a), the speed of wave propagation v is calculated as

$$v = \sqrt{\frac{E}{\rho}},$$
3.3

where ρ is the material density and E is Young's modulus. Different types of transverse waves exist including electromagnetic waves, material shear waves and seismic waves. Of particular interest for this project are the shear waves (see an example of a shear wave in Figure 3.1b). The speed of propagation v_t of a shear wave in a material is calculated as

$$v_t = \sqrt{\frac{G}{\rho}},$$
3.4

where G is the shear modulus of the solid material. These waves originate from various sources including seismic (ground) vibration, acoustic vibration, and directly or indirectly applied forces [58]. A frequency spectrum of the vibration encountered in a typical lab environment was measured and is presented in Section 5.3. Seismic vibration includes all the excitations that shake the floor on which a machine is placed, for example, footsteps, motion of vehicles, and air conditioning and ventilation systems. Sources of seismic vibration generate acoustic vibration (frequency range between 20 Hz to 20 kHz) as well in many cases. The third source, applied forces, includes elastic vibration in the form of mechanical forces directly applied on the machine, for example, forces arising from moving

27

stages and rotating machine tools [54,58]. Attenuation of vibration is important to reduce the displacement of the end effector relative to the workpiece and ensure the accuracy and precision of machining and measurements.

3.1   Calculation of vibrational response

Understanding wave propagation and the system response to vibration is important for designing structures with vibration attenuation capabilities. For calculating the vibrational response of a structure, analytical methods were used before advances in computational mathematics. Consider an analytical representation of geometrically simple lattice unit cell as sets of mass m and stiffness k (see Figure 3.5).
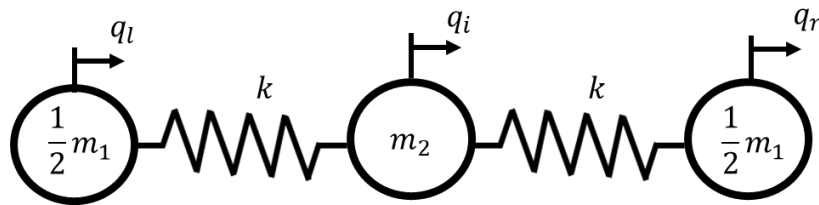
Figure 3.5. Representation of simple lattice unit cell.

The equations of motion for free undamped vibration of the unit cell is given by

$$\frac{1}{2}m_1\ddot{q}_l + k(q_l - q_i) = 0,$$

$$m_2\ddot{q}_i + k(2q_i - q_l - q_r) = 0, \qquad\qquad 3.5$$

$$\frac{1}{2}m_1\ddot{q}_r + k(q_r - q_i) = 0.$$

where $\ddot{q}$ is the second derivative (acceleration) of the displacement vector q. The subscripts l, i and r represent left, right, and inner finite element (FE) nodes as shown in Figure 3.5. The acceleration vector featured in Equation 3.5 can be obtained by taking the second derivative of q in Equation 3.2.

$$\ddot{q} = -\omega^2 A \sin(\omega t - \o). \qquad\qquad 3.6$$

Substituting Equation 3.6 into Equation 3.5 and dividing all terms by $\sin(\omega t - \o)$ gives

$$\frac{1}{2}m_1(-\omega^2 A_l) + k(A_l - A_i) = 0,$$

$$m_2(-\omega^2 A_i) + k(2A_i - A_l - A_r) = 0, \qquad\qquad 3.7$$

$$\frac{1}{2}m_1(-\omega^2 A_r) + k(A_r - A_i) = 0.$$

Equation 3.7 can be written in matrix format as

$$\begin{bmatrix} 2k/m_1 & -2k/m_1 & 0 \\ -k/m_2 & 2k/m_2 & -k/m_2 \\ 0 & -2k/m_1 & 2k/m_1 \end{bmatrix} \begin{bmatrix} A_l \\ A_i \\ A_r \end{bmatrix} = \omega^2 \begin{bmatrix} A_l \\ A_i \\ A_r \end{bmatrix}. \qquad\qquad 3.8$$

Equation 3.8 is an eigenvalue problem of type $AX = \lambda X$ which can be solved for the values of ω^2. Taking the square root of ω^2 and dividing the real part by 2π gives the natural frequencies of the unit cell in hertz. In metrology and precision engineering, the natural frequency of the instruments and machines has to be greater than or lower than the operational frequency range; this is to prohibit undesirable displacement of components if the operational frequency coincides with the natural frequency. Coinciding with the natural frequency leads to detrimental effects on measurement and machining accuracy and, in some cases, can cause structural damage of components. To obtain the maximum displacements at the natural frequencies, Equation 3.7 can be solved for the amplitude A by substituting the values of ω. If q_l, q_i and q_r are associated with external forces f, then the right side of the equations of motion in Equation 3.7 can be substituted with their values f_l, f_i and f_r. These equations enable us to obtain numerical results of the natural frequencies of a lattice and its response to harmonic excitations, to identify good lattice candidates for vibration attenuation.

3.2   Bloch's theorem and wave propagation

Wave propagation in the entire lattice can be understood by analysing a single unit cell through the application of Bloch's theorem. The use of a single unit cell for analysing wave propagation leads to savings in computation and time costs in comparison to analysing lattices with infinite and semi-infinite number of unit cells [61–63]. Bloch's theorem states

that for any repetitive unit cell the propagation of waves without attenuation does not depend on the location of the unit cell within the lattice. The Bloch's theorem for a 1D lattice (i.e. a lattice of one degree of freedom [DOF]) gives

$$q_r = e^{-kL}q_l,$$ 3.9

where k is the plane wave vector, given by $k = \delta + i\mu$, where the real part δ is the attenuation constant of the wave as it propagates through the unit cells, and the imaginary part μ is the phase constant of the wave. In this work, the wave is assumed to be propagating without attenuation (δ is zero), thus, $k = i\mu$. The displacement vectors of the unit cell q_l, q_{in} and q_r are grouped into one displacement vector $\boldsymbol{q}$ to simplify matrix operations. The displacement vector $\boldsymbol{q}$ can be projected to a reduced vector $\tilde{\boldsymbol{q}}$ that denotes the displacement of the FE nodes in reduced coordinates using the following Bloch's transformation

$$\boldsymbol{q} = \boldsymbol{N}\tilde{\boldsymbol{q}},$$ 3.10

where,

$$\boldsymbol{q} = \begin{bmatrix} q_l \\ q_i \\ q_r \end{bmatrix}, \qquad \boldsymbol{N} = \begin{bmatrix} \boldsymbol{I} & 0 \\ \boldsymbol{I}e^{-kL} & 0 \\ 0 & \boldsymbol{I} \end{bmatrix}, \text{ and } \tilde{\boldsymbol{q}} = \begin{bmatrix} q_l \\ q_i \end{bmatrix},$$ 3.11

where $\boldsymbol{I}$ denotes an identity matrix of proper size. To obtain the governing equations in the new reduced coordinates, the Bloch's transformation appearing in Equation 3.10 can be inserted into the governing equations of motion in Equation 3.5. To ensure the equilibrium of the forces in the new and old coordinates, the resultant equation is multiplied by $\boldsymbol{N}^H$ to give

$$\tilde{\boldsymbol{D}}\tilde{\boldsymbol{q}} = \boldsymbol{0},$$ 3.12

where

$$\tilde{\boldsymbol{D}} = \boldsymbol{N}^H \boldsymbol{D} \boldsymbol{N},$$

and 3.13

$$\boldsymbol{D} \equiv \boldsymbol{K} - \omega^2 \boldsymbol{M},$$

where D is the dynamic stiffness matrix (assuming a harmonic motion of $e^{i\omega t}$) and H is the Hermitian transpose [63,64]. The Hermitian transpose of an m×n matrix of complex entries is the n×m matrix and is obtained by taking the transpose of the original matrix and then taking the complex conjugate of each entry. Equation 3.12 is an eigenvalue problem for a harmonic free wave motion the can be solved for the frequencies of the propagating waves. These equations allow for an understanding of the ability of lattices to propagate vibration waves within their structure and can be used to identify good candidate lattice structures for vibration attenuation.

3.3   Methods for vibration attenuation

Vibration attenuation is commonly required to reduce the amount of vibration in instruments and machines. In this section, the methods for passive vibration attenuation are discussed. See elsewhere [65] for details on active and nonlinear vibration attenuation methods. Although these attenuation methods will not form part of the main findings and novelty of this thesis, it is worth acknowledging them to identify limitations and provide a detailed description for direct use or further research and development elsewhere. Different methods for vibration attenuation exist, for example, pneumatic mounts, metal springs and rubber mounts. These vibration attenuation methods are applied either to protect the base of a vibrating instrument from vibration or to protect the instrument from the vibration of the base. In both cases, the transmissibility of a vibration attenuation system is adjusted at a given frequency to suppress the displacement of the instrument. Consider the single DOF vibration attenuation mechanism shown in Figure 3.6.
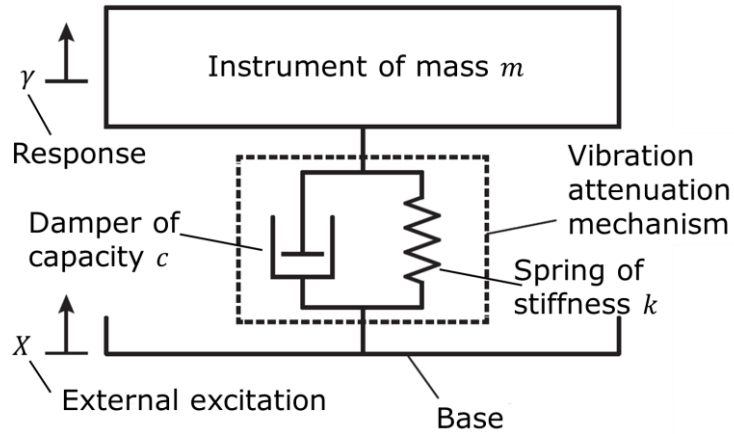
Figure 3.6. An illustration of a single DOF vibration attenuation mechanism.

The instrument of mass m is protected from the vibration of the base using a vibration attenuation mechanism. The vibration attenuation mechanism can be modelled as a set of spring of stiffness k and a damper of capacity c. The transmissibility of such single DOF vibration attenuation mechanism can be calculated as [56,58]

$$T = \left| \frac{F_o}{F_i} \right| = \left| \frac{\gamma}{X} \right| = \sqrt{\frac{(1 + (2\zeta r)^2}{(1 - r^2) + (2\zeta r)^2}}, \qquad\qquad 3.14$$

where T is the transmissibility, ζ is the damping ratio, r is the ratio of the input frequency to the undamped natural frequency of the spring and mass, γ is the motion of the ground and X is the amplitude of the response at the mass. The damping ratio ζ is calculated as

$$\zeta = \frac{c}{2\sqrt{km}}. \qquad\qquad 3.15$$

Apparent from Equation 3.14, the transmissibility can be used to calculate the displacement of the system due to the motion of the ground. Given the excitation frequency and the desired maximum allowed transmissibility, it is possible to specify the isolation frequency. In the following sections, the various methods for vibration attenuation are discussed.

32

3.3.1 Pneumatic mounts

A Pneumatic mount consists of a piston maintained inside a container of compressed air for providing vibration attenuation at frequencies down to 0.7 Hz [66]. Figure 3.7 shows a typical example of a pneumatic mount that comprises a piston of cross-sectional area A moving inside a cylinder. The cross-sectional area can take any shape, but it is usually square or round in cross-section. Consider v_i to be the instantaneous initial volume of the cavity between the piston and the cylinder which a fluid occupies. With the settings in Figure 3.7, the initial absolute pressure in the cavity P_i is given by

$$P_i = P_a + \frac{mg}{A},$$
3.16

where P_a is the atmospheric pressure at the level where the pneumatic mechanism is installed and m is the mass of the instrument to be isolated [56,58].
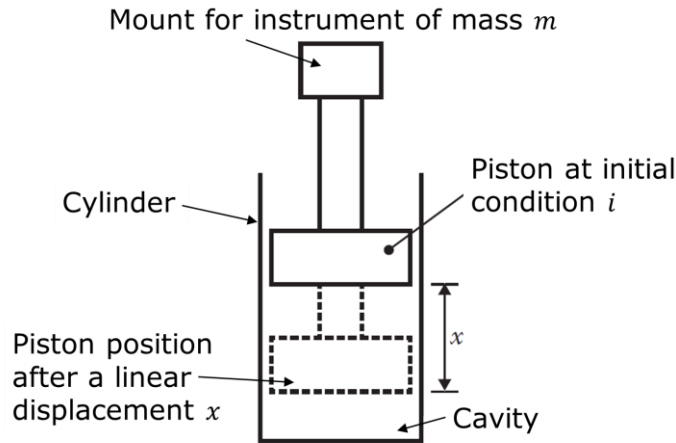
Figure 3.7. Schematic of a pneumatic mount for vibration attenuation.

Assuming the compression process of the fluid in the cavity to be adiabatic (no energy is transferred between the internal cavity and the surrounding) the pressure and volume after a linear displacement of the piston x is calculated as

$$P_i V_i{}^n = P_x V_x{}^n,$$
3.17

where n is the ratio of specific heats, which depends on the fluid occupying the cavity. The ratio n is 1.4 when air is used in adiabatic conditions.

Pneumatic isolators have smaller sizes than other passive isolators used to isolate the same loads and frequencies. The gas volume provides low stiffness and supports the load with pressure. However, pneumatic isolators have relatively high vibration transmissibility for frequencies above 20 Hz, which is a shortfall that can be overcome by isolating the piston from the hard cylinder by a rolling diaphragm seal, as shown in Figure 3.8.
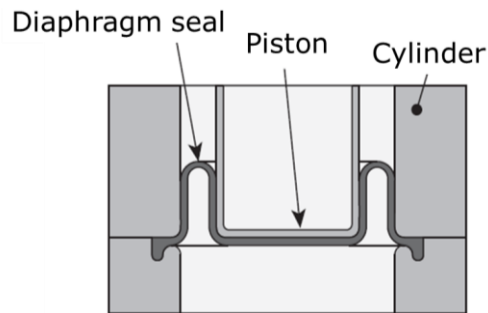
Figure 3.8. Illustration of a rolling diaphragm seal.

A rolling diaphragm seal reduces the transmissibility of the pneumatic isolation mechanism above 20 Hz, however, it has relatively high stiffness and very low damping properties in the horizontal direction. A method for identifying the design parameters of these diaphragms can be found in [67].

The stiffness of a pneumatic isolator k_0 can be calculated as the first derivative of the pressure $\frac{dP}{dx}$ and is given by

$$k_0 = \frac{dP}{dx} = \frac{nP_i A^2}{V_i} \left[\frac{1}{1 - \left(\frac{A}{V_i}\right)x} \right]^{n+1}.$$ 3.18

Equations 3.16 to 3.18 are used to design the parameters of the pneumatic mount, for example, initial volume, stiffness and working pressure, for an instrument of given mass [66].

3.3.2 Elastomer mounts

Similar to the pneumatic mounts, elastomer mounts are used to provide vibration attenuation so as to protect instruments and equipment. Elastomers are used due to their low modulus of elasticity and their high strain capabilities (above 100 %), in comparison to metal vibration attenuation mounts. Different materials can be used in the design of elastomer mounts, for example, rubber, silicone and neoprene. A typical example of an elastomer mount is the elastomer cup mount shown in Figure 3.9. This design is used in a wide range of equipment such as operating machinery, electronic compressors and generators. The operating frequency of an elastomer cup mounts is 12 Hz to 30 Hz and can provide an elongation of up to 300 % as a response to vibration. The cup housing limits the elongation of the rubber mount so as to allow for safe elongation of the rubber without snapping. Other versions of the elastomer mounts exist without the cup housing for higher elongation rates than that achievable with the elastomer cup mounts [68].
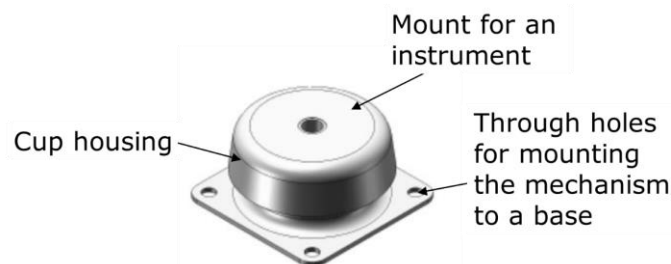
Figure 3.9. Example of an elastomer cup mount mechanism for attenuating vibration of the base [68].

3.3.3 Metal and composite mounts

Metal and composite mounts are used for attenuating vibration in heavy equipment where the environmental conditions can degrade/break the elastomer mounts. Metal and composite mounts provide stability under extreme long-term exposure to temperature fluctuations and dynamic loads. The design and material of these mounts determine the transmissibility, stiffness and damping of the attenuation mechanism. The properties of metal and composites are constant under a large range of temperature; this allows for

accurate modelling of the deflection and damping properties over a wide temperature range. The most common example of a metal mount is the steel-spring axial mount shown in Figure 3.10.
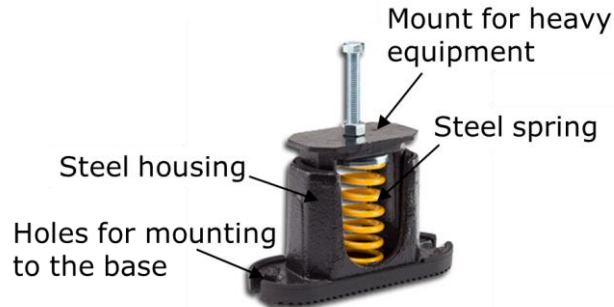
Figure 3.10. Example of a steel-spring mount for vibration attenuation [69].

The steel-spring axial mount is reliable for long-term use with good creep resistance. The mount consists of a steel spring with a housing of metal for protection and axial alignment of the spring. These mounts are commonly used in heating, ventilation and air conditioning (HVAC) systems and marine engines for reducing the amount of transmissibility. The open end of the housing allows for easy examination of the steel-spring. For examining the effectiveness of the spring to provide vibration attenuation, the spring is loaded and unloaded multiple of times; the spring is considered defective if it does not go back to within permissible limits within its original height. The vertical operating frequency of the steel-spring mount f_n is expressed as a function of the static deflection of the spring δ using the formula [68]

$$f_n = 3.13\sqrt{1/\delta}.$$

3.19

3.3.4 Advances in vibration attenuation methods

Advances in the mechanism for vibration attenuation lead to improvements in the energy dissipation mechanisms, for example, frictional and viscous damping. A damping system that does not depend on the relative velocity between the moving components in the damping system is called frictional damping system. A common example of a frictional

36

damping system is the Coloumb damping system. Coulomb damping occurs when a mass slides on a dry surface and is produced by dissipating energy through friction. According to Coulomb's law of dry friction, the damping force is proportional to the normal force which acts on the contact plane, giving a sliding force F of [58,68]

$$F = \mu N = \mu W = \mu mg, \qquad\qquad 3.20$$

where N is the normal force acting on the contact plane, which is sometimes equal to the weight of the sliding object; and μ is the coefficient of friction, which depends on the surface condition and the materials in contact but is otherwise considered to be independent of load, speed, surface texture and contact area. The damping force direction is opposite to the displacement direction and does not depend on the displacement magnitude nor the velocity; it depends on the force acting normally between the sliding surfaces [56,58].
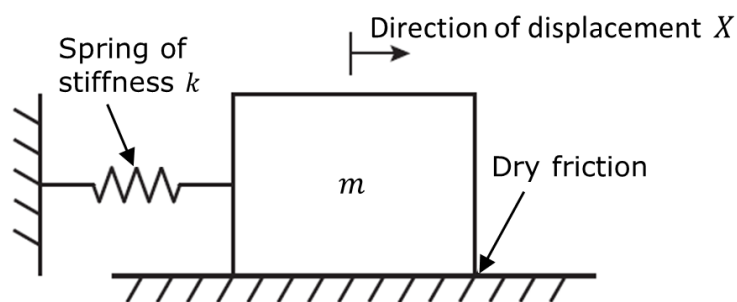
Figure 3.11. Illustration of a frictional damping system.

Consider the single DOF frictional damping system shown in Figure 3.11. The mass m slides on the surface, and the spring causes the displacement to have two values of $+X$ and $-X$ with regard to the initial position. The amplitude of vibration is found to be attenuated by an amount $4\mu N/k$ in each cycle.

The second type of energy dissipation mechanism, viscous damping, is the most commonly applied damping mechanism for reducing the amount of vibration energy induced in the system. In viscous damping, the damping force is considered to be proportional to the relative velocity between two bodies. This is typically achieved using eddy currents or by

using the motion of the body to force the fluid to flow (typical fluids being water, oil or air). Examples include fluid flow between a piston and a cylinder wall; fluid present between two sliding surfaces, or fluid being squeezed out of two parallel surfaces (called squeeze film damping); and fluid present between a bearing and a journal.
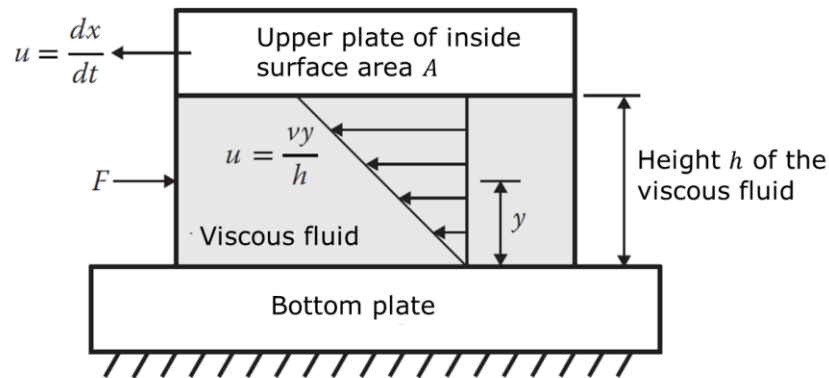
Figure 3.12. Illustration of a viscous damping system.

In Figure 3.12, the two parallel plates of a viscous damper have a distance h and a fluid of viscosity μ between them. The two plates can move parallel to each other in the same direction with different velocities v, or in opposite directions with equal or unequal velocities. For simple modelling of the viscous damping system, one plate should be considered stationary, while the other plate is moved with a relative velocity v to the stationary plate. The fluid particles in contact with the stationary plate do not have any velocity ($v = 0$), while those in contact with the upper moving plate (as shown in the example in Figure 3.12) travel with the same speed v as the plate. Newton's second law for viscous flow, indicates that the shear stress τ of a fluid particle in a layer of distance y from the lower fixed plate can be expressed as

$$\tau = \mu \frac{du}{dy},$$ 3.21

where the differential term $\frac{du}{dy}$ is the velocity gradient. The resisting force developed on the inside surface of the upper plate is the product of shear stress and area

$$F = \tau A = \mu \frac{Av}{h}, \qquad\qquad 3.22$$

where A is the surface area of the upper plate. Since μ, A and h are all constants, can be written as

$$F = cv, \qquad\qquad 3.23$$

where $c = \mu A/h$ is the damping constant [56,58].

An example of the advances in energy dissipation mechanisms (i.e. in frictional and viscous damping) is the elastomeric seismic bearing and the friction pendulum system. The elastomeric seismic bearing consists of a bearing made of an elastomeric material and filled with lead. The bearing is used for providing high damping of ground vibration. An example of an elastomeric bearing is shown in Figure 3.13 where the elastomeric layers are constrained by intermediate plates to maintain compression stiffness under vertical loads. The equivalent viscous damping of an elastomeric bearing is a property of the material and has a damping ratio ζ in the range from 0.1 to 0.15. The natural frequency of the elastomeric bearing is typically between 0.75 Hz to 1.5 Hz.
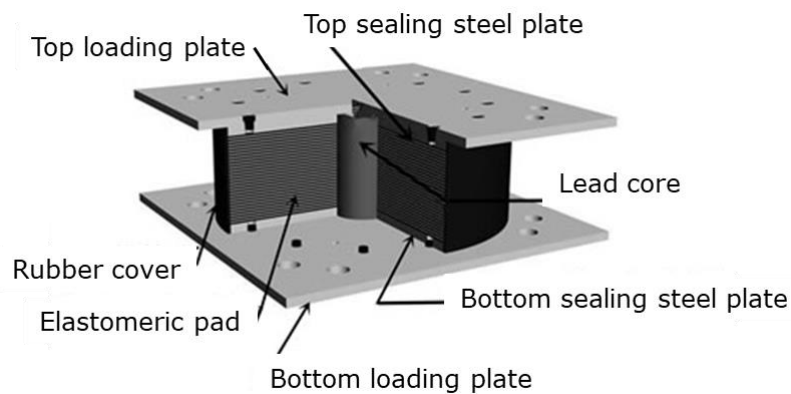
Figure 3.13. Illustration of an elastomeric bearing used for attenuating seismic vibration [70].

The friction pendulum system is a vibration attenuation mechanism for protecting equipment against seismic vibration. The pendulum system is made from steel and consist

of an articulated friction slider that slides along the concave of a spherical surface. This system, shown in Figure 3.14, reduces the amplitude of pendulum motion of the supported structure.
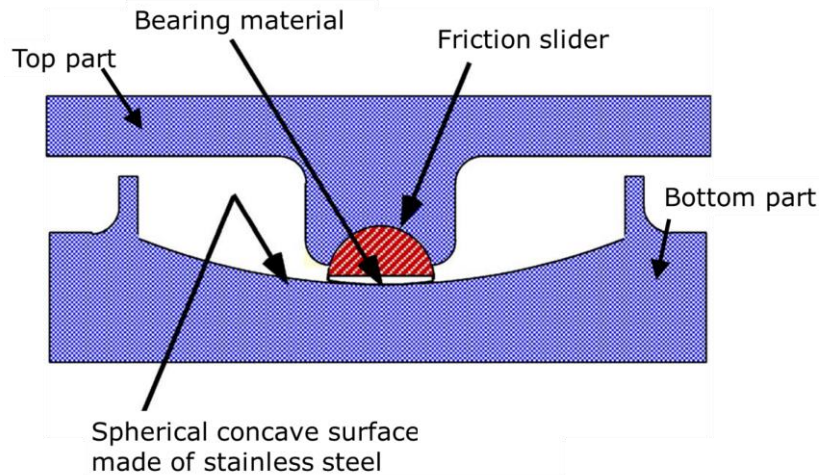
Figure 3.14. Illustration of a friction pendulum system [71].

The upper part of the system is attached to the supported structure. Relative sliding motion between the upper part and the lower part of the system starts when the friction force is exceeded. The natural frequency of the frictional pendulum system is between 0.5 Hz to 1.0 Hz.

The vibration attenuation methods discussed in this section reduces the magnitude of vibration through isolation or damping of excitation waves [54,72,73]. Damping is different from isolation in the sense that it reduces a vibration amplitude by using high mass - high stiffness structures. Damping reduces the magnitude of vibration transmission in frequency regions close to the natural frequency (see Figure 3.15). The characteristics of a damping system include having an attenuation system of high stiffness for the purpose of increasing the natural frequency of the attenuation system and providing a frequency range of attenuated vibration as illustrated in Figure 3.15. The second approach for attenuation of excitation waves, vibration isolation, reduces the magnitude of vibration magnitudes (kept below 0 dB) by isolating certain frequency ranges through energy

absorption and results in much higher attenuation than in damping (which is limited to transmission values $\geq$ 0 dB, see Figure 3.16).
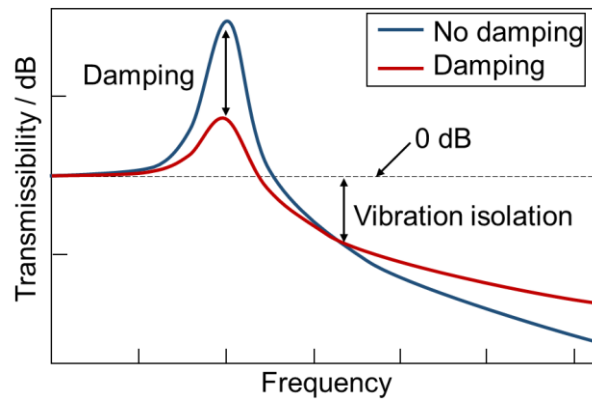
Figure 3.15. Illustration of the difference between damping and vibration isolation; vibration isolation is more favourable because it provides higher attenuation of vibration magnitudes [54].

The energy absorption mechanism in vibration isolation necessitates having a structure of relatively lower stiffness than in damping for the same frequency of interest (see Figure 3.16b). This is to reduce the natural frequency of the structure which is proportional to the square root of the stiffness of a structure. The energy absorption characteristics of vibration isolation structures are similar to that of lattice structures discussed in Section 2.4 (i.e. releases the absorbed energy in mechanical forms that include bending, compression and stretching). If lattice structures with vibration isolation capabilities are used in metrology and precision engineering, then instruments and machines could have a vibrational response below 0 dB. This also leads to savings in mass and material.
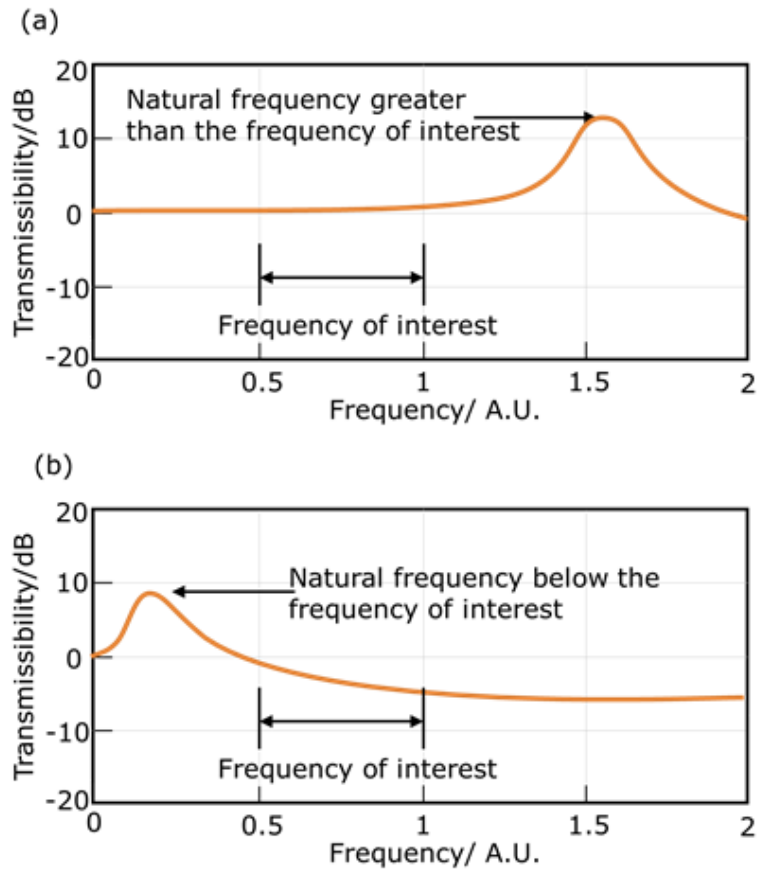
Figure 3.16. Illustration of the response of (a) high stiffness-high mass damping structure, and (b) low mass isolation structure, tailored for a certain frequency of interest.

3.4 Lattice structures and vibration attenuation

Wang et al. [74] drew on the importance of lattice structures to provide vibration attenuation through damping and suggested a method for optimisation of the natural frequency of 3D printed lattice structures. The method targets reduction in mass as well as optimisation of natural frequency for dynamical design problems. Wang et al. experimentally verified the natural frequency on a cantilever plate-like lattice (i.e. a lattice with unit cells tessellated in space along two directions) and showed a reduction in mass and optimisation of the natural frequency. This method can be used for providing vibration attenuation at frequencies lower than the optimised natural frequency. The drawbacks of the study are that it neglected different types of strut-based and triply periodic minimal

surface (TPMS) lattice structures, not necessarily plate-like lattice structures, for their ability to provide vibration isolation at frequencies lower than and greater than the natural frequency. As shown in Figure 3.16b, at frequencies greater than the natural frequency (vibration isolation) the attenuation can be higher than the attenuation at frequencies below the natural frequency (damping). There is a need to design lattice structures and test their ability to provide tunable vibration isolation at frequencies greater than the first natural frequency for use in metrology and precision engineering applications.

3.5 Bandgaps

Both damping and vibrational isolation (the two conventional methods for vibration attenuation) do not restrict the propagation of elastic waves. This limits the extent of the achievable vibration attenuation. Additive manufacturing phononic bandgap structures based on repeating lattice unit cells provide a new approach to vibration attenuation, with low vibration transmission and high tunability to meet the requirements of metrology and precision engineering applications, without the cost of high-mass structures.

Phononic bandgap structures are those in which elastic wave propagation is restricted at certain frequencies. These have received considerable attention recently, mainly for their ability to provide enhanced vibration attenuation compared to that resulting from conventional vibration attenuation approaches. The concept of bandgaps emerged from solid-state physics, with recent use in electronic systems [75–77], photonics [78–81] and phononic structures [63,82–86]. Bandgaps generally result from Bragg-scattering, in which transmitted and reflected waves within a periodic medium undergo destructive interference [62,64,87–90]. The bandgap frequencies depend on the geometry and size of the repeating lattice unit cell [91]. Bandgaps can also arise through a different phenomenon called internal resonance, where the energy of elastic waves of certain frequencies is absorbed by internal resonators embedded in the structure [92–96]. These bandgap formation mechanisms are illustrated in Figure 3.17. In Figure 3.17a, elastic

43

waves are reflected due to the difference in mechanical impedance within the lattice structure. These waves destructively interfere with the propagating wave when they are out of phase with one another, leading to a Bragg-scattering bandgap.
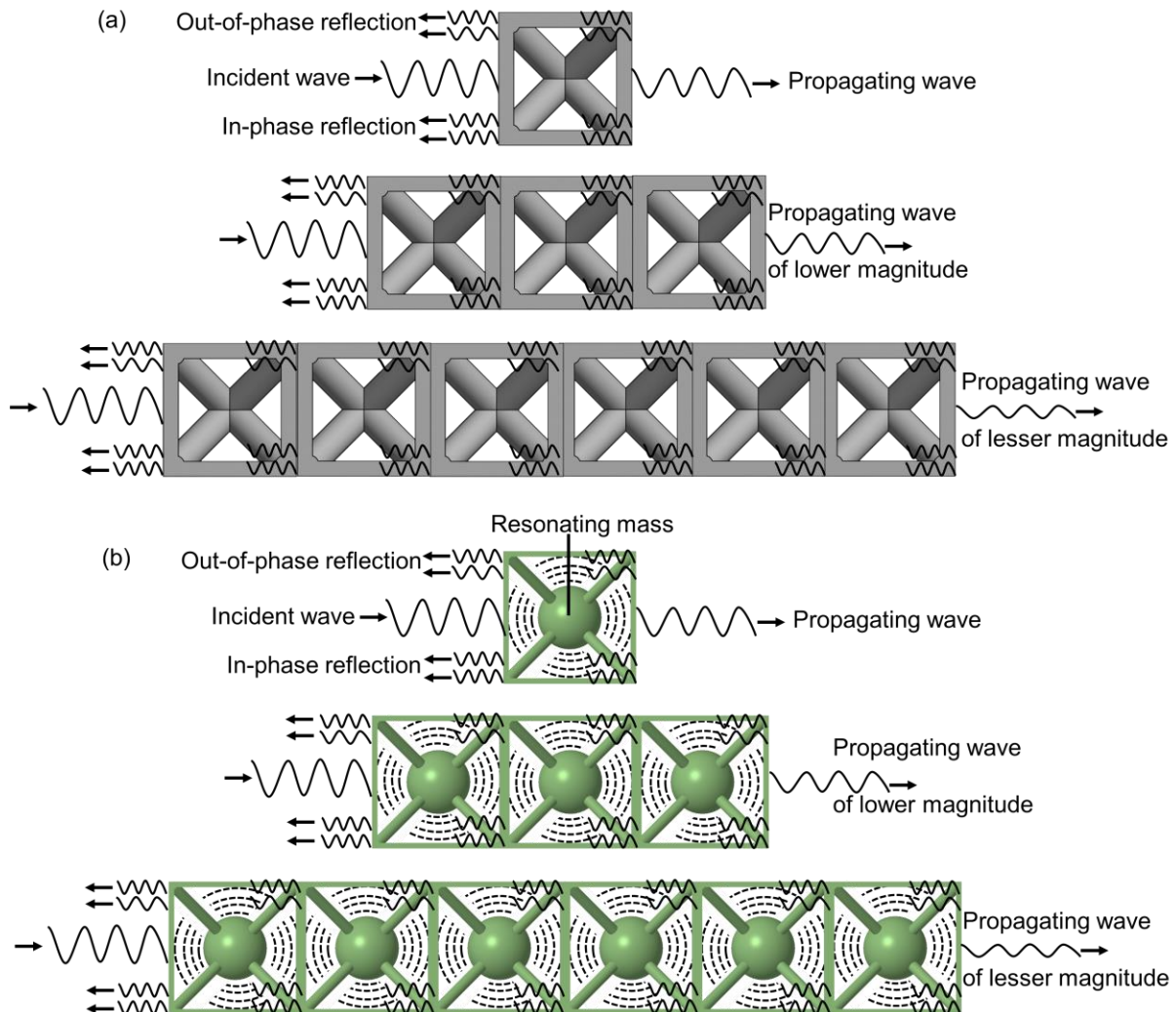
Figure 3.17. Illustration of the bandgap mechanism in (a) Bragg-scattering lattices and (b) internal resonance lattices.

In Figure 3.17b, another bandgap formation mechanism co-exists alongside Bragg-scattering; the energy of the elastic waves is absorbed by a resonating mass in each unit cell to create an internal resonance bandgap. For both bandgap formation mechanisms, increasing the lattice periodicity leads to higher attenuation of transmitted waves within the bandgap frequency range [90,91].

The reflection of waves in Bragg-scattering occurs due to the difference in the impedance, for example, local density, of the bandgap structure. For the in-phase reflection to occur, the Bragg law has to be satisfied [91] which is expressed as

$$n\lambda \sim 2L, \qquad\qquad 3.24$$

where λ is the wavelength, n is an integer number and L is the unit cell size of the lattice. From Equation 3.24 it can be seen that Bragg's law is highly dependent on the unit cell size of the lattice structure. Bragg-scattering starts to occur when the wavelength is approximately equal to twice the cell size of the lattice [91]; around a normalised frequency (the quotient of cell size and wavelength) of 0.5. Thus, there is a limiting dependency on the size of the unit cell of the lattices to form bandgaps by Bragg-scattering. As a result of this dependency, unrealistic cell sizes need to be employed to satisfy the Bragg law at low frequencies. For example, consider a bandgap lattice with normalised bandgap frequency of 0.5.
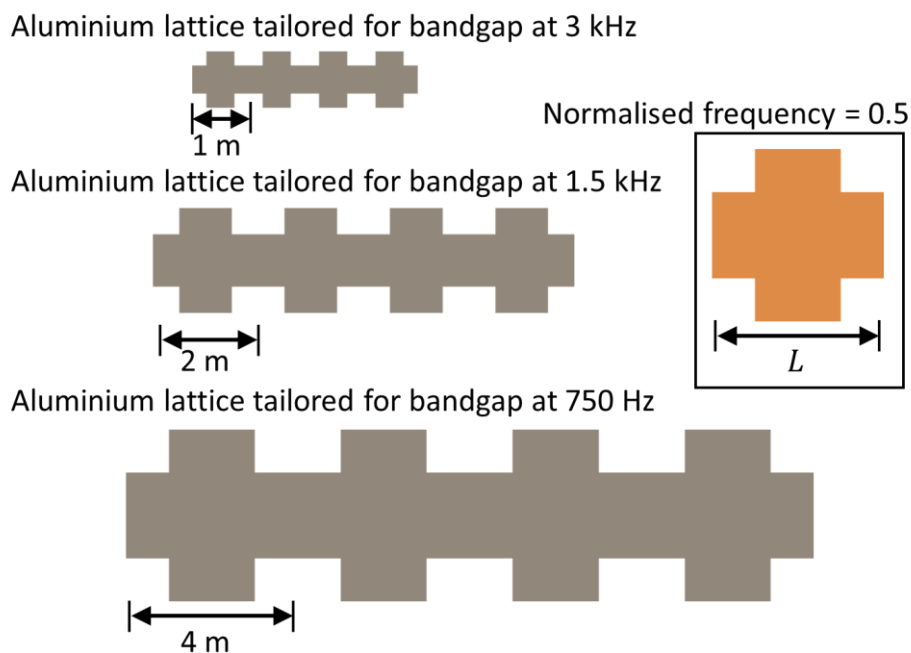
Figure 3.18. An illustrative example of the relationship between the normalised bandgap frequency and the cell size L.

When manufactured from aluminium (speed of longitudinal wave is 6320 m·s^{-1}) [82] to obtain bandgaps frequencies below 3 kHz (corresponds to common vibration frequencies in metrology and precision engineering), this Bragg-scattering lattice has to have a unit cell at least 1 m in length (see Figure 3.18). Despite being challenging to manufacture, a lattice with cells as large as 1 m has limited periodicity within a constrained design volume (as that of metrology and precision engineering instruments) which causes reduced attenuation within the bandgaps. See Figure 3.3 for example of metrology and precision engineering instruments. For this reason and as will be shown in later chapters, the bandgap lattices that will be developed in this thesis for metrology and precision engineering will mainly depend on the internal resonance mechanism.

Bandgaps are classified, according to the periodicity required for their presence in a material, into 1D bandgaps, 2D bandgaps and 3D bandgaps. A 1D bandgap requires a periodicity of the single unit cell in a single direction to form a beam-like structure; a 2D and 3D bandgap structures require periodicity of the single unit cell in two and three directions to form plate-like, and cubic-like structures, respectively. Figure 3.19 shows examples of different types of bandgap structures. The frequency of the bandgap (bandwidth) would differ depending on the periodicity. In other words, if a unit cell has a 1D bandgap, it does not necessarily mean it has 2D or 3D bandgap. Even if this unit cell has a 2D and a 3D bandgap, it is most probably not going to be within the same frequency range. This is because the underlying wave propagation and, as a consequence, wave reflection occurring at each of the structures are completely different. The reflection of waves illustrated earlier by Figure 3.17a is one of the simple forms. However, in reality, the reflection is much more complicated, differs with the types of propagating waves and can be understood through the study of the corresponding dispersion curves (see Section 3.6).
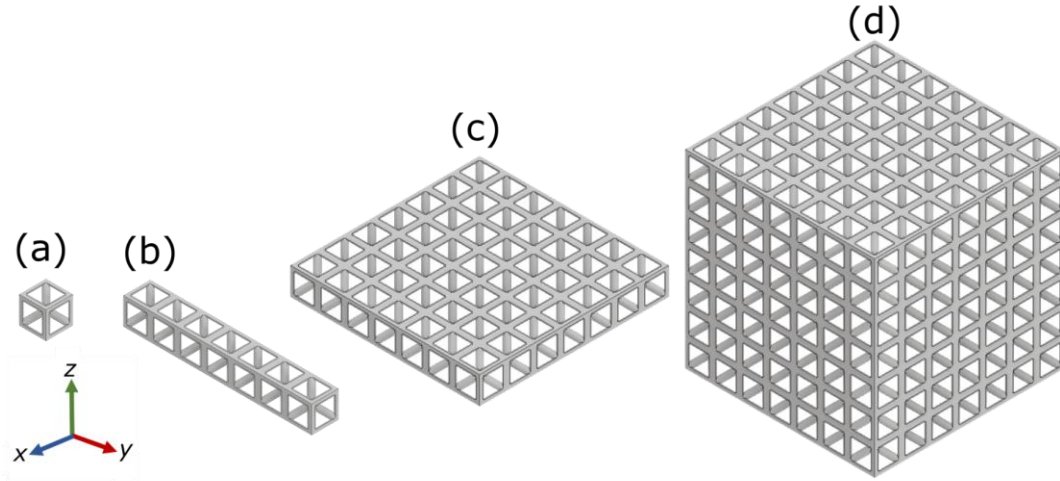
Figure 3.19. Example of (b) 1D, (c) 2D and (d) 3D bandgap structures of the single unit cell shown in (a).

3.6 Methods for identification of bandgaps

The complex forms of wave propagation and reflections can be represented using dispersion curves (bandplots) from which the bandgap frequency regions are identified. Dispersion curves show propagation frequency in one axis and wave vectors in the other axis (see illustrative example in Figure 3.20). The wave vectors describe the wave number (number of radians per unit cell) and the direction of travel of the waves. The wave number k is calculated as [64,98]

$$k = \frac{2\pi}{L}.$$ 3.25

Dispersion is a characteristic of mediums in which the speed of propagation of a wave depends on the medium. The relationship between the frequency and the wave vector is non-linear in dispersive mediums and linear in non-dispersive mediums. For two points along a wave band in a dispersion curve, the dispersion s can be calculated as

$$s = \frac{\omega_2}{k_2} - \frac{\omega_1}{k_1},$$ 3.26

where ω is the frequency of wave propagation. This is to say that the phase velocity is changing with the frequency. For any two points on a wave band, if $s = 0$, then the medium is non-dispersive and if $s \neq 0$, then the medium is dispersive.
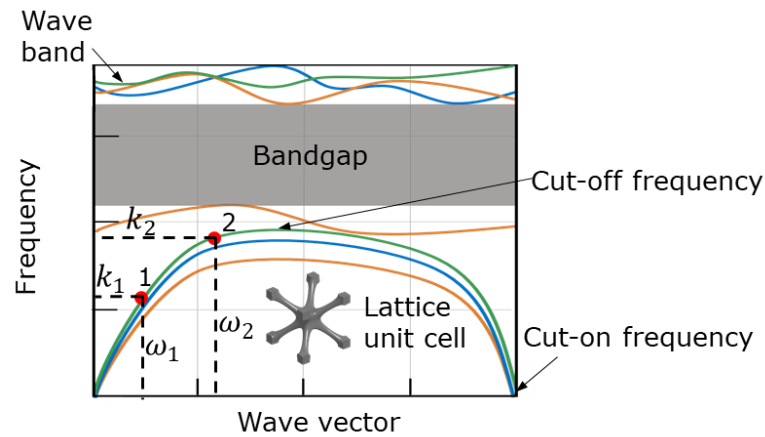
Figure 3.20. Illustration of the dispersion curves (bandplot) from which bandgaps are identified. The shaded grey area represents the bandgap where no wave bands exist.

Dispersive medium has the ability to cut-off (i.e. stop the propagation) of a wave at a certain frequency. At frequencies higher than the cut-off frequency of a wave travelling in a dispersive medium, some other types of waves can cut-on (i.e. start propagating). Any frequency range between any two wave bands is a bandgap where there is no propagation of waves [91] (see Section 3.5 for further details). Dispersion curves can be modelled using many different techniques, of which the most elementary is the analytical technique by which the structure is modelled as a set of mass and springs elements (see Section3.2). An analytical technique is fast and easy to use for very simple structures (noncomplex structures like that in the work of Raghavan et al. [99] and James et al. [100]) and for modelling individual types of waves. The classification of lattices into simple and complex is arbitrary and no characterisation technique is found in the literature for that. In this work, we define simple lattices as periodic structures assembled from single or multiple beams or slabs; these simple lattices are suitable for modelling using the analytical methods (see Figure 3.21a). We define complex lattices as periodic lattices of higher

48

number of geometrical features than simple lattices and can not be modelled using analytical techniques (see Figure 3.21b).

For modelling complex structures and/or multiple types of waves, many methods exist. For example, a plane wave expansion method (PWE) is a Fourier space method that is highly efficient in calculating vibration modes in periodic structures. Despite being more accurate and efficient than the analytical method for modelling more complex structures, like in the work of Trainiti et al. [101] and Kuang et al. [102], the PWE method provides highly inaccurate results when modelling the dispersion curves of structures of high difference in local impedance. The difference in local impedance is what provides the wave reflection (see Section 3.5) and is essentially the difference in densities and modulus within certain regions in a structure.
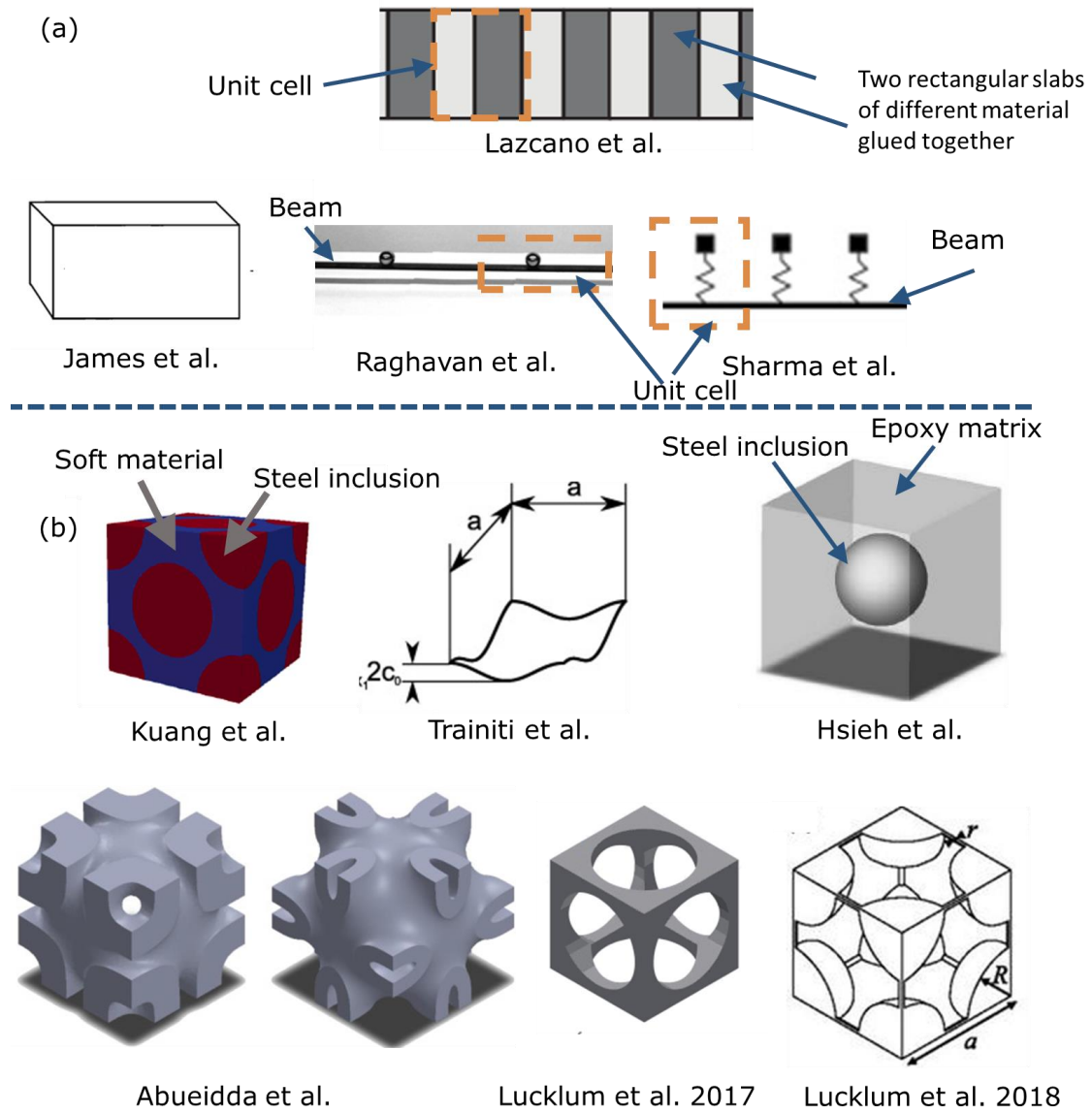
Figure 3.21. Illustration of different types of (a) simple lattices and (b) complex lattices.

PWE also suffers from the scaling effect. This means that, in comparison to other modelling techniques, there is higher scaling of the mathematical problem with the number of plane waves used in the modelling [103] (i.e. the mathematical problem becomes larger and more complicated to solve). Dispersion curves can also be modelled using finite-difference time-domain method (FDTD). FDTD operates in the time-domain and replaces all time derivatives with finite-difference approximations. FDTD can parallelise large problems and model structures with high difference in impedance like that in the work of Hsieh et al.

50

[104] and Sigalas et al. [105]. The main issue with FDTD is that it can not efficiently model curved regions or narrow bands. FDTD requires a higher number of time steps for a suitable representation of narrow bands in comparison to wider bands [106]. By far the most computationally efficient and most accurate method for modelling dispersion curves of both complex and simple structures is the finite element method (FEM) [96,107]. FEM subdivides the whole structure into elements [108]. The subdivision results in accurate representation of complex structures, easy capture of local effects, for example, local resonance, and incorporation of dissimilar regions and materials. For these reasons, FEM is used in structural, heat transfer, fluid flow, mass transport, acoustic, and elastic, wave propagation and electromagnetic analyses [109]. An example of the use of FEM for modelling wave propagation in complex structures can be seen in the work of Abueidda et al. [82] who modelled the acoustic dispersion curves of various TPMS lattices and Lucklum et al. [110] who studied elastic wave propagation in a simple cubic lattice with local resonators.

3.7   Recent work on bandgap structures

In this section, the recent work on bandgap structures is reviewed based on their bandgap type, modelling method, material type and frequency scale. This section is important for identifying any gaps in knowledge about bandgaps which were addressed in this study. Various AM Bragg-scattering bandgap lattices have been studied. For example, Warmuth et al. [111] manufactured and tested bandgap lattices based on interconnected struts. Wormser et al. [112] experimentally identified bandgaps in lattices similar to those of Warmuth et al. [111]. Lucklum et al. [113] presented strut-based lattices at the millimetre scale. Non strut-based AM bandgap lattices can be seen in the work of Abueidda et al. [82] who tested some forms of TPMS lattices. The work of Abueidda et al. [82] targeted acoustic waves only (not elastic waves) and only examined the network and matrix forms of primitive, Schoen and Nevious TPMS lattices. The most common types of

TPMS lattices still need to be investigated for their ability to provide bandgaps (i.e. gyroid and diamond lattices). Nevertheless, the literature on bandgaps also does not examine the ability of any of the TPMS lattices to provide bandgaps of elastic waves. Since TPMS have higher stiffness than strut-based lattices, the addition of bandgaps to their existing properties would allow for their multifunctional use in applications that require structural and dynamic support. Non strut-based AM bandgap lattices can also be seen in the ceramic lattice work of Kruisova et al. [114] and Ampatzidis et al. [88]. Ampatzidis et al. designed and manufactured a 1D bandgap structure from two materials glued together. The structure included a composite panel for the use in aerospace applications and provided bandgaps above 7 kHz. Kruisova et al. obtained multiple 2D bandgaps within the megahertz frequency range using single-material structures.

On the structural side, research on TPMS lattices has mainly focused on their mechanical and heat dissipation properties [41,45,115]. It is critical to examine the ability of TPMS lattices to provide elastic waves bandgaps if these lattices are to be employed in general cases for vibration attenuation. Because of their high specific stiffness and large surface-to-volume ratio [4,116], TPMS lattices could see use in the aerospace sector, where heat exchangers are commonly integrated into structural elements [117], and in precision and measuring instruments. Further applications exist as support structures in the automotive and aerospace sectors, where vibration attenuation and impact resistance are essential properties [118].

Previous work on strut-based lattices, namely the body-centred cubic (BCC) lattice, showed that it has good manufacturability from polyamide and metal with L-PBF [54] [29]. The BCC lattice has a high strength-to-weight ratio in comparison with other strut-based lattices, for example, those comprising simple cubic (SC) and face-centred cubic (FCC) cells [119]. BCC lattices with additional reinforcement struts along a single direction were studied by Leary et al. [119], who concluded that these lattices have higher impact energy

absorption than the conventional BCC design. To the best of the author's knowledge, the propensity for BCC lattices with reinforcement struts to form bandgaps has not been studied. Syam et al. [54] determined the natural frequencies of BCC lattices with additional reinforcement struts in the x-, y- and z-directions (designated as BCC$_{xyz}$) for vibration attenuation purposes, but did not model the dispersion curves of the lattice, and did not report on the effect of the lattice volume fraction on achieving vibration attenuation. Lu et al. [86] and Hsieh et al. [104] independently predicted the dispersion curves of multimaterial BCC lattice designs, but to date, there have been no reports on the manufacturability or performance of these designs. In comparison to single material AM, which is well-established, multimaterial AM currently requires manual assembly (such as in the lattice work of Matlack et al. [62]), requires support structures which constrain the design of the part, necessitates post-processing (such as in the work of Choi et al. [120]) and is limited to a small range of materials.

It is possible to form bandgaps below the lowest Bragg limit, as discussed in Section 3.5, by using internal resonators which are independent of the Bragg law. The bandgaps in internal resonance lattices are formed by hindering the wave propagation at frequencies close to the natural frequency of the internal/local resonators [92,121,122]. The benefits of internal resonance lattices include increased design freedom and flexibility to obtain bandgaps in structures of suitable sizes for AM and of higher periodicity within a design volume in comparison to Bragg-scattering lattices [123–125]; resulting in better-defined bandgaps, more homogenous structures, more predictable mechanical properties and higher tolerance to the effects of defects. The single unit cell has less contribution towards the overall stiffness and properties in higher periodicity lattices, for example, internal resonance lattices, when compared to structures of lower periodicity. Research on internal resonance lattices includes the work of Liu et al. [126], who first developed an internal resonance lattice using solid cores and silicone rubber coatings. The periodic coated spheres of Liu et al. [126] exhibited bandgaps at low frequencies (400 Hz). Numerous

locally resonant internal resonance lattices have been proposed. An example by Fang et al. [127] showed arrays of resonators with high vibration attenuation at frequencies close to their natural frequency. Qureshi et al. [128] numerically investigated the existence of bandgaps in cantilever-in-mass lattices. Lucklum et al. [110] and D'Alessandro et al. [129] independently verified the existence of bandgaps in ball-rod resonating lattices. Zhang et al. [130] presented results of a beam lattice with local resonance bandgaps. Bilal et al. [131] reported on the concept of combining local resonance with Bragg-scattering to form trampoline lattice with subwavelength bandgaps. Matlack et al. [62] developed a multi-material structure that has wide bandgaps using a similar concept to that of Bilal et al [131]. Most of the above work, regarding both Bragg-scattering lattices and internal resonance lattices, has employed analytical techniques to model and optimise the suggested unit cells. Because analytical techniques can only model simple designs, the potential for exploring the elastic capabilities of complex internal resonance lattices designs has been limited.

Table 3.1 summarises the most recent work on bandgap structures by reviewing the dimensionality of the bandgaps (i.e. 1D, 2D or 3D), material type (single- or multi-material), structure type and frequency scale. Despite the advancement achieved by the use of internal resonance lattices, these lattices still suffer from manufacturing and size issues when targeting bandgaps in the hertz to low kilohertz scale (10 Hz to 3 kHz). Of significance here is the work of Sharma et al. [124] who suggested a multi-material bandgap structure that provided bandgap between 147 Hz to 364 Hz. Despite the fact that this frequency range is very low, the structure is only effective in 1D and no information has been provided about the manufacturability or the experimental response of the structure of Sharma et al. [124]. Demonstrating the manufacturability and the experimental response of the proposed lattices is important for its adoption in metrology and precision engineering applications.

Table 3.1. Review of recently published work on phononic bandgaps. Bragg-Scattering: BS, Internal resonance: IR, Elastic waves: EW,

Longitudinal: L, Flexural: F, Acoustic waves: AW, Single material: SM, Multi-material: MM.

Authors	Lattice type	Material type	Bandgap type	Dimensionality	Frequency scale	Dispersion curves calculation method	Targeted waves	Manufacturing and experimental validation
Kruisova et al. [132]	Strut-based/complex	SM	BS	2D	MHz	FEM	EW	Yes
D'Alessandro et al. [129]	Novel/complex	SM	IR	3D	kHz	FEM	EW	Yes
Raghavan et al. [99]	Simple	MM	IR	1D	Hz	Analytical	L EW	Yes
Lazcano et al. [133]	Simple	MM	BS	1D	GHZ	Analytical	L AW	Yes
James et al. [100]	Simple	MM	BS	1D	-	Analytical	L AW	Yes
Sharma et al. [124]	Simple	MM	BS and IR	1D	Hz	Analytical	F EW	No
Trainiti et al. [101]	Simple	SM	BS	1D and 2D	kHz	PWE	EW	No
Abueidda et al. [82]	TPMS/complex	MM	BS	3D	kHz	FEM	AW	No
Lucklum et al. [110]	Novel/complex	SM	IR	3D	kHz	FEM	EW	Yes
Phani et al. [63]	Strut-based	MM	BS	2D	-	FEM	EW	No
Croenne et al. [134]	Simple	MM	BS	2D	MHz	MST	EW	Yes
Kuang et al. [102]	Simple	MM	BS	3D	-	PWE	EW	No
Wormser et al. [112]	Strut-based/complex	SM	BS	3D	kHz	FEM	EW	Yes
Matlack et al. [62]	Strut-based/complex	MM	BS and IR	1D	kHz	FEM	EW	Yes
Ampatzidis et al. [88]	Novel	MM	BS	1D and 2D	kHz	FEM	EW	Yes
Hsu et al. [135]	Simple	SM	BS	1D	-	FEM	AW	Yes
Wang et al. [136]	Novel/complex	SM	BS	3D	MHz	FEM	EW	No
ZhiZhong et al. [137]	Simple	MM	BS	1D	-	PWE	EW	No
Hsieh et al. [104]	Simple	MM	BS	3D	Above 100 kHz	FDTD	EW	No
Bilal et al. [131]	Novel	SM	BS and IR	2D	-	FEM	EW	No
Lu et al. [86]	Simple	MM	BS	3D	Above 60 kHz	FEM	EW	No

3.8 Summary

Lattice structures have geometries which foster the occurrence of destructive wave interference. The destructive interference of waves can lead to the development of bandgaps, which are frequency regions with no wave propagation of high vibration attenuation capabilities (typically of transmissibility below 0 dB). For creating bandgaps, the work from literature examines multi-material lattices. In comparison to single material AM, which is well-established, multi-material AM currently requires manual assembly (such as in the lattice work of Matlack et al. [62]), requires support structures which constrain the design of the part, necessitates post-processing (such as in the work of Choi et al. [120]) and is limited to a small range of materials. Development of lattices that can obtain bandgaps using only a single material would facilitate the process of obtaining bandgap structures and would provide better vibration attenuation performance. The work on bandgap lattices for low-frequency vibration attenuation has also mainly focused on 1D lattices. In reality, a 3D lattice (i.e. lattice with periodicity in 3D) is essential if they are to be used in metrology, precision, aerospace and automobile applications; this is because they can provide enhanced, and tailorable, mechanical and vibrational capabilities in comparison to solid structures. In addition, a wide range of lattice structures has not been tested for their ability to develop bandgaps. The existence of 3D phononic bandgaps would add vibration attenuation to the existing panoply of controllable mechanical performance of the lattice structures [46,47,115,116,119]; thus enabling them to simultaneously fulfil various mechanical and vibration attenuation functions.

Chapter 4

Methodology

The motivation behind this project, as described in Section 1.1, is to enhance the vibration attenuation of precision engineering and measuring instruments. Lattice structures, manufactured and realised by the advancement in AM, are suitable structures to be used in the manufacturing of precision and measuring instruments; due to their intrinsic load-bearing and vibration attenuation capabilities (see Chapter 2 and 3). However, different knowledge gaps as discussed in Chapter 2 and Chapter 3 prevent the realisation of enhanced vibration attenuation performance in lattice structures. In the context of vibration attenuation, the knowledge gaps are related to the design techniques, modelling methods, and vibration attenuation performance of lattice structures and they are as follows:

- No knowledge on the ability of additively manufactured lattices to provide vibration attenuation at frequencies greater than the natural frequency. At frequencies greater than the natural frequency, high attenuation (below 0 dB) is usually achieved.

- No knowledge about the bandgap formation ability of some strut-based lattices and all TPMS lattices (standard lattices). Within the bandgap frequency range, it is guaranteed that the attenuation is below 0 dB.

- No sufficiently detailed methodology published for modelling 3D wave propagation.

- Little research on single-material lattices for obtaining 3D bandgaps in the hertz to low kilohertz frequency range. This is particularly important to provide 3D attenuation of lab environment vibration.

The work for filling the knowledge gaps will be broken down into three work packages (WPs) as shown in Figure 4.1.
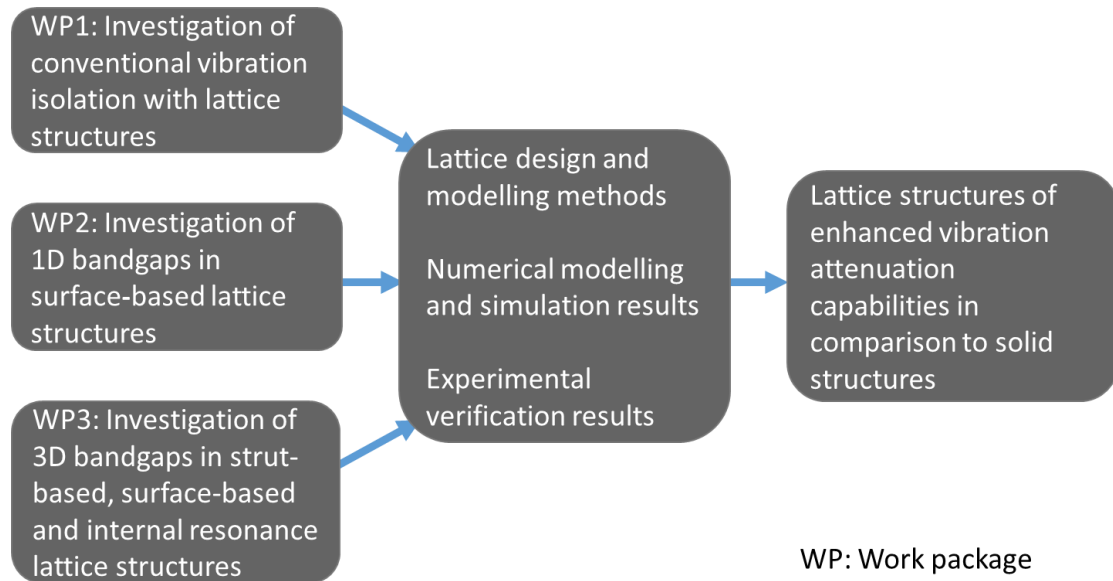
Figure 4.1. Breakdown of the work in this project into manageable work packages.

4.1 Methodology for conventional vibration isolation with lattice structures

This section details the methods used in WP1 of this project. The aim of WP1 is to examine the ability of lattice structures for providing vibration attenuation at frequencies greater than the natural frequency (called vibration isolation). The methodology for approaching this is outlined in Figure 4.2. WP1 will characterise lattice structures (i.e. determining the minimum number of unit cells required to form a lattice) and study the effect of lattice unit cell size, volume fraction and tessellation on the natural frequency. A case study for showcasing the ability of lattice structures to provide vibration isolation at frequencies greater than the first natural frequency will be presented. The results of WP1 are discussed in Chapter 5.
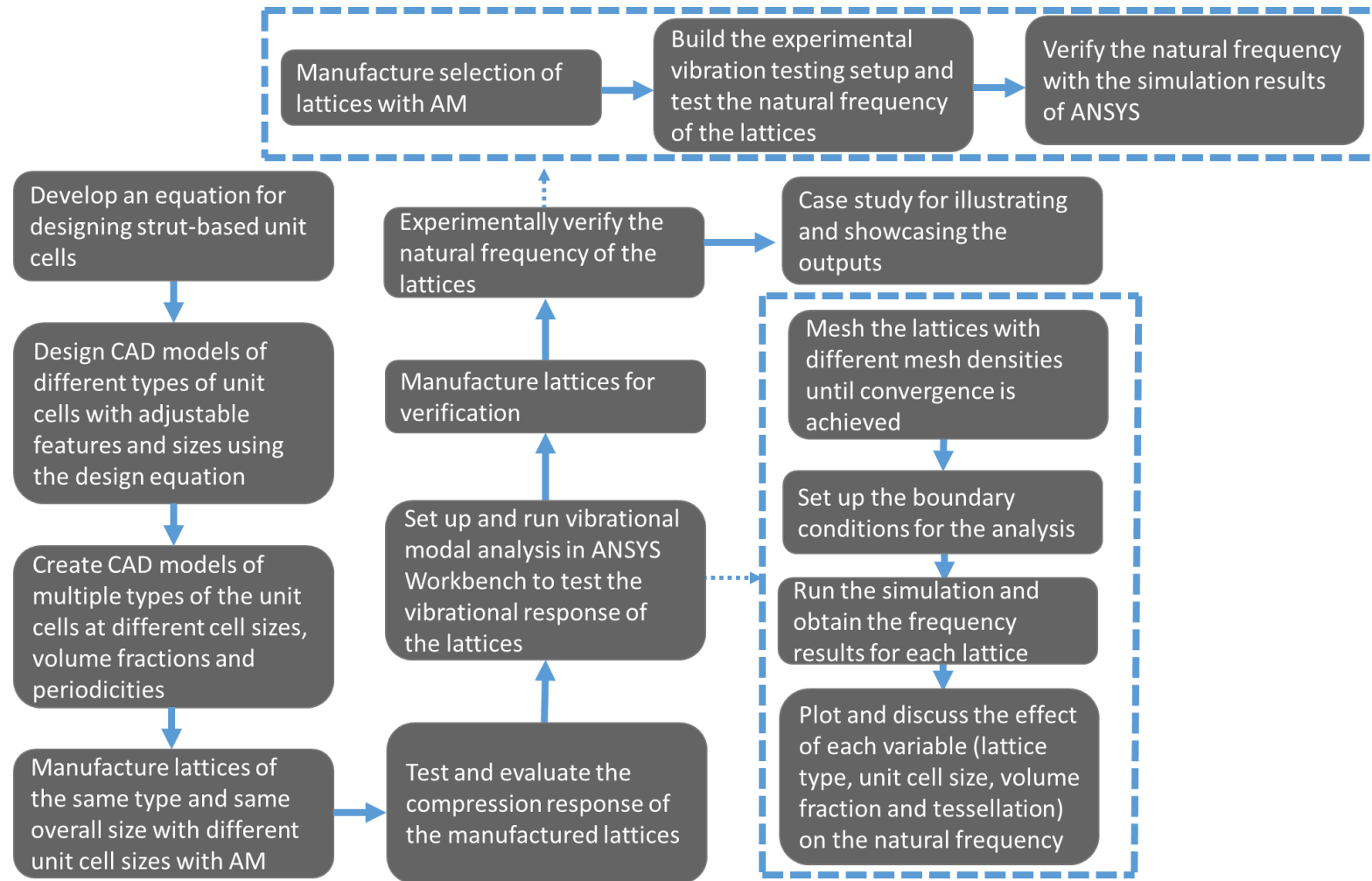
Figure 4.2. Methodology for examining the ability of lattices to provide vibration isolation.

4.1.1 Strut-based lattice design

The design of lattice structures for AM is a significant challenge. A simple tool in the form of an equation will be developed to allow the design of various strut-based lattices based on the desired volume fractions. The equation allows the calculation of the exact diameter of a strut-based unit cell based on the pursued volume fraction ρ^* and number, and type, of struts. The solid volume V_s of a strut of length L_t and circular cross-section of diameter d is calculated as

$$V_s = \frac{\pi}{4}d^2L_t.$$

4.1

Multiple struts of different lengths exist in a strut-based lattice. As detailed in Section 2.3, inaccurate calculations of the volumes of lattice structures are obtained when the intersection volumes between the struts are not considered (see Figure 4.3). To remedy this, the orientation, total length and intersection length of the struts should be represented in the design equation.
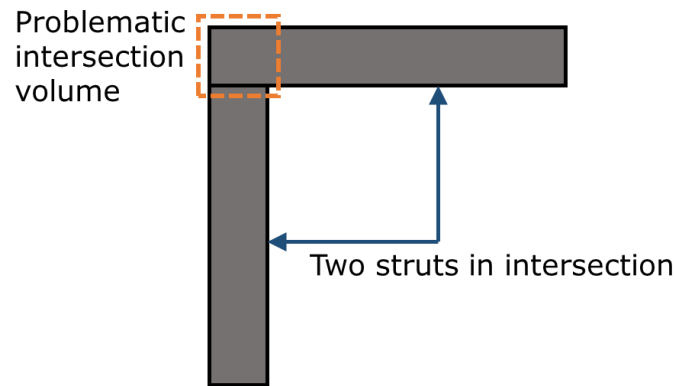
Figure 4.3. Illustration example of two struts intersecting with each other.

The total length L of all cylindrical members in a strut-based lattice is calculated as follows

$$L_t = a_1L + a_2C_l + a_3C_l + b\sqrt{2}C_l + c\sqrt{3}C_l,$$

4.2

where a_1 is the number of horizontal struts of length L as they appear in the top and bottom views of a single lattice cell; a_2 is the total number of vertical struts of length C_l as

they appear in top and bottom views of a single lattice cell; a_3 is the total number of vertical struts of length C_l as they appear in front, back and side views; b is the total number of diagonal struts on all faces and c is the number of diagonal members across the centre of the lattice cell (see example in Figure 4.4).
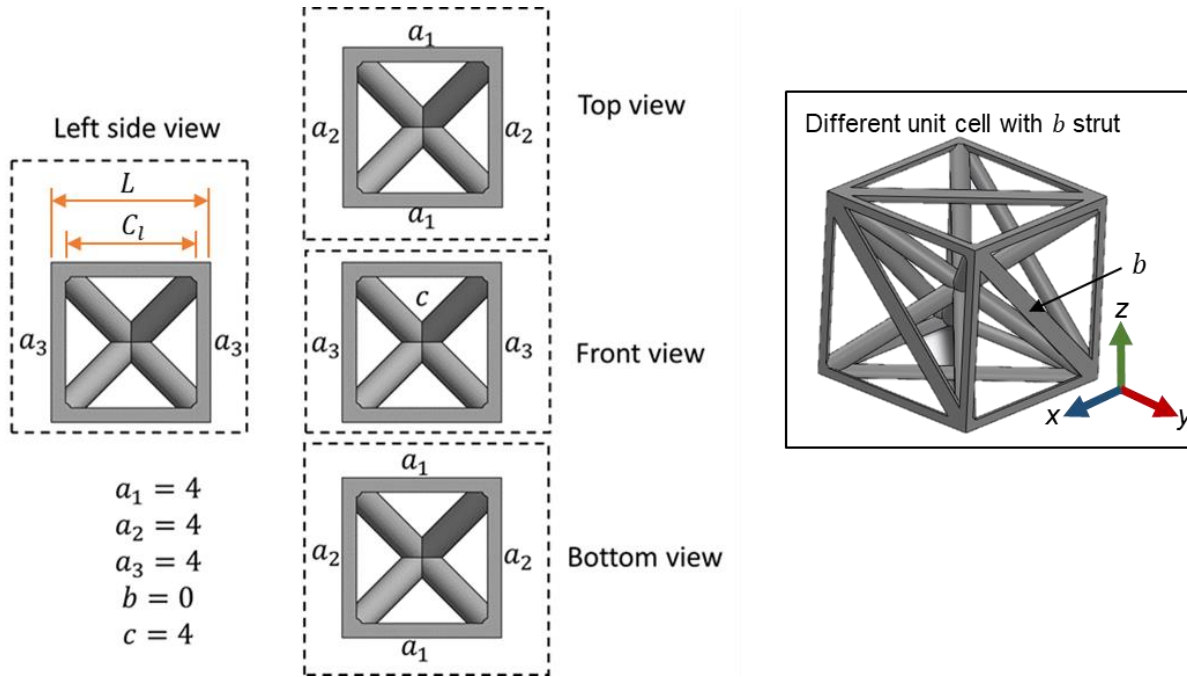
Figure 4.4. An illustrative example of the naming of struts in a strut-based lattice.

One way of designing strut-based lattice structures is by specifying the volume fraction and the unit cell size L. The diameter d of the strut can then be calculated if the orientation and number of struts are known. Each of the members a_1, a_2 and a_3 in a single unit cell has a cross-sectional area represented by a quarter of a circle, each of the members b has a cross-sectional area represented by half a cylinder, and each of the members c has a cross-sectional area of a full circle. The volume V of a lattice unit cell can be expressed as

$$V = \rho^* L^3 = \frac{\pi}{4} d^2 \left(\frac{a_1 L}{4} + \frac{a_2 C_l}{4} + \frac{a_3 C_l}{4} + \frac{b\sqrt{2}C_l}{2} + c\sqrt{3}C_l \right) - (c-1)e_c, \qquad 4.3$$

where e_c is the intersection volume of struts c of diameter d. The intersection volume equals 0 when $c = 0$, 0.181021 when $c = 2$, and 0.636638 when $c = 4$ [138].

Since
$$L = C_l + d,$$
4.4

then
$$C_l = L - d.$$
4.5

Substituting the value of C_l from Equation 4.5 in Equation 4.3 gives

$$\frac{\pi d^3}{L^3}\left(\frac{a_2}{16} + \frac{a_3}{16} + \frac{b\sqrt{2}}{8} + \frac{c\sqrt{3}}{4} + e_c\right) + \frac{\pi d^2}{L^2}\left(\left(\frac{a_1}{16} + \frac{a_2}{16} + \frac{a_3}{16} + \frac{b\sqrt{2}}{8} + \frac{c\sqrt{3}}{4}\right)\right) - \rho^*$$

4.6

$$= 0,$$

Equation 4.6 can be solved to obtain the diameter of a lattice strut at a given number of struts, volume fraction and unit cell size. The diameter can then be used in CAD to design the intended structure. For example, for a lattice structure of 10 % volume fraction and 30 mm cell size (see Table 4.1 for full details) the strut diameter obtained using Equation 4.6 is 2.52 mm.

Table 4.1. Example of calculation of the diameter of a lattice unit cell using Equation 4.6

Nominal lattice filled volume / mm^3	27,000
Number of cells	1
Unit cell size (L) / mm	30
Calculated diameter d from Equation 4.6 / mm	2.52
Nominal filled volume / mm^3	2700
Filled volume as calculated from CAD file / mm^3	2,696.08
Nominal volume fraction	10 %
a_1	4
a_2	4
a_3	4
b	0
c	4
Volume error of Equation 4.6	0.14 %
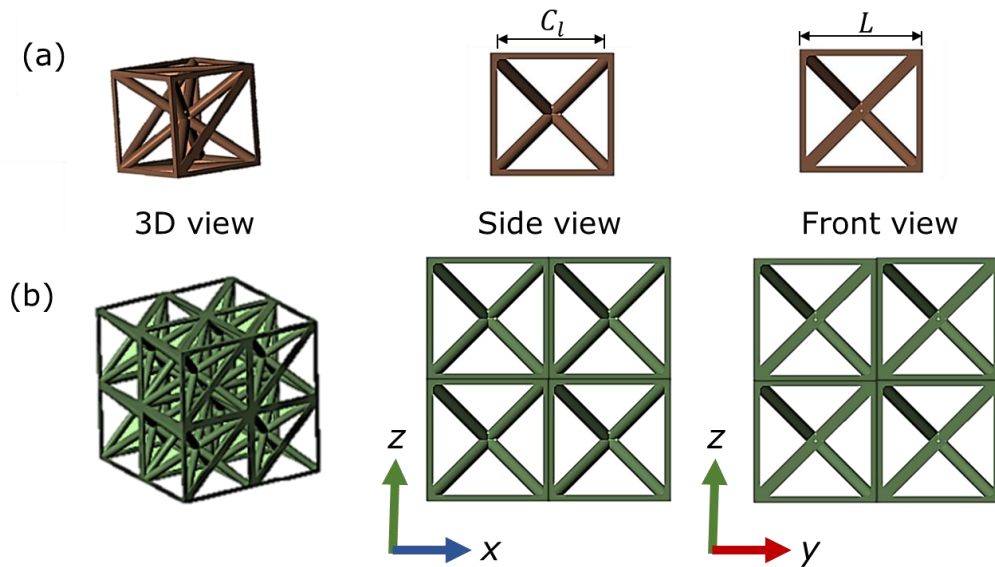
Figure 4.5. (a) Example of a single lattice cell as designed with Creo Parametric CAD software, and (b) example of 2×2×2 periodic lattice as tessellated with Autodesk Inventor CAD software.

To calculate the error in the lattice volume, two volume values were recorded: the originally intended volume (the nominal volume V as calculated using ρ^* from Equation 4.6), and the volume obtained from the CAD file of the lattice. The error was then calculated as the absolute difference between the nominal volume and the volume obtained from CAD divided by the nominal volume. The calculated error in the lattice volume was negligible; less than 0.14 %. This error originates from the intersection between the struts as approximated by Equation 4.6. CAD was used for the design of single unit cells which were then tessellated in 3D to create lattice structures as illustrated in Figure 4.5.

4.1.2   Lattice mechanical properties

Drawing from the lattice discussion in Section 2.4, convergence of the number of unit cells in a lattice with respect to the relative elastic modulus should be ensured in order to achieve accurate modelling of the properties of the lattice structures. Hence, the designed lattices should be tested to determine: 1) whether or not the stress-strain curve reaches

the densification region [9], and 2) ensure convergence of the number of tessellations with the relative elastic modulus. Section 2.4 describes how lattice structures are identified. Experimental compression tests were carried out on representative samples of the same overall size of 30 mm, 20 % volume fraction and BCC_{xyz} cell configuration. The number of tessellations was 2×2×2, 3×3×3 and 4×4×4. The samples are shown in Figure 4.6a and the experimental setup is shown in Figure 4.6b.

(a)

(b)
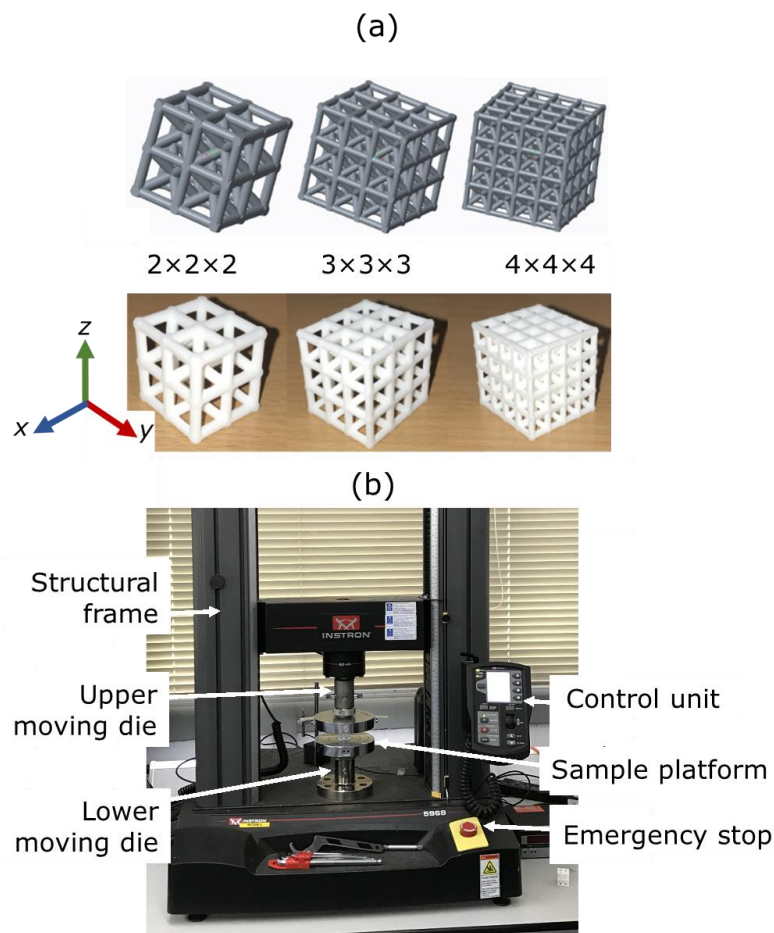
Figure 4.6. (a) Compression samples as designed in CAD (top) and manufactured from Nylon-12 on an EOS P100 L-PBF system with a building powder layer height of 100 μm, and (b) Compression test machine setup.

The samples were compressed at a constant compression speed of 1 mm·min^{-1} using a 50 kN moving die. The selection of the attributes of the representative samples is made based on their suitability for manufacturing with AM (see Figure 2.12). The relative elastic

modulus E^* of each sample was calculated using Equations 2.7 and 2.8. The three samples were enough to represent the linear trend between the relative elastic modulus and the number of tessellations of the unit cell which is presented in Section 5.2.1.

4.1.3 Lattice structure naming scheme

The lattice structures used in this study are of different volume fraction (10 %, 20 % and 30 %), different number of lattice nodes and different cell configurations. For the purpose of individual characterization, every lattice cell was assigned a unique code in the form of ($x_1x_2x_3x_4$-x_5), where x_1 is the number of lattice nodes in the unit cell and $x_2x_3x_4$ denotes the volume fraction taking, for example, a value of '010' for a 10 % lattice cell. The value x_5 is an arbitrary identification number of the struts configuration (topology) as shown in Figure 4.7. In Chapter 5, "x" is used for generalisation of the naming, for example, 9010-x refers to all lattices of any cell configuration (hence the x in place of x_5) that have 9 lattice nodes and are of 10 % volume fractions.
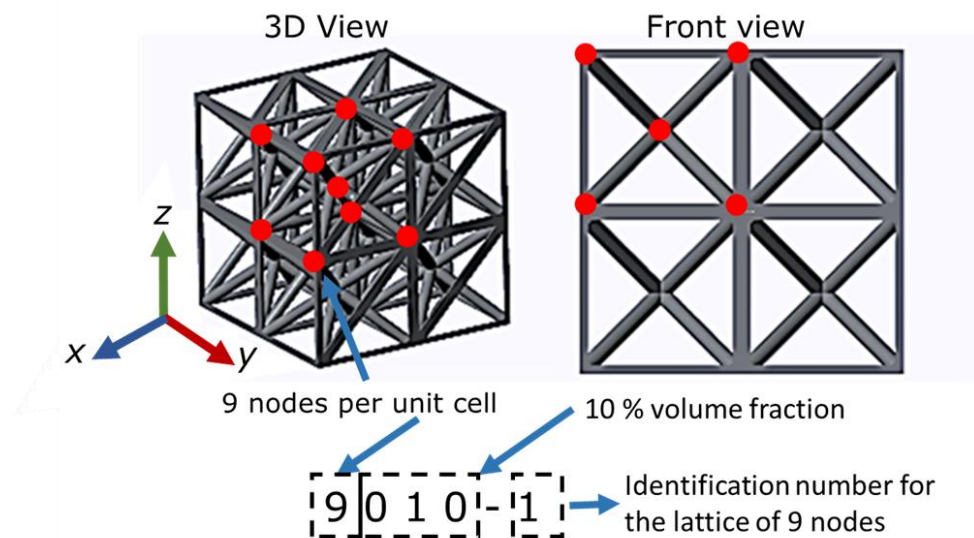
Figure 4.7. An illustrative example of the naming scheme of the lattice.

65

4.1.4 Finite element modelling and experimental testing

For testing of the response of the lattices, CAD models of the lattices were prepared with the minimum number of unit cells, which is obtained with the method of Section 4.1.2. Finite element modelling was used to test the response of the lattices at certain frequencies under excitation inputs of 1 N. The excitations are sent through the crystallographic [001] direction.

For experimental verification of the results, samples of 8010-7 and 5010-1 lattices were manufactured with L-PBF (method prescribed in Section 4.1.5). The harmonic responses in the crystallographic [001] direction were tested using the general description (provided below) in this section. The vibration testing range was from 0.1 Hz to 1000 Hz for the 8010-7 samples, and from 0.1 Hz to 3000 Hz for the 5030-1 samples, all with < 1 Hz frequency intervals (see Figure 4.8b).
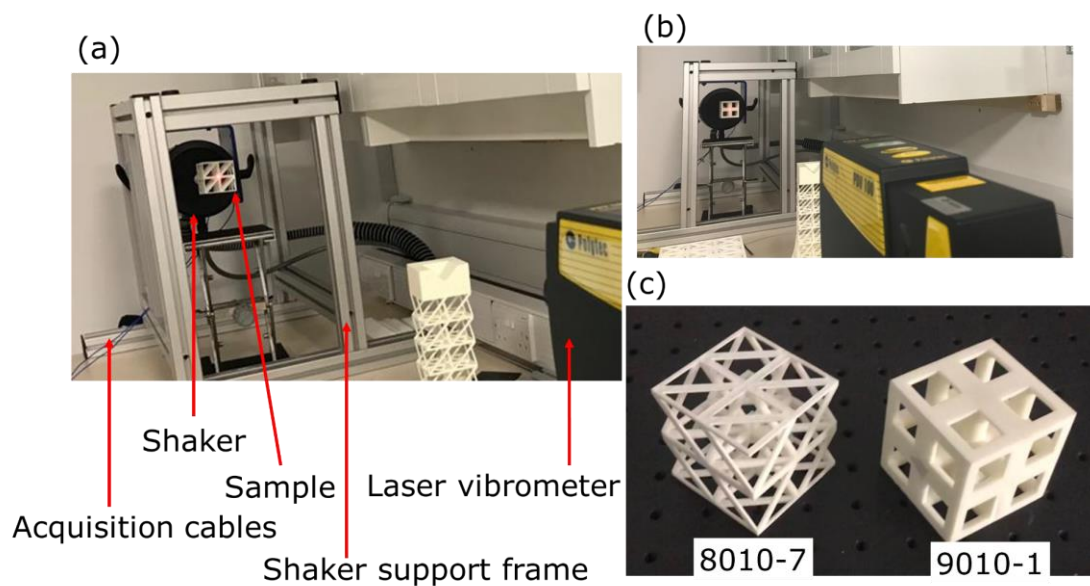
Figure 4.8. An illustrative example of the experimental verification setup for (a) 8010-7 lattice and (b) 9010-1 lattice, and (c) lattice structures manufactured with laser powder bed fusion for experimental verification.

General description of the experimental setup: The lattice sample was suspended using piano wire to approximate free-free boundary conditions. The approach, taken to suspend

the lattice, is similar to the approach taken by Zhang et al.[130] and Chen et al. [139], supports the lattice uniformly. An alternative approach, which can also be used for approximation of free-free boundary conditions, can be found in the work of D'Alessandro et al. [129] who used a soft material in the form of bubble wrap to support the structure. The lattice was fixed on one side to a connector which was, in turn, bolted to an acceleration sensor. The acceleration sensor was linked to the armature of the shaker (the Modal Shop Shaker 2060E) [140] through a stinger. The stinger is a 1.5 mm rod which connects to the acceleration sensor and decouples cross-axis force inputs, thus, minimising errors during measurements [141]. As part of the experimental setup, the beam of a laser vibrometer was projected perpendicularly to the opposite surface of the lattice to take longitudinal acceleration measurements.

- Laser vibrometer

A laser vibrometer uses coherent laser beam to measure the vibration of a surface. The coherent laser beam splits into a reference beam and a measurement beam, both of the same frequency. The reference beam is focused towards a photo detector housed within the body of the laser vibrometer while the measurement beam is focused on the measured surface. Shifting of the phase and frequency of the measurement beam is done using a Bragg cell (see Figure 4.9a). When the measured surface vibrates, the scattered light changes in frequency and phase due to the change in the velocity of the measured surface. The reflected beam carries characteristic information of the motion of the measured surface which is analysed with that of the reference beam to obtain information about the output signal to detect the change in frequency. The displacement, velocity and acceleration data of the measured surface is then obtained by analysing the output signal [142]. The benefits of the laser vibrometer used in this project, Polytec PDV 100, is that it is low in mass (less than 1.5 kg), has high measurement resolution of 2 nm/s and is

capable of measuring vibration up to 22 kHz. The laser vibrometer is non-contactless which means that the measured surface is not damaged with this measurement process.
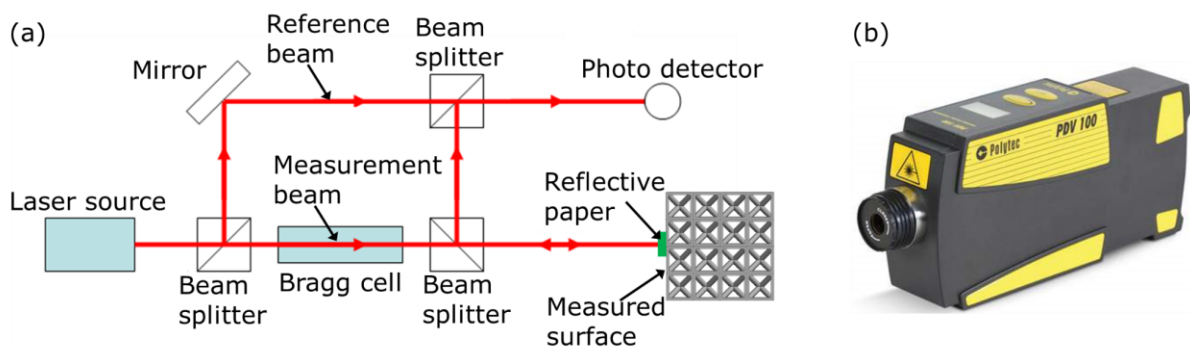
Figure 4.9. (a) Operation concept of a laser vibrometer and (b) photo of Polytec PDV 100 laser vibrometer [143].

The effective measurement distance of this vibrometer is between 0.2 m and 30 m. However, in this project, the measurement distance between the laser vibrometer and the measured surfaces was between 0.2 m and 3 m [143]. The drawback of this laser vibrometer is that it is single-axis which required reorientation of the laser vibrometer position, as will be required particularly for WP3, to obtain 2D and 3D vibrational results. In addition, and since this vibrometer can only measure surfaces with sufficient surface reflectance, shiny reflective papers had to be glued to the measured surfaces in this project [142,143]. The mass of the reflective papers at which the laser beam was projected is negligible in reference to the mass of the samples measured in this project, thus, the vibrational results were not affected by the addition of the reflective papers. Figure 4.9b shows a photo of the used laser vibrometer.

- Acceleration sensor

This project used an acceleration sensor which formed one part of an impedance head. In principle, the impedance head contains a force sensor as well (see the work of Ampatzidis et al. [88] for an example of the use of the force sensor of the impedance head). The acceleration sensor uses the piezoelectric effect of piezoelectric material, for

example, barium titanate, to measure the acceleration of a vibrating surface. Piezoelectric materials respond to mechanically applied stress by producing a charge. The accelerometer uses these materials to generate a voltage signal that is proportional to the acceleration [144]. A schematic diagram of the acceleration sensor and its assembly in the vibrational test set up is shown in Figure 4.10.
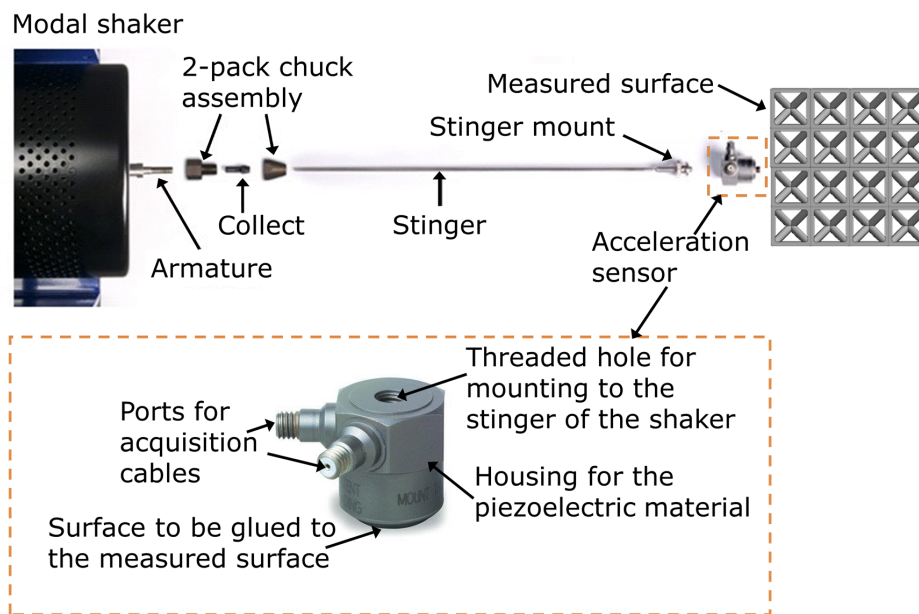
Figure 4.10. Schematic of the impedance head and its assembly.

The accelerometer is glued to the measured surface from one end and is mounted to the stinger of the shaker at the other end. Vibration of the measured surface causes variation in the inertial forces applied to the mass of the piezoelectric material and leads to its deformation. This deformation is proportional to the acceleration of the measured surface which allows for measuring the vibration of the surface. In general, piezoelectric acceleration sensors are low in mass (less than 200 g), has a good response to frequencies up to 5 kHz and are easy to mount. The acceleration sensor used in this project is the PCB 288D01 and is shown in Figure 4.10. This model is compact in size $(17.5 \times 17.5 \times 20.8)$ mm and has a good sensitivity of 10.2 mV·(m·s^{-2})$^{-1}$. The natural frequency of this model when mounted is above 20 kHz [145] which is four times higher

than the operating frequency of the tested samples (below 5 kHz), thus, the measurement results are not affected by the natural frequency of the model.

4.1.5 Laser powder bed fusion: additive manufacturing

All lattices in this work were fabricated on a laser powder bed fusion (L-PBF) system using Nylon-12 polymer material (see Section 2.1.1 for a description of other lattice fabrication methods). The material properties for Nylon-12 can be found in Table 4.2. The L-PBF system used a 21 W laser of scan speed and hatch spacing of 2500 mm$\cdot$s^{-1} and 0.25 mm, respectively. The nominal spot size of the laser was 0.3 mm and the layer thickness was 0.1 mm. Nylon-12 powder was used to fill the powder bed volume of dimensions 1320 mm × 1067 mm × 2204 mm at a temperature of 173 °C. Geometrical features of sizes below 0.8 mm are usually manufactured with considerable losses in mechanical properties and geometrical inaccuracy, due to the existence of unsolidified powder within the manufactured features [23]. To ensure that all geometrical features were manufactured in agreement with the specified design, the size of the narrowest lattice feature was designed to be 1 mm [23].

The choice of Nylon-12 is based on its compatibility with the L-PBF process. Nylon-12 has a large temperature processing window that allows for uniform crystallisation during cooling of the part; thus leading to reduction of material warpage and lamination [146], which is essential for manufacturing parts with predictable geometries and mechanical properties. Details about the physics and the challenges of L-PBF can be found elsewhere [20].

Table 4.2. Properties of L-PBF Nylon-12 used for modelling lattice structures in this work [147].

Tensile modulus	Density	Poisson's ratio
1500 MPa	950 kg$\cdot$m^{-3}	0.3

4.2 Methodology for investigation of 1D bandgaps

This section details the methods used in WP2 of this project. The aim of WP2 is to explore the ability of TPMS lattices to provide bandgaps. The methodology is outlined in Figure 4.11. First, a modelling method for examining 1D wave propagation in 3D lattices was obtained. Then, lattices with ability to form 1D bandgaps were designed and their bandgap was verified. A tuning method for control of the wave propagation in lattice structures in 1D was suggested and the manufacturability of these lattices with L-PBF was examined; this was done by studying the differences in volume fractions, cell sizes between the manufactured part and the original CAD file. The results of WP2 are discussed in Chapter 6.

4.2.1 Modelling of 1D dispersion curves

A finite element (FE) based wave propagation method was used to calculate the elastic dispersion curves of the lattice structures. In comparison to other dispersion calculation methods, for example, analytical method, PWE [84] and FDTD [105,148,149], the FE method provides higher computational efficiency and greater wave modelling accuracy [103,150]. The FE method incorporates Bloch's theorem, which governs the displacement of the FE nodes, and infinite tessellation of the unit cell along the tested propagation directions [61].
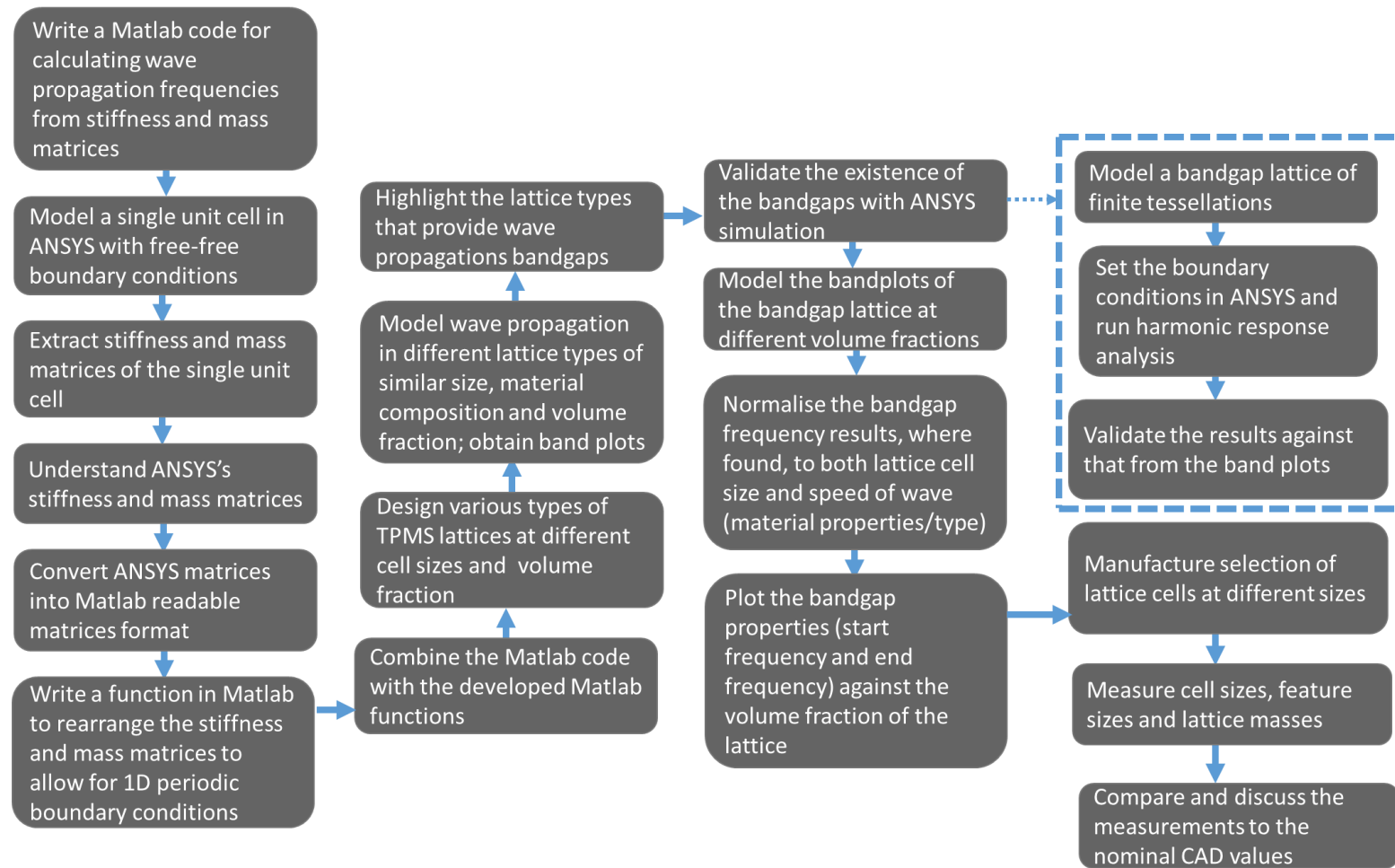
Figure 4.11. Methodology for examining wave propagation and bandgap formation in manufacturable 1D lattices.
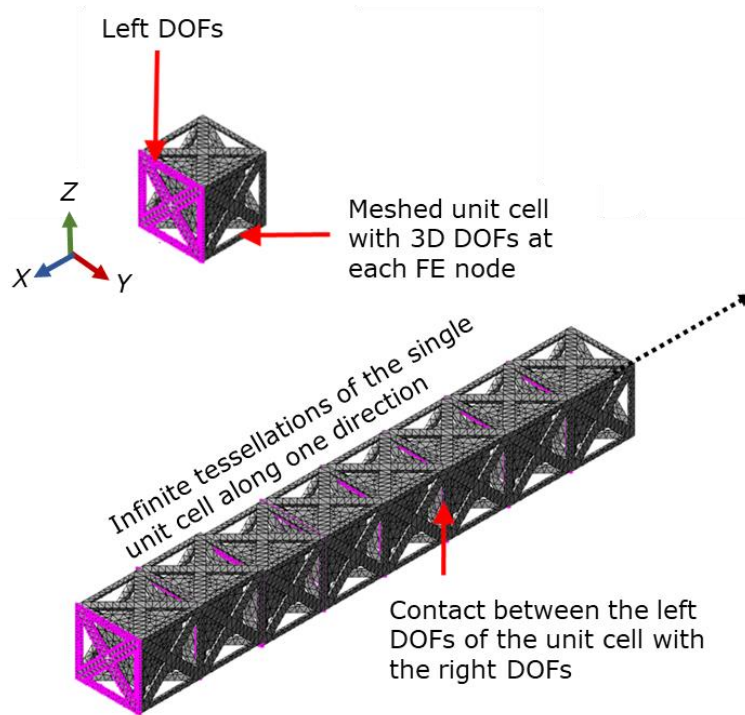
Figure 4.12. Illustrative example of a unit cell modelled with infinite boundary conditions.

The simulation work throughout this thesis used 3D lattice models with three DOFs at each FE node to capture all the possible modes of vibration (see Section 3.5 for information on lattice periodicity). The stiffness and mass of an individual mesh element were recorded in x-, y- and z- directions. No rotational degrees of freedom were considered for the individual mesh elements (i.e. the individual elements had no bending stiffness). However, the ability of the simulation to model the bending behaviour of the whole structure was not put at risk since the three DOF proved to be sufficient for the modelling as can be seen in other work [113,129]. A lattice can be visualised as a set of discrete points in reciprocal space with the distance between the neighbouring points equal to π/L. Understanding the propagation of waves within the reciprocal space of the lattice provides fundamental understanding of the dynamic behavior of the lattice, i.e. the types of waves, their propagation directions and propagating frequencies can be understood with ease. However, the reciprocal space is an infinite space and, thus, it is inconvenient to fully model it. Fortunately, for symmetric lattices, the reciprocal space is also symmetric which

provide a chance for modelling finite regions within this space. In this work, modelling of wave propagation was restricted to the contour of a region called the irreducible Brillouin zone (IBZ) of the examined lattices. A Brillouin zone (BZ) is a representation of the lattice in reciprocal space. The IBZ is the first BZ of the lattice reduced by all of the geometrical symmetries. The contour of the IBZ is bounded by critical points Γ, X, M and R. The critical points of a simple cubic lattice are shown in Figure 4.13 and the IBZ is highlighted. The propagation of the wave across an IBZ can be understood by studying the motion of the wave in a single 3D unit cell. For example, the 1D IBZ of a cubic lattice spans from 0 to π/L, where L is the unit cell size. According to a statistical study by Maurin et al. [151], restricting the detection of bandgaps to only the contour of the IBZ rather than the full IBZ provides accurate results for symmetric unit cells as well as savings in computation time [151–153]. Modelling waves in the IBZ provides time savings in the analysis of wave propagation in periodic structures, rather than modelling waves in the full BZ.
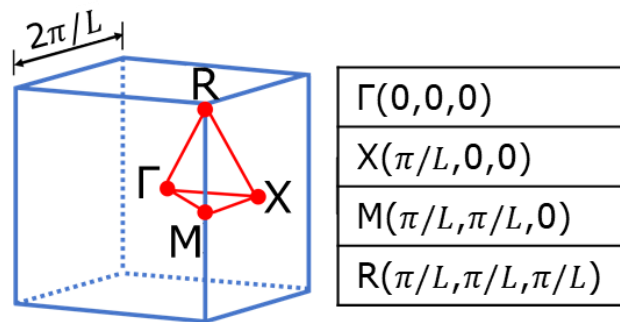
Figure 4.13. The 3D IBZ of a cubic lattice with the reciprocal space coordinates of the critical points.

The equation of motion for a unit cell without an external driving force can be described as

$$M\ddot{q} + Kq = 0, \qquad\qquad 4.7$$

where M, K and q represent the global mass matrix, the global stiffness matrix and the displacement vector of the structure of interest, respectively. The effect of damping is not

included in this work, as is the case with most of the work on phononic bandgaps. This means that the wave is assumed to be propagating without attenuation, hence the wavenumber k in this work is calculated as $k = i\mu$. This assumption is very common in literature as can be seen in [62,82,110,154]. The addition of damping may only alter the propagation outside the bandgap or increase the width of the bandgap [155]. In addition, assuming that the wave propagates without attenuation when analysing wave propagation in solid materials will provide generalised results that are applicable to a wide variety of materials, for example, Nylon 12 and stainless steel, irrespective of their damping properties. For each examined lattice type, the FE nodes located at the unit cell edges and faces were identified to allow for the 1D periodicity of the unit cell. Their DOFs were rearranged into a nodal displacement matrix q of the following order [62,156]

$$q = \begin{bmatrix} q_l \\ q_i \\ q_r \end{bmatrix}, \qquad 4.8$$

where q_r q_l and q_{in} denote the DOFs of the right, left and inner FE nodes of the 3D unit cell respectively (see Figure 4.14) and k is the wave number of a specific wave in the first BZ.
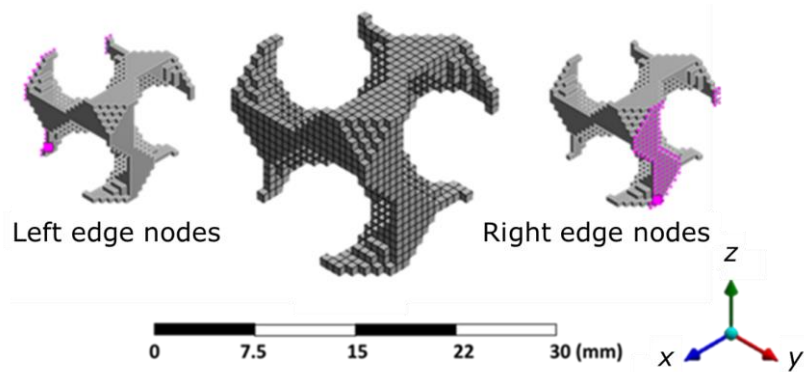
Figure 4.14. A hexahedral mesh of a gyroid unit cell used in this work. The highlighted areas illustrate the FE nodes of the right and left edges of the cells which need to be identified for the application of the finite element method.

The displacement matrix q_{IN} contains all the DOFs of FE nodes that are not located at the unit cell edges and faces. The naming scheme is arbitrary, as it depends on the orientation of the cell; the important principle is the grouping of the FE node sets according to their location.

Bloch theory describes the wave propagation in an infinite periodic medium using the wave vectors of the reciprocal space. The Bloch response is a product of a Bloch periodic function and a phase multiplier. The phase multiplier is the plane wave e^{-ikL} (see Section 3.2 for details on Bloch theory). For the application of Bloch's theorem, the Bloch response is the displacement matrix q and the Bloch periodic function is a reduced nodal displacement matrix $\bar{q}$ that is specified in Bloch's reduced coordinates [63]. The reduced displacement matrix $\bar{q}$ is used to reduce the stiffness and mass matrices so that they only contain information on the sets of FE nodes relevant to each examined wavevector. Bloch theory has been successfully implemented to analyse wave propagation for the purpose of identifying bandgap structures in most of the studies discussed in Section 3.7. The reduced nodal displacement matrix $\bar{q}$ was obtained by introducing a transformation matrix N, that contains information about the plane wave e^{-kL}, of the following shape

$$N = \begin{bmatrix} I & 0 \\ Ie^{-kL} & 0 \\ 0 & I \end{bmatrix}.$$ 4.9

Then we have

$$q = N\bar{q},$$ 4.10

with

$$\bar{q} = \begin{bmatrix} q_l \\ q_i \end{bmatrix}.$$ 4.11

Projected stiffness and mass matrices of the reduced sets of FE nodes, $\bar{K}$ and $\bar{M}$ respectively, were then computed using

$$\bar{K} = N'KN,$$ 4.12

and

$$\overline{M} = N'MN,$$ 4.13

where K and M are the global stiffness and mass matrices extracted from the FE model of the single unit cell and rearranged in the same order of q, and N' is a transpose matrix used for ensuring force equilibrium [63,88]. The following generalised eigenvalue problem was then constructed and solved numerically

$$\overline{K} - \omega^2 \overline{M} = 0,$$ 4.14

where ω denotes the frequency of a propagating wave corresponding to each of the sampled wave vectors. An example of the calculation of the dispersion curves of a test lattice unit cell is shown in Figure 4.15.
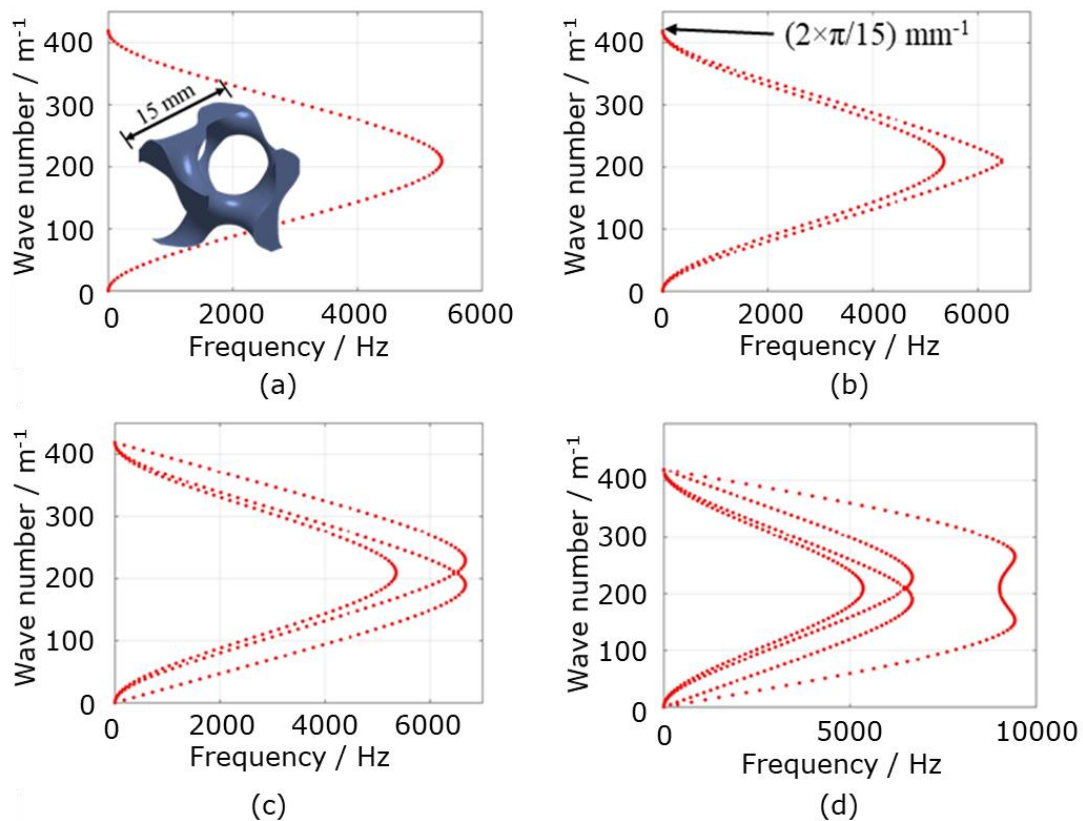
Figure 4.15. Illustration of 1D Dispersion curves calculated for a test unit cell with 100 wavenumber intervals. Solving for one, two, three and four eigenvalues for each wave number interval provides (a) one wave band, (b) two wave bands, (c) three wave bands and (d) four wave bands, respectively.

When equation 4.14 is solved once for a specific range of wavenumbers, one wave band can be formed as can be seen in Figure 4.15a. In this project, a wave band is defined as a visual representation of the dispersion that happens to one elastic wave when it propagates through a material. It can be seen from Figure 4.15a that the propagation of the first wave band starts at zero Hz and stops around 5000 Hz. The wave bands can sometimes overlap, especially wave bands of geometrically complex lattices as can be seen in Figure 4.15c. In other research areas, for example in structural health monitoring [157], the overlapping of wave bands may lead to difficulties in spotting where they start and finish. However, in bandgap engineering, which is the main focus of this project, the overlapping of wave bands does not impose an issue. This is because the goal is to discover frequency ranges where no wave bands exist. A Total of 100 wavenumbers were specified between 0 to $2\pi/L$. At each wavenumber, the eigenvalue in Equation 4.14 was constructed and solved to give the frequency of the propagating waves. The wave numbers and propagating frequencies were stored in matrix format and plotted in the form of the dispersion curves shown in Figure 4.15.

- Preparation of the lattices

FE models of the TPMS unit cells are assigned the mechanical and density properties of laser powder bed fusion Nylon-12 prescribed in Section 4.1.5. The voxelised network gyroid cell is shown in Figure 4.14 in which the leftmost and rightmost FE nodes are highlighted. The modelling assumes an infinite tessellation of lattice cells along the *x*-direction.

The mass and stiffness matrices of the unit cells are rearranged with the help of the FE nodes numbering obtained from a commercial finite element package. The mass and stiffness matrices are then arranged in the form shown in Equation 4.8. The generalised eigenvalue problem of Equation 4.14 is constructed. The frequency eigenvalue problems are solved for 100 equally spaced wave numbers which were enough to provide sufficient

description of waves in the first BZ of the TPMS unit cells. All wave bands below 15 kHz in each lattice were included in the analyses. Tailoring the lattice to attenuate the vibration of certain frequencies depends on the specific application. For the purpose of using lattices in metrology and precision engineering applications, the interest is mostly in the hertz to low kilohertz range (see Section 5.3 for a range of problematic frequencies for a measuring instrument). It is assumed that bandgaps found below 15 kHz are tuneable using the methods described in Section 4.2.2. To obtain normalised frequencies, all frequency results were normalised to the unit cell size L and the speed of longitudinal waves in the lattice material v, which was introduced in Equation 3.2. With the normalisation of the results, bandgaps below and above 15 kHz can be obtained by selecting the appropriate material and cell size.

4.2.2 Bandgap tuning method

The properties of lattice structures that can be tuned to potentially induce a phononic bandgap include cell size, volume fraction and cell geometry. The unit cells had been analysed first, with the most promising candidate for bandgap development (i.e. with the widest and more number of bandgaps) then chosen for bandgap tuning. The characteristic wave bands for the initial settings of the chosen cell found under 15 kHz were examined under different volume fractions and cell sizes. The range of volume fractions used in this study extended from 20 % to 40 %, while the examined cell sizes were of 15 mm, 20 mm, 25 mm, 30 mm and 40 mm. Although the selected volume fraction and cell size ranges are arbitrary, their exact values hold no bearing on our results and conclusions.

4.3 Methods for investigation of three-dimensional bandgaps

This section details the methods used in WP3 of this project. The aim of WP3 is to develop 3D wave propagation modelling techniques and develop single material lattices with 3D bandgaps at low frequencies. Details of the methodology for developing the 3D modelling

technique can be found in Figure 4.16 and that for developing of the 3D bandgap lattices is shown in Figure 4.17.
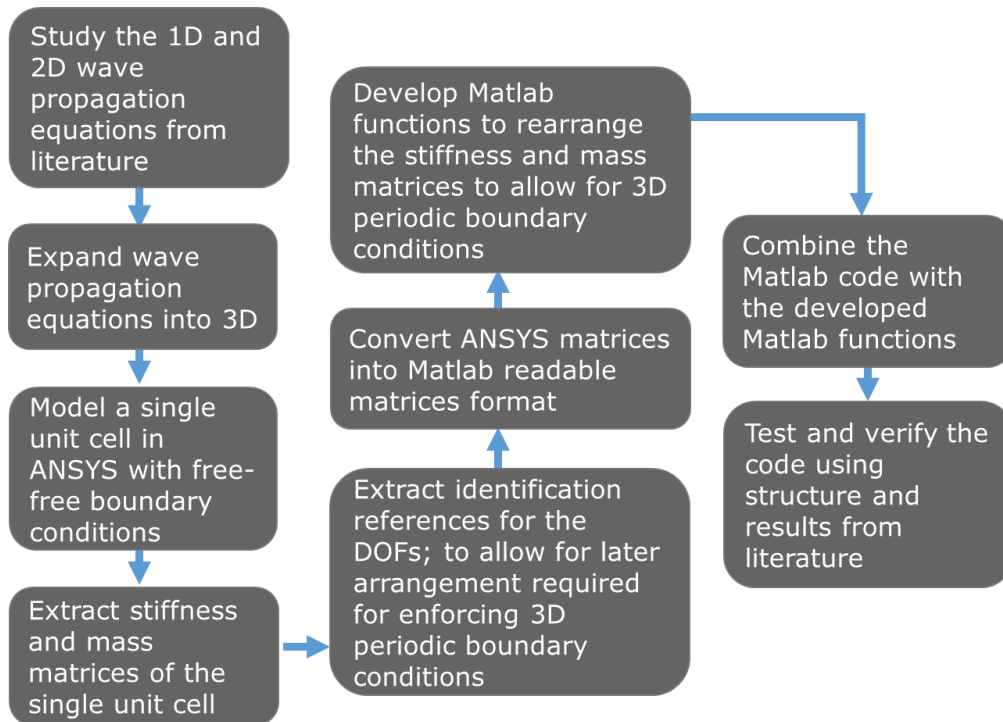
Figure 4.16. Methodology for developing 3D wave propagation technique.

The work will include providing a detailed description of the analysis required for modelling 3D wave propagation and validation of the modelling technique with published literature. Lattices, of featured developed with the help of FlattPack and the design equation developed in Section 4.1.1 will be tested with the developed 3D wave modelling technique. Tuning methods for control of the wave propagation in lattice structures in 3D will be suggested for all the developed structures using the methods detailed in Section 4.2.2. Verification of the existence of the bandgaps will be carried out by simulation modelling and experimental testing of a selection of lattices of suitable periodicities as detailed in Section 4.1.4 and Section 4.3.2. The results of WP3 are discussed in Chapter 7 and Chapter 8.
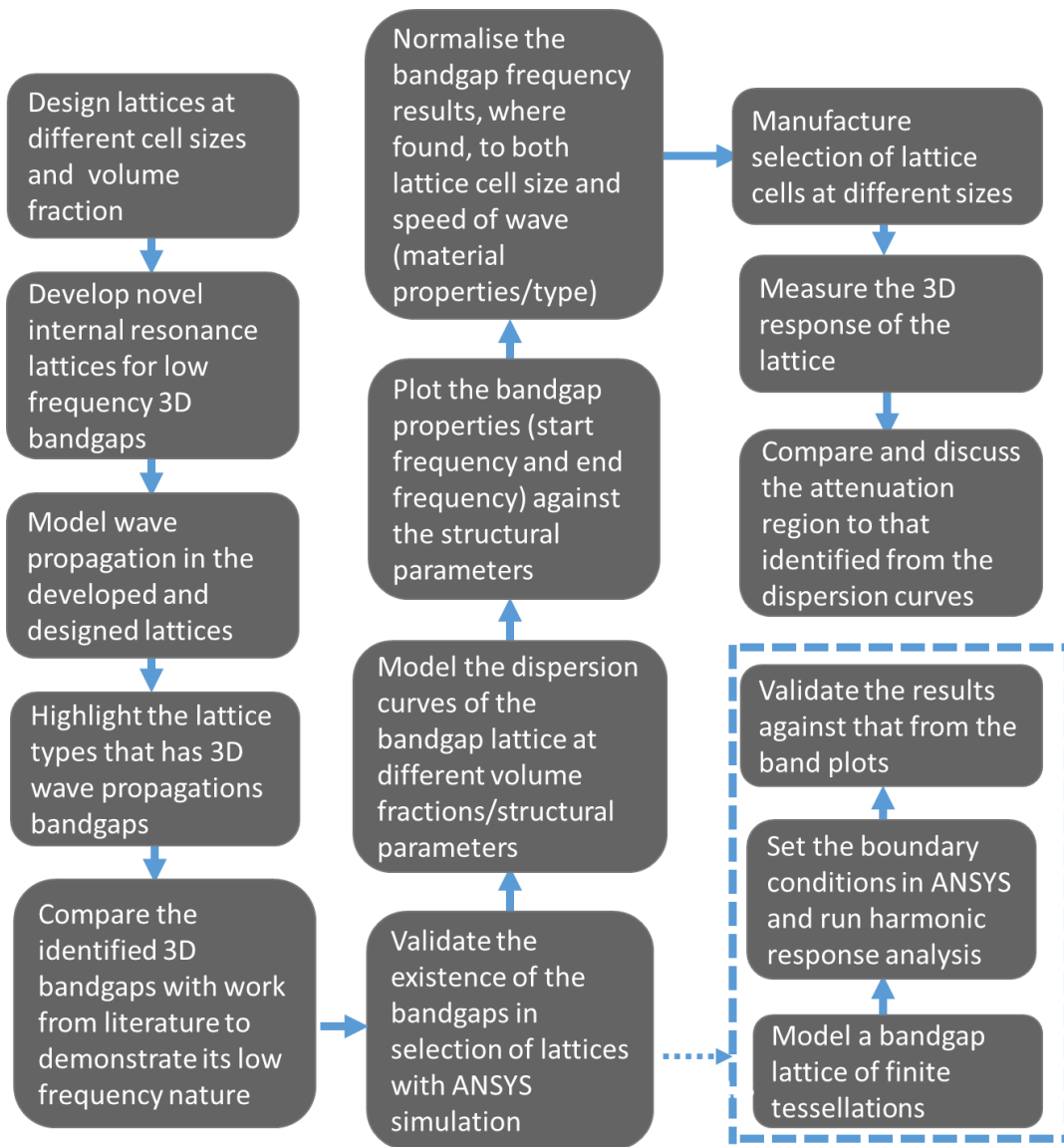
Figure 4.17. Methodology for development of 3D lattices for 3D wave propagation bandgaps at low frequencies.

CAD modelling provides the freedom to design strut-based lattices of different shapes and can create CAD files of different formats for the use in different commercial simulation software. Due to the availability of FlattPack at university of Nottingham and its demonstrated capabilities to design geometrically complex lattices, it is used for modelling the TPMS unit cells used in this work. Modelling and simulation of the vibration properties are made using a commercial finite element software (ANSYS) and due to its high accuracy, high computation efficiency for modelling complex structures (see Chapter 3).

Modelling of the dispersion curves in this work (for identification of bandgap structures) is carried out using dedicated wave propagation modelling techniques that incorporate finite element modelling with Matlab codes and functions developed specifically for this project as discussed in Section 4.3.1. See Section 3.6 for other bandgap modelling methods.

4.3.1 Modelling of 3D dispersion curves

The method presented in this section draws on from the FE modelling technique of 1D bandgaps which was introduced in Section 4.2.1. In the case of investigation of 3D bandgaps, the displacement matrix q of the lattice unit cell is rearranged in the way that would allow for the 3D periodicity of the unit cell in the following order

$$q = [q_{IN}\ q_F\ \ q_S\ q_B\ q_T\ q_L\ q_R\ q_{FB}\ q_{FT}\ q_{SB}\ q_{ST}\ q_{FL}\ q_{FR}\ q_{SL}\ q_{SR}\ q_{BL}\ q_{BR}\ q_{TL}\ q_{TR}]^{\mathrm{T}}, \qquad 4.15$$

where the subscripts IN, L, R, F, B, T and S denote the DOFs at the inside, left, right, front, bottom, top and back of the single unit cell, respectively (see Figure 4.18). Similar to the case of 1D dispersion curves, the displacement matrix q_{IN} contains all the DOFs of FE nodes that are not located at the unit cell edges and faces. For the same unit cell, the size of the matrix q_{IN} in the case of 3D modelling is smaller than that in the case of 1D modelling. This is because in 3D modelling it is essential to decouple some of the DOFs which were part of the inner FE nodes matrix in the case of 1D, for example, those located at the front and back of the unit cell. The transformation matrix N in the case of 3D takes the form

$$N = \begin{bmatrix} I & 0 & 0 & 0 & 0 & 0 & 0 \\ 0 & I & 0 & 0 & 0 & 0 & 0 \\ 0 & Ie^{-k_yL} & 0 & 0 & 0 & 0 & 0 \\ 0 & 0 & I & 0 & 0 & 0 & 0 \\ 0 & 0 & Ie^{-k_zL} & 0 & 0 & 0 & 0 \\ 0 & 0 & 0 & I & 0 & 0 & 0 \\ 0 & 0 & 0 & Ie^{-k_xL} & 0 & 0 & 0 \\ 0 & 0 & 0 & 0 & I & 0 & 0 \\ 0 & 0 & 0 & 0 & Ie^{-k_zL} & 0 & 0 \\ 0 & 0 & 0 & 0 & Ie^{-k_yL} & 0 & 0 \\ 0 & 0 & 0 & 0 & Ie^{-k_y}e^{-k_zL} & 0 & 0 \\ 0 & 0 & 0 & 0 & 0 & I & 0 \\ 0 & 0 & 0 & 0 & 0 & Ie^{-k_xL} & 0 \\ 0 & 0 & 0 & 0 & 0 & Ie^{-k_yL} & 0 \\ 0 & 0 & 0 & 0 & 0 & Ie^{-k_xL}e^{-k_yL} & 0 \\ 0 & 0 & 0 & 0 & 0 & 0 & I \\ 0 & 0 & 0 & 0 & 0 & 0 & Ie^{-k_xL} \\ 0 & 0 & 0 & 0 & 0 & 0 & Ie^{-k_zL} \\ 0 & 0 & 0 & 0 & 0 & 0 & Ie^{-k_xL}e^{-k_zL} \end{bmatrix}, \qquad 4.16$$

to get a reduced nodal displacement matrix $\bar{q}$ of the form

$$\bar{q} = [\,q_{IN}\ q_F\ q_B\ q_L\ q_{FB}\ q_{FL}\ q_{BL}\,]^{\mathrm{T}}, \qquad 4.17$$

where k are wave vectors in the irreducible Brillouin zone (IBZ) corresponding to the lattice structure.
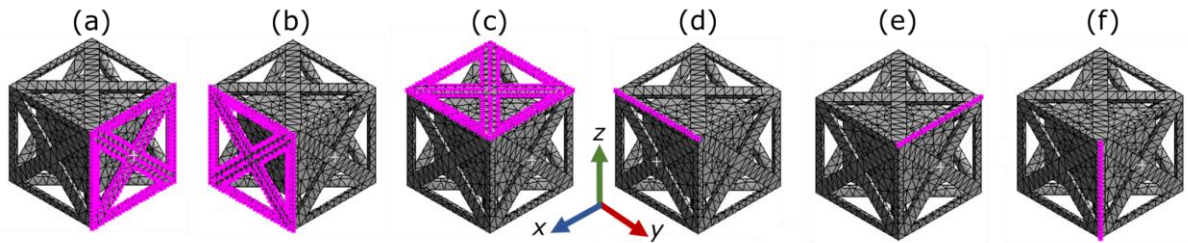
Figure 4.18. Selection of the segmentation of the unit cell of the lattice into DOF as used for modelling the periodicity of the unit cell. The magenta points represent the FE (a) front nodes, (b) left nodes, (c) top nodes, (d) top-left nodes, (e) top-front nodes, and (f) front-left nodes.

Waves propagating along the path Γ-X, X-R, R-M, and M-Γ of the IBZ were modelled using a minimum of eighty combinations of wave vectors which were sufficient to model the dispersion curves. The full contour of the IBZ has six paths, however, it is common practice to examine only four of these paths for investigation of 3D bandgaps, as seen in references

83

[86,96,111,112]. The preparation analysis further reinforced this common practice by showing that waves propagating in paths M-X and Γ-R has minimal/zero effect on the bandgap position as can be seen in Figure 4.19. Similar to in the method for 1D dispersion curves, the frequency eigenvalues were normalised to the unit cell size L and the longitudinal speed of the wave in the lattice material v to obtain normalised frequencies. The dispersion curves were then constructed as corresponding pairs of wavevector and normalised frequency.
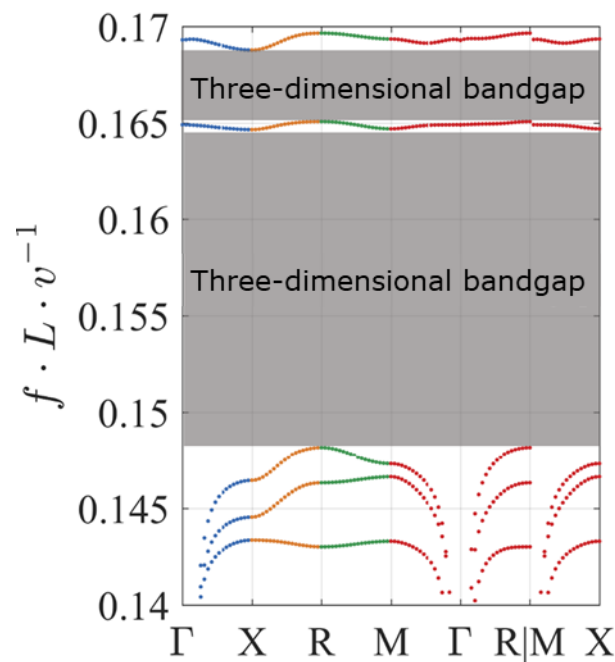
Figure 4.19. Three-dimensional bandgap identified from calculations of the full contour of the IBZ.

4.3.2 Numerical modelling of vibration transmissibility

Calculation of the dispersion curves made use of infinite periodic boundary conditions in the FE models. In practical applications, only lattice structures of finite periodicity are realisable (i.e. manufacturable). This limitation is expected to reduce the extent of vibration attenuation achievable with these lattices. Thus, the transmission of waves was calculated through lattice structures with very low periodicity (single, 3 and 6 periods in

3D). The choice of the unit cell for this study was made from the unit cells that exhibited bandgaps under infinite periodic boundary conditions, as depicted by their respective dispersion curves. The transmission of waves in the selected lattices was conducted using ANSYS Workbench. Longitudinal (primary) waves were modelled passing through the lattice structures. The wave transmission between the input side and the opposite side of the lattice was determined with a normalised frequency resolution of 0.0025 to ensure sufficient representation of all vibration modes within the examined frequency range. A damping coefficient of 0.1 has been used throughout all FE simulations.

The damping coefficient is different for each material. The addition of damping reduces vibration transmission around the resonance, which is the frequency range within which the highest vibration transmissibility levels are expected (see Section 3.4 for more illustration of the effect of damping on the vibration response). Generally, metals have low damping coefficient (below ~0.03) whilst polymers have high damping coefficient (above ~0.05) [158]. Since AM of polymers is less expensive than that of metals, Nylon-12 properties were used in the simulation which was carried out using a damping coefficient of 0.1.

4.3.3 Manufacturing and experimental testing

Lattice structure with 3D bandgap was manufactured with L-PBF and experimentally tested using the set up described in Section 4.1.4. As part of the experimental setup, the beam of a laser vibrometer (Polytec PDV-100) was projected perpendicularly to the opposite surface of the lattice to take longitudinal acceleration measurements. See Section 4.1.4 for more details of the laser vibrometer. The transverse acceleration measurements were taken by projecting the beam of the laser vibrometer perpendicularly to the side surfaces of the lattice. The laser vibrometer was set to measure the structural response in the longitudinal and transverse directions from a normalised frequency of 0 to 0.15 which includes the bandgap frequency range of the tested lattice. The acceleration data within

the tested frequency range were also obtained through the acceleration sensor (PCB 288D01). See Section 4.1.4 for more details of the acceleration sensor. The combination of the measurements of both the laser vibrometer and the acceleration sensor provided the transmissibility of the specimen. Figure 4.20 shows a representative photograph of the experimental setup. All measurements were taken with a normalised frequency resolution of less than 3.7×10^{-5}. In practice, four or five spectral sweeps are usually used, however, we have used over 100 spectral sweeps to ensure accuracy of the results which were then complexly averaged, considering both the phase and the magnitude of the measurements.
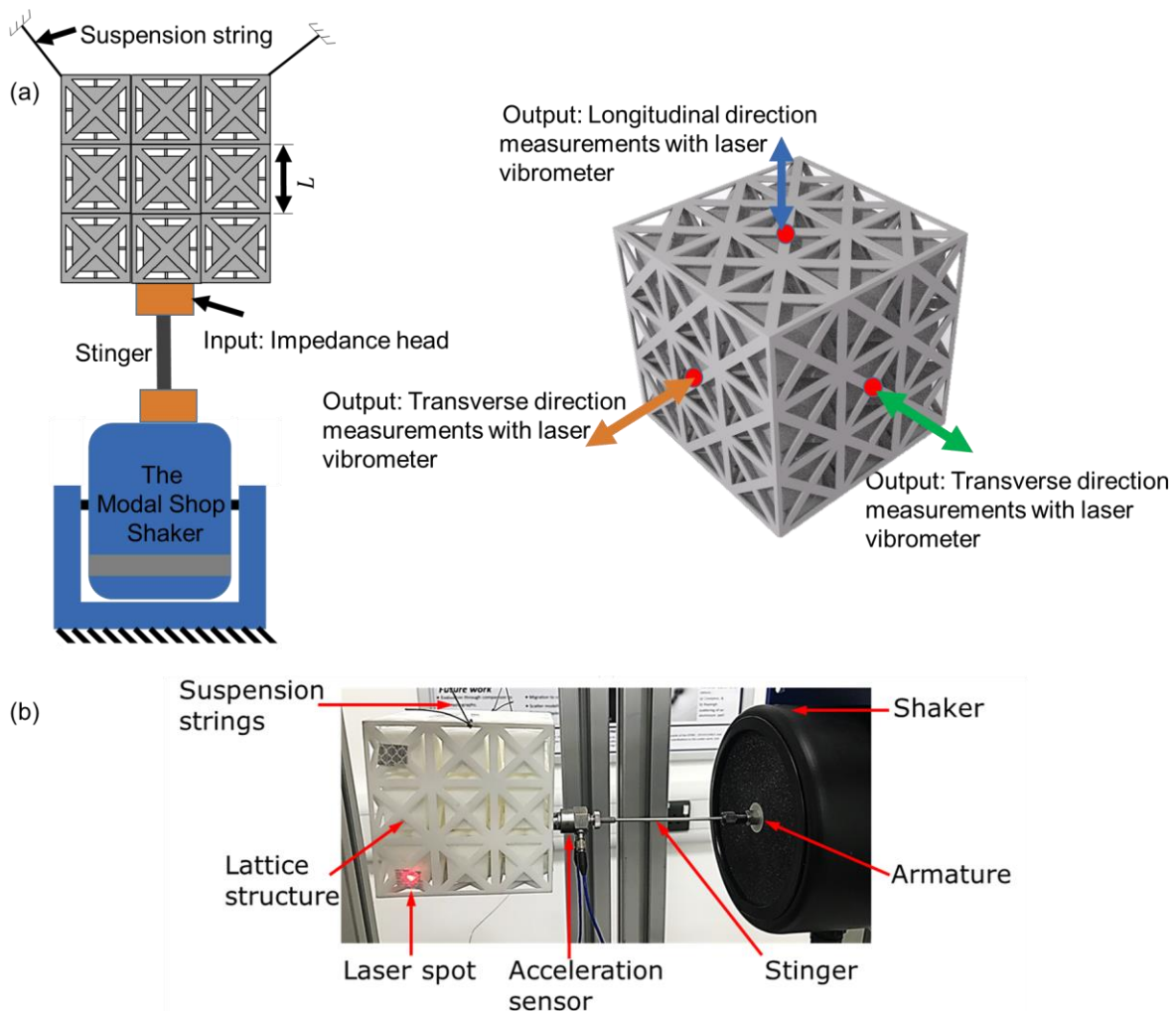
Figure 4.20. (a) An illustrative example of the 3D vibration testing experimental setup and (b) a photo of the experimental setup with the laser beam projected perpendicular to the side surface of the lattice to take transverse direction measurements.

4.4 Summary

This chapter outlined the methodology for studying the vibration attenuation capabilities of lattice structures. Strut-based lattices are produced using CAD and integrated a design tool that was developed specifically for this project. The design tool provides the volume fraction of the strut-based lattices based on the unit cell size, strut orientation and the number of struts. The volume fractions achievable with the developed design tool has an error of less than 1 %. TPMS lattices are developed using in-house software (FLattPack) that modelled TPMS lattices with different parameters. The methodology split the work of this project into three main WPs. WP1 studies the ability to control the natural frequency of lattices so that vibration isolation can be achieved. WP1 examines the effect of cell size, volume fraction and number of tessellations of the lattice on the natural frequency of the lattices. Verification of the ability to control lattice structures is demonstrated by testing the vibration transmissibility of representative lattices with simulation and experimental testing. The experimental testing used a laser vibrometer set up that includes a modal shaker for exciting the lattice samples, a piezoelectric accelerometer for measuring the acceleration at the input and a laser vibrometer for measuring the acceleration at the output of the lattice samples. The lattice samples were produced from Nylon-12 using L-PBF. WP2 and WP3 examine the ability of lattice structures to develop bandgaps for complete elimination of wave propagation. The bandgaps are identified from the dispersion curves of each of the examined lattice structures. While WP2 studies 1D wave propagation and WP3 studies 3D wave propagation, dedicated Matlab codes were developed to produce the dispersion curves of each WP. The Matlab codes solve the eigenvalue problem which was constructed using Bloch theorem and infinite boundary conditions. The equations in WP3 are much more complex than WP2 and uses matrices of a higher number of rows and columns than that of WP2. The project aim is to develop lattices for metrology and precision engineering applications which usually operate within the hertz to low kilohertz frequency range, thus, WP2 and WP3 examined the ability of the developed bandgaps to

be tuned through the volume fraction and cell size of the lattices. This would allow for the bandgap to match the operating frequency of a specific application. WP3 examines the ability of new types of internal resonance lattices to develop internal resonance bandgaps to obtain low-frequency bandgaps. The results for WP1 can be seen in Chapter 5, results for WP2 are presented in Chapter 6, and the results of WP3 are available in Chapter 7 and Chapter 8. The methodology presented in this chapter formed part of these publications [54,56,159–163].

Chapter 5

Tuning of natural frequency for vibration isolation with lattice structures

Part of the results in this chapter are published in these journal and conference papers [54,163]. Lattice structures have high strength to weight ratio and good energy absorption properties. The literature review of lattice structures for vibration attenuation, presented in Chapter 2 and Chapter 3, showed that lattices can be used to damp excitation waves at frequencies lower than the first natural frequency, as discussed in Section 3.3. In vibration isolation, the attenuation of vibration can get higher at frequencies greater than the first natural frequency (can get below 0 dB) as shown in Section 3.3. However, no reported work has shown that lattice structures can provide attenuation at frequencies higher than the first natural frequency. In this chapter, lattices structures are examined for their ability to provide tunable vibration isolation through adjustment of the natural frequency with the cell size, volume fraction and number of unit cell tessellations of the structures. The literature review, as shown in Chapter 2, showed that there is a minimum number of unit cells that a structure should have so that it could be characterised as a lattice [55].

Characterisation of lattices (i.e. determining the minimum number of unit cells) was determined through analysing compression test data. This compression test included multiple samples at various number of tessellations (see Section 4.1 for detailed

methodology). The minimum number of unit cells was then used to construct the lattice CAD models used in this vibration isolation study. A case study for demonstrating the ability to provide vibration isolation with lattice structures is presented towards the end of this chapter.

5.1   Lattice design and fabrication

A total of twenty-three lattice cell configurations were developed using the method described in Section 4.1.1. Each configuration formed the basis for three different volume fraction cells: 10 %, 20 % and 30 %. Figure 5.1 shows the lattice cells of 10 % volume fraction in a 2×2×2 tessellation.
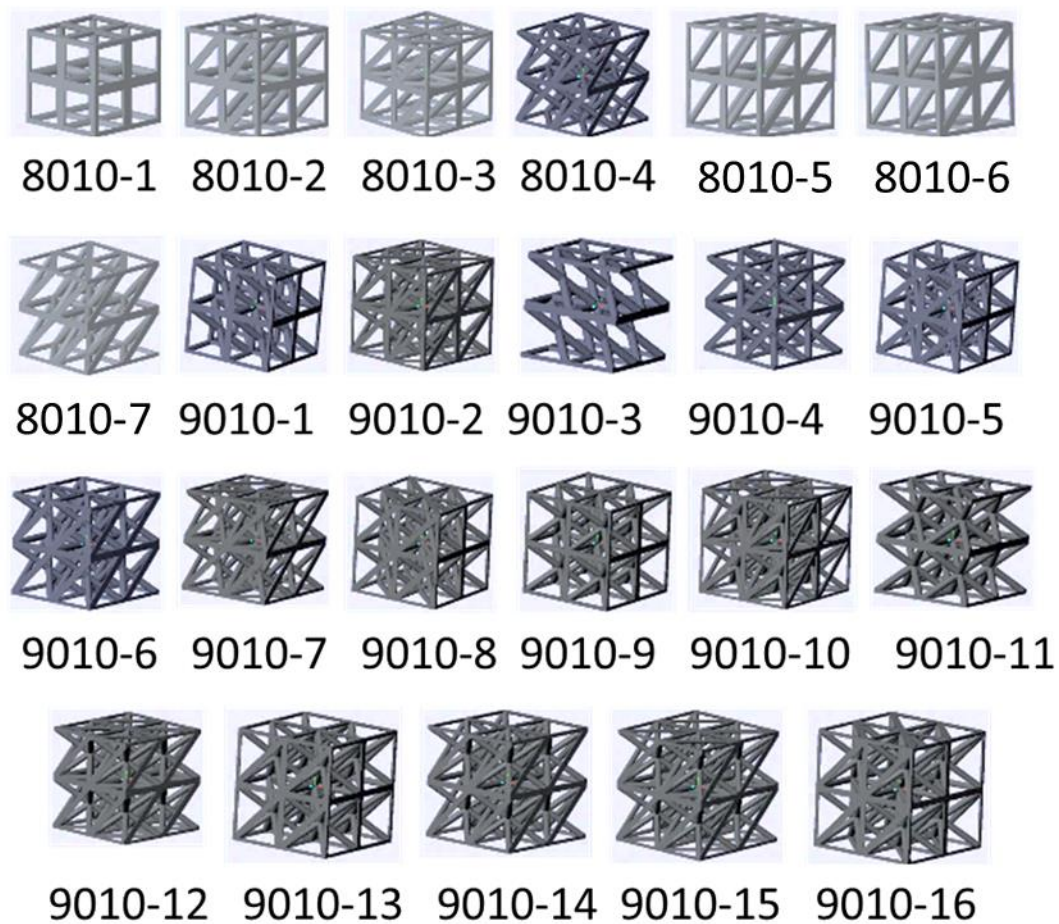
Figure 5.1. CAD models of the lattices used in this study, all in 2×2×2 tessellation and of 10 % volume fraction.

Two lattice structures were manufactured from Nylon-12 using L-PBF, namely 9030-1 and 8010-7. See Section 4.1.5 for details on L-PBF and Section 4.1.3 for details on the lattice naming scheme.

5.2   Results and discussion

5.2.1   Compression testing results

As discussed in Section 2.4, the minimum number of unit cells required for effective modelling of the lattice behaviour should be established. This was done by producing three compression test samples (see Section 4.1.2), examining the load-displacement curve and studying the relative modulus of the lattice. The results of the compression tests of the three samples are shown in the form of load-displacement curves in Figure 5.2a. During compression, it was observed that the gaps in the middle of the lattice samples narrowed down as the die pushed down. The gap in the 3×3×3 lattice shrank faster than in the 2×2×2 lattice. The bottom cells in the 3×3×3 lattice started collapsing first through bending outwards. The signs of tear and breakage in overall was considerably less in the 3×3×3 samples than in the 2×2×2 samples, which indicates that higher energy was absorbed through bending rather than breakage in 3×3×3 lattice. The 4×4×4 lattices experienced no observable tearing and breakage, which indicates higher energy absorption through bending than in the other lattices. The plateau region in the 4×4×4 lattice is shorter in comparison to the other tested lattices and the densification region started at higher compression force (15 kN) than in the other lattice (~10 kN); this is due to their slightly higher mass (by ~6 %) compared to the other lattices as appears in Table 5.1. The standard error of the measurements of the mass is also presented in Table 5.1 and is determined as the standard deviation of the measurements from the mean over the square root of the number of experimental repetitions (three repetitions for each lattice).

91
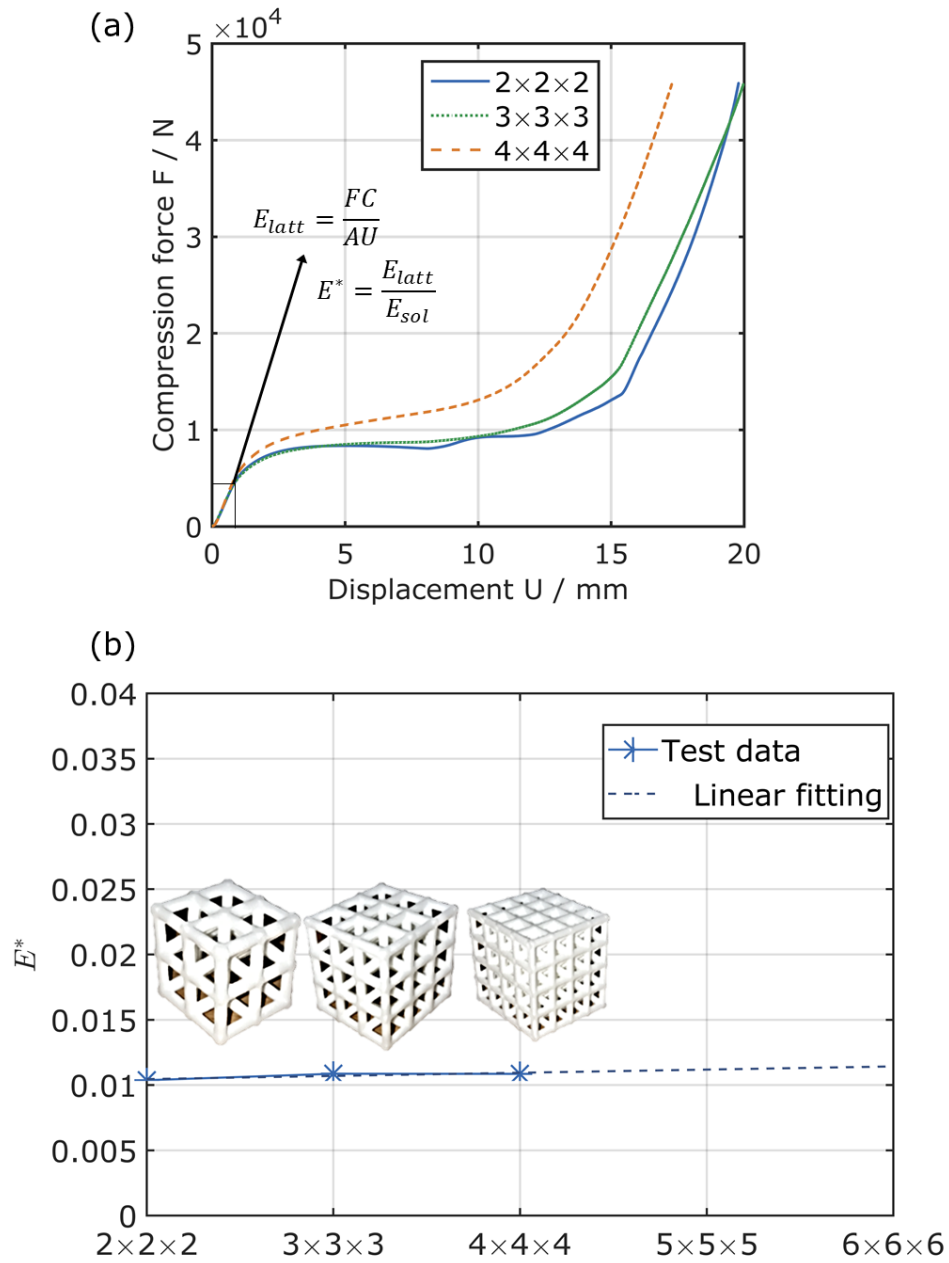
Figure 5.2. (a) Compression testing of lattice structures at multiple numbers of tessellations, and (b) relative elastic modulus E^* of the tested lattices.

The errors in calculation of the effective elastic modulus are calculated considering the error in force measurements which is ±0.5 % and the error in displacement measurements which is ±0.15 % or ±0.02 mm, whichever is greater [164]. It can be seen that for small displacements, like that in the linear region of the tested lattices, the displacement error

is relatively high (±1.99 %). For metal structures, the linear region is expected to be considerably longer than reported here, thus, a much lower displacement error is expected in those structures ~ ±0.15 %. By propagation of the errors, the error in calculation of the effective elastic modulus for the tested lattices is calculated to be ±1.99 %. All lattices took the curves up to the densification area. In addition, the calculated relative modulus E^* saw convergence with respect to the number of lattice unit cells at 2×2×2 (see Figure 5.2b). This essentially means that all tested lattices exhibited lattice behaviour and that 2×2×2 lattices (eight unit cells) can be used as the minimum number of unit cells to represent a lattice. This will ensure that the structures used in this study meet the lattice criteria set by Gibson and Ashby [2] (see Section 2.4 for more details). The minimum number of unit cells is used throughout the study to ensure modelling accuracy, and save in computation time and cost.

Table 5.1. Mass of compression test samples as measured using a mass balance with the calculated standard errors.

Cell configuration	Sample configuration	Mass, g
9010-9	2×2×2	9.001±0.051
	3×3×3	9.333±0.025
	4×4×4	9.600±0.006

5.2.2   Simulation and experimental results

The natural frequencies of the lattices shown in Figure 5.1a were analysed using a commercial FE package (ANSYS). To ensure the calculations had converged with respect to the element size, the first natural frequency of the structures was determined using a range of element sizes from 25 mm to 0.25 mm. At an element size of 1 mm, the difference between subsequent results had fallen below 1 % for Nylon-12 samples of (60×60×60) mm size (see Figure 5.3). Therefore, all subsequent calculations used elements of 1 mm size (also due to manufacturing limitations as mentioned in Chapter 4).
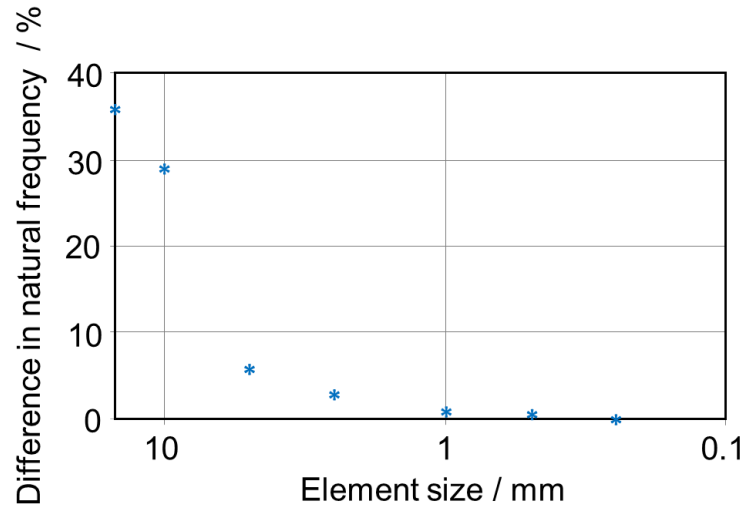
Figure 5.3. Results of the convergence test of 8010-1 lattice in 2x2x2 tessellations.

The first natural frequencies of 8010-x lattices are shown in Figure 5.4 and that of 9010-x lattices are shown in Figure 5.5. Most of the lattices with nine lattice nodes (9xxx-x lattices) showed higher first natural frequency. This is due to the existence of diagonal struts across the centre of their bodies; this fosters increased stiffness k and, thus, increased natural frequency. The lowest natural frequency was for 8010-7 and 9010-3 lattices (< 250 Hz) and the highest first natural frequency was for 5010-9 lattice (> 900 Hz).
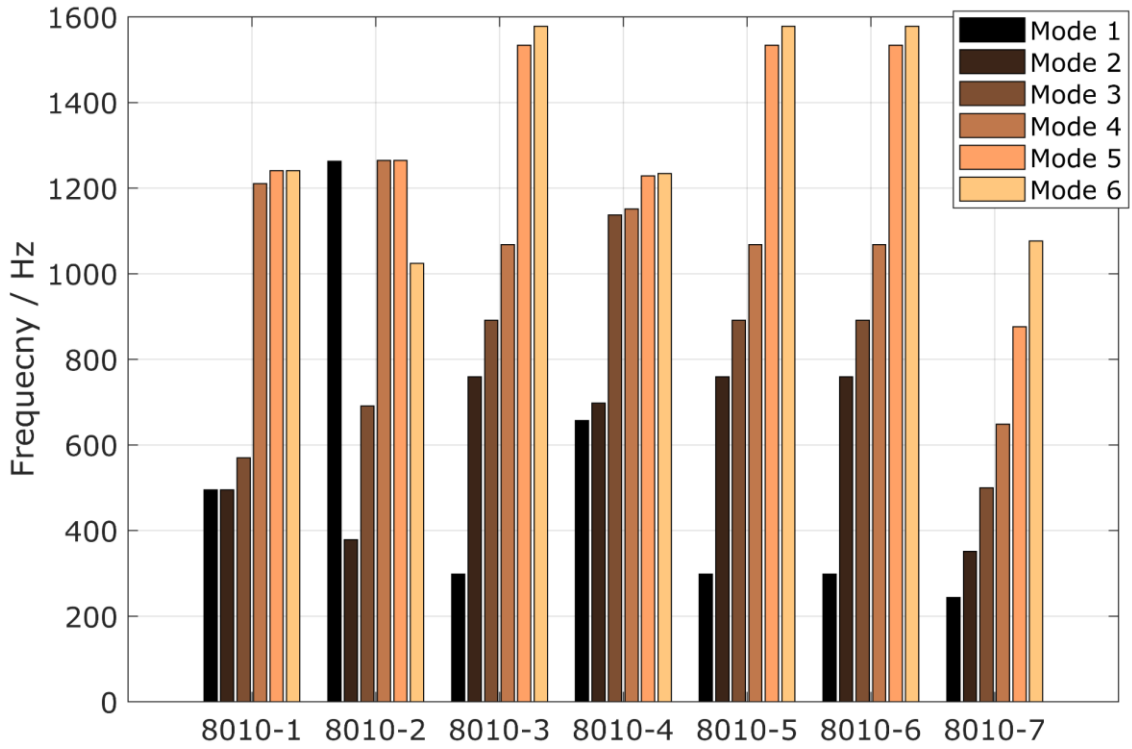
Figure 5.4. Natural frequencies of 8010-x lattices.

The unit cell design of 9010-9 is symmetric (i.e. similar number of struts and orientation in 2D and 3D), while 8010-7 unit cell design is asymmetric with missing vertical pillars (see Figure 4.8). The absence of vertical pillars meant that the support of top and bottom faces are through inclined struts (which is a less stiff connection than vertical pillar). Structures of less stiffness and of the same overall mass and size, generally, have a lower natural frequency. All 9xxx-x unit cell designs have two or four diagonal struts across their body while 8xxx-x designs do not.
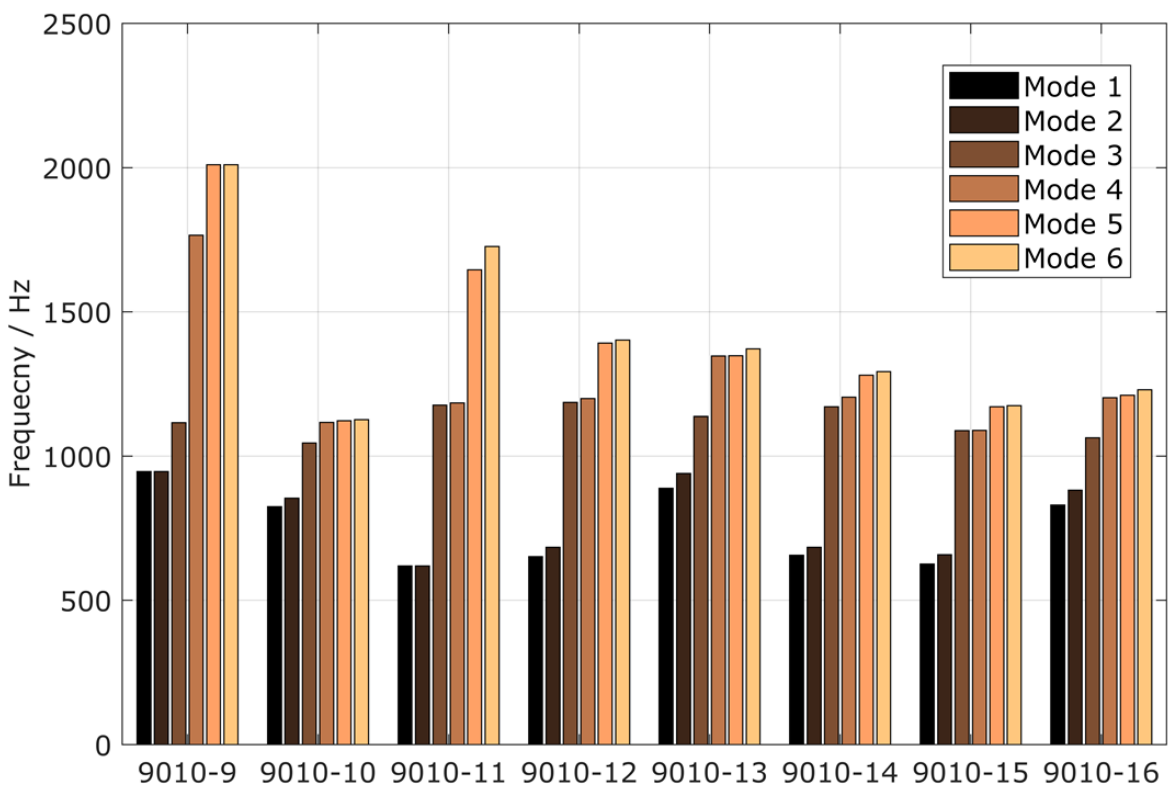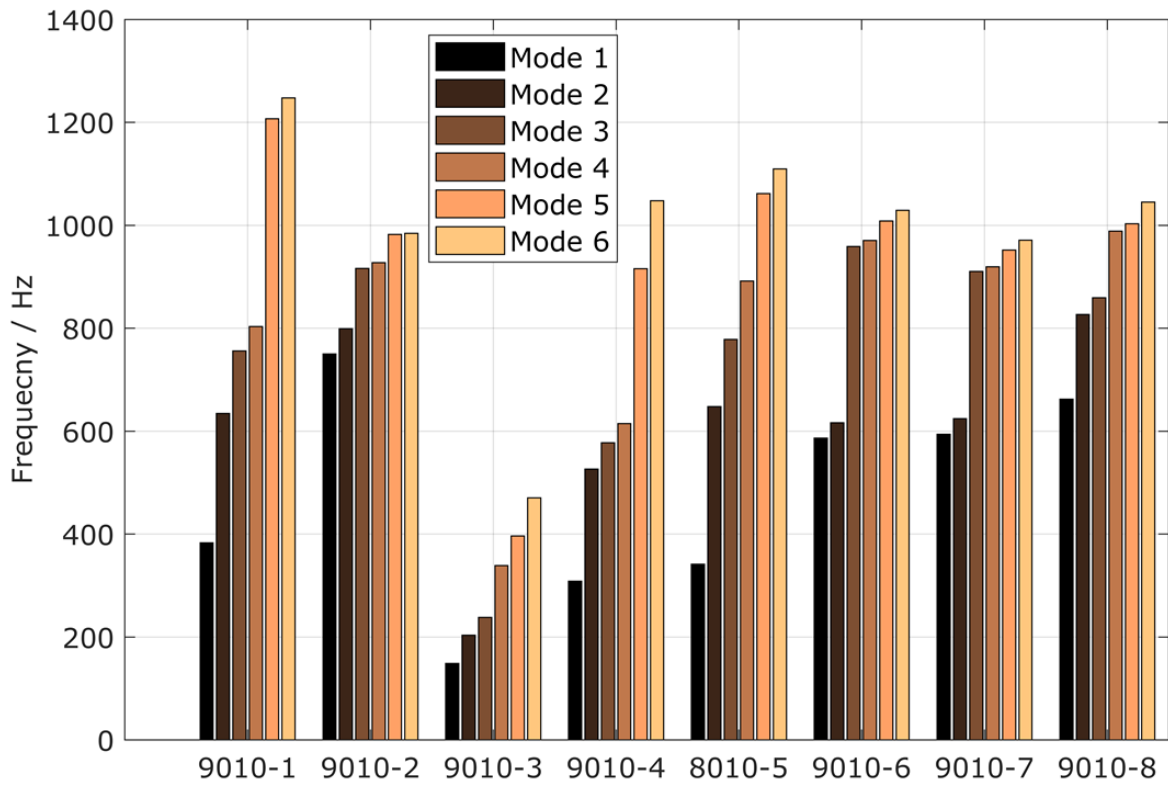
Figure 5.5. Natural frequencies of 9010-x lattices.

Harmonic response analyses in the longitudinal direction were obtained with simulation and experiment; see Section 4.1.4 for a detailed description of the methods. The tested and simulated structures were one lattice of high first natural frequency (9030-1) and one lattice with the lowest natural frequency (8010-7). The experimental and simulation results are shown in Figure 5.6.
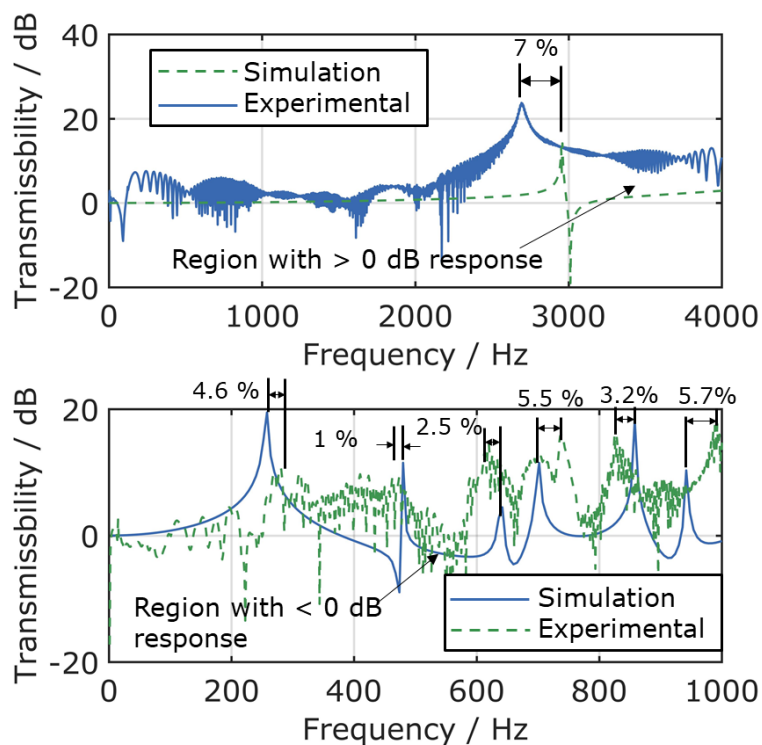
Figure 5.6. Longitudinal harmonic response analysis obtained with experiment (solid line) and simulation (dashed line) of 9030-1 (top) and 8010-7 (bottom) lattice of 2×2×2 tessellations.

The experiment included suspending the structure using piano strings to approximate free-free boundary conditions. A signal sweeping the tested frequency range has been sent through one surface of the lattice and the acceleration data of the signal input surface and the opposite surface were acquired. The frequency sweep has been performed 100 times and the averaged measurements have been reported (see Chapter 4 for more details). The experimental first natural frequency of 9030-1 lattice was less by 7 % than the

simulated value. For 8010-7 lattice, several natural frequencies existed within the tested frequency range. The difference between simulation and experimental values are due to experimental error and difference in structural properties, for example, Young's modulus and density between the modelled parts and those manufactured with L-PBF.

The effect of the volume fraction of lattices on the natural frequency was studied to provide means for control of natural frequency; using 4xxx-7 lattices in 2x2x2 tessellations and of various volume fractions: 10 %, 20 % and 30 %. Lattices with lower volume fraction showed lower natural frequencies than lattices of higher volume fractions (see Figure 5.7). This is due to the lower stiffness of the lower volume fraction models.
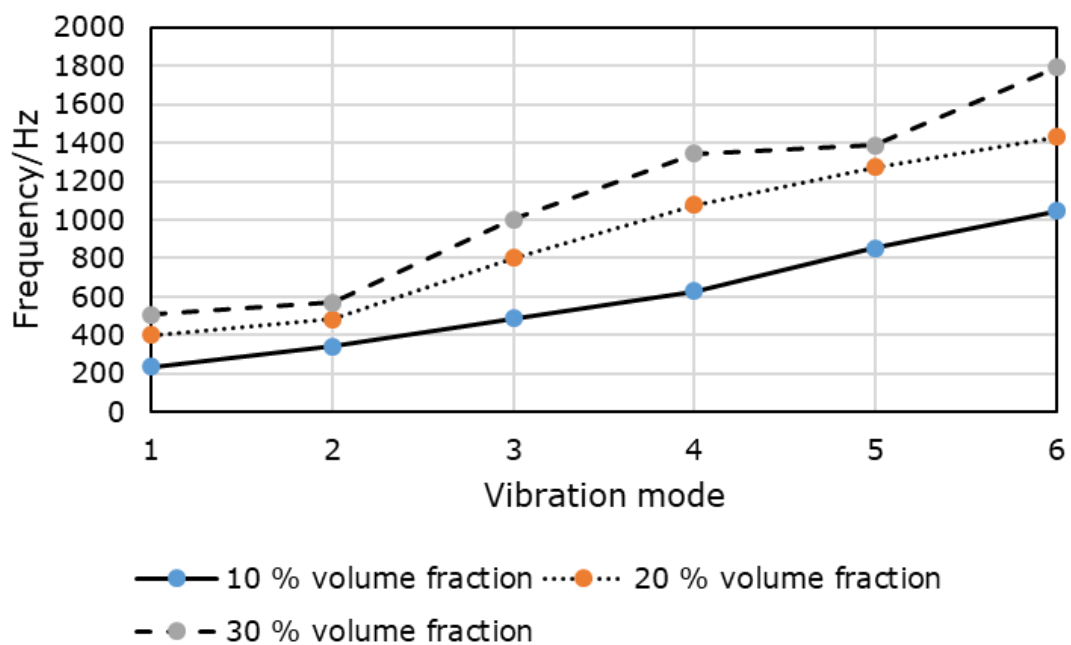
Figure 5.7. The effect of volume fraction of lattice cells on the natural frequency; based on 80xx-7 lattices in 2x2x2 tessellations.

The effect of the size of the lattice cells on the natural frequencies was simulated. The following macro-scale sizes were chosen for their suitability for manufacturing with L-PBF: 30 mm, 22.5 mm and 16.875 mm, while keeping the number of tessellations constant at 2×2×2. From the FE modelling results shown in Figure 5.8, it can be concluded that decreasing the cell size results in higher natural frequencies. This is due to lower

stiffness of taller structures; this behaviour is similar to that reported for tall buildings which tend to have lower natural frequencies than shorter ones [165]. This behaviour happens because the natural frequency of a structure depends on the stiffness k and mass m. When the stiffenss of the structure is increased, the natural frequency is increased and when the mass is increased, the natural frequency is reduced.
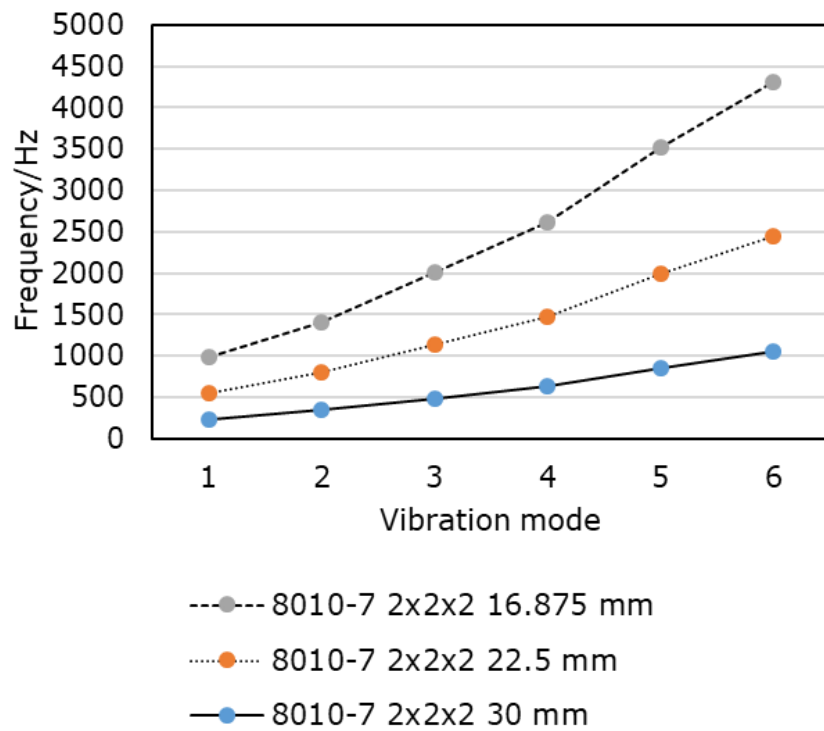
Figure 5.8. The effect of lattice cell size on the natural frequency.
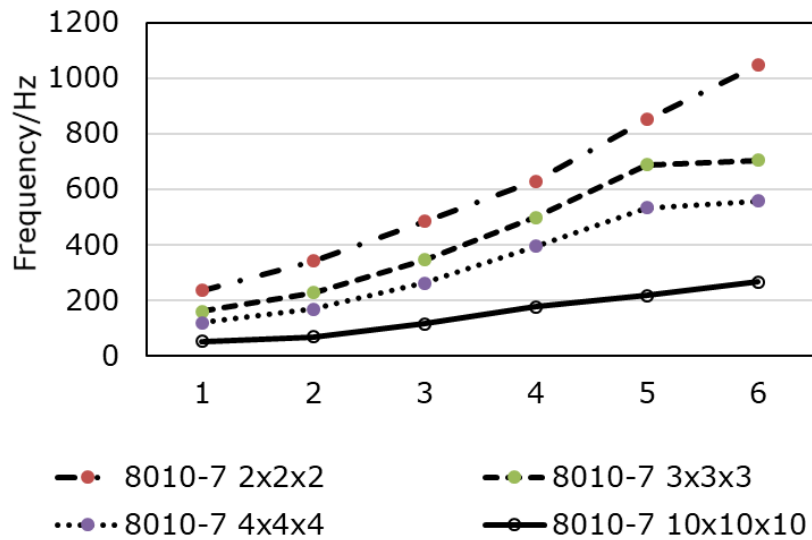
Figure 5.9. The effect of the number of tessellations of lattice cells on the natural frequency.

The effect of the number of tessellations of the lattice was studied using lattices of tessellations of 2, 4, 5 and 10, in three-dimensions, as shown in Figure 5.9. It was shown that increasing the number of tessellations, for constant cell size and volume fraction, reduces the natural frequency of the structure, which is related to increased strut bending in structures with a higher number of tessellations.

5.3   Case study

The structural frame of a new all-optical coordinate measuring system (AODMS) was manufactured with L-PBF from Nylon-12 using lattice structures. The vibration attenuation method of the structural frame of the AODMS relies on vibration isolation (not the bandgap mechanism) by shifting the natural frequency below the frequency of interest. The structural frame is to hold the mass of a 1 kg probe and isolate mechanical vibration in the z-direction propagating to the structural frame from the lab environment. The AODMS is a flexible and open-architecture system for measuring the geometry and surface topography of micro-scale components. The system is designed to operate in a cube of 100 mm sides, with micrometre or sub-micrometre measurement uncertainties.

The open nature of the architecture allows full flexibility in the design and configuration of the instrument control and communication software, as well as of the data analysis and processing software [166].

To design the structural frame of the AODMS, the lab vibration spectrum was measured using a laser vibrometer. Vibration of the wall and floor were measured by pointing the laser vibrometer perpendicular to the wall and floor, respectively, of the lab where the AODMS will operate. See Section 4.3.3 for information about laser vibrometer. Then the structural frame was designed to isolate a problematic frequency region for illustration of the capabilities of lattice structures to provide vibration isolation. The vibration spectrum of the wall and floor of the lab were measured using a vibrometry set up as shown in Figure 5.10. The results of the lab measurements are shown in Figure 5.11.
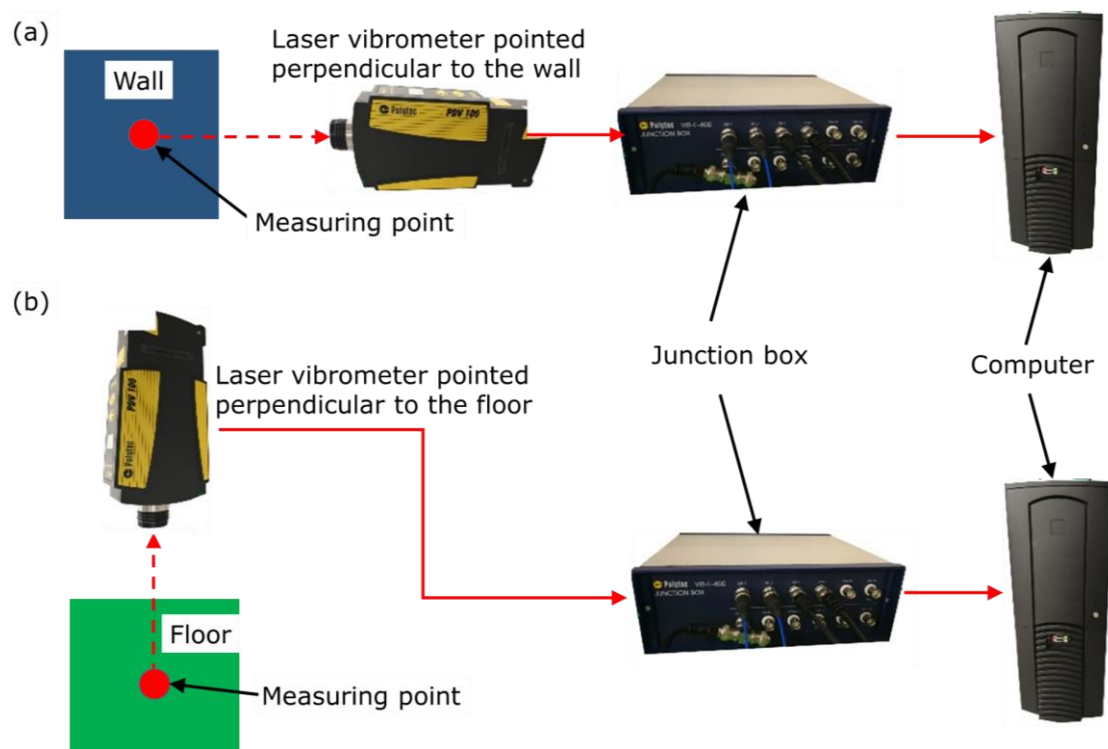
Figure 5.10. Experimental setup of the laser vibrometer for taking measurements of (a) wall excitations, and (b) floor excitations of the lab.

Spectrum A spans from 0 Hz to 20 Hz and appears as two natural frequency spikes on both wall and floor vibrometry measurements. Spectrum B spans from 30 Hz to 57 Hz and appears on only the wall vibrometry measurements. This corresponds to the vibration of nearby elevators, handling equipment, low-frequency machinery and street traffic. Spectrum C spans from 70 Hz to 200 Hz and appears only on the wall vibrometry measurements. The vibration magnitude in spectrum C is below 1 mm·s^{-2} in the lower and upper third of the spectrum and is above 1 mm·s^{-2} in the middle third of the spectrum. This corresponds to the frequency of motorised equipment and machinery. The vibrometry measurements of the floor show spikes at 150 Hz, 250 Hz, 350 Hz and 450 Hz (referred to as floor excitations) which corresponds to vibration of high-way traffic, machinery and motorized equipment.
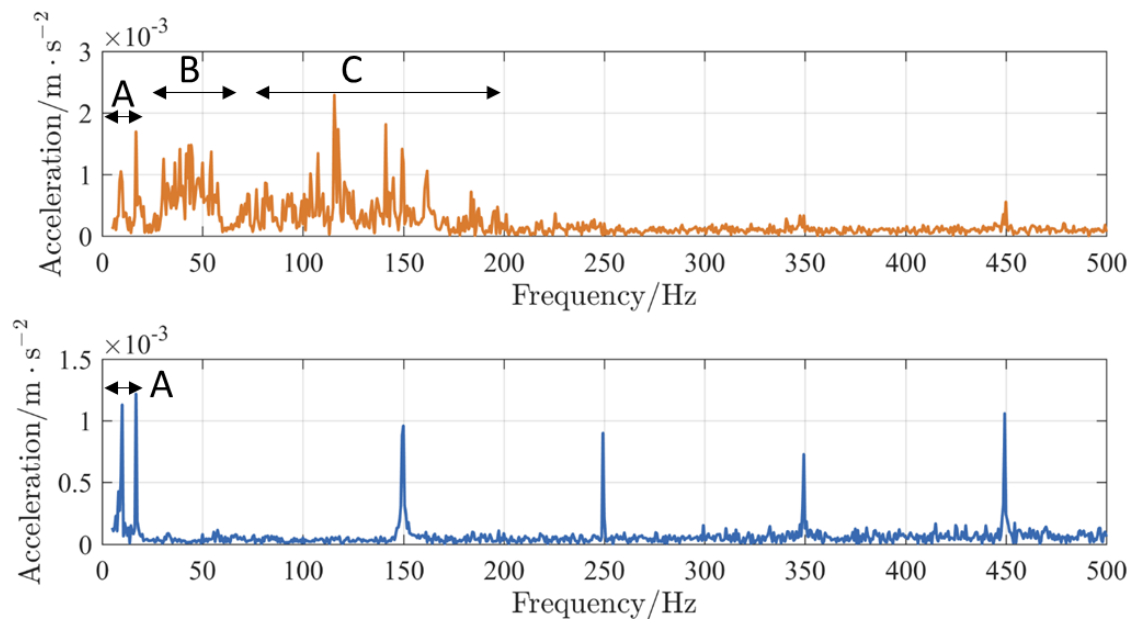
Figure 5.11.Vibrational spectrum of the lab as measured from the wall (top) and floor (bottom) of the lab.

For the purpose of this case study, we target the frequency range 60 Hz to 150 Hz for illustration of the capabilities of the lattices structures to provide vibration isolation at low

frequencies. This frequency range corresponds to the common noise frequencies from rotating instruments, handling equipment and near-by street traffic.

5.3.1 Determining the lattice cell size

There are two options for the selection of the cell size and the number of cell tessellations that can fill a volume in space with low natural frequency: (a) large size cells with a low number of tessellations, or (b) smaller cells with a higher number of tessellations. The results, so far, do not suggest which route is more appropriate for the purpose of vibration isolation. So, a study was conducted to suggest the most appropriate route to obtain lower natural frequency. The study comprised the design of (30×30×30) mm lattice structure samples using 8010-7 cells of different sizes: 15 mm, 7.5 mm, and 3.75 mm. By default, cells of lower size need a higher number of tessellations to fill the (30×30×30) mm space. FE modelling (results are summarised in Table 5.2) showed that larger size cells had lower first natural frequency than smaller ones with a higher number of tessellations (see Figure 5.11 for vibration spectrum of lab environment).

Table 5.2.The coupled effect of cell size and the number of tessellations at constant volume fraction on the first natural frequency of the lattice structures.

Cell size/ mm	Sample size/mm	Number of cells	First natural frequency / Hz
15	30	8	410
7.5	30	64	421
3.75	30	512	468

5.3.2 Verification with in-situ harmonic test

The design of the structural frame comprises three identical sub-frames each kinematically coupled to the stage of the optics through balls in v-grooves located on top of each sub-frame. The v-grooves provide kinematic constraint through contact with the ball in two points, thus, constraining linear and rotational movement of the optical stage in x- and y-directions [167]. The three sub-frames are oriented at an angle 120° between each other

as shown in Figure 5.12; this is to reduce movement between the sub-frames due to thermal expansion by creating a thermal centre [59]. The sub-frame, shown in Figure 5.12, is stiffened at the back through the use of a solid swept stiffener and in both sides through the use of perforated swept surfaces. The swept surfaces are used to increase the stiffness of the structure in x- and y-directions, however, no further analyses were carried on that since the focus of this chapter is on 1D attenuation (see Chapters 6 to 8 for 3D attenuation). As a result, the most suitable cell size for the structural frame must have two tessellations in the direction of the shortest dimension (two is the lowest number of tessellations that can represent a lattice as previously established in Section 5.2). Subsequently, 30 mm cells were used to construct the body of the structural frame because the shortest dimension was the thickness of the structural frame (60 mm).

The support structure, developed in this section for the AODMS, is selected from a predefined list of lattices and is not solely based on an optimised solution. The structure used the 4010-7 lattice, because it proved to have the lowest natural frequency among those examined in Section 5.2.2. Then, we varied the volume fraction and the number of tessellations based on the results shown in Figure 5.7 and Figure 5.9 to bring the natural frequency below the frequency of interest (below 60 Hz). When the first natural frequency is below the frequency of interest, the second natural frequency lied within the frequency of interest and thus destroyed the intended attenuation region. However, when both the first natural frequency (as appears in Figure 5.12) were brought below 60 Hz, the targeted attenuation region was not affected (i.e. no natural frequency existed between 60 Hz to 150 Hz). This was based on longitudinal transmissibility of the structure which was simulated and experimentally tested using the methods detailed in Section 4.1.4.
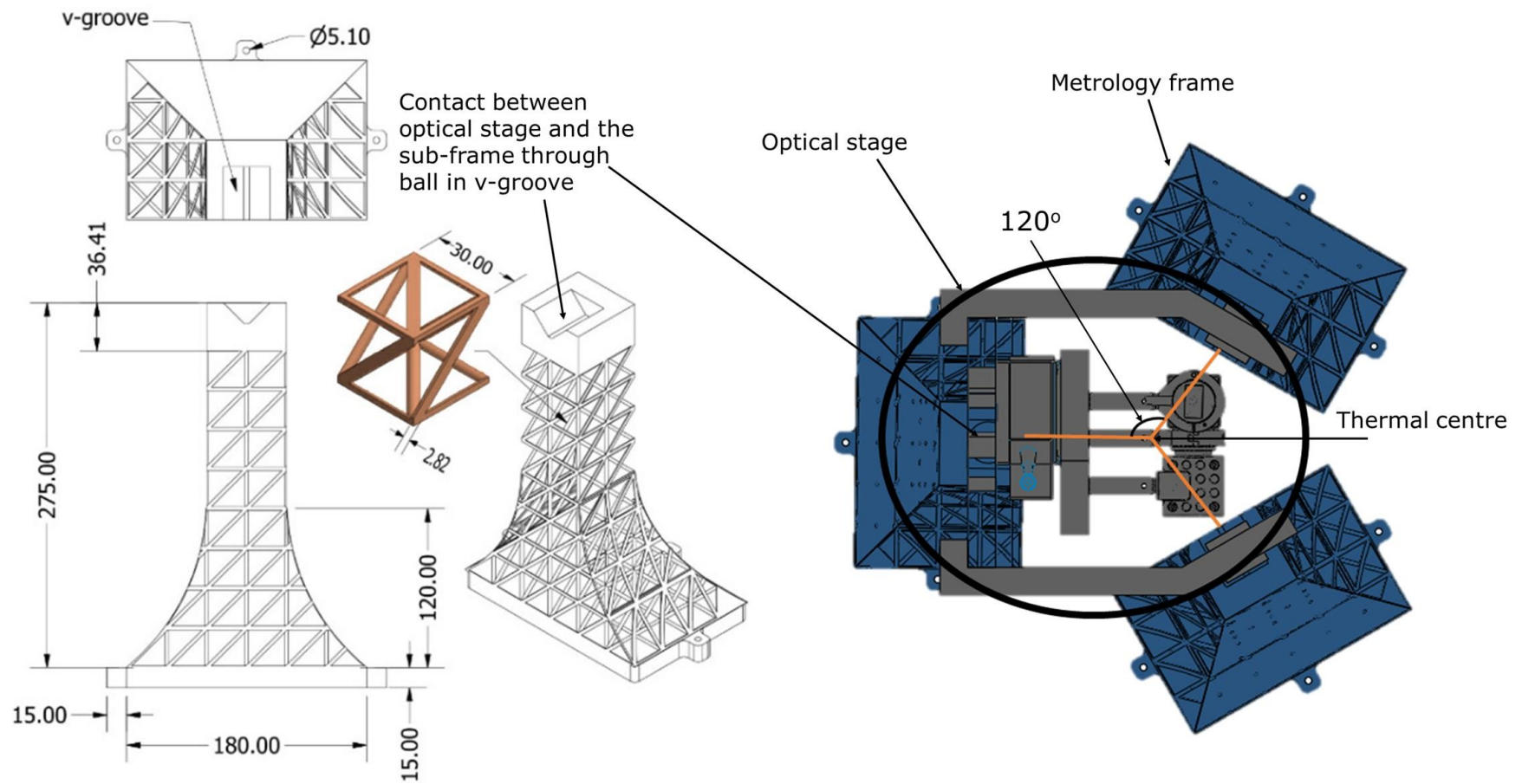
Figure 5.12. Design of the structural sub-frame with an illustration of its full assembly to the optical stage.
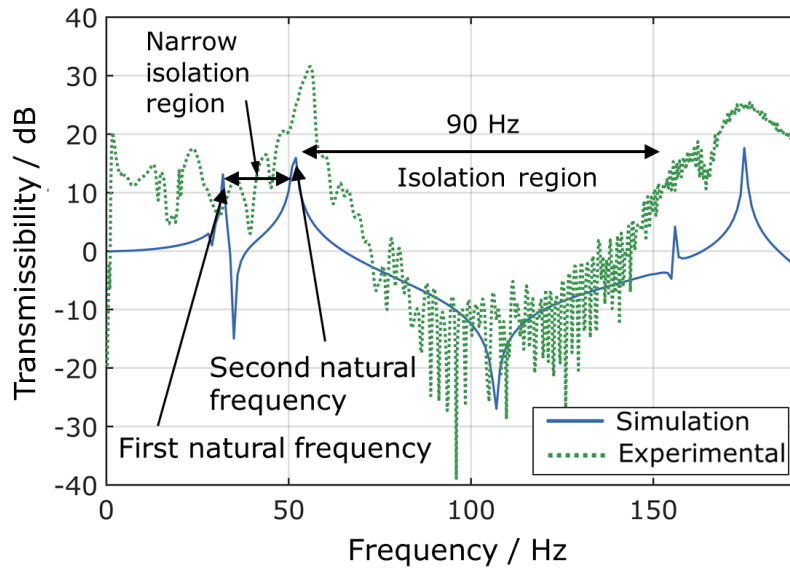
Figure 5.13. The harmonic response of one sub-frame as obtained with simulation (solid-line) and experiment (dotted-line).

As can be seen from Figure 5.13, the structure succeeds in isolating excitations in the range of 60 Hz to 150 Hz (90 Hz in width). However, if we had relied on the first and second natural frequency, then the width of the attenuation region would have been only 22 Hz (see the narrow attenuation region in Figure 5.13) which would cover only 24 % of the intended isolation region.

5.4 Summary of results

Before lattice structures can be used for vibration isolation of a system, the dynamic behaviour of the system has to be understood. Then, the lattice characteristics can be tailored to isolate the resonance peaks of the system. The control of the natural frequency is the first step towards tailoring the dynamic behaviour of lattice structures. The study revealed that the natural frequency of a lattice structure can be reduced by increasing cell size, reducing volume fraction, and/or increasing the number of tessellations of a singular lattice cell, and vice versa. The findings of this chapter are very important for understanding the vibrational response of lattices for the purpose of designing lattices with

106

vibration isolation capabilities especially at low-frequency. The major drawback of relying on this attenuation method to achieve vibration attenuation are:

- difficulty to tune in 2D and 3D. The unit cell designs that showed low frequencies were asymmetric (i.e. had a different number of struts in 2D and 3D). This lead to a reduction in the natural frequency of these unit cells compared to symmetric unit cells of the same volume fractions and size. Dynamic characterisation of such unit cells in 2D and 3D, and consequently their control, will become much more challenging. The solution for this is to use symmetric unit cells (Chapter 6 to Chapter 8 will address this).

- the amount of attenuation achievable with vibration isolation is not guaranteed. For example, as shown in Figure 5.6, the response at frequencies higher than the natural frequency did not fall below 0 dB. To give confidence in the amount of achievable attenuation, a more comprehensive approach for vibration attenuation has to be proposed; one that guarantees attenuation below 0 dB. This chapter paves way for work on 1D bandgap lattices which is presented and discussed in Chapter 6.

Chapter 6

One-dimensional bandgaps in triply periodic minimal surface lattices

The results of this Chapter are published in this peer-reviewed journal paper [159]. The novelty of the work presented in this chapter lies in the discovery of 1D bandgaps in TPMS lattices, which has not been presented before, and in providing numerical results that can be used to design an AM lattice structure with a desirable bandgap. Many applications in different industries are expected to exploit the ability of TPMS structures to provide vibration bandgaps due to their controllable mechanical and vibration properties. For example, the transport sector could make use of TPMS lattice structures for sound absorption in vehicles, while benefitting from their inherently light-weight nature. The aerospace sector could benefit from TPMS lattices for designing heat exchangers with vibration attenuation capabilities [117]. Structural frames for precision machines, which are the focus of this work, will also benefit from TPMS lattices; they could be used to attenuate environmental vibration within certain frequency ranges; for example, those associated with laboratory or workshop equipment. In general, lattices that are manufacturable with current AM methods, and have broad bandgaps with low starting frequencies are the most desirable. This is because they can be tailored for use in various applications, including precision engineering and metrology, providing a wide frequency range over which vibration transmission is restricted.

This chapter is structured as follows: Section 6.1 introduces the TPMS lattice unit cells used in the study. Section 6.2 presents and discusses the dispersion curves of the TPMS lattices. The dependence of the frequency and bandwidth of the bandgaps on the cell size and volume fraction is presented in Section 6.2.1 and Section 6.2.2, respectively, to provide a simple tool for designing bandgaps at desired frequencies. As detailed in Section 4.2.1, the bandgap analyses assume infinite tessellations of the lattice cell along the *x*-direction, so the response of TPMS structures of finite lengths was simulated and presented in Section 6.2.1 and Section 6.2.2. Prototype structures are fabricated with AM to demonstrate the manufacturability of TPMS lattices; the results are reported on in Section 6.2.3. Conclusions are provided in Section 6.3. For details on the theoretical background of the finite element method, see Section 3.6. The methodology of this work is provided in Section 4.2.

6.1   TPMS bandgap lattice design

The lattice unit cells used in this study are the network and matrix phases of the gyroid and diamond TPMS lattices, as shown in Figure 6.1, due to their high stiffness when compared to strut-based lattices [42,46]. Network phase cells have one void region and one solid region, both of which retain their connectivity in every part of the structure. Matrix phase lattices have two non-connected void regions separated everywhere by a solid wall or sheet.

(a)   (b)   (c)   (d)
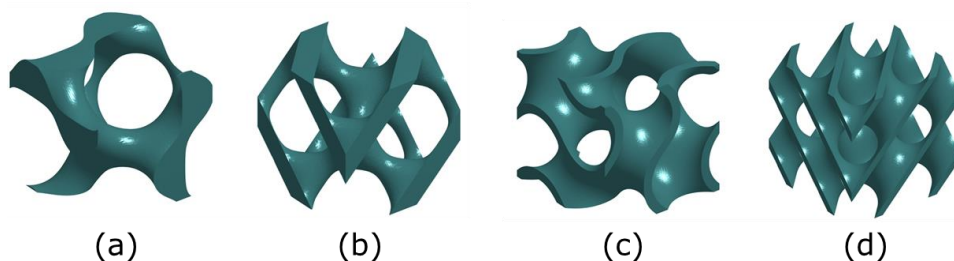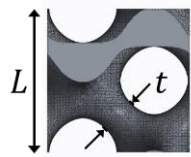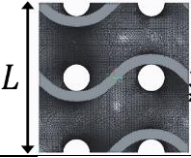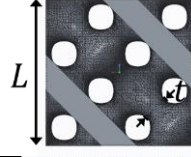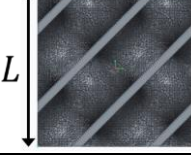
Figure 6.1. Representations of the TPMS unit cells used in the study. (a) Network gyroid, (b) network diamond, (c) matrix gyroid and (d) matrix diamond.

In addition, matrix phase lattices are known to have higher specific stiffness than their network phase equivalents [43]. The determination of phonon dispersion curves requires analysis of a single lattice unit cell. The unit cells are designed using FLatt Pack [49] (see Section 2.3 for more details). The volume fraction and size of the cells shown in Figure 6.1 is 20 % and 15 mm (initial settings), respectively. The results will be normalised to the cell size and manufacturing material to obtain normalised results that are applicable to a wide range of materials and permissible sizes for the chosen manufacturing technique.

Table 6.1. Geometric specifications of the unit cell used in this study. The parameter t identifies the thickness of the minimum feature in each unit cell.

Unit cell	Unit cell size, L/mm	Volume fraction /%	t/mm	t/L	Schematic
Network gyroid	15	20	3.8	0.25	
Matrix gyroid	15	20	1.05	0.07	
Network diamond	15	20	2.55	0.17	
Matrix diamond	15	20	1.05	0.07	

The geometrical specifications of the unit cells are shown in Table 6.1. The minimum feature size of the matrix unit cells is the sheet thickness t. For network type unit cells, the thickness differs across the unit cell. The parameter t for the network unit cells is, therefore, defined as the thickness in the slimmest regions. Design equations of gyroid and diamond TPMS can be found in the AM work of Maskery et al. [41] and chemistry work of Gandy et al. [168], respectively.

6.2   Results and discussion

The mass and stiffness matrices on which the phonon dispersion curves depend were found to have converged with respect to the number of FE nodes as shown in Figure 6.2. This was done by simulating the first natural frequency in ANSYS which used the stiffness and mass matrices of the structure. The simulated structures used different number of FE nodes representing hexahedral mesh elements of different sizes. The results showed convergence with a difference of less than 1 % when 28,312 FE nodes were used, which corresponds to 20 mesh elements along one Cartesian direction as shown in Figure 6.3.
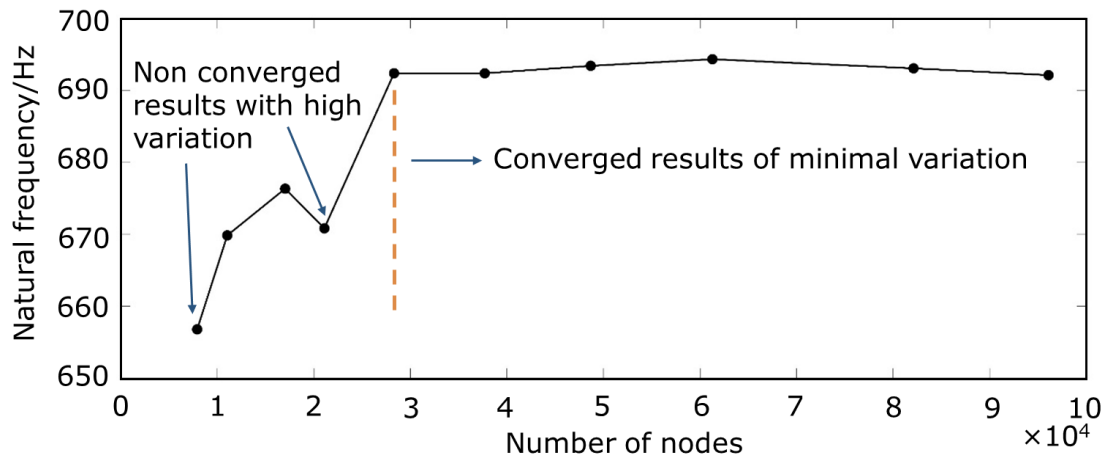
Figure 6.2. Convergence results of 2x2x2 network gyroid lattice of 20 % volume fraction, and 30 mm cell size.

The dispersion curves of the TPMS lattices which were presented in Section 6.1 were modelled using the 1D dispersion curves modelling method detailed in Section 4.2.1. The dispersion curves for the network gyroid lattice is shown in Figure 6.4. The dispersion curves were modelled with the properties of AM Nylon-12. The wave bands are numbered from the 1st to the 11th wave band. The top axis of the dispersion curves shows the frequency f normalised to the lattice unit cell size L and the speed of the wave v in the material, while the right axis shows the wavenumber normalised to the lattice unit cell size L.

111
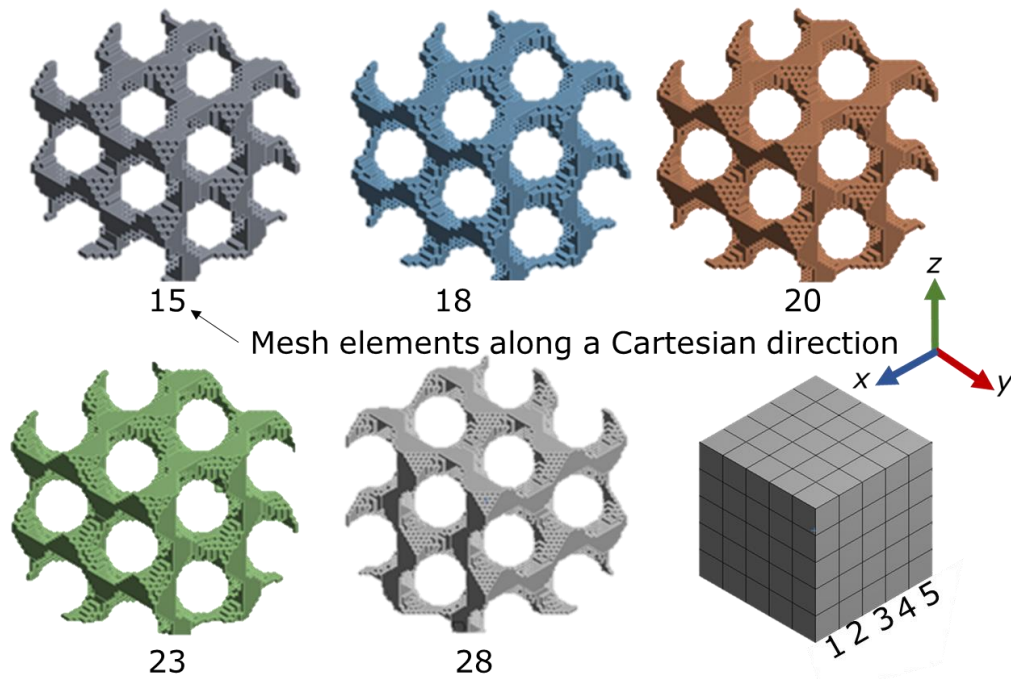
Figure 6.3. Selection of the structures used in the convergence study, more elements along a Cartesian direction show higher structural definition. Illustration of the number of elements along a Cartesian direction is shown in bottom right using a solid cube.

The bandgaps are identified from the dispersion curves by observing the frequency regions between the wave bands. If the two wave bands disperse to close the gap between them, as is the case between wave band 5 and wave band 6 in Figure 6.4, then no bandgap is developed between them. If the two wave bands disperse away from each other to open a frequency gap between them, as is the case with wave band 6 and wave band 7 in Figure 6.4, then a bandgap is formed. A total of four bandgaps in the sub-15 kHz region were found from the dispersion curves in Figure 6.4. The broadest bandgap is formed between the 6th and 7th wave bands, is 1047 Hz wide and starts from 7905 Hz. A bandgap of similar width spans 978 Hz from 11349 Hz to 12327 Hz and is formed by the 9th and 10th wave bands. A bandgap narrower in width than the previous two appears in the range of 9340 Hz to 9506 Hz, and another one appears in the range of 10134 Hz to 10238 Hz.
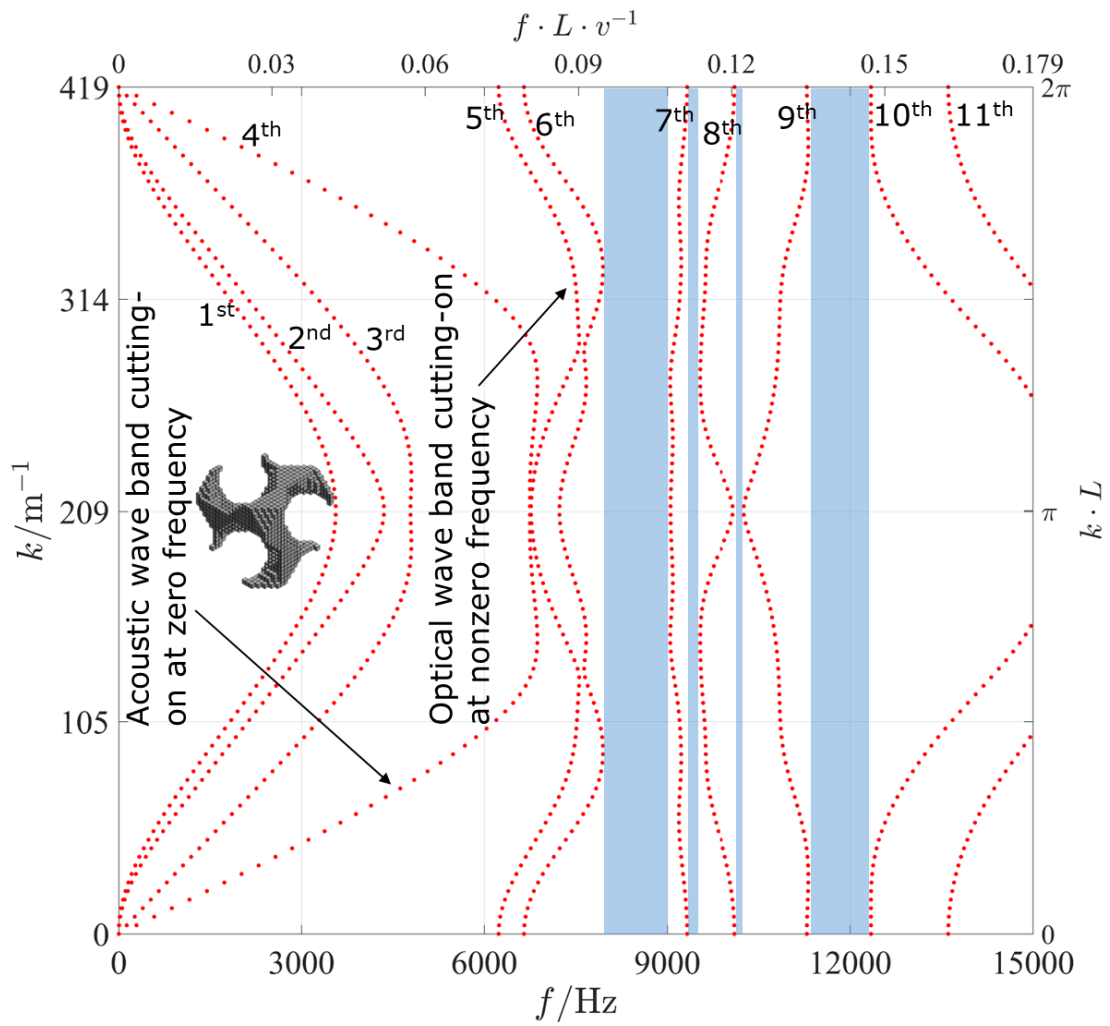
Figure 6.4. 1D phonon dispersion curves for the network gyroid lattice with 15 mm cell size and 20 % volume fraction. Shaded areas represent the bandgaps.
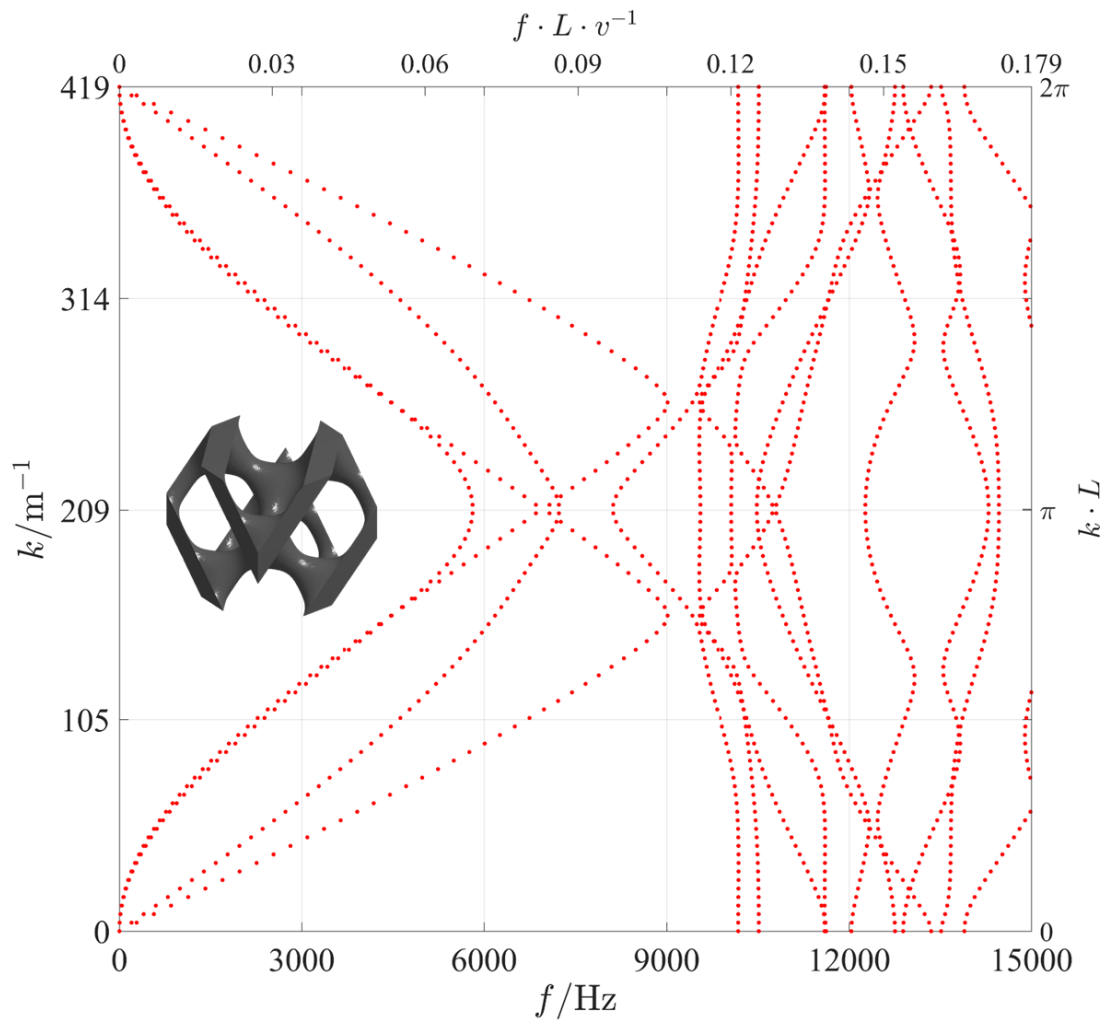
Figure 6.5. 1D phonon dispersion curves for the network diamond lattice with 15 mm cell size and 20 % volume fraction.

The scattering of the mechanical waves in a structure relies on the impedance mismatch between two adjacent geometrical features [169]. This is because a travelling wave in a medium disperses when its propagation speed changes, thus, causing it to reflect. As shown in Figure 6.4 and Figure 6.5, the network gyroid lattice possesses phononic bandgaps below 15 kHz while the network diamond lattice does not. This can be explained by considering the differing internal geometries of the respective cells. As a wave travels from a thicker to a thinner solid region of the cell, or from the solid phase to the void phase, it is partially reflected, owing to the change in local impedance. This process is repeated for each reflected wave, giving rise to complex dispersion curves such as those

114

in Figure 6.4 and Figure 6.5. The absence of bandgaps from the dispersion curves of diamond TPMS suggests that no destructive interference occurs within the tested range.
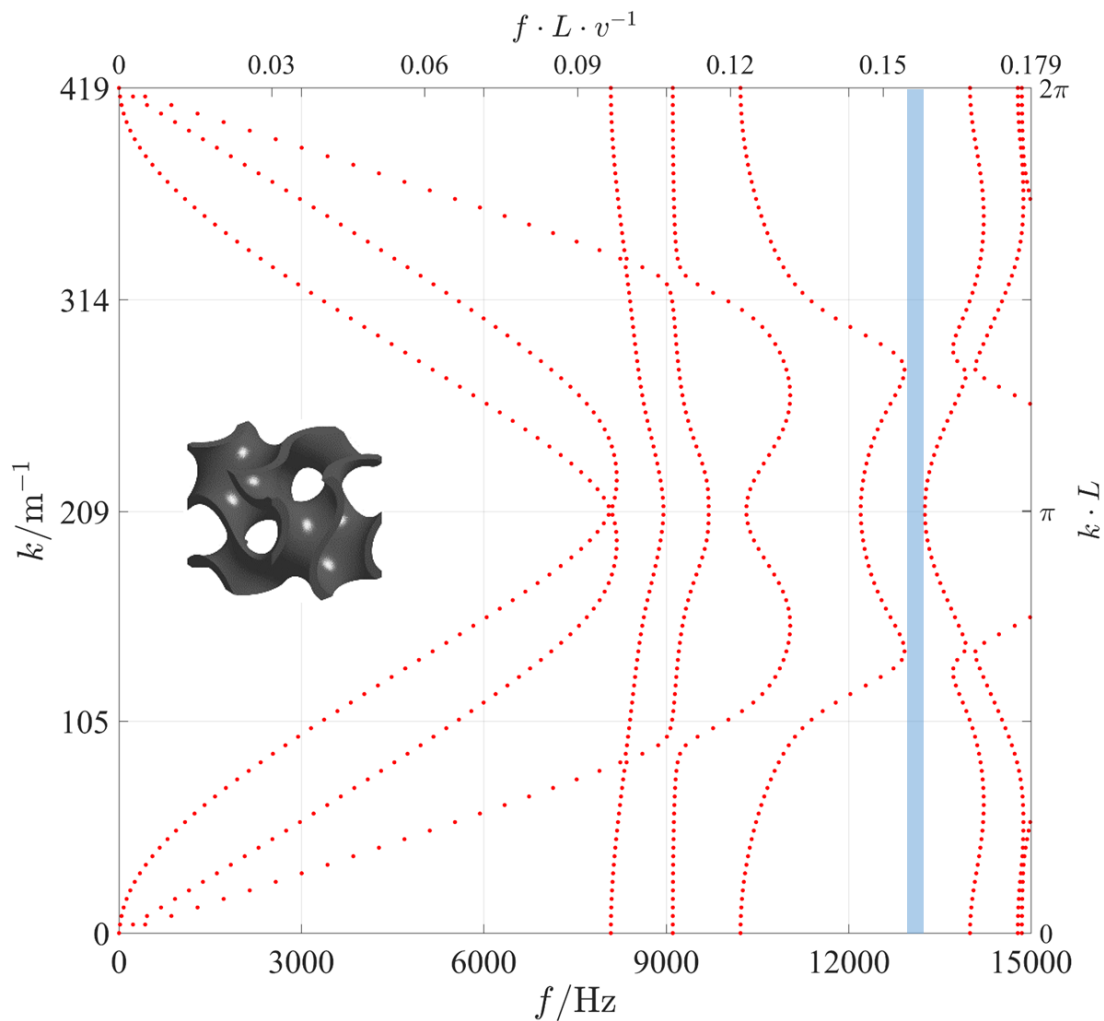
Figure 6.6. 1D phonon dispersion curves for matrix gyroid lattice with 15 mm cell size and 20 % volume fraction.

The lowest frequency bandgap is usually formed by one acoustic wave band (a wave band cutting-on at 0 Hz) and one optical wave band (a wave band cutting-on at a nonzero frequency) [64]. Although Bragg bandgaps can also be formed by two optical wave bands, which is the case of all the bandgaps in this chapter, it is impossible for a Bragg bandgap to be formed at frequencies lower than the cut-off frequency of acoustic wave bands. This is because the acoustic wave bands of a Bragg-scattering lattice, which always start to

propagate from 0 Hz, does not split into two halves, as is the case in internal resonance lattices which are discussed in Chapter 7 and Chapter 8. Since there is a continuous presence of the same acoustic wave bands from 0 Hz until their cut-off frequency, no bandgap is formed before their cut-off frequency. We compare the ability of the network diamond and the matrix diamond lattices to form bandgaps by examining the cut-off frequency of their acoustic wave bands.
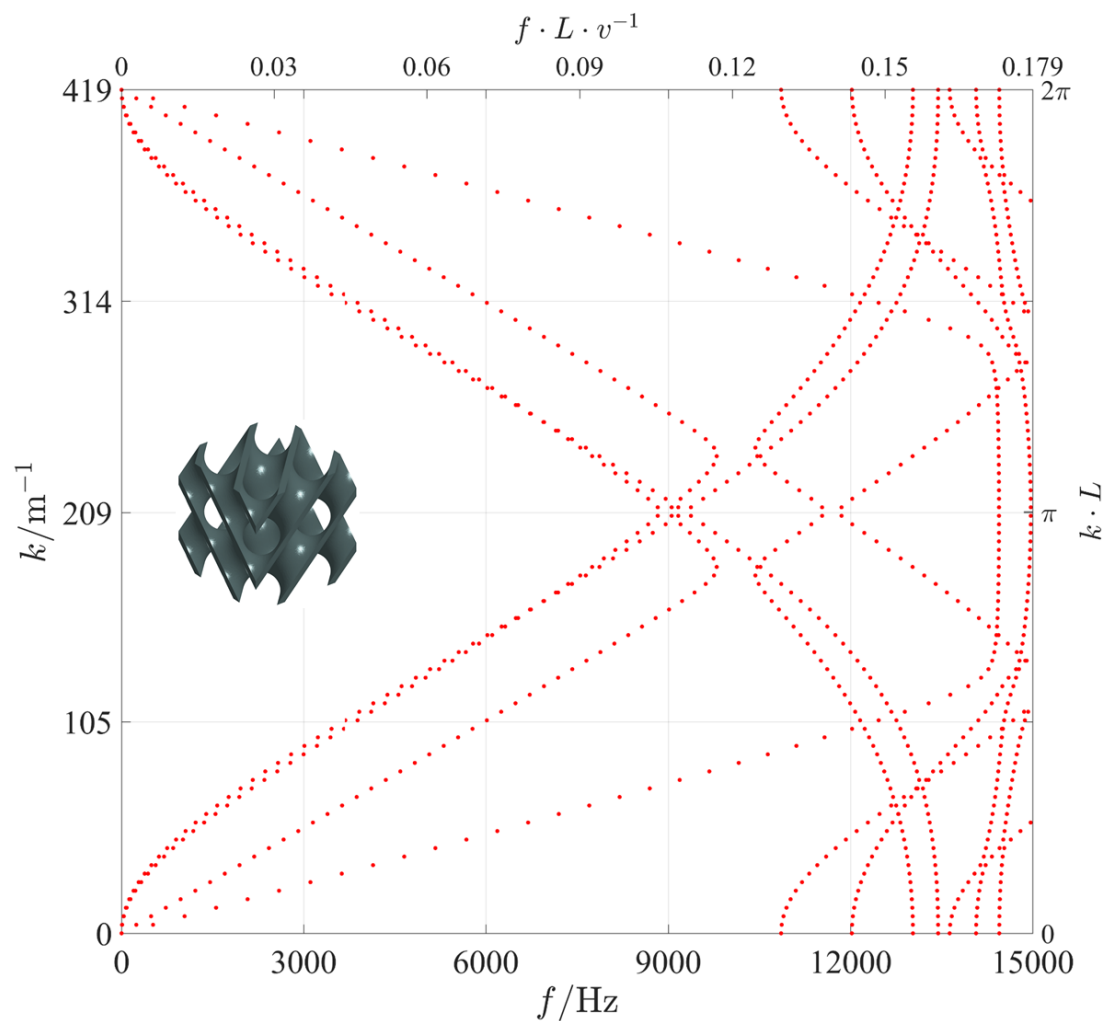
Figure 6.7. 1D phonon dispersion curves for matrix diamond lattice with 15 mm cell size and 20 % volume fraction.

As can be seen in Figure 6.5 and Figure 6.7, respectively, the acoustic wave bands cut-off at a higher frequency in the matrix diamond cell (around 14000 Hz) while they cut off at a much lower frequency (around 9000 Hz) in the network diamond cell. The network

diamond lattice also showed a larger number of wave bands within the tested frequency region. However, similar to its matrix counterpart, the network diamond cell did not possess bandgaps within the examined frequency range.

Similar behaviour is observed by the network gyroid and the matrix gyroid cells; the cut-off frequency of acoustic wave bands of the network gyroid cell is around 7000 Hz while the corresponding frequency in the matrix gyroid cell is around 9600 Hz. The matrix gyroid formed a bandgap spanning from 12952 Hz to 13220 Hz. This bandgap is higher in terms of the starting frequency and narrower in terms of width than the lowest frequency bandgap observed in the gyroid network cell. In addition, matrix type lattices have almost constant wall thickness across the inner parts of the cell. This suggests that matrix cells would have reduced capacity to hinder wave propagation from one end of the cell to the other than in the network type lattices. This is because wave reflection, which is the mechanism by which Bragg induced bandgaps are formed, is expected to be higher when there is a large difference in densities; or a large difference in wall thickness.

The dispersion curves of the matrix lattices support the claim presented by Kapfer et al. [43] in that matrix type lattices have higher stiffness than network type lattices. The examined lattices are of identical volume fraction and cell size and, therefore, identical mass. If the two lattices have the same natural frequency, then they would have the same stiffness (see Equation 3.1). However, the natural frequency of a matrix type lattice is higher than its corresponding network counterparts. This implies that the stiffness of the matrix type lattice is higher than that of the network type lattice. In wave reflection by Bragg-scattering, the bandgap does not appear at frequencies lower than the natural frequency of the structure. Thus, the high natural frequency of matrix gyroid lattice, as can be seen from Figure 6.8, prohibits the opening of bandgaps at lower frequencies than the network gyroid lattice. This is seen in Figure 6.4 and Figure 6.6, where one bandgap appears in the matrix gyroid dispersion curves, while several bandgaps appear within the

117

same frequency range using the network gyroid lattice. The reader is referred to Section 2.3 for more information on matrix and network type TPMS lattices.
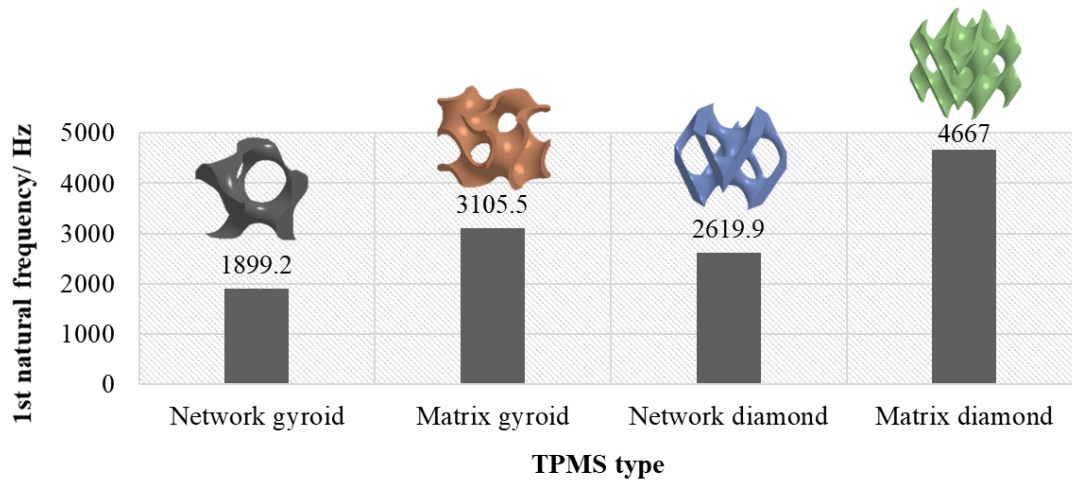
Figure 6.8. 1st natural frequency of the same natural frequency mode for four types of TPMS lattices unit cells as modelled in FE with the initial settings of 15 mm cell size and 20 % volume fraction. A matrix TPMS has a higher 1st natural frequency than its corresponding network counterpart.

6.2.1 Tuning lattice bandgaps through cell size selection

The network gyroid lattice represents a suitable candidate to examine the control of bandgaps because we have established that it supports multiple bandgaps at a manufacturable cell size and volume fraction, as demonstrated in Section 6.2. The absolute bandgap frequencies arising from the network gyroid lattice with cell sizes of 15 mm, 20 mm, 25 mm, 30 mm and 40 mm, at a constant volume fraction of 20 %, are calculated. Figure 6.9 shows the dependence of the absolute bandgaps frequencies on the cell size of Nylon-12 gyroid TPMS. The bandgap with the largest bandwidth was seen for the 15 mm cell, where the bandgap spanned approximately 1048 Hz from 7905 Hz to 8953 Hz.
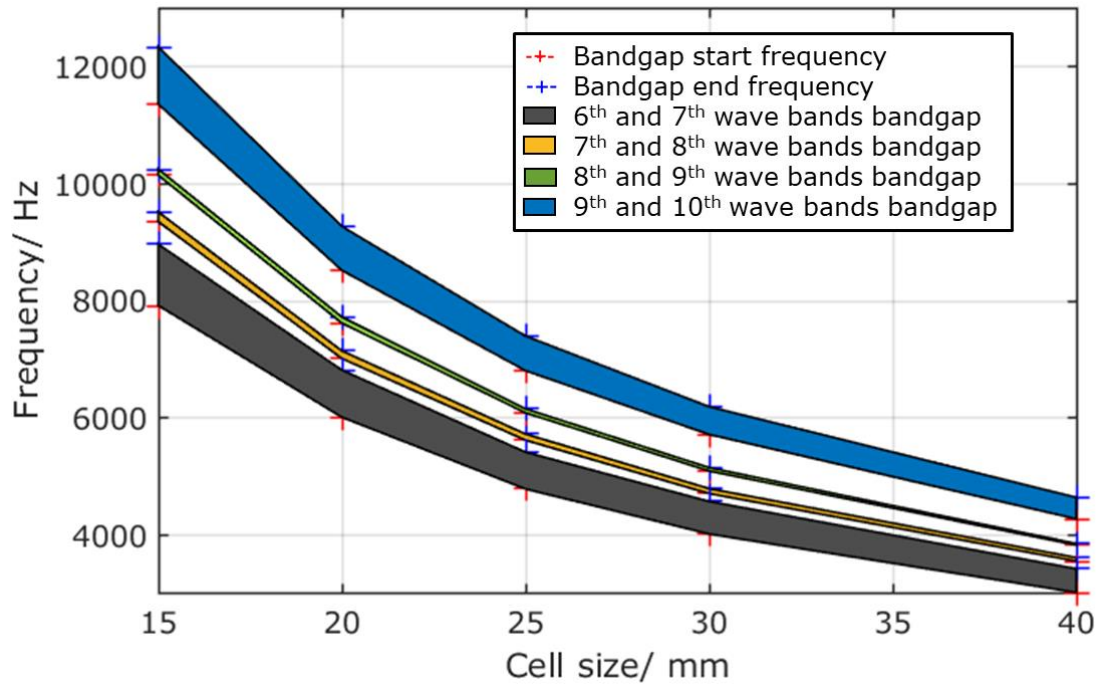
Figure 6.9. Dependence of network gyroid bandgaps on the cell size.

Of the examined network gyroid cell sizes, the 40 mm lattice showed a bandgap of the lowest frequency. This bandgap is formed between wave bands 6 and 7. The starting frequency of this bandgap is around 60 % lower than the corresponding bandgap in the 15 mm cell.

Since the bandgap analyses assume infinite tessellations of the lattice cell along the x-direction, we have chosen settings of nine unit cells to examine the harmonic response of this network gyroid cell. According to Chen et al. [170], any number of unit cells higher than seven is enough to spot the bandgap with harmonic response analysis. The criteria of Chet al. determined the number of finite unit cells required to obtain vibration attenuation within the bandgap frequency region of a Bragg-scattering lattice. Such criterion is important because the bandgaps are obtained by assuming infinite periodicities of the unit cells and that is not applicable in real life. Thus, only finite lattices are applicable for use in real life. The number of unit cells which we chose, nine, is an arbitrary one that fits the finite criteria of Chen et al. The analyses were carried on the 40 mm network gyroid

119

cell structure by exciting one of its faces with an oscillating load. The load was 1 N and was applied to the leftmost FE nodes in the structure. The movement of the rightmost FE nodes in x-, y- and z-directions are depicted to obtain the response of the finite lattice with transfer and cross-transfer receptance setups. The transfer receptance setup saw the harmonic load being applied to the leftmost nodes in the x- direction and the movement of the rightmost nodes was also depicted along the x-direction. In the y-direction cross-transfer and z-direction cross-transfer setups, the movement of the rightmost nodes was depicted along the y-direction and z-direction, respectively, whilst the oscillating load was applied to the leftmost nodes along the x-direction. Figure 6.10 highlights the frequency range of the bandgaps as identified from the 1D dispersion curves of their infinite lattices. It can be seen that the bandgaps of 40 mm network gyroid correspond to attenuation in the harmonic response diagram. The natural frequencies appearing within some of the bandgap frequencies in Figure 6.10 can be the cause of the finite length of the lattice. From our previous work [54,163], we assert that 40 mm cells are less stiff than 15 mm cells of similar configurations due to higher dominance of bending behaviour in larger cells. This lower stiffness, of the 40 mm gyroid cell compared to the 15 mm cell, is translated into lower bandgap frequency.
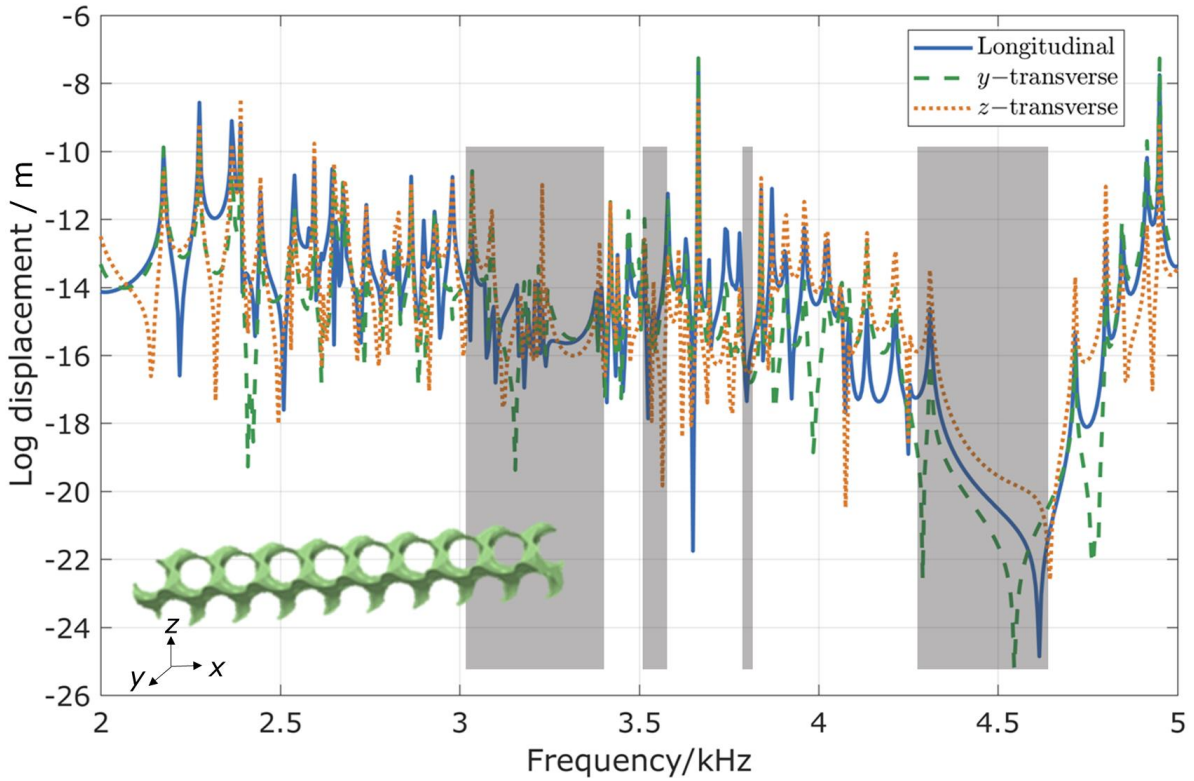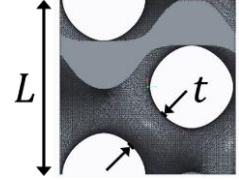
Figure 6.10. The harmonic response of 40 mm network gyroid cell with nine tessellations along the longitudinal (transfer receptance, solid-line), *y*-transverse (cross-transfer receptance, dashed-line) and *z*-transverse (cross-transfer receptance, dotted-line) directions. The shaded regions represent the bandgap frequency range obtained from the dispersion curves.

6.2.2 Tuning lattice bandgaps through volume fraction selection

Phonon dispersion curves for the network gyroid lattices with volume fractions of 20 %, 25 %, 30 %, 35 % and 40 % were simulated at a constant cell size of 15 mm. These volume fractions were selected arbitrary, however, their exact values bear no significance in the conclusions of this chapter; the important thing is depicting the effect of varying the volume fraction on the bandgap. The unit cell information, including the t/L ratio for the network gyroid unit cells at different volume fraction, are shown in Table 6.2.

Table 6.2. Network gyroid unit cells specification at different volume fractions.

Unit cell size L/mm	Volume fraction/%	t/mm	t/L	Schematic
15	20	3.8	0.25	
15	25	4.35	0.29	

121

15	30	4.9	0.33	
15	40	5.95	0.4	

The phonon dispersion curves of these lattices are presented in Figure 6.4 and Figure 6.11 to Figure 6.14. The dependence of the bandgaps on the volume fraction of the 15 mm gyroid unit cell is shown in Figure 6.15. The width of the bandgap between the 9th and the 10th wave bands was the largest at a volume fraction of 25 % and spanned a frequency range of around 1900 Hz. Increasing the volume fraction above this value reduced the width of this bandgap. In addition, the starting frequencies of all bandgaps increased with the increase in volume fraction, except between wave bands 9 and 10, where the starting frequency showed a reduction of approximately 1 % over that of 20 % volume fraction network gyroid.

The bandgap between the 8th and 9th wave bands disappeared when the volume fraction went from 20 % to 25 %, but it returned when the volume fraction was 30 %, 35 % and 40 %. Similar behaviour is observed by the bandgap of wave bands 6 and 7; this one does not appear in the 35 % and 40 % volume fraction dispersion curves. Thus, the bandgap formed by the 9th and the 10th wave bands and the bandgap formed by the 7th and the 8th wave bands are the only bandgaps that sustained the variation of the volume fraction and the cell size.
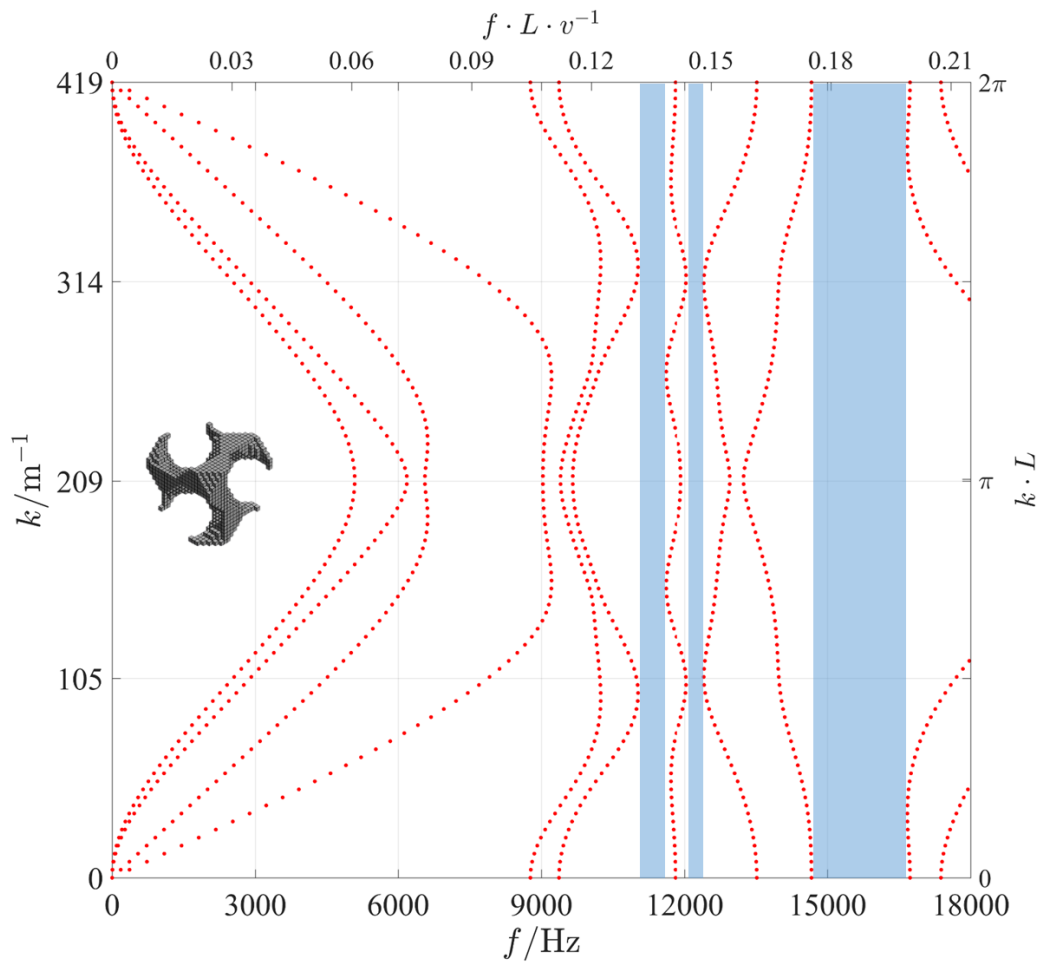
Figure 6.11. 1D phonon dispersion curves for the network gyroid lattice with 15 mm cell size and 25 % volume fraction.
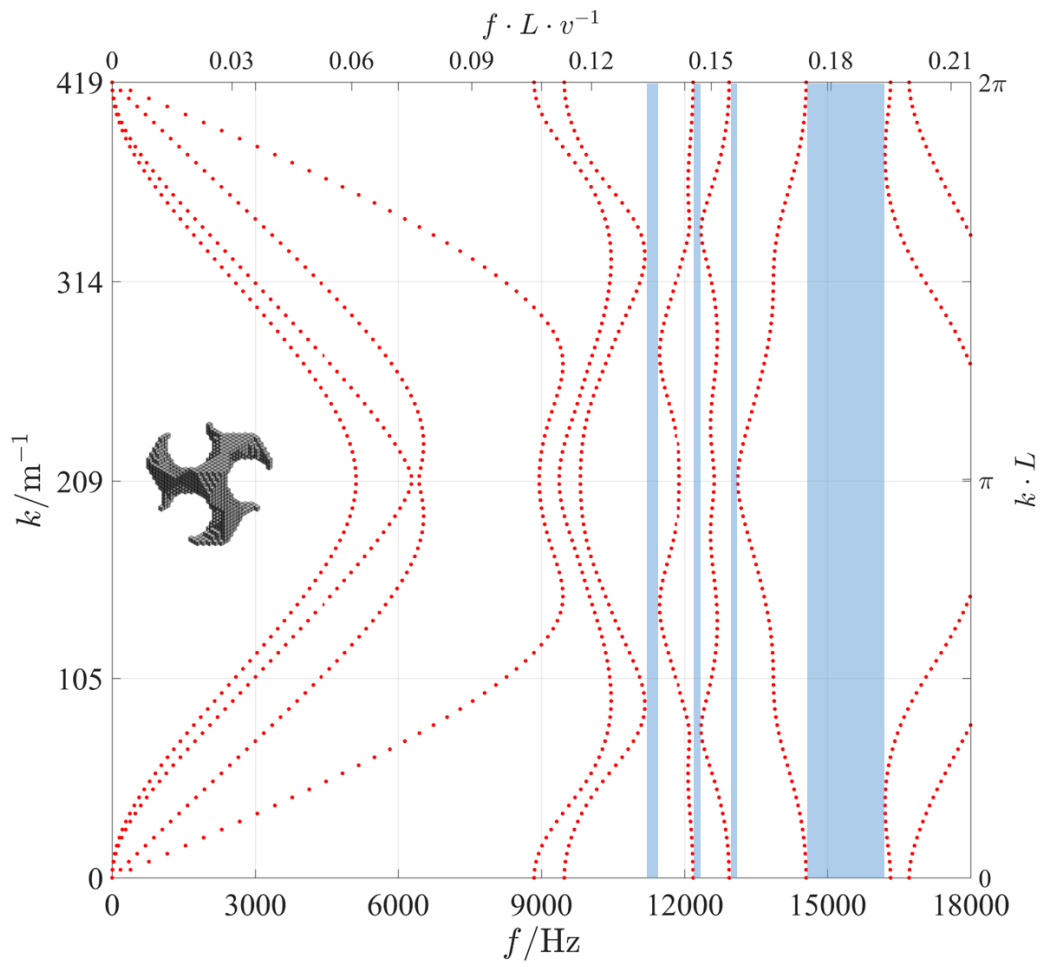
Figure 6.12. 1D phonon dispersion curves for the network gyroid lattice with 15 mm cell size and 30 % volume fraction.
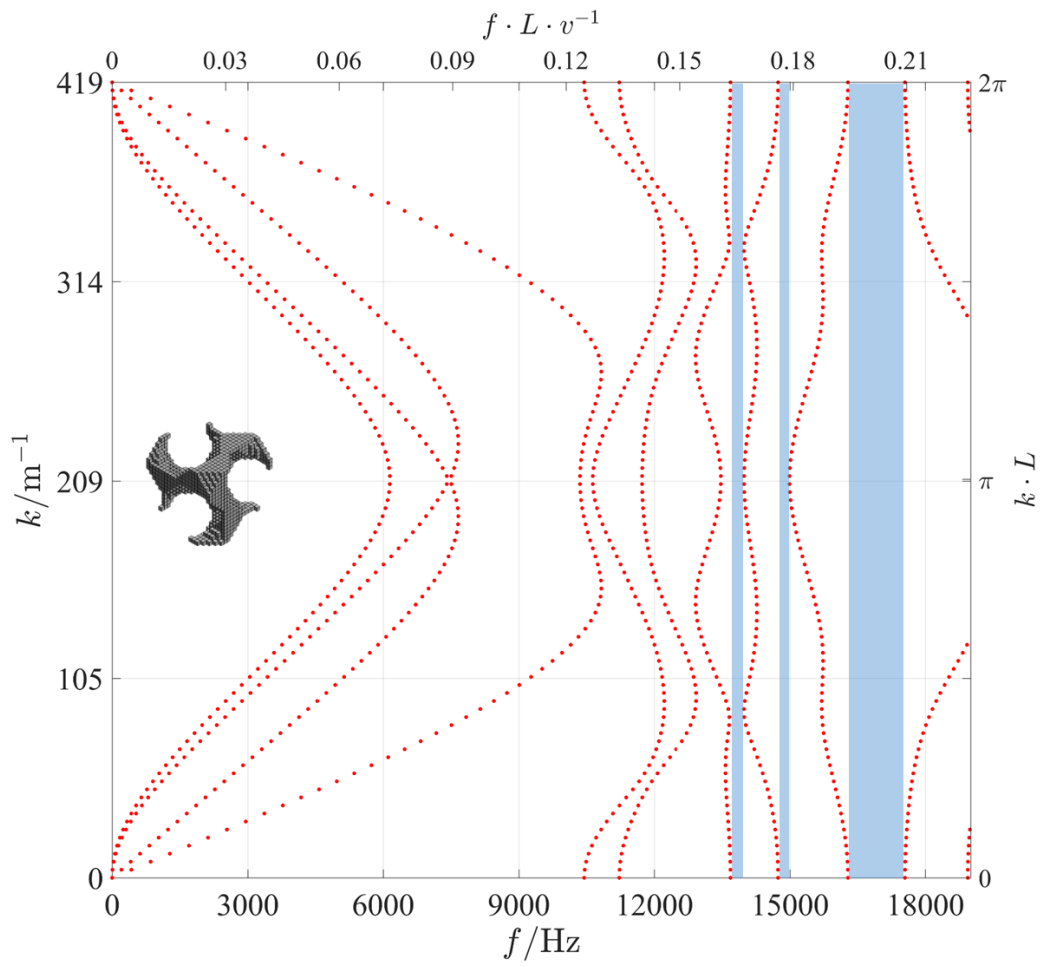
Figure 6.13. 1D phonon dispersion curves for the network gyroid lattice with 15 mm cell size and 35 % volume fraction.
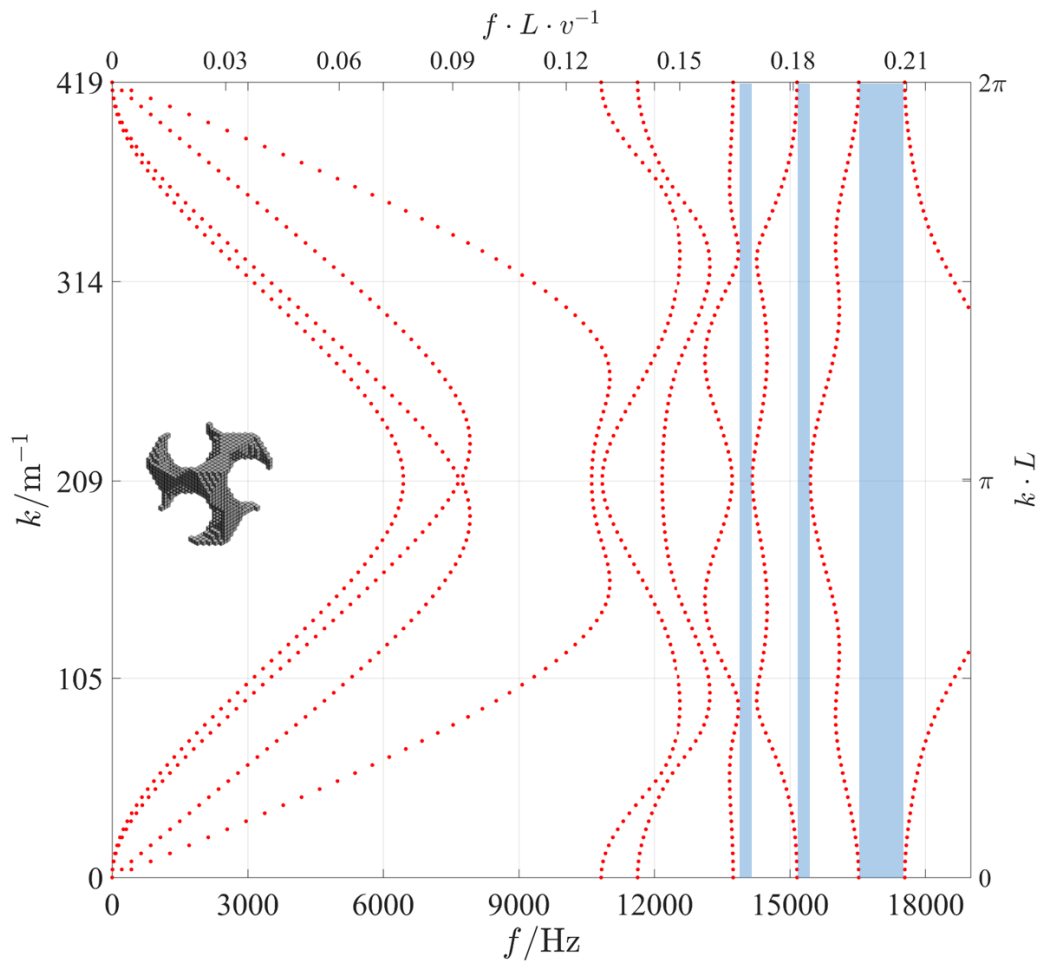
Figure 6.14. 1D phonon dispersion curves for the network gyroid lattice with 15 mm cell size and 40 % volume fraction.

The network gyroid cell with 40 % volume fraction shows a bandgap between wave bands 9 and 10 which appears at a starting frequency 45 % greater than that of the 20 % volume fraction cell. These results indicate a means to control the frequency and width of phononic bandgaps in lattice structures by controlling their volume fraction.
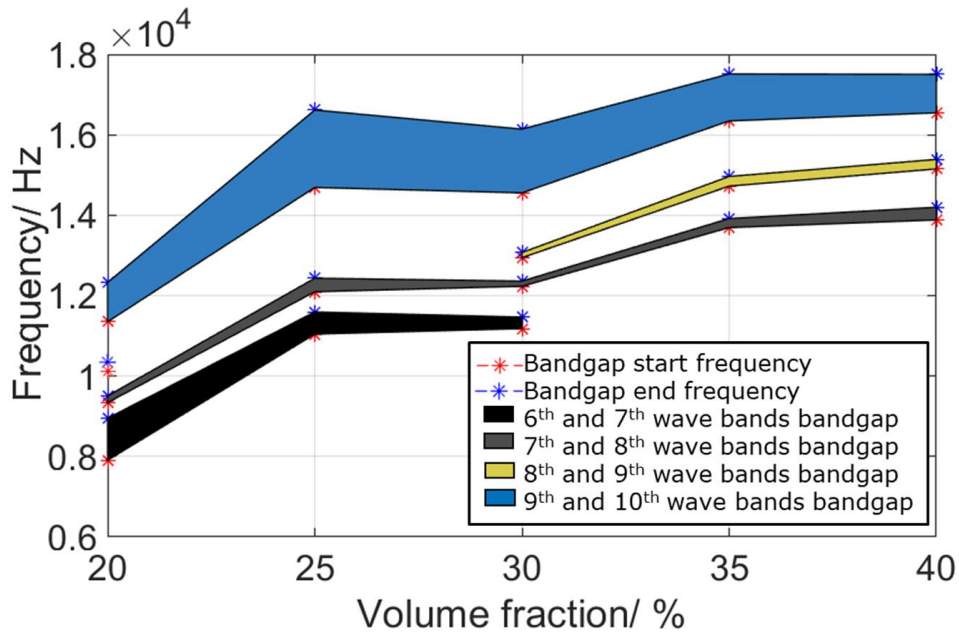
Figure 6.15. Dependence of network gyroid bandgaps on the volume fraction. A bandgap exists between the 8th and 9th wavebands at 20 % and 30 % volume fraction, but it does not exist at 25 % volume fraction.

Similar to the harmonic analyses carried on the 40 mm network gyroid cell structure, harmonic response analyses were carried on the 40 % volume fraction network gyroid cell, with nine tessellations along the x-direction, by exciting one of its faces with an oscillating load. The load was 1 N and was applied in the x-direction to all the leftmost FE nodes in the structure. The movement of the rightmost FE nodes in x-, y- and z-directions are depicted. From Figure 6.16, it can be seen that the bandgaps present in 40 % volume fraction cell's dispersion curve, which are shown in Figure 6.14, correspond to vibration attenuation in the harmonic response diagram. In addition, it is observed that the TPMS structure has the ability to provide attenuation at non-bandgap frequencies as labelled in Figure 6.16. The results suggest that the development of wide bandgaps is possible with the network gyroid lattice. The starting frequency of the bandgaps can be reduced for specific applications by reducing the volume fraction of the lattice.
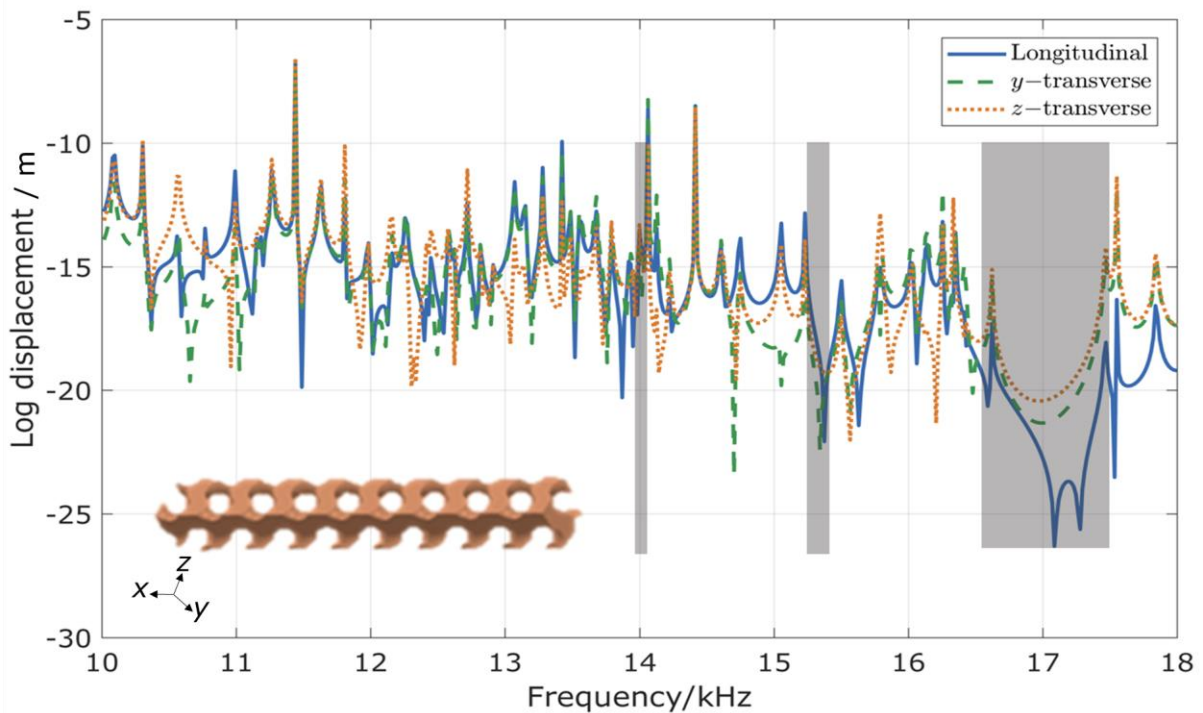
Figure 6.16. The harmonic response of 40 % volume fraction gyroid cell with nine tessellations along the longitudinal (transfer receptance, solid-line), *y*-transverse (cross-transfer receptance, dashed-line) and *z*-transverse (cross-transfer receptance, dotted-line) directions.

The bandgap behaviour of AM TPMS lattice structures has not received much attention. Of relevance to our investigation is the work of Matlack et al. [62], who used internal resonators lattices, allowing the development of bandgaps with starting frequencies of 3000 Hz to 4000 Hz. Our work shows that TPMS structures have the ability to open up bandgaps at similar starting frequencies with the potential to go even lower by choosing an appropriate cell size and volume fraction.

Using multi-material unit cells can result in large differences in impedance and ultimately a wider bandgap than those reported in this work; Ampatzidis et al. [88] presented a structure of Nylon-12 glued to a composite panel that provided a 1D bandgap. The normalised bandgap frequency of their structure was from 0.24 to 0.27. In comparison to the first bandgap of 20 % volume fraction gyroid examined in this work, the structure of Ampatzidis et al. is higher by 160 % in terms of the starting normalised bandgap frequency

and wider by 50 %. Lucklum et al. [113] presented a bandgap of normalised frequency between 0.15 to 0.25. In this work, the normalised frequency of the first bandgap formed by the 20 % gyroid unit cell is from 0.09 to 0.11. This bandgap is lower by 40 % in terms of the starting frequency and narrower by 90 % in terms of width than the bandgap presented by Lucklum et al [113].

However, single material designs are more easily made with AM than multi-material designs. Single material structures are reported by Kruisove et al. [114] who presented four bandgap structures of lattice unit cell sizes as low as 200 μm. Kruisove et al. used an extrusion-based AM technology to manufacture these strut-based micro lattices with bandgaps from 3 MHz. The closest bandgap structure, reported by Kruisova et al., to the bandgap structures in this work, in terms of equal lattice constants in 3D is their "SS model". The SS model had dimensions of 308 μm, 219 μm and 261 μm in x-, y- and z-directions with a starting bandgap frequency of 9 MHz. Normalising this bandgap with the average lattice constant of 262 μm and the speed of the wave in SiC material to provide a fair comparison with the network gyroid bandgap gives a normalised starting bandgap frequency of 0.26. This starting bandgap frequency is higher by 180 % than the normalised starting frequency of the first bandgap formed by 20 % volume fraction gyroid reported here. This indicates that TPMS lattices have the ability to form Bragg-scattering bandgaps at frequencies lower than the corresponding ones found in the literature.

6.2.3 Fabrication with additive manufacturing

Network gyroid prototype samples were fabricated using L-PBF (see Section 4.1.5). A theoretical size threshold below which the network gyroid would be fabricated with major defects (i.e. deviations from the nominal or CAD geometry) is determined by the accuracy of the L-PBF system and the geometry of the network gyroid cell. The L-PBF properties affecting the precision of a produced part include the laser spot size, layer thickness, powder size and laser scanning strategy. The network gyroid cell properties are the cell

129

size L, and the volume fraction ρ^*, which together determine the minimum feature thickness t. Features of sizes close to the laser spot size and below 0.8 mm are expected to be fabricated with significant losses in mechanical properties; this is because a higher amount of unmelted or partially melted powder exists in features of sizes below 0.8 mm, in comparison to thicker features [171].

Figure 6.17 shows the dependency of t on the volume fraction and cell size of the unit cell. The lower L-PBF manufacturing limit is set to 0.8 mm to ensure minimal loss of mechanical properties [171]. The t/L ratio was obtained from CAD models at volume fractions between 5 % to 40 % using a step of 5 %. The relationship between t, L and ρ^* as obtained by linear fitting to the data from the CAD models is expressed as

$$t = L \times (0.0075 \times \rho^* + 0.1).$$
<div align="right">6.1</div>

By substituting $t = 0.8$ mm, and $\rho^* = 0.2$ while solving for L, we theoretically obtain the lowest achievable cell size at 20 % volume fraction which is 7.8 mm. More generally, Equation 6.1 can be used to determine the minimum value of ρ^* or L for the gyroid lattice produced once the other is specified.

L-PBF is employed to fabricate 20 % volume fraction lattices of four tessellations along the x-direction, with cell sizes of 15 mm, 25 mm and 40 mm. These will be referred to as lattice 1, 2 and 3, respectively. Two copies of each lattice were fabricated and they are shown in Figure 6.18. Table 6.3 shows the nominal and average length and mass properties. The nominal values were extracted from the CAD models.
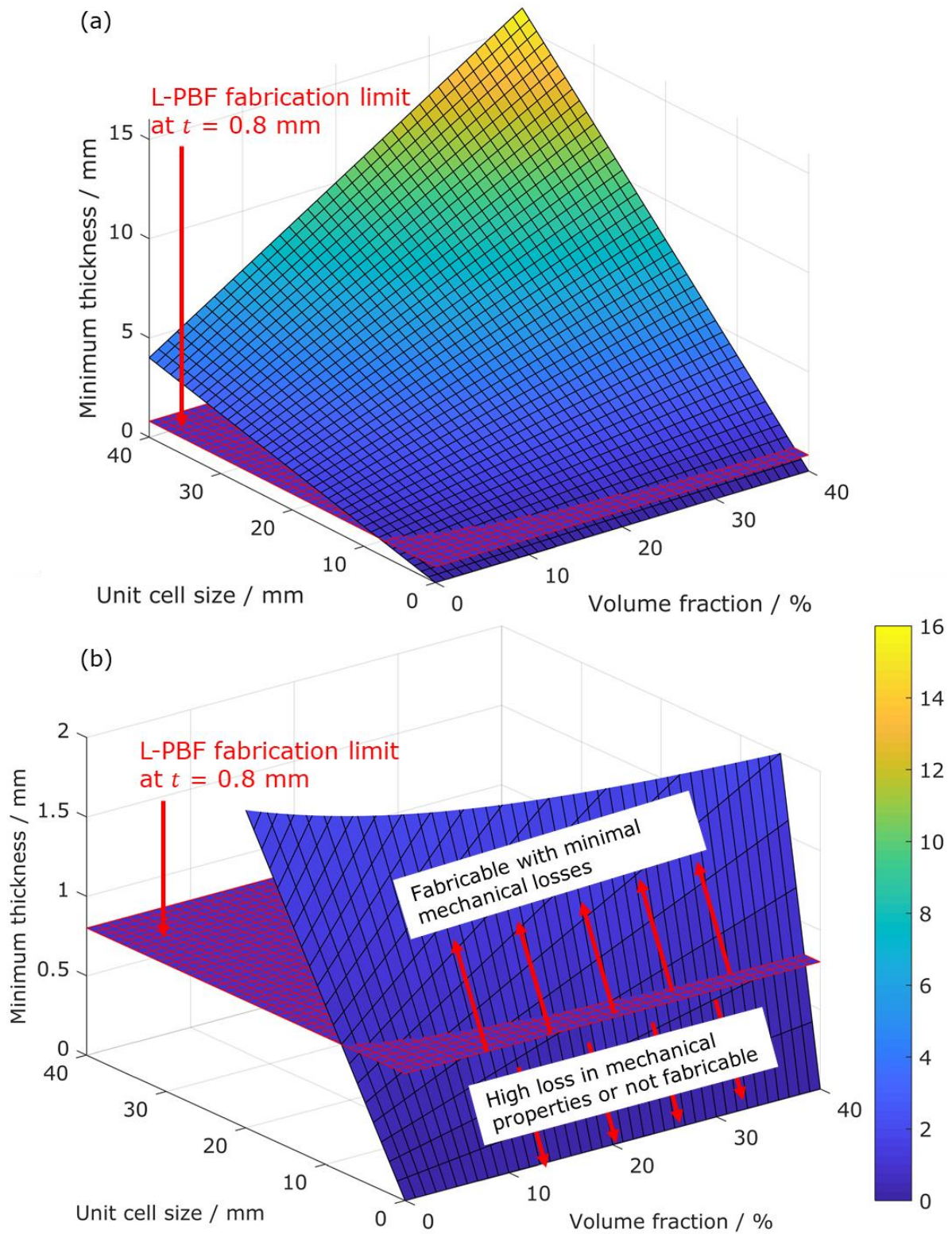
Figure 6.17. (a) Minimum thickness t of network gyroid unit lattice at different volume fractions and unit cell sizes L, and (b) zoomed in view with labeled fabricable and not fabricable design spaces.

131
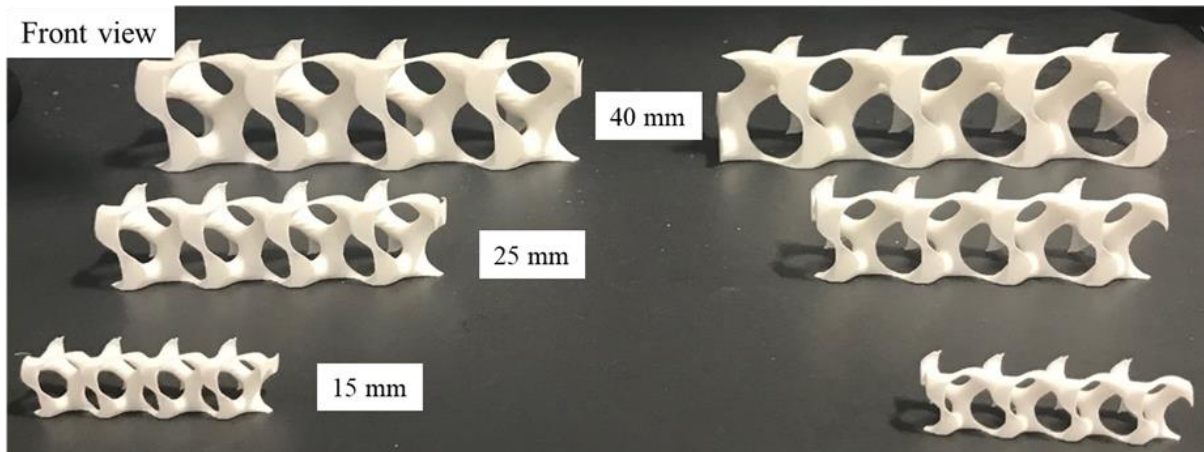
Figure 6.18. Prototype samples of network gyroid lattice of 15 mm, 25 mm, and 40 mm unit cell sizes, all in 4×1×1 tessellations. The size of the single unit cell is indicated. Fabrication is made with L-PBF using Nylon-12 powder.

The length and mass values were measured using a vernier calliper and a mass balance, respectively. Each measurement was repeated four times and the standard error of the measurements, calculated as the standard deviation from the mean over the square root of the number of repetitions, are shown alongside the mean properties in Table 6.3. The measured volume fraction is calculated as the ratio between the measured mass and the mass of a solid structure of dimensions identical to the measured lattice assuming a 950 kg$_*$m^{-3} density (see Section 4.1.5) [147].

The differences between the properties of copies of the lattice structures were insignificant, as they all fell within the standard error of the measurements of each property. Comparing the measured properties to the nominal properties, the mass of the fabricated lattices was lower by 4.9 %, 2.1 %, and 0.3 % in lattice 1, lattice 2, and lattice 3, respectively. The difference in the mass translated into a reduction of 10 % and 2.4 % from the nominal volume fraction of lattice 1 and lattice 2, respectively. The length measurements showed a 3.2 % decrease in the t values of lattice 1. For lattice 2, the deviation from the nominal t value was lower, 1.52 %.

132

Table 6.3. Nominal and measured properties of 4×1×1 network gyroid lattice fabricated with L-PBF. The standard error is provided for each measured property.

Property	Lattice 1	Lattice 2	Lattice 3
Nominal L / mm	15	25	40
Measured L / mm	15.26 ± 0.03	25.03 ± 0.02	39 .98 ± 0.03
Nominal mass / g	2.56	11.88	48.712
Measured mass / g	2.43473 ± 4 ×10^{-5}	11.6314 ± 5 ×10^{-5}	48.56755 ± 2 ×10^{-5}
Nominal t / mm	3.75	6.25	10
Measured t / mm	3.63 ± 0.04	6.16 ± 0.03	10.01 ± 0.03
Nominal volume fraction / %	20	20	20
Measured volume fraction / %	17.99 ± 0.06	19.52 ± 0.02	19.99 ± 0.02

The measured cell size showed deviations of 1.8 %, and 0.11 % from the corresponding nominal values of lattice 1, and lattice 2, respectively. However, the measured deviations in the minimum thickness, cell size and volume fraction from the nominal values of lattice 3 are insignificant as they are smaller than the standard error of their measurements. All length deviations are below the laser spot size in L-PBF which is 0.3 mm. These results prove that the suggested 1D bandgap lattices are manufacturable through L-PBF. The designer of the attenuation structure for an application of interest can use these results to predict the manufacturability of the selected unit cells.

Future advances in the accuracy and minimum feature sizes of L-PBF systems are expected to reduce the gap between the nominal and fabricated lattices. These improvements may also push the theoretical cell size limit for gyroid lattices below the fabrication limits which are set in Figure 6.17, for example, below 7.8 mm for 20 % volume fraction gyroid cells. This will provide an opportunity to open bandgaps at higher frequencies by manufacturing unit cells of lower cell sizes.

6.3   Summary of results

This chapter demonstrated that TPMS lattice structures can induce mechanical bandgap behaviour which can be tailored for vibration attenuation purposes. The novelty of the

presented work lies in predicting the 1D bandgaps of beam-like TPMS lattices, which have not been studied before. Our analysis showed that:

- At manufacturable cell sizes and volume fractions for AM capabilities, the network gyroid and the matrix gyroid lattices have bandgaps, while other examined lattice types do not.

- Changing the lattice cell size and volume fraction of TPMS lattices can alter the width of a pre-existing bandgap, the starting frequency, or both. In addition, the potential to open up bandgaps that did not exist previously between two wave bands was demonstrated.

- The network gyroid and the matrix gyroid TPMS lattices have several bandgaps under 15 kHz when their volume fraction is 20 % and cell size is 15 mm.

- Bandgaps at frequency regions as low as 3000 Hz are demonstrated to be achievable using a cell size of 40 Hz and 20 % volume fraction.

- Simulation of the vibration response was carried out using network gyroid lattices of nine unit cells tessellated along the x- axis. The simulation used 1 N dynamic load at one side of the lattice and the response of the opposite side was picked up (with transfer and cross-transfer receptance setup). It was shown that a reduction in the vibration response of the gyroid lattices is achieved within the bandgaps.

- Fabrication of prototype lattice structures was done using L-PBF system which fabricated 4×1×1 lattices of cell sizes of 15 mm, 25 mm, and 40 mm. The L-PBF system fabricated the lattices with a maximum deviation of 1.8 % and 10 % from the nominal cell sizes and volume fractions, respectively. The measured minimum feature t showed a maximum difference of 3.2 % from the nominal value. All the differences between measured and nominal values are below the laser spot size in L-PBF which is 0.3 mm.

134

Introduced here are new design factors for tuning bandgaps of phononic structures which are realised by the nature of TPMS lattices and the manufacturing freedom of AM. The designer of lattice structures can now use these results to assist with designing parts for use in metrology and precision engineering applications. These results can be used as guidelines so that high attenuation of vibration magnitudes is achieved in lattice structures that are fabricated with AM.

The major drawbacks of the attenuation method discussed in this chapter are its 1D nature, which means that it can only be realised in beam-like structures, and its relatively high frequency of attenuation. Chapter 7 discusses 3D bandgap lattices (i.e. with tessellations in 3D) in search for lower vibration attenuation frequencies.

Chapter 7

Exploration of three-dimensional bandgaps for vibration attenuation

The results of this chapter are published in this peer-reviewed journal paper [160]. The design freedom of additive AM enables the production of complex structures with 1D bandgaps as presented in Chapter 6. The novelty of this chapter (Chapter 7) is in the examination of 3D bandgaps in three types of single material lattice which have not been studied previously. These lattices are the BCC_{xyz} (lattice 50xx-9 following the naming scheme established in Section 4.1.3) the network gyroid (gyroid TPMS) and a modified BCC_{xyz} lattice with internal resonators (res-BCC_{xyz}). The existence of 3D phononic bandgaps would add vibration attenuation to the existing panoply of controllable mechanical performance of the examined lattice structures [20,21,96]; thus enabling them to simultaneously fulfil various mechanical and vibrational functions. The bandgaps of the examined lattices were identified from their respective dispersion curves and predicted using the 3D FE wave propagation modelling method.

The dispersion curves computational method was developed as an expansion of the 1D (used in Chapter 6) and 2D FE techniques used elsewhere [62,64,87–89] and is described in Section 4.3.1. In Section 7.1, the designs and structural parameters of the examined lattices are presented. The 3D dispersion curves of the lattices are presented in Section 7.2. The results are discussed in Section 7.2.2 with respect to a selection of relevant findings from the literature, while 'tuning' of the lattice bandgaps through volume

fraction control is discussed in Section 7.2.3. Lastly, the evolution of the predicted bandgaps with finite periodicity, as opposed to the infinite periodicity of computational models, is presented in Section 7.2.4.

7.1 Design of three-dimensional bandgap lattices

The BCC$_{xyz}$ unit cell, shown in Figure 7.1, was designed using the strut-based lattice design equations presented in our previous work [163]. In designing BCC$_{xyz}$ lattice structures for this study, a range of volume fractions was considered from 5 % to 30 %.
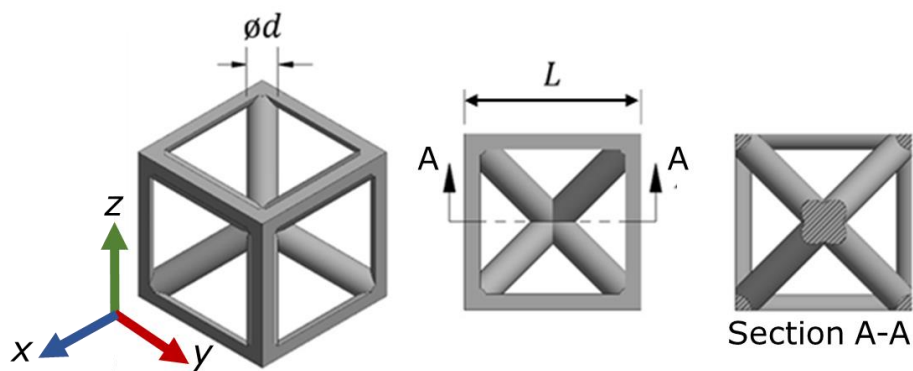
Figure 7.1. BCC$_{xyz}$ lattice unit cell as designed in CAD with strut diameter d and cell size L.

Table 7.1. Design data of multiple BCC$_{xyz}$ lattices.

Volume fraction/ %	d/L
5	0.084
10	0.121
20	0.178
30	0.226

The corresponding ratios of strut diameter d to cell width L are provided in Table 7.1. A change in the d/L ratio leads to a change in the volume fraction of the lattice.

The unit cell of the gyroid TPMS lattice is the same as that used in Chapter 6. The design information, expressed again as the ratio of strut thickness to cell width, for gyroid TPMS unit cells of different volume fractions, is available in Table 7.2. In this case, d represents the diameter of the unit cell's solid region at its narrowest point.
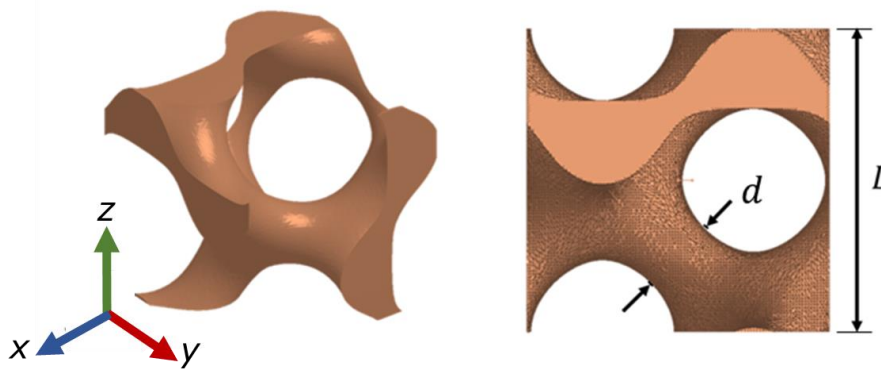
Figure 7.2. Gyroid TPMS unit cell with minimum thickness d and cell size L.

Table 7.2. Design data of multiple gyroid TPMS lattices.

Volume fraction/ %	d/L
5	0.138
10	0.175
20	0.250
30	0.325

For exploring internal resonance bandgaps in strut-based lattices, a solid spherical mass of diameter s was added to the centre of the BCC$_{xyz}$ unit cell to create a BCC$_{xyz}$ unit cell with an internal resonator (res-BCC$_{xyz}$), as shown in Figure 7.3. Internal resonance bandgap structures generally have lower bandgap frequencies than Bragg-scattering ones (see Section 3.5 for detailed description and comparison between the two bandgaps formation mechanisms). The outer scaffold of the res-BCC$_{xyz}$ is a 5% volume fraction BCC$_{xyz}$ cell. Although different scaffolds can be considered using the same concept, the 5% volume fraction BCC$_{xyz}$ lattice features a central void of sufficient size to host spherical masses with a wide range of sizes. The design information for the res-BCC$_{xyz}$ unit cells at different volume fractions is presented in Table 7.3. See Section 3.5 and Section 3.7 for more explanation about internal resonance structures.
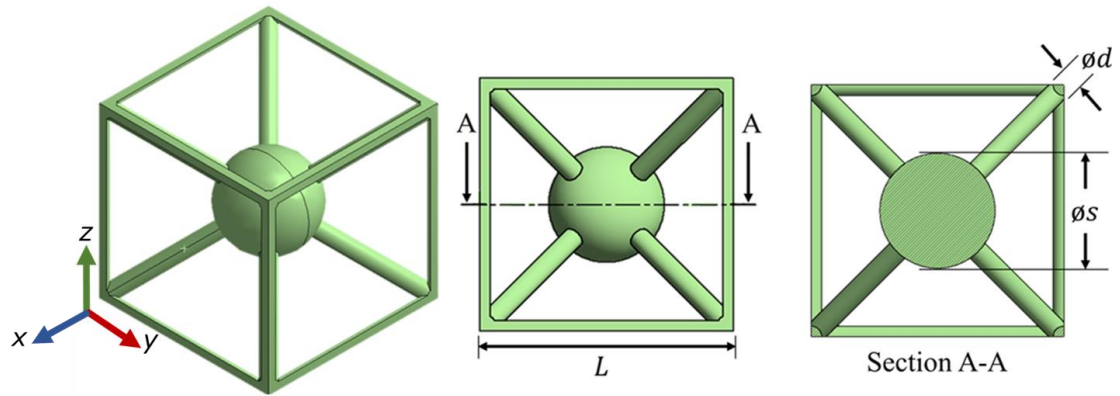
Figure 7.3. Res-BCC$_{xyz}$ unit cell as designed in CAD with strut diameter d, spherical mass of diameter s and cell size L.

Table 7.3. Design data of multiple res-BCC$_{xyz}$ lattices.

Volume fraction/ %	d/L	s/L
10	0.084	0.480
20	0.084	0.680
30	0.084	0.796

7.2 Results and discussion

BCC$_{xyz}$ and res-BCC$_{xyz}$ unit cells were modelled in CAD and meshed in ANSYS using tetrahedral elements which are more economical to use than hexahedral elements [172]. Gyroid TPMS unit cells were generated using FlattPack (see Section 2.3 for more information), however, FlattPack currently allows hexahedral meshes only; this was used for meshing the gyroid TPMS lattices. Mesh convergence was determined through examination of the structure's first natural frequency (similar to that in Chapter 6), which in each case was found to be well converged with respect to the mesh density (see Figure 7.4a).
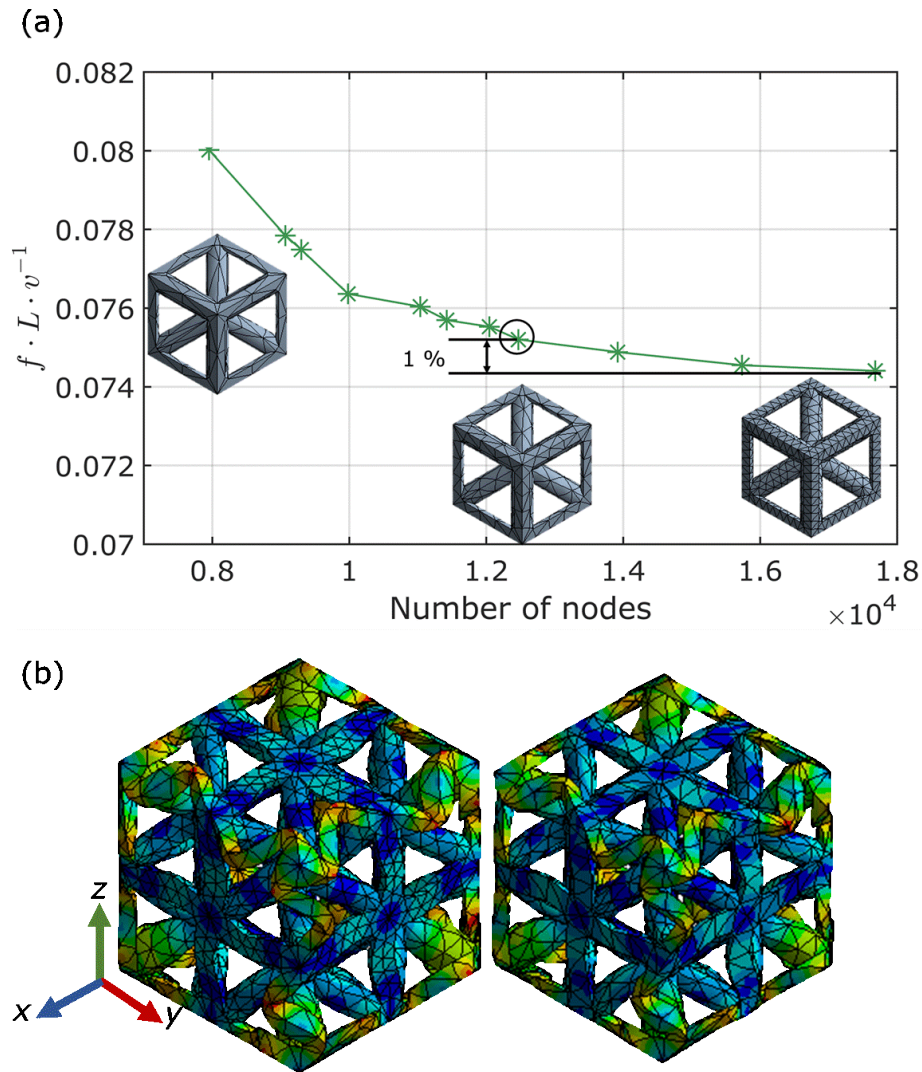
Figure 7.4. (a) Convergence results of the first natural frequency with respect to the mesh density of a 2×2×2 BCC$_{xyz}$ lattice (converged mesh density is highlighted) and (b) comparison of high-frequency vibration modes (existing above a normalised frequency of 0.3) of converged mesh (right) and finer mesh (left).

To ensure convergence of high-frequency results (particularly above a normalised frequency of 0.3), a high-frequency vibration mode of the converged mesh was compared to that of a finer mesh. The results, shown in Figure 7.4b, showed minimal discrepancies in the vibration mode and frequency.

7.2.1 Verification of three-dimensional dispersion curve calculations

The FE wave modelling technique, detailed in Section 4.3.1, was used to calculate the dispersion curves of the lattice examined by Wang et al. [96] for verification purposes. This lattice was selected due to its CAD modelling simplicity and clear bandgap. The lattice is modelled in CAD using the design parameters in Figure 7.5 and a Poisson's ratio of 0.33.
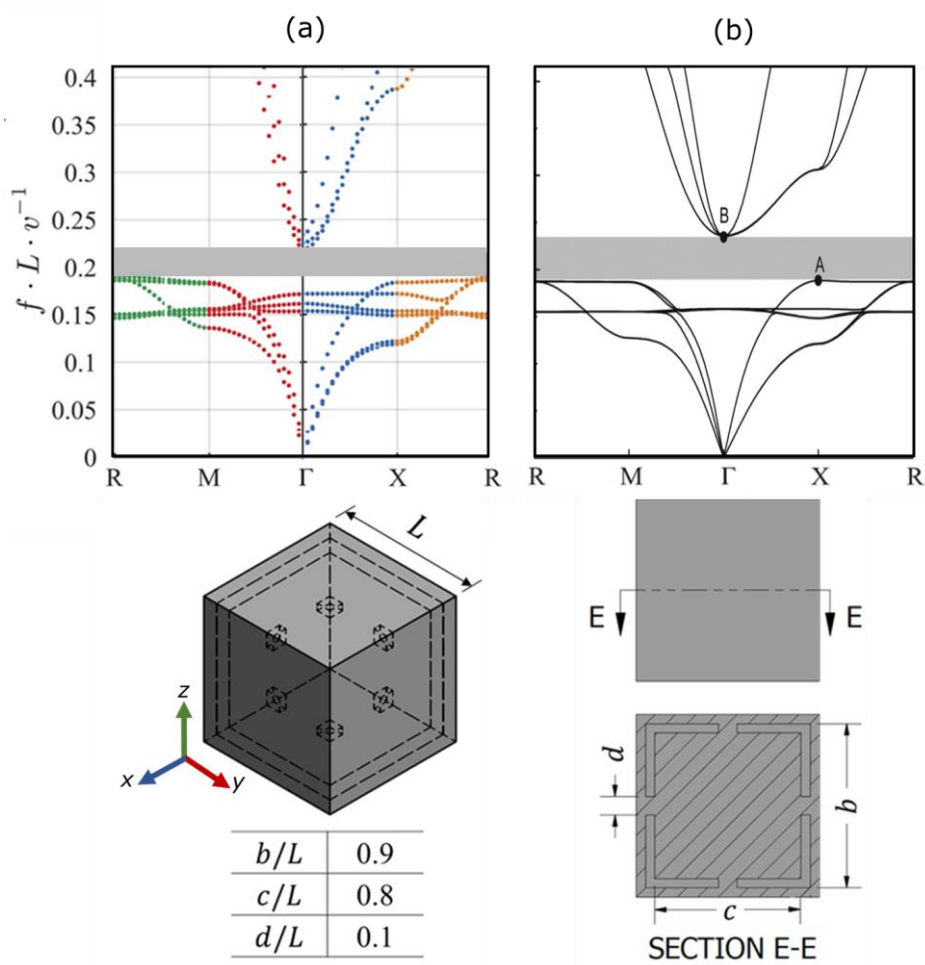
Figure 7.5. Three-dimensional bandgap dispersion curves of the lattice proposed by Wang et al. [96] (a) as remodelled using our FE modelling technique in comparison to (b) the dispersion curves presented by Wang et al. [96] The shaded grey area in the dispersion curve plot represents the identified bandgap.

As can be seen in Table 7.4, the dispersion curves resulting from the FE method employed in this work exhibited a very similar bandgap to that predicted by Wang et al. The difference of 0.01 in the normalised bandgap end frequency (4.3 % difference) is likely

due to the difference in our respective meshing techniques (Wang et al. did not report an exact mesh density) and bandgap identification methods.

Table 7.4. Bandgap properties as identified in this work and reported by Wang et al. [96].

	Remodelled structure (this work)	Wang et al. ([96])
Normalised bandgap start frequency	0.19	0.19
Normalised bandgap end frequency	0.22	0.23
Normalised bandgap frequency width (bandwidth)	0.03	0.04

7.2.2   Wave dispersion in lattices with infinite periodicity

The wave propagation dispersion curves of the three considered lattice types, all with 20 % volume fraction, are shown in Figure 7.6. 3D bandgaps are identified in the dispersion curves of the BCC$_{xyz}$ and res-BCC$_{xyz}$ lattices. The gyroid TPMS lattice did not show a 3D bandgap, although it is known to exhibit a 1D bandgap as shown in chapter 6 [89]. Below a normalised frequency of 0.2, the res-BCC$_{xyz}$ lattice was the only lattice that showed a bandgap. Above a normalised frequency of 0.2, both the BCC$_{xyz}$ and res-BCC$_{xyz}$ lattices possess one bandgap. The first bandgap of the res-BCC$_{xyz}$ lattice is wider by 57 % and has a bandgap starting frequency lower by 68.5 % than that of the BCC$_{xyz}$ lattice. The bandgap frequency width of the BCC$_{xyz}$ lattice is eight times that of the second bandgap of the res-BCC$_{xyz}$ lattice.

As discussed in Chapter 6, lattices that are manufacturable with current AM methods, and have broad bandgaps with low starting frequencies are the most desirable. In comparison, if the intrinsic bandgap frequency of a particular lattice type is high, efforts to tune its frequency by modifying the cell size will generally result in unrealistic (i.e. very large in size for applications in metrology and precision engineering) and/or non-manufacturable cell sizes [62].
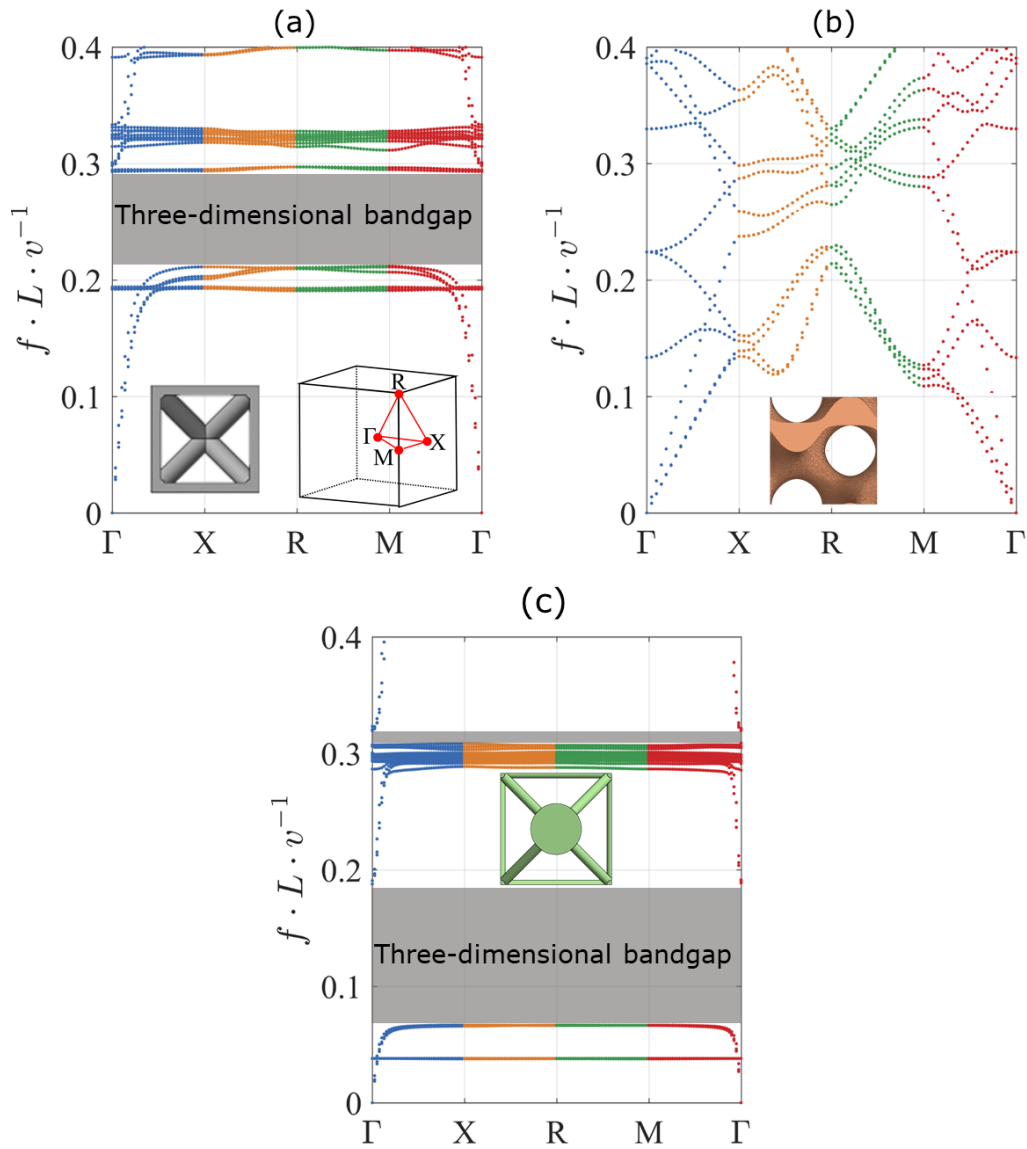
Figure 7.6. Dispersion curves of (a) BCC$_{xyz}$, (b) gyroid TPMS, and (c) res-BCC$_{xyz}$ lattice structures with 20 % volume fraction.

A relative gap to mid-gap ratio (relative bandgap width) can be used to compare the calculated bandgaps of the BCC$_{xyz}$ and res-BCC$_{xyz}$ lattices to those of the BCC-inspired multi-material lattices of Lu et al. [86] and Husieh et al. [104]. A relative bandgap width is calculated as

$$\text{Relative bandgap width } = \frac{\text{Bandgap frequency width}}{(\text{bandgap mean frequency})} . \qquad 7.1$$

143

A high relative bandgap width is more desirable as it indicates a wide bandgap (at high- or low-frequency) or a low-frequency bandgap (of narrow width). The bandgap of Lu et al. had a relative width of ~60 %, while that of Husieh et al. was ~40 %, both at a volume fraction of ~23 %. Interpolation of our bandgap results for the BCC_{xyz} and res-BCC_{xyz} lattices at 23 % volume fraction was done linearly considering the bandgap attributes at 20 % and 30 % volume fractions of each lattice; the interpolation results showed a relative bandgap width of 30 % and 98.7 % for the BCC_{xyz} and res-BCC_{xyz}, respectively. This indicates that the res-BCC_{xyz} lattice has the ability to provide wide bandgaps of low starting frequencies using single material lattices.

For comparison of the width and starting frequency, the 3D bandgap of the BCC_{xyz} lattice is compared to the 1D bandgap of the gyroid TPMS, which was presented in Chapter 6. At similar volume fraction, the BCC_{xyz} lattice shows bandgaps at higher frequencies than the gyroid TPMS lattice. For example, at 20 % volume fraction, several bandgaps are present below a normalised frequency of 0.2 in the gyroid TPMS lattice. However, the bandwidth of this BCC_{xyz} lattice is almost five times wider than that of the 1D gyroid TPMS.

The normalised results in Figure 7.6 can be used to predict bandgaps in BCC_{xyz} lattices of various materials and unit cell sizes. For example, bandgaps of Ti-6Al-4V BCC_{xyz} lattices can be predicted. Ti-6Al-4V is used in the aerospace and the biomedical sectors due to its high corrosion resistance, biocompatibility and high fracture toughness [173]. The phononic properties of Ti-6Al-4V strut-based lattices have been studied previously [111]. For the purpose of comparison with the BCC_{xyz} and res-BCC_{xyz} lattices presented here, a unit cell 10 mm in size and 20 % volume fraction, based on the design of Warmuth et al. is considered. The bandgap properties can be calculated using the bandgap tuning tool in Equation 1 from reference [111]

$$\text{Bandgap frequency} \sim \sqrt{\frac{E}{\rho}} \cdot \frac{d}{L^2}, \qquad\qquad 7.2$$

where d is the strut thickness of the lattice of Warmuth et al. The bandgap starting frequency and bandgap ending frequency of the BCC$_{xyz}$, res-BCC$_{xyz}$ and the Warmuth et al. lattice of 10 mm unit cell size and 20 % volume fraction are presented in Figure 7.7.
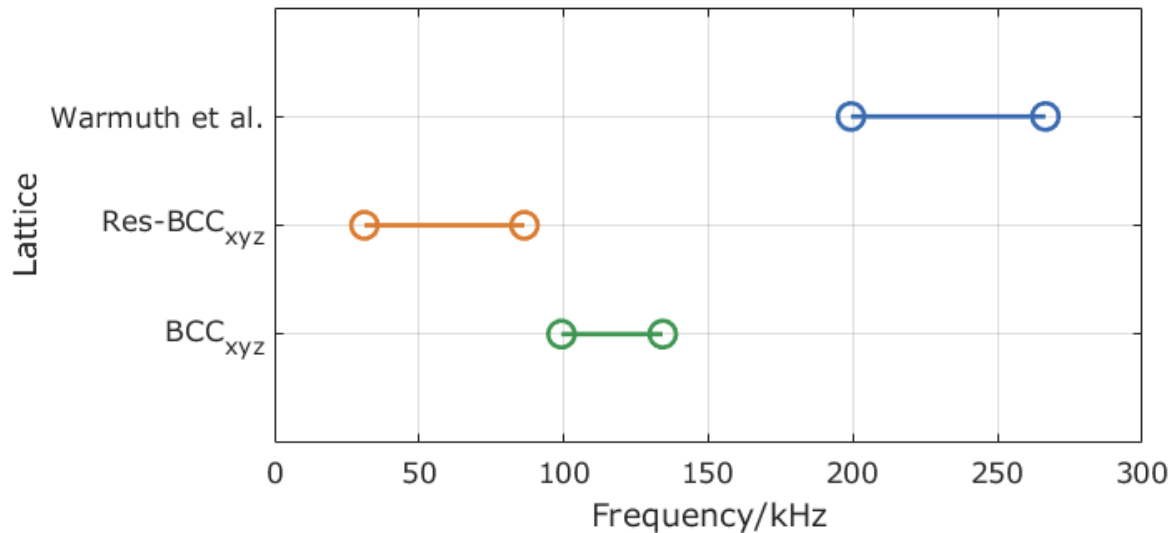
Figure 7.7. Bandgap properties of the BCC$_{xyz}$, res-BCC$_{xyz}$ and Warmuth et al. lattices of 20 % volume fraction and 10 mm unit cell size, as predicted using the material properties of Ti-6Al-4V.

The relative bandgap width of the BCC$_{xyz}$ and res-BCC$_{xyz}$ lattices at 20 % volume fraction were 30 % and 94 %, respectively, while the relative bandgap width of the Warmuth et al. structure is 28.8 % at the same volume fraction. The bandgap of the BCC$_{xyz}$ lattice has a lower bandwidth than the lattice of Warmuth et al.; the bandgap of the BCC$_{xyz}$ lattice spanned 99.2 kHz to 134.2 kHz, which is approximately 52 % of the bandwidth of the lattice of Warmuth et al. However, the BCC$_{xyz}$ lattice had the ability to provide bandgaps at frequencies lower by 50.2 % than those of Warmuth et al. at similar cell size and volume fraction.

7.2.3 Tuning of three-dimensional bandgaps

For a range of volume fractions, the properties of the lowest frequency bandgap were identified from the dispersion curves of the BCC$_{xyz}$ and res-BCC$_{xyz}$ lattices. The 5 % and 10 % volume fraction BCC$_{xyz}$ lattices showed two bandgaps below a normalised frequency

of 0.4. The lowest frequency bandgap of the 5 % volume fraction BCC$_{xyz}$ lattice spanned a normalised bandwidth of 0.014, from 0.151 to 0.165. This bandgap is the narrowest in width and is formed by an acoustic wave band (wave cutting-on at zero frequency) and an optical wave band (wave cutting-on at a nonzero frequency). However, 20 % and 30 % volume fraction BCC$_{xyz}$ lattices had no second bandgaps.

The BCC$_{xyz}$ lattice of 30 % volume fraction showed the highest predicted bandgap, which spanned from 0.25 to 0.34. The res-BCC$_{xyz}$ lattice of 30 % volume fraction showed the lowest predicted bandgap, which spanned from 0.067 to 0.187. The res-BCC$_{xyz}$ lattice has a bandgap mean frequency lower by an average of 43 % than the bandgap mean frequency of the BCC$_{xyz}$ lattice, as calculated from the bandgap mean frequency of lattices with volume fractions of 5 % to 30 %. The bandwidth increased approximately fivefold, and tenfold upon increasing the volume fraction of the BCC$_{xyz}$ and res-BCC$_{xyz}$ lattices respectively, from 5 % to 30 % as can be seen in Figure 7.8.

Bragg-scattering bandgaps are bounded by a natural frequency of the Bragg-scattering unit cell (BCC$_{xyz}$) [64], while internal resonance bandgaps (res-BCC$_{xyz}$) occur around the natural frequency of the internal resonance mechanism [125]. Thus, the two bandgap mechanisms can be explained by referring to the natural frequency f_n equation, $f_n \propto \sqrt{k/m}$. Above a volume fraction of 5 %, additional material uniformly enlarges the struts of the BCC$_{xyz}$ lattices, which results in stiffer lattices of higher mass. It has been shown that the bandgap frequency increases with the increase in volume fraction of Bragg-scattering bandgaps lattices [86,89]; indicating that the stiffness increases at a greater rate than the rate at which the mass increases.
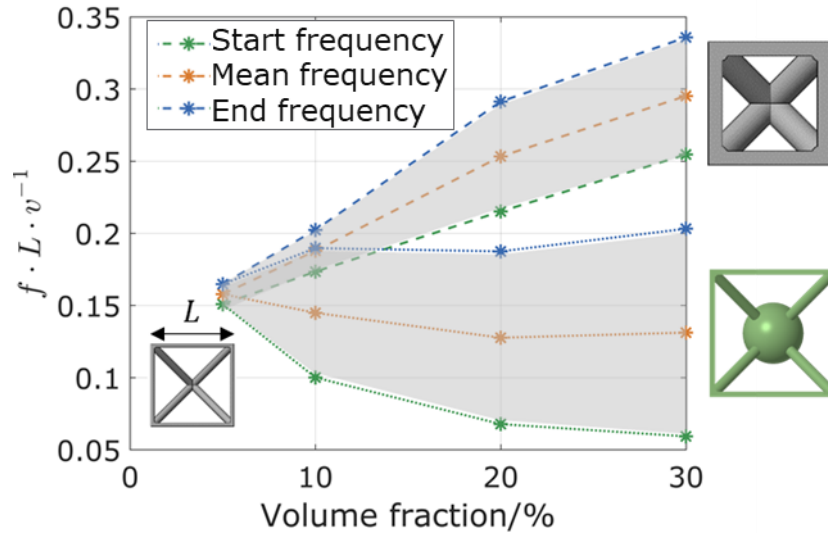
Figure 7.8. Attributes of the bandgaps as identified from the dispersion curves of the BCC$_{xyz}$ (dashed lines) and res-BCC$_{xyz}$ (dotted lines) lattices at different volume fractions.

The bandgap mechanism for the res-BCC$_{xyz}$ lattice is different since the mass of the resonance mechanism is dictated by the mass of the solid sphere, while the stiffness is dictated by the stiffness of the resonance struts. Since above a volume fraction of 5 % additional material enlarges the size of the sphere of the res-BCC$_{xyz}$ lattices, but does not increase the diameter of the struts, an overall reduction of the natural frequency of the resonance mechanism is achieved, thus, reducing the internal resonance bandgap frequency, as shown in Figure 7.8.

7.2.4 Evolution of the wave transmission in lattices with finite periodicity

The transmission spectrum of lattice structures with different periodicities was modelled to examine the evolution of the bandgap in physically realisable components. The res-BCC$_{xyz}$ lattice at 20 % volume fraction was selected for this study. This lattice was found to have a wide bandgap spanning normalised frequencies from 0.067 to 0.187, as seen in Figure 7.8. The examined lattice structures, shown in Figure 7.9, had periodicities of one, three and six (i.e. they contained a single unit cell, 3×3×3 and 6×6×6 cells, respectively).
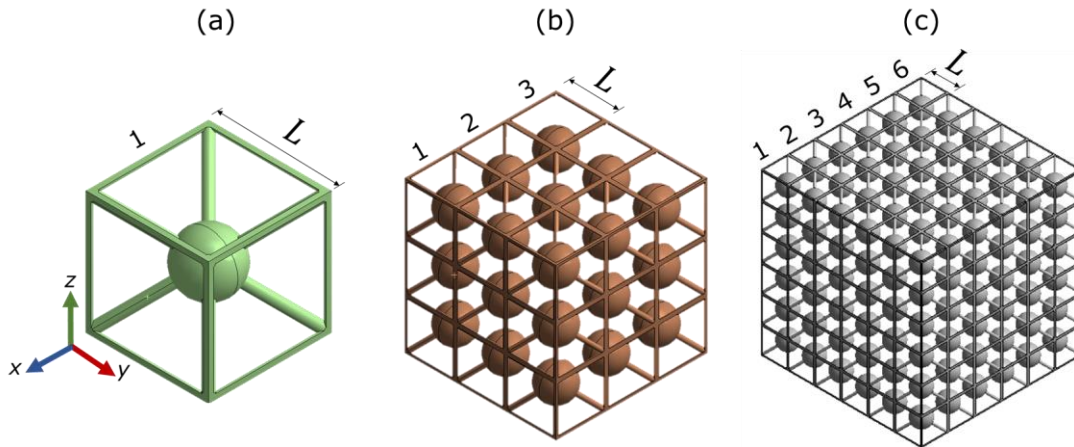
Figure 7.9. Res-BCC$_{xyz}$ lattice structures of finite periodicities of (a) one, (b) three and (c) six.

Outside the bandgap region identified from the dispersion curves in Section 7.2.2, the transmission of the waves in the finite lattices varied between ±20 dB as can be seen in Figure 7.10. There is no established way for identification of bandgaps from the transmission spectrums. However, since outside the infinite bandgap frequency range (i.e. bandgap identified form the dispersion curves) the attenuation reaches -20 dB, thus, it is sensible to use -20 dB as the upper limit for the transmission within a bandgap. For the single unit cell, the bandgap was shown between normalised frequencies of 0.06 to 0.11; this bandwidth is narrow (only 37 % of that identified from the dispersion curves). The narrow bandwidth can be traced back to the lack of spatial periodicity which is essential for obtaining transmission bandgaps. The width of the bandgap for the 3×3×3 lattice is higher than that of the single unit cell and spanned from 0.06 to 0.15. The largest bandgap, with the assumption of -20 dB as the upper amplitude limit, is for 6×6×6 lattice.
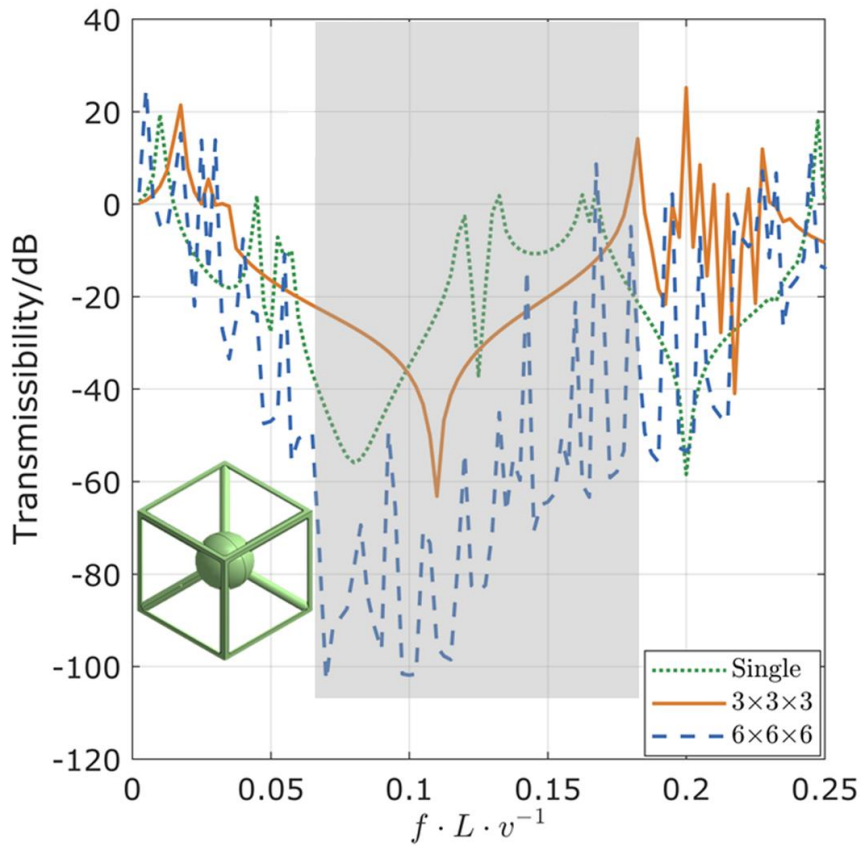
Figure 7.10. Transmissibility of longitudinal waves in 20 % volume fraction res-BCC$_{xyz}$ lattices of finite periodicity.

The shaded area in Figure 7.10 represents the bandgap region as depicted by the dispersion curves with infinite periodicity assumptions. The percentage values denote the bandgap width of the finite lattice to that of the infinite one. In addition to the change in width, the minimum and mean amplitudes within the infinite bandgaps also changed with the periodicity of the finite lattice.

Table 7.5. Summary of the evolution of the bandgap as obtained from studying the transmissibility of longitudinal waves in bandgap lattices of different periodicity.

Periodicity	Mean transmissibility/dB	Lowest transmissibility/dB
One	-23	-56
Three	-24	-63
Six	-66	-103

Table 7.5 summarises the mean and minimum transmissibility of longitudinal waves in finite lattices of various periodicities. As the lattice periodicity increases, the transmissibility within the bandgap decreases.

In search for enhanced performance lattices for use in precision and metrology applications, bandgap structures have been proposed. The bandgaps provided by the lattices proposed in this chapter are 3D which promises high amount of vibration attenuation in 3D; the guaranteed attenuation is a feature that is unmatched by the vibration isolation method of the lattices featured in Chapter 5. The 3D nature of the proposed lattices gives more freedom in designing lattices for precision engineering and metrology applications than the TPMS lattices in Chapter 6, which only showed 1D bandgaps. In addition, the bandgap frequencies of the lattices in this chapter are lower (for the same cell size and material) than those featured in Chapter 6. This allows low-frequency bandgaps to be realised in structures with a higher number of tessellations and of better suitability for manufacture within a constrained design volume (considering AM building size and the smallest manufacturable features).

7.3   Summary of results

Reported here is an investigation into the potential for 3D AM lattice structures to provide 3D bandgaps for the purpose of vibration attenuation. The bandgaps were identified from the structures' dispersion curves calculated using a FE based wave propagation modelling technique and infinite periodic boundary conditions. The FE technique provides high computational efficiency and high wave modelling accuracy. Key results included:

- Single material BCC_{xyz} and res-BCC_{xyz} lattices can provide bandgaps that are tunable with the volume fraction of the lattice. This allows the performance of metrology and precision structures to be enhanced by reducing the magnitudes of vibration at their problematic frequency ranges.

- BCC$_{xyz}$ and res-BCC$_{xyz}$ lattices have bandgaps of high width and intrinsically low-frequency compared to results reported for similar structures in the literature.

- Although gyroid TPMS lattices are known to have 1D bandgaps, they do not exhibit 3D bandgaps.

- Increase in the finite periodicity of the lattice leads to an increase in the bandwidth and to decrease in transmissibility within the bandgap. In the context of precision and metrology structures, this is an important feature to attenuate vibration using lattices of high number of tessellations, higher attenuation and of sizes that are better suited for AM; especially when tied up with the lower bandgap frequency nature of the proposed structures.

- The transmissibility of longitudinal waves within the finite lattices was low within the bandgap (far below 0 dB) which indicates that these lattices are suitable for vibration attenuation.

These results complement the set of design tools already available for AM parts, which are mainly concerned with the static support and load-bearing properties, by adding a tuning tool for enhanced mechanical vibration attenuation. In Chapter 8, the concept of internal resonators is used to design 3D bandgap lattices of lower bandgap frequencies than that reported in this chapter and is experimentally verified in 3D.

Chapter 8

Three-dimensional bandgaps in internal resonance lattices for low-frequency vibration attenuation

The results in this chapter are published in this peer-reviewed journal paper [162]. This chapter reports on 3D lattices comprising internal resonators, designed for targeting maximum elastic wave attenuation below a normalised frequency of 0.1. This normalised frequency limit, chosen arbitrarily to design structures with 3D bandgaps at low frequencies, is four times lower than the lowest theoretical limit allowed for Bragg-scattering bandgaps (see Section 3.5 for a detailed description of bandgap mechanisms and Bragg limits). Bandgaps of normalised frequencies below 0.1 would allow for guaranteed vibration attenuation in structures of smaller unit cells and a higher number of tessellations within a constrained design volume; thus resulting in more homogenous structures, more predictable mechanical properties and higher tolerance to defects. A novel approach for tuning and designing the unit cell of the internal resonance lattice is presented. The computation scheme of the wave dispersion curves uses finite element (FE) modelling (see Section 3.6 for comparison with other modelling techniques). L-PBF is employed for the fabrication of the internal resonance lattice, which is experimentally tested for verification of the numerical predictions. The fundamental unit cell of the internal

152

resonance lattice is shown in Figure 8.1 and is periodically tessellated in 3D to allow a local resonance effect. The 3D wave propagation and the complete bandgaps of the lattice are presented in Figure 8.4. The experimental response of the manufactured internal resonance lattice is shown in Figure 8.6. Details of the computation, manufacturing and experimental methods are provided in the subsequent sections.

8.1 Design of low-frequency bandgap lattices

The unit cell of the internal resonance lattice featured in this work is shown in Figure 8.1. The design is a cubic unit cell with face-centred struts (FCC), and reinforcement struts in the x-, y- and z-directions (FCC$_{xyz}$). FCC lattices generally have good compressive strength [119], in comparison to body-centred cubic (BCC) lattices which is featured in Chapter 7.
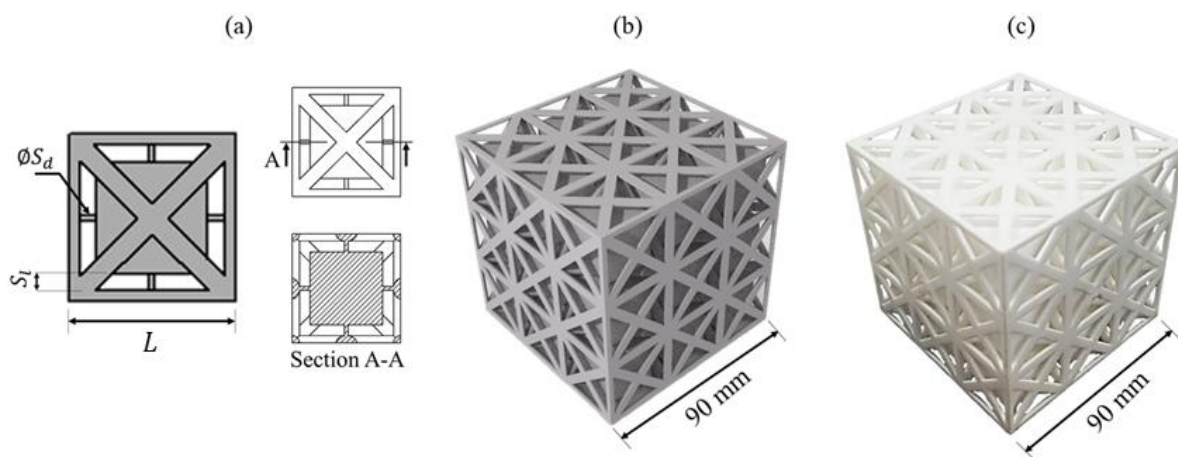
Figure 8.1. The design of the resonating lattice: (a) Schema of the single unit cell of the lattice as modelled in CAD, the labels show the strut diameter (S_d), strut length (S_l), and cell size (L), and a photograph of the 3×3×3 lattice as (b) digitally rendered, and (c) manufactured with L-PBF.

Since the lattice is directed towards metrology and precision applications in which load-bearing is as essential as vibration attenuation, the FCC$_{xyz}$ lattice is used as the host for the internal resonance mechanism of the lattice due to its good compressive strength. The internal resonance mechanism consists of six struts; each connects one side of a cubic mass to the inner walls of the FCC$_{xyz}$ unit cell. Increasing the strut diameter S_d would

increase the stiffness of the resonator, while increasing the strut length S_l would reduce its volume fraction, which will have an impact on the bandgap frequencies and the total mass.

The 3D dispersion curves in this work were modelled using the method developed in Section 4.3.1. A complete description of each passing wave, including *x-*, *y-* and *z*-directional wavenumbers, at a certain frequency range, is acquired. As illustrated in Figure 8.2, the lattice used in this chapter can be viewed as a simple cubic lattice (eight lattice nodes on each corner), a FCC lattice (one lattice node on each of the six faces) or a BCC lattice (one lattice node at the centre that represents the solid cubic mass).
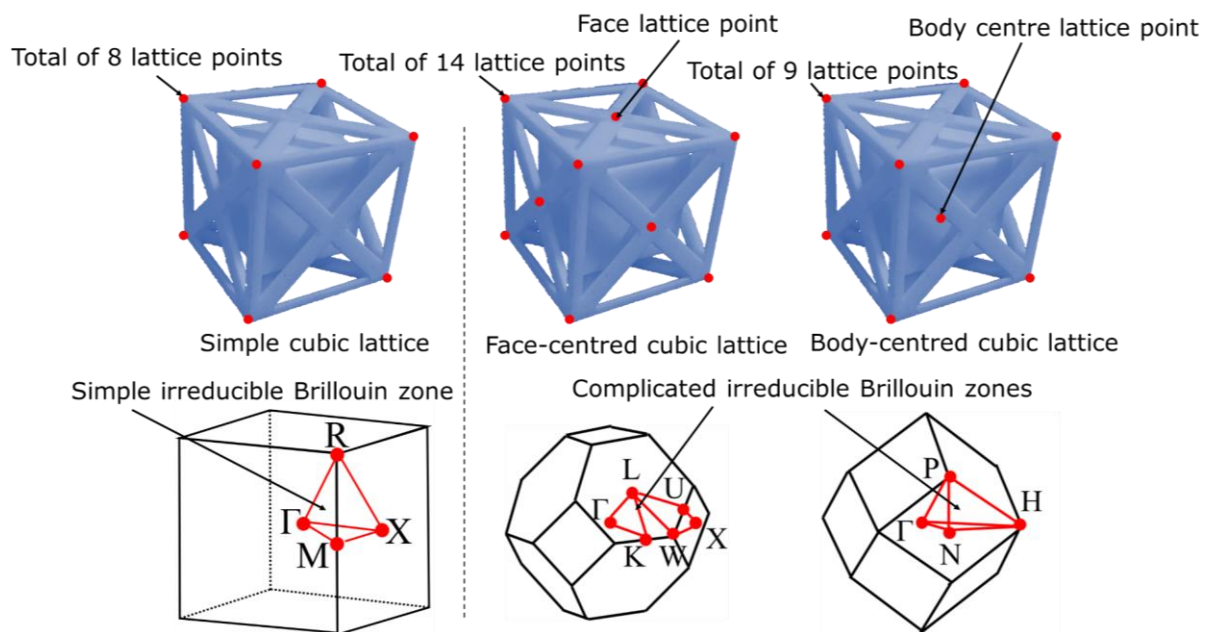
Figure 8.2. Illustration of various approximations for the internal-resonance lattice in this chapter and their corresponding irreducible Brillouin zones.

When modelling the dispersion curves of this lattice, suitable 3D translation of all solid features and voids within the unit cell is obtained when the design is approximated as a simple cube, thus, allowing for the use of the simple IBZ of simple cubic lattice for modelling the dispersion curves (see a detailed description of the IBZ of simple cubic lattice in Section 4.2.1). Such approximation can also be seen elsewhere [96,154,174]. Our

preliminary analysis showed minimal/zero discrepancies between the bandgap calculated with the approximation of the design as FCC and the bandgap calculated with the approximation of the design as a simple cube as in Figure 8.3.
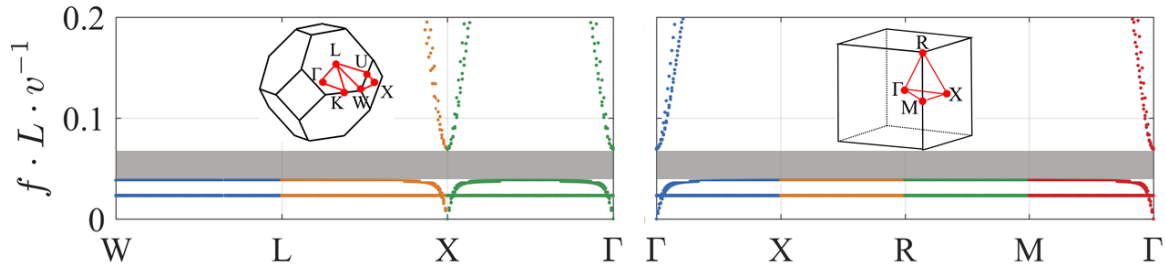
Figure 8.3. The bandgap of the lattice as calculated considering several paths in the IBZ of FCC lattice (left) and simple cubic lattice (right). The inset shows the IBZ of each lattice type. The shaded grey area represents the bandgap.

8.2 Results and discussion

Modelling of the elastic wave propagation in the lattices used sufficient tetrahedral elements, such that the frequency of the first vibration mode converged with the FE mesh density (approximately 6000 FE nodes per unit cell). The elements of the converged mesh used three DOF per FE node with an adaptive mesh size to sufficiently model narrow regions in the lattices [175]. To mathematically model the elastic wave propagation, the contours of the irreducible Brillouin zone (IBZ) of the unit cells of the lattices were scanned. Several characteristic points exist within the contours of the IBZ including $\Gamma(0,0,0)$, $X(\pi/L,0,0)$, $M(\pi/L,\pi/L,0)$, and $R(\pi/L,\pi/L,\pi/L)$, where L is the unit cell size (also referred to as a or C in other literature [62,63,135]). The scan of the IBZ was carried out using a total of 360 combinations of wavenumbers (90 combinations for each examined path in the reciprocal space). The corresponding dispersion properties along the path Γ–X–R–M–Γ of the IBZ were predicted and the complete bandgaps were identified. The dispersion curves of a lattice unit cell with S_d/L and S_l/L values of 0.033 and 0.1, respectively, are presented in Figure 8.4a. It was observed that the lattice exhibits a bandgap below a normalised frequency of 0.1. The bandgap spans a normalised frequency range of 0.028,

155

starting from 0.039 to 0.067, and is formed by an internal resonance that cuts the first three acoustic wave bands (wave bands cutting-on at zero frequency) and splits them into two branches (i.e. top and bottom acoustic branches).

The dispersion curves of multiple lattices of different values of S_d/L and S_l/L were predicted. The considered S_d/L values were 0.005, 0.01, 0.02, 0.025 and 0.033, and the considered S_l/L values were 0.05 (large-size resonator), 0.1 (mid-size resonator) and 0.2 (small-size resonator). In Figure 8.4a, the dispersion curves are shown for the internal resonance lattice with S_d/L and S_l/L values of 0.033 and 0.1, respectively, and the eigenmodes are shown at a selection of high symmetry points. Figure 8.4b presents the bandgaps for each of the considered lattices to show the impact of the design of the internal resonators on forming complete 3D bandgaps. All frequencies f are normalised to the longitudinal wave speed in the medium v and the unit cell size L. The relative gap to mid-gap percentages of a selection of the presented bandgaps (width of the bandgap divided by its central frequency) are highlighted in Figure 8.4b. The large-size resonator showed the largest relative gap to mid-gap percentage of 68 %. The cut-on frequency of the top acoustic branches (i.e. the bandgap end frequency) increased with the increase in the diameter of the struts, and with the increase in the size of the resonator. The bandgaps of all the considered unit cell designs were below a normalised frequency of 0.1, as can be seen in Figure 8.4b.
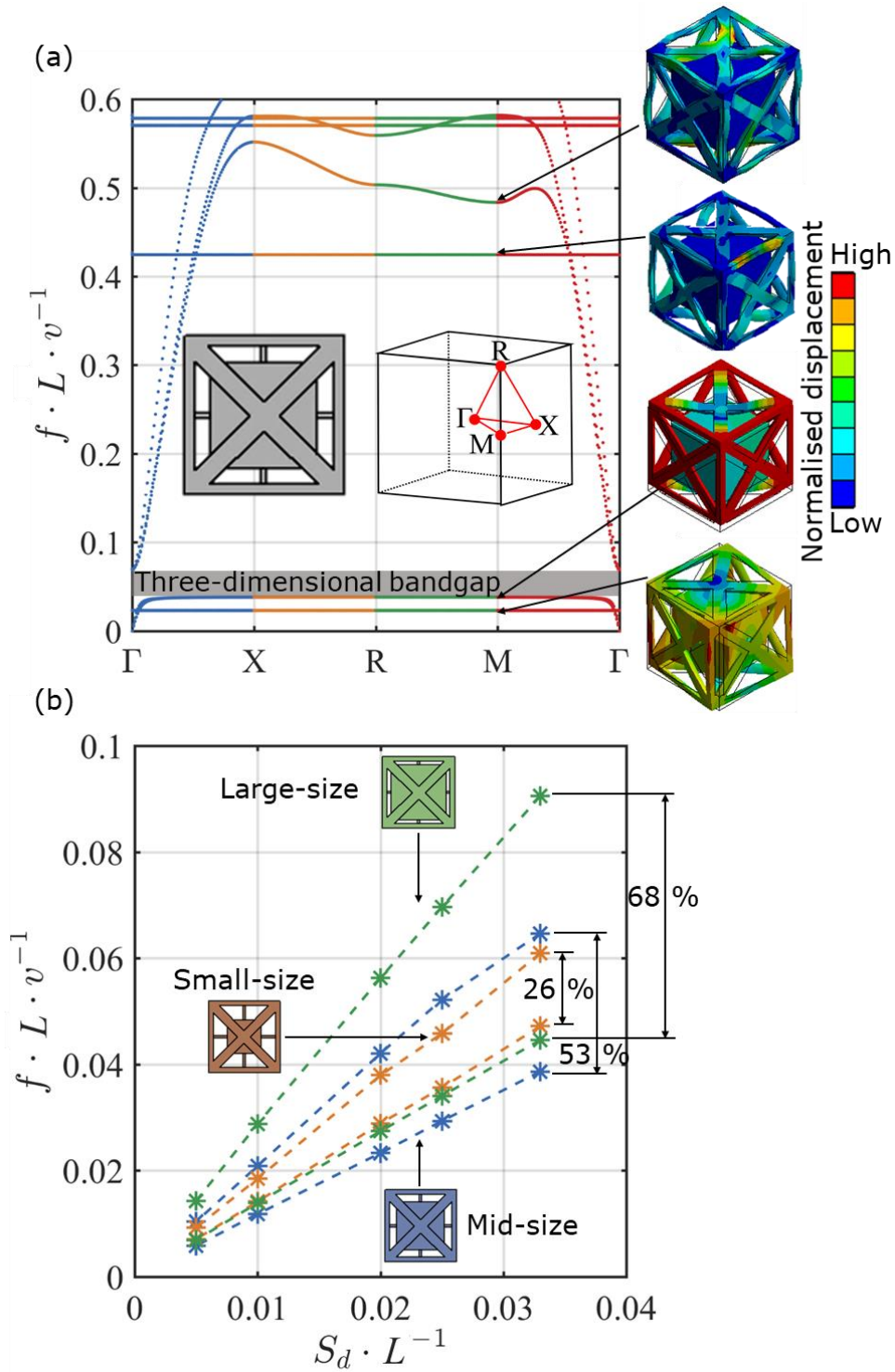
Figure 8.4. Wave propagation properties of the internally resonating lattice: (a) Dispersion curves for the internal resonance lattice. and (b) start and end frequencies of the complete bandgaps of lattices of different S_d/L values with the struts connected to resonators of large-size (green), mid-size (blue), and small-size (orange).

The bandgaps of the large-size resonator had wider bandgaps than that of the mid-size resonator. The average bandgap width in the large-size resonator was calculated to be wider by 63 %, and 236 % than that of mid-size and small-size resonators, respectively. The mean frequency of the bandgap showed a change of 2.4 % with the change in the resonator size (see Figure 8.5 for comparison with recent literature).
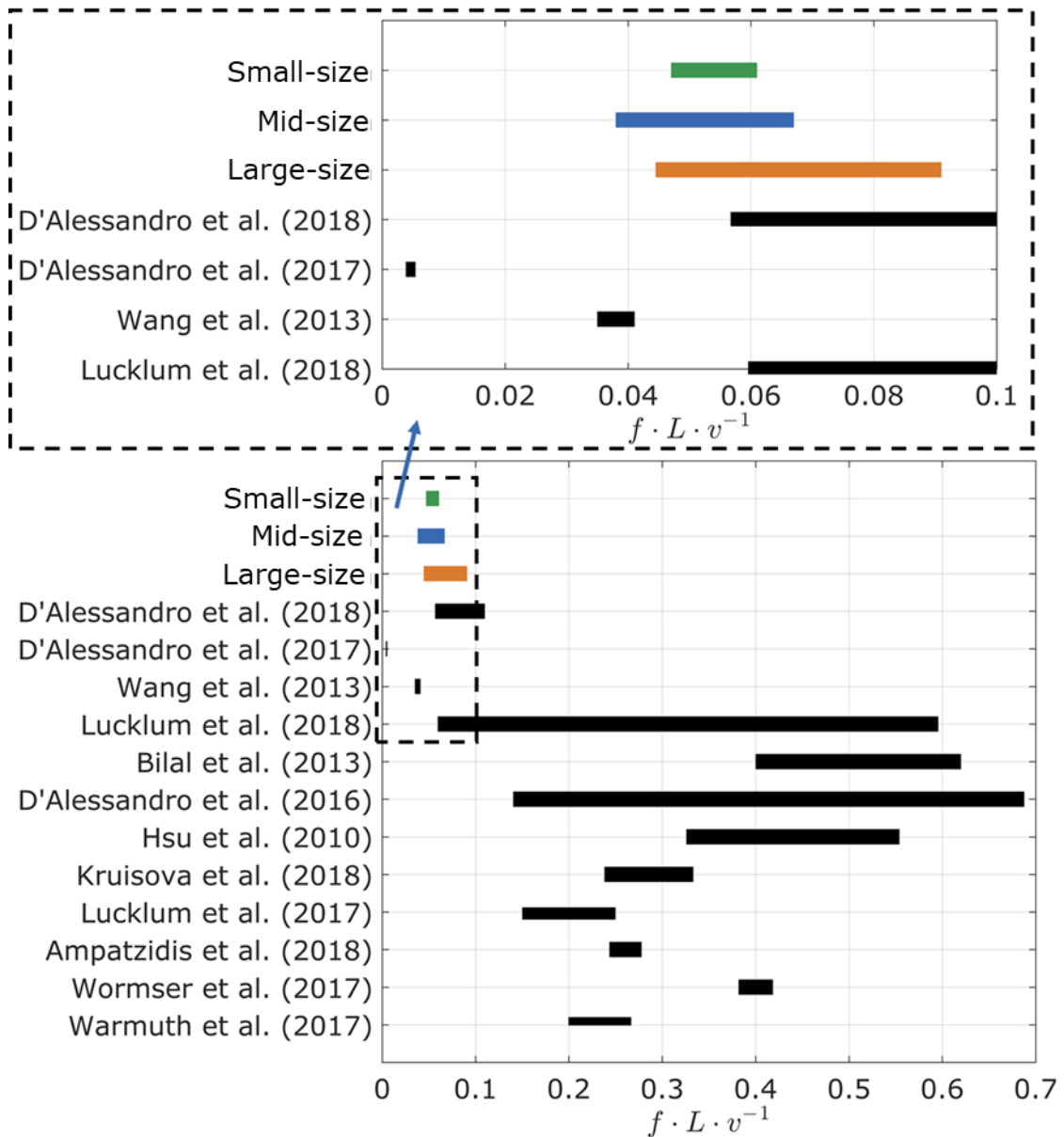
Figure 8.5. Comparison of the bandgaps in this work with the bandgaps of relevant literature. The indicated percentages show the relative gap to mid-gap percentage.

The results shown in Figure 8.4b can be used as a means of tuning the bandgaps of the lattice for a specific application. As can be seen in Figure 8.5, the frequencies of the bandgaps presented here are among the lowest reported in the literature (see Section 3.7 for a full list of work on bandgap). Only two published studies showed bandgaps with lower frequencies than those reported here: Wang et al. [96] and D'Alessandro et al. [174]. Wang et al. did not demonstrate the manufacturability of the lattices and, as a consequence, did not provide experimental validation of their findings, which is something D'Alessndro et al. did. However, the bandgap width of the lattice of D'Alessandro et al. [174] represents only 3 %, 5 % and 11 % of the bandgap width of the orange design, blue design and green design (see Figure 8.5).

8.3   Experimental verification of the bandgap

For verification of the complete bandgap in the proposed lattice, L-PBF was used to manufacture a 3D structure of finite periodicity. Details about the L-PBF process can be found in Section 4.1.5. The geometrical dimensions and periodicity of the lattice were selected to be suitable for the L-PBF process. The manufactured lattice, presented in Figure 8.1c, had a unit cell size of 30 mm and a 3D periodicity of three. The S_d/L and S_l/L values were selected to provide the lowest bandgap start frequency, when referenced to the bandgap start frequencies presented in Figure 8.4b while considering the lowest manufacturable feature size with L-PBF [23] (see Section 4.1.5); this meant that the S_d/L and S_l/L values had to be 0.033 and 0.1, respectively.

The 3D transmissibility of the lattice was obtained experimentally and is presented in Figure 8.6a. An experimental setup was assembled, comprising a modal shaker, a laser vibrometer, and accelerometer. See Section 4.3.3 for full details on the experimental testing. The longitudinal transmissibility had a value of 0 dB near the normalised frequency of zero, which indicates complete transmission of the excitation waves.

159
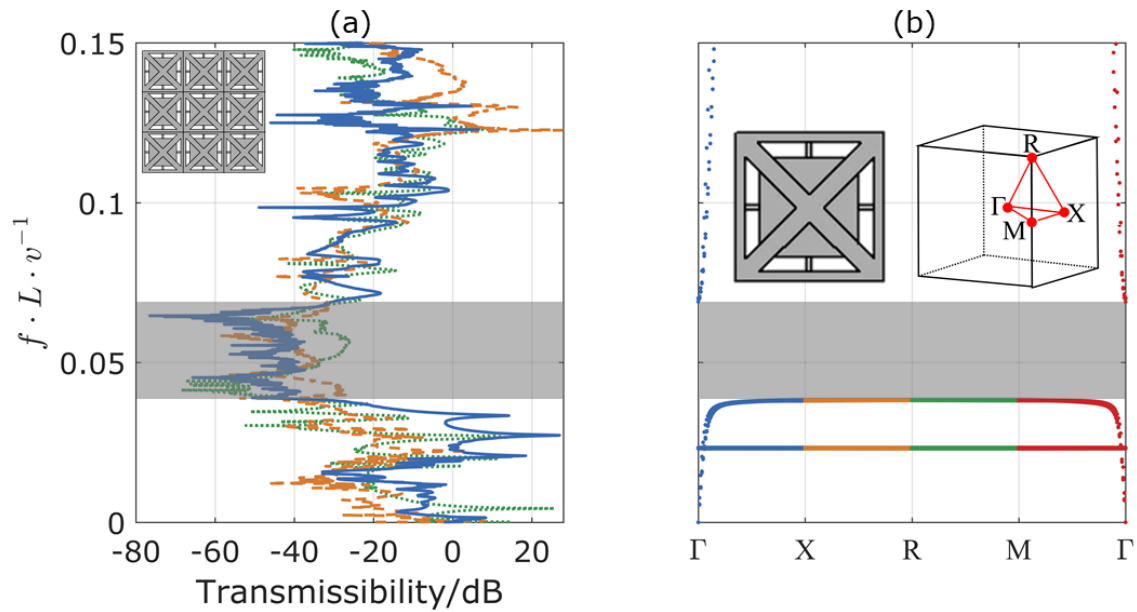
Figure 8.6. Experimental results acquired for the resonating lattice: (a) Transmissibility of the 3×3×3 lattice in the *x*-longitudinal direction (solid line), *y*-transverse direction (dotted line), and *z*-transverse direction (dashed line) vis-à-vis the corresponding bandgap as illustrated by the dispersion curves of the infinite lattice shown in (b), and (c) representative photograph of the experimental setup. The shaded areas show the identified bandgaps.

At the vibration resonances, the longitudinal transmissibility was greater than 0 dB and reached 28 dB, which indicates high amplification of the excitation waves. Within the bandgap, the longitudinal transmissibility reached -77 dB. For this particular lattice, the bandgap was from 1.63 kHz to 2.8 kHz with a unit cell size of 30 mm. In light of the example of aluminum Bragg-scattering lattice presented earlier on in Section 3.4, stopbands below 3 kHz are obtainable with metamaterials of 30 mm unit cell size rather than 1 metre for the aluminum Bragg-scattering lattice. Thus, unit cells of suitable dimensions for AM and applications, and higher periodicity within a certain design volume, in comparison to Bragg-scattering lattices, can be employed to obtain low absolute frequency bandgaps; resulting in higher attenuation within the bandgaps. The effect of lattice periodicity on the transmissibility within the bandgap can be seen elsewhere [134,176]. For this investigation, considering the manufacturable feature size of L-PBF, we have chosen 3×3×3 as a reasonable example. The results showed that the lattice in

this work has double the transmissibility reduction experimentally reported by Croënne et al. [134] for their 3D Bragg-scattering lattice which had double the spatial periodicity used in this work.

8.4   Summary of results

The 3D elastic wave propagation in the internal resonance lattices was modelled using a FE method combined with infinite periodicity assumptions. It was shown that the lattices exhibit complete bandgaps far below the lowest frequency limit of Bragg-scatteirng bandgaps, which exist in traditional Brag scattering lattices. A lattice of finite periodicity was manufactured using L-PBF. The experimental results showed that, within the bandgap, the longitudinal transmissibility of vibration waves in the lattice reached -77 dB. Tuning of the bandgap can be achieved by adjusting the size of the resonator and the diameter of the struts to suit the requirements of various applications. With these lattices, structures of more realistic cell sizes and higher periodicity within a certain design volume, in comparison to Bragg-scattering lattices, can be employed to obtain low-frequency bandgaps; resulting in higher attenuation within the bandgaps, more homogenous structures, more predictable mechanical properties and higher tolerance to defects.

Chapter 9

Summary and future work

The advancement in AM technology has allowed the realisation of complex lattice structures with tailorable properties. The first research question was "can lattices be used for vibration attenuation?" The project investigated the development and use of lattice structures for vibration attenuation. Different attenuation techniques have been tested and proposed including vibration isolation through shifting the natural frequency below the frequency of interest and 1D, and 3D, vibrational bandgaps with which wave propagation is prohibited at certain frequency regions. The study answered the first research question and revealed that lattice structures can be used to provide vibration attenuation through all of the tested mechanisms.

For vibration isolation by shifting the natural frequency below the frequency of interest, it was found that the response of the structure can be below or above 0 dB. When the response is below 0 dB, the attenuation is high and this is useful for providing vibration attenuation for applications in metrology and precision engineering. The frequency response region can be tailored through tuning of the natural frequency of the lattice with:

- the volume fraction: The higher the volume fraction of the lattice, the lower is the natural frequency,
- the cell size: The bigger the cell size, the lower is the natural frequency,
- and the number of tessellations: The higher the number of tessellation of the unit cell, the lower is the natural frequency.

The study used both simulation and experimental techniques to test the transmissibility of the lattices manufactured with laser powder bed fusion. The discrepancies between simulation and experiment results were minimal (4 % to 7 %). The results of the lattice vibration isolation study were used to successfully design and test a metrology frame for 1D vibration isolation at low frequencies (60 Hz to 150 Hz). In comparison to the existing methods of vibration attenuation, for example, metal and composite mounts, vibration isolation with lattices provide a low-mass solution to redesign metrology and structural frames for enhanced vibration attenuation performance. The redesign is done by replacing the solid parts of the structure with unit cells of suitable sizes, volume fractions and number of tessellations for the frequency of interest. When tailored to a specific frequency of interest, the vibration isolation lattice structure can provide response below 0 dB; this response is lower than that achievable with conventional vibration damping method (typically $\geq$ 0 dB) and, thus, it is better for vibration attenuation. One of the major drawbacks of this vibration isolation method was found to be its 1D nature; in metrology and precision engineering applications, for example in the case of a metrology frame, vibration attenuation in 2D and 3D is just as important as vibration attenuation in 1D to ensure minimal displacement between the effective end of the instrument/machine relative to the workpiece. In addition, the response at frequencies greater than the natural frequency is not guaranteed to be below 0 dB with vibration isolation; this is because longitudinal and transverse waves are still able to propagate in the structure.

To address the identified drawbacks of the vibration isolation method, the project successfully investigated and developed lattice structures for complete elimination of vibration waves in 3D. This was done by examining wave propagation and identifying bandgaps in 3D TPMS lattices with unit cell tessellations made along 1D. This answered the second research question "how can wave propagation be eliminated in lattices for the purpose of achieving vibration attenuation below 0 dB?" It was shown that gyroid TPMS lattices can develop bandgaps above a normalised frequency of 0.2 with transmissibility

below 0 dB in the bandgap frequency region, which is something the vibration isolation method failed to provide. However, this 1D bandgap investigation method showed bandgaps at relatively high frequency (< 9000 Hz). The project raised new research questions regarding the manufacturing and the fit of bandgap lattices for metrology and precision engineering applications. To illustrate, for tuning down the frequency of the bandgap to the hertz and low kilohertz frequency regions, which corresponds to the operating frequencies of metrology and precision engineering instruments, large unit cells with small features have to be used. This is quite challenging for the current state of L-PBF technology, for example, the smallest manufacturable feature size which is currently around 1 mm, and limits the number of tessellations available for applications with constrained design volume. In addition, the 1D bandgaps are only applicable to the unit cells tessellated along a single direction which limits their use in practical applications. For addressing these new issues, the project developed a method for modelling 3D wave propagation (with tessellations of the unit cell made in 3D) and with the aim of attaining lower and wider bandgap frequencies. It was found that strut-based lattices have 3D bandgaps above a normalised frequency of 0.2; this is a higher frequency than the TPMS bandgap but is five times wider than the widest TPMS bandgap, which is essential for covering wide frequency ranges in practical and research applications.

The project also showed that 3D low-frequency bandgaps below a normalised frequency of 0.1 can be obtained using strut based lattices with a resonator designed within their body. The outer scaffold of the internal resonance lattice is a strut-based lattice that is used for structural support, while the inner resonance mechanism is tunable to frequencies lower than can be realised with TPMS and strut-based lattices. This is because gyroid and strut-based lattices rely on Bragg-scattering for creating bandgaps which are highly dependant on the unit cell size for creating destructive wave interference. The internal resonance lattice showed transmissibility below 0 dB with finite number of tessellations (one, three and six unit cells along each direction). The internal resonance lattices can

164

create bandgaps at much lower frequencies (below a normalised frequency of 0.1). L-PBF was used to manufacture an internal resonance lattice which showed attenuation of up to -77 dB within its bandgap frequency region. Tuning of the frequency of the bandgap in all of the proposed bandgap lattices was demonstrated through control of the volume fraction, unit cell size and the AM material of the lattice. The volume fraction controlled the thickness and size of the struts in strut-based lattices, the wall thickness in TPMS lattices and the size of the resonator in the internal resonance lattices. This answered the third research question "how can the vibrational performance of lattices be tailored to meet different vibrational needs?" The designer of lattice structures can now use these results to assist with designing parts for use in metrology and precision engineering applications. Bandgap structures exhibit remarkable vibration attenuation capabilities through complete elimination of vibration waves; this is not obtainable with the existing vibration attenuation methods which do not prohibit wave propagation. The elimination of vibration waves translates into very low vibration responses (typically below 0 dB) that can get even lower with the increase in the number of tessellation of the bandgap unit cell. These results can be used as guidelines so that high attenuation of vibration magnitudes is achieved in lattice structures that are fabricated with AM.

For future work:

- Although bandgap structures are always better than vibration isolation structures for obtaining high magnitudes of vibration attenuation, the vibration isolation method can be useful in some case. For example, it can provide fast design and modelling of lattice structures for specific metrology and precision applications in comparison to bandgap engineering. This is because bandgap engineering relies on complex calculations of dispersion curves which are memory and CPU expensive. Future work will study vibration isolation in 2D and 3D as well as exploring methods to control the response at frequencies higher than the natural frequency.

- The internal resonance lattice of this project will be used in a future study to design a metrology frame for an all-optical dimensional measuring system (AODMS) with 3D bandgaps. This will ensure minimum move of the optical lens relative to the measured workpiece and thus take more accurate and repeatable measurements. The metrology frame will use three identical legs made of internal resonance lattices while using the thermal centre principle to minimise thermal expansion in *x*- and *y*-directions. Reduction of the thermal expansion in the *z*-direction will be achieved by shielding the lattice with invar sheets. The invar sheets will have very low thermal expansion under thermal fluctuations, in comparison to polymer and most metallic materials. The workpiece stage of the AODMS will also be made from internal resonance bandgap lattices with invar shielding to achieve vibration attenuation and reduce the thermal expansion.

- This work could benefit from further experimental testing to give more confidence in these lattices. For example, the effect of the number of tessellations of the lattice on its 3D bandgap can be experimentally studied by producing and testing various lattices of similar topology and different number of tessellations. Future work will also consider setting up more vibration testing studies, for example testing the durability of the lattices under random excitation and carrying vibration phase analysis.

- This project showed bandgap results that are normalised to the speed of wave of the material v. These results opened the door for investigation of new materials for AM that can be useful for metrology and precision engineering applications. New hybrid material for AM will also be explored so as to design structures of enhanced load-bearing and vibration attenuation capabilities in comparison to the existing AM technologies.

- Although the demonstrated bandgap of internal resonance lattice in this work has one of the lowest 3D bandgap frequencies ever reported, further reduction of the

166

normalised frequency is preferable. This can be done by exploring new unit cell designs, for example by varying the volume fractions within the unit cells to create a high difference in impedance.

- Lattice structures, in general, will benefit from advancement in the precision, accuracy and minimal manufacturable features of L-PBF and AM methods. The results presented in this thesis will also be useful when such technological progress is achieved. For example, if the minimum feature size of L-PBF is reduced by half, then the unit cell that gives the same bandgap frequency can be of half the original cell size. Consequently, twice as much unit cells can be suited within a specified volume. By successfully enhancing the precision, accuracy and minimal manufacturable features, bandgaps can be engineered within the micro-scale of the materials used for manufacturing. This will allow for almost infinite number of unit cells to be suited side by side for complete elimination of all mechanical vibration waves at tailorable frequencies.

References

1. Rogin, M. Isolation of Noise & Vibration in HVAC & Plumbing Piping Systems.

2. Gibson, L.J.; Ashby, M.F. *Cellular solids: structure and properties*; Cambridge Solid State Science Series; Cambridge University Press, 1999; ISBN 9780521499118.

3. Panesar, A.; Abdi, M.; Hickman, D.; Ashcroft, I. Strategies for functionally graded lattice structures derived using topology optimisation for additive manufacturing. *Addit. Manuf.* **2018**, *19*, 81–94.

4. Al-Ketan, O.; Rowshan, R.; Abu Al-Rub, R.K. Topology-mechanical property relationship of 3D printed strut, skeletal, and sheet based periodic metallic cellular materials. *Addit. Manuf.* **2018**, *19*, 167–183.

5. Hasan, R. Progressive collapse of titanium alloy micro-lattice structures manufactured using selective laser melting, University of Liverpool, 2013.

6. Amazing AM LLC What is Additive Manufacturing?

7. Parthasarathy, J.; Starly, B.; Raman, S. A design for the additive manufacture of functionally graded porous structures with tailored mechanical properties for biomedical applications. *J. Manuf. Process.* **2011**, *13*, 160–170.

8. Nakajima, H. Fabrication, properties and application of porous metals with directional pores. *Prog Mater Sci* **2007**, *52*, 1091–1173.

9. Evans, A.; Hutchinson, J.; Fleck, N.; Ashby, M.; Wadley, H. The topological design of multifunctional cellular metals. *Prog Mater Sci* **2001**, *46*, 309–27.

10. Rehme, O. *Cellular design for laser freeform fabrication*; Gottingen, 2010;

11. Luxner, M.H.; Woesz, A.; Stampfl, J.; Fratzl, P.; Pettermann, H.E. A finite element study on the effects of disorder in cellular structures. *Acta Biomater.* **2009**, *5*, 381–390.

12. D., P.; Arabnejad, S. Elastostatics of lattice materials. In *Dynamics of Latice Materials*; Phani;, A.S., Hussein, M.I., Eds.; John Wiley and Sons: Hoboken, 2017; pp. 21–22.

13. Kingyear Aluminum Industrial Germany develops lightweight structure of aluminum foam.

14. Mullen, L.; Stamp, R.C.; Fox, P.; Jones, E.; Ngo, C.; Sutcliffe, C.J. Selective laser melting: a unit cell approach for the manufacture of porous, titanium, bone in-growth constructs, suitable for orthopedic applications. II. Randomized structures. *J. Biomed. Mater. Res. - Part B Appl. Biomater.* **2010**, *92*, 178–188.

15. Rashed, M.G.; Ashraf, M.; Hazell, P.J. An overview on the structure and applications of metallic microlattices. In Proceedings of the Proc. Compos. Aust. CRC-ACS Conf.CRC-ACS; Newcastle, Australia, 2014.

16. Deshpande, V.S.; Fleck, N.A.; Ashby, M.F. Effective properties of the octet-truss lattice material. *J. Mech. Phys. Solids* **2001**, *49*, 1747–1769.

17. Bikas, H.; Stavropoulos, P.; Chryssolouris, G. Additive manufacturing methods and modelling approaches: a critical review. *Int. J. Adv. Manuf. Technol.* **2016**, *83*, 389–405.

18. Yadroitsev, I.; Smurov, I. Selective laser melting technology: from the single laser melted track stability to 3D parts of complex shape. *Phys. Procedia* **2010**, *5*, 551–560.

19. Rashed, M.G.; Ashraf, M.; Mines, R.A.W.; Hazell, P.J. Metallic microlattice materials: a current state of the art on manufacturing, mechanical properties and applications. *Mater. Des.* **2016**, *95*, 518–533.

20. King, W.E.; Anderson, A.T.; Ferencz, R.M.; Hodge, N.E.; Kamath, C.; Khairallah, S.A.; Rubenchik, A.M. Laser powder bed fusion additive manufacturing of metals; physics, computational, and materials challenges. *Appl. Phys. Rev.* **2015**, *2*, 41304.

21. Bertling, J.; Rommel, S. A critical view of 3D printing regarding industrial mass customization versus individual desktop fabrication. In *The decentralized and networked future of value creation: 3D printing and its implications for society, industry, and sustainable development*; Ferdinand, J.-P., Petschow, U., Dickel, S., Eds.; Springer International Publishing: Cham, 2016; pp. 75–105 ISBN 978-3-319-31686-4.

22. Tsopanos, S.; Mines, R.A.W.; McKown, S.; Shen, Y.; Cantwell, W.J.; Brooks, W.; Sutcliffe, C.J. The influence of processing parameters on the mechanical properties of selectively laser melted stainless steel microlattice structures. *J. Manuf. Sci. Eng.* **2010**, *132*, 41011–41012.

23. Tasch, D.; Mad, A.; Stadlbauer, R.; Schagerl, M. Thickness dependency of mechanical properties of laser-sintered polyamide lightweight structures. *Addit. Manuf.* **2018**, *23*, 25–33.

24. Khairallah, S.A.; Anderson, A.T.; Rubenchik, A.; King, W.E. Laser powder-bed fusion additive manufacturing: Physics of complex melt flow and formation mechanisms of pores, spatter, and denudation zones. *Acta Mater.* **2016**, *108*, 36–45.

25. Tang, M.; Pistorius, P.C.; Beuth, J.L. Prediction of lack-of-fusion porosity for powder bed fusion. *Addit. Manuf.* **2017**, *14*, 39–48.

26. Rehme, O.; Emmelmann, C. Rapid manufacturing of lattice structures with selective laser melting. *Proc. SPIE Int. Soc. Opt. Eng.* **2006**, *6107*, 192–203.

27. Yoon, H.; Lee, J.; Kim, H.; Kim, M.; Kim, E.; Shin, Y. A Comparison of energy consumption in bulk forming , subtractive , and additive processes : Review and case study. *Int. J. Precis. Eng. Manuf. Technol.* **2014**, *1*, 261–279.

28. Syam, W.P.; Al-shehri, H.A.; Al-wazzan, K.A.; Mannan, M.A. Preliminary fabrication of thin-wall structure of Ti6Al4V for dental restoration by electron beam melting. *Rapid Prototyp. J.* **2012**, *3*, 230–240.

29. Syam, W.P.; Mannan, M.A.; Al-Ahmari, A.M. Rapid prototyping and rapid manufacturing in medicine and dentistry. *Virtual Phys. Prototyp.* **2011**, *6*, 79–109.

30. Cansizoglu, O.; Harrysson, O.L. a.; Ii, H. a. W.; Cormier, D.R.; Mahale, T.

Applications of structural optimization in direct metal fabrication. *Rapid Prototyp. J.* **2008**, *14*, 114–122.

31. Cansizoglu, O.; Harrysson, O.; Cormier, D.; West, H.; Mahale, T. Properties of Ti-6Al-4V non-stochastic lattice structures fabricated via electron beam melting. *Mater. Sci. Eng. A* **2008**, *492*, 468–474.

32. Syam, W. P., Al-Ahmari, A. M., Mannan, M. A., Al-Shehri, H. A., & Al-Wazzan, K.A. Metallurgical, accuracy and cost analysis of Ti6Al4V dental coping fabricated by electron beam melting process. In Proceedings of the The 5th International Conference on Advanced Research in Virtual and Rapid Prototyping; 2011; pp. 375–383.

33. Gibson, I.; Rosen, D.W.; Stucker, B. *Additive manufacturing technologies: rapid prototyping to direct digital manufacturing*; Springer, 2009;

34. Wadley, H.N.G.; Fleck, N.A.; Evans, A.G. Fabrication and structural performance of periodic cellular metal sandwich structures. *Compos. Sci. Technol.* **2003**, *63*, 2331–2343.

35. Chiras, S.; Mumm, D.R.; Evans, A.G.; Wicks, N.; Hutchinson, J.W.; Dharmasena, K.; Wadley, H.N.G.; Fichter, S. The structural performance of near-optimized truss core panels. *Int. J. Solids Struct.* **2002**, *39*, 4093–4115.

36. Smith, M. The compressive response of novel lattice structures subjected to static and dynamic loading, University of Liverpool, 2012.

37. Wang, J.; Evans, A.G. On the performance of truss panels with Kagom e cores. **2003**, *40*, 6981–6988.

38. Radford, D.D.; Fleck, N.A.; Deshpande, V.S. The response of clamped sandwich beams subjected to shock loading. *Int. J. Impact Eng.* **2006**, *32*, 968–987.

39. Kooistra, G.W.; Deshpande, V.S.; Wadley, H.N.G. Compressive behavior of age hardenable tetrahedral lattice truss structures made from aluminium. *Acta Mater.* **2004**, *52*, 4229–4237.

40. Kooistra, G.W.; Wadley, H.N.G. Lattice truss structures from expanded metal sheet. *Mater. Des.* **2007**, *28*, 507–514.

41. Maskery, I.; Sturm, L.; Aremu, A.O.; Panesar, A.; Williams, C.B.; Tuck, C.J.; Wildman, R.D.; Ashcroft, I.A. Insights into the mechanical properties of several triply periodic minimal surface lattice structures made by polymer additive manufacturing. *Polymer (Guildf).* **2017**, 1–10.

42. Maskery, I.; Aboulkhair, N.T.; Aremu, A.O.; Tuck, C.J.; Ashcroft, I.A. Compressive failure modes and energy absorption in additively manufactured double gyroid lattices. *Addit. Manuf.* **2017**, *16*, 24–29.

43. Kapfer, S.C.; Hyde, S.T.; Mecke, K.; Arns, C.H.; Schröder-Turk, G.E. Minimal surface scaffold designs for tissue engineering. *Biomaterials* **2011**, *32*, 6875–6882.

44. Gandy, P.J.F.; Cvijović, D.; Mackay, A.L.; Klinowski, J. Exact computation of the triply periodic D (`diamond') minimal surface. *Chem. Phys. Lett.* **1999**, *314*, 543–551.

45. Panesar, A.; Abdi, M.; Hickman, D.; Ashcroft, I. Strategies for functionally graded lattice structures derived using topology optimisation for additive manufacturing. *Addit. Manuf.* **2018**, *19*, 81–94.

46. Hussein, A.Y. The development of lightweight cellular structures for metal additive manufacturing. **2013**, 228.

47. Khaderi, S.N.; Deshpande, V.S.; Fleck, N.A. The stiffness and strength of the gyroid lattice. *Int. J. Solids Struct.* **2014**, *51*, 3866–3877.

48. Brooks, W.; Sutcliffe, C.; Cantwell, W.; Fox, P.; Todd, J.; Mines, R. Rapid design and manufacture of ultralight cellular materials. In Proceedings of the Solid Freeform Fabrication Proceedings; Bourell, D.L., Crawford, R.H., Beaman, J.J., Wood, K.L., Marcus, H., Eds.; The University of Texas: Texas, 2005; pp. 231–241.

49. Added Scientific Software and modelling Available online: http://addedscientific.com/resources/software-and-modelling (accessed on Apr 24, 2018).

50. Santorinaios, M.; Brooks, W.; Sutcliffe, C.J.; Mines, R.A.W. Crush behaviour of open cellular lattice structures manufactured using selective laser melting. *WIT Trans. Built Environ.* **2006**, *85*, 481–490.

51. McKown, S.; Shen, Y.; Brookes, W.K.; Sutcliffe, C.J.; Cantwell, W.J.; Langdon, G.S.; Nurick, G.N.; Theobald, M.D. The quasi-static and blast loading response of lattice structures. *Int. J. Impact Eng.* **2008**, *35*, 795–810.

52. Yan, C.; Hao, L.; Hussein, A.; Raymont, D. Evaluations of cellular lattice structures manufactured using selective laser melting. *Int. J. Mach. Tools Manuf.* **2012**, *62*, 32–38.

53. Carmignato, S.; Dewulf, W.; Leach, R.K. *Industrial X-Ray Computed Tomography*; Springer International Publishing, 2018;

54. Syam, W.P.; Jianwei, W.; Zhao, B.; Maskery, I.; Elmadih, W.; Leach, R.K. Design and analysis of strut-based lattice structures for vibration isolation. *Precis. Eng.* **2017**, *52*, 494–506.

55. Maskery, I.; Aremu, A.O.; Parry, L.; Wildman, R.D.; Tuck, C.J.; Ashcroft, I.A. Effective design and simulation of surface-based lattice structures featuring volume fraction and cell type grading. *Mater. Des.* **2018**, *155*, 220–232.

56. Elmadih, W.; Nefzi, M.; Bruice, E. Environmental isolation. In *Basics of precision engineering*; Leach, R., Smith, S., Eds.; 2018; pp. 565–600.

57. Giurgiutiu, V. Chapter 5 - Elastic Waves. In *Structural Health Monitoring with Piezoelectric Wafer Active Sensors (Second Edition)*; Giurgiutiu, V., Ed.; Academic Press: Oxford, 2014; pp. 199–292 ISBN 978-0-12-418691-0.

58. Rao, S.S. *Mechanical vibrations*; 6th editio.; Pearson Education: Hoboken, 2016; ISBN 9780134361895.

59. Bosmans, N.; Reynaerts, D. Force loops. In *Basics of precision engineering*; Leach, R.K., Smith, S., Eds.; 2018; pp. 505–506.

60. Thorlabs Sources of vibration Available online:

https://www.thorlabs.com/tutorials/tables2.cfm (accessed on Jul 1, 2018).

61.   Collet, M.; Ouisse, M.; Ruzzene, M.; Ichchou, M.N. Floquet–Bloch decomposition for the computation of dispersion of two-dimensional periodic, damped mechanical systems. *Int. J. Solids Struct.* **2011**, *48*, 2837–2848.

62.   Matlack, K.H.; Bauhofer, A.; Krödel, S.; Palermo, A.; Daraio, C. Composite 3D-printed meta-structures for low frequency and broadband vibration absorption. *Proc. Natl. Acad. Sci. U S A* **2015**, *113*, 8386–8390.

63.   Phani, a S.; Woodhouse, J.; Fleck, N. a Wave propagation in two-dimensional periodic lattices. *J. Acoust. Soc. Am.* **2006**, *119*, 1995–2005.

64.   Phani, A.S. Elastodynamics of lattice materials. In *Dynamics of lattice materials*; Phani, A.S., Hussein, M.I., Eds.; John Wiley and Sons, 2017; pp. 53–59.

65.   Ledezma-Ramirez, D.F.; Tapia-Gonzalez, P.E.; Ferguson, N.; Brennan, M.J.; Tang, B. Recent advances in shock isolation: an overview and future possibilities. *Appl. Mech. Rev.* **2019**, *71*.

66.   Rivin, E.I. *Passive vibration isolation*; ASME Press: New York, 2003; ISBN 9781860584008.

67.   Chen, P.-C.; Shih, M.-C. Modeling and robust active control of a pneumatic vibration isolator. *J. Vib. Control* **2007**, *13*, 1553–1571.

68.   Piersol, A.G.; Paez, T.L. *Harris' Shock and Vibration Handbook*; 6th Editio.; McGraw-Hills: Ney York, 2010; ISBN 9780071633437.

69.   ISOTECH Inc. Spring mount vibration isolators.

70.   DACHENG Rubber Co. Ltd. Lead rubber bearing.

71.   Okamura, S.; Fujita, S. Motion Analysis of Pendulum Type Isolation Systems During Earthquakes (Probabilistic Study of Isolation Performance of Base Isolated Structure Considering Characteristic Dispersion of Pendulum Type Isolation Systems). *J. Press. Vessel Technol.* **2006**, *129*, 507–515.

72.   Nakra, B.C. Vibration control in machines and structures using viscoelastic damping. *J. Sound Vib.* **1998**, *211*, 449–465.

73.   Harris, C.M. *Shock and Vibration Handbook*; 4th ed.; McGraw-Hill: New York., 1997;

74.   Wang, X.; Zhang, P.; Ludwick, S.; Belski, E.; To, A.C. Natural frequency optimization of 3D printed variable-density honeycomb structure via a homogenization-based approach. *Addit. Manuf.* **2017**, 1–10.

75.   Qi, X.-L.; Zhang, S.-C. Topological insulators and superconductors. *Rev. Mod. Phys.* **2011**, *83*, 1057–1110.

76.   Hasan, M.Z.; Kane, C.L. Colloquium: Topological insulators. *Rev. Mod. Phys.* **2010**, *82*, 3045–3067.

77.   Roldán, R.; Castellanos-Gomez, A. A new bandgap tuning knob. *Nat. Photonics* **2017**, *11*, 407.

78. Zoorob, M.E.; Charlton, M.D.B.; Parker, G.J.; Baumberg, J.J.; Netti, M.C. Complete photonic bandgaps in 12-fold symmetric quasicrystals. *Nature* **2000**, *404*, 740.

79. Slobozhanyuk, A.; Mousavi, S.H.; Ni, X.; Smirnova, D.; Kivshar, Y.S.; Khanikaev, A.B. Three-dimensional all-dielectric photonic topological insulator. *Nat. Photonics* **2016**, *11*, 130.

80. Cheng, X.; Jouvaud, C.; Ni, X.; Mousavi, S.H.; Genack, A.Z.; Khanikaev, A.B. Robust reconfigurable electromagnetic pathways within a photonic topological insulator. *Nat. Mater.* **2016**, *15*, 542.

81. Lu, L.; Fu, L.; Joannopoulos, J.D.; Soljačić, M. Weyl points and line nodes in gyroid photonic crystals. *Nat. Photonics* **2013**, *7*, 294.

82. Abueidda, D.W.; Jasiuk, I.; Sobh, N.A. Acoustic band gaps and elastic stiffness of PMMA cellular solids based on triply periodic minimal surfaces. *Mater. Des.* **2018**, *145*, 20–27.

83. Khelif, A.; Hsiao, F.L.; Choujaa, A.; Benchabane, S.; Laude, V. Octave omnidirectional band gap in a three-dimensional phononic crystal. *IEEE Trans. Ultrason. Ferroelectr. Freq. Control* **2010**, *57*, 1621–1625.

84. Zhou, X.Z.; Wang, Y.S.; Zhang, C.Z. Three-Dimensional sonic band gaps tunned by material parameters. *Appl. Mech. Mater.* **2010**, *29–32*, 1797–1802.

85. Trainiti, G.; Rimoli, J.J.; Ruzzene, M. Wave propagation in periodically undulated beams and plates. *Int. J. Solids Struct.* **2015**, *75*, 260–276.

86. Lu, Y.; Yang, Y.; Guest, J.K.; Srivastava, A. 3-D phononic crystals with ultra-wide band gaps. *Sci. Rep.* **2017**, *7*, 43407.

87. Richards, D., Pines, D.J. Passive reduction of gear mesh vibration using a periodic drive shaft. *J. Sound Vib.* **2003**, *2*, 317–342.

88. Ampatzidis, T.; Leach, R.K.; Tuck, C.J.; Chronopoulos, D. Band gap behaviour of optimal composite structures with additive manufacturing inclusions. *Compos. Part B* **2018**.

89. Elmadih, W.; Wahyudin, S.; Maskery, I.; Chornopolous, D.; Leach, R.K. Mechanical vibration bandgaps in surface-based lattices. *Addit. Manuf.* **2019**, *25*, 421–429.

90. Jensen, J.S. Phononic band gaps and vibrations in one- and two-dimensional mass–spring structures. *J. Sound Vib.* **2003**, *266*, 1053–1078.

91. Maldovan, M. Phonon wave interference and thermal bandgap materials. *Nat. Mater.* **2015**, *14*, 667.

92. Raghavan, L.; Phani, A.S. Local resonance bandgaps in periodic media: Theory and experiment. *J. Acoust. Soc. Am.* **2013**, *134*, 1950–1959.

93. Zhou, X.; Jun, W.; Wang, R.; Lin, J. *Band gaps in grid structure with periodic local resonator subsystems*; 2017; Vol. 31;.

94. Yu, D.; Liu, Y.; Wang, G.; Zhao, H.; Qiu, J. *Flexural vibration band gaps in*

Timoshenko beams with locally resonant structures; 2006; Vol. 100;.

95. Liu, Y.; Yu, D.; Li, L.; Zhao, H.; Wen, J.; Wen, X. *Design guidelines for flexural wave attenuation of slender beams with local resonators*; 2007; Vol. 362;.

96. Wang, Y.-F.; Wang, Y.-S. Complete bandgap in three-dimensional holey phononic crystals with resonators. *J. Vib. Acoust.* **2013**, *135*, 041009.

97. NDT Resource Center Speed of sound.

98. Eric W. Weisstein Wavenumber - from Eric Weisstein's World of Physics.

99. Raghavan, L.; Phani, A.S. Local resonance bandgaps in periodic media: Theory and experiment. *J. Acoust. Soc. Am.* **2013**, *134*, 1950–1959.

100. James, R.; Woodley, S.M.; Dyer, C.M.; Humphrey, V.F. Sonic bands, bandgaps, and defect states in layered structures—Theory and experiment. *J. Acoust. Soc. Am.* **1995**, *97*, 2041–2047.

101. Trainiti, G.; Rimoli, J.J.; Ruzzene, M. Wave propagation in undulated structural lattices. *Int. J. Solids Struct.* **2016**, *97*, 431–444.

102. Kuang, W.; Hou, Z.; Liu, Y.; Li, H. The band gaps of cubic phononic crystals with different shapes of scatterers. *J. Phys. D. Appl. Phys.* **2006**, *39*, 2076–2071.

103. Qian, D.; Shi, Z. Using PWE/FE method to calculate the band structures of the semi-infinite beam-like PCs: Periodic in z-direction and finite in x–y plane. *Phys. Lett. A* **2017**, *381*, 1516–1524.

104. Hsieh, P.-F.; Wu, T.-T.; Sun, J.-H. Three-dimensional phononic band gap calculations using the FDTD method and a PC cluster system. *IEEE Trans. Ultrason. Ferroelectr. Freq. Control* **2006**, *53*, 148–158.

105. Sigalas, M.M.; García, N. Theoretical study of three dimensional elastic band gaps with the finite-difference time-domain method. *J. Appl. Phys.* **2000**, *87*, 3122–3125.

106. Laakso, I. Introduction the FDTD method - Aalto University.

107. Bonomo, A.L.; Isakson, M.J.; Chotiros, N.P. A comparison of finite element and analytic models of acoustic scattering from rough poroelastic interfaces. *J. Acoust. Soc. Am.* **2015**, *137*, EL235–EL240.

108. Reddy, J.N. *An introduction to the finite element method*; 3rd ed.; McGraw-Hill, 2006;

109. Logan, D.L. *A First Course in the Finite Element Method*; 6th ed.; CENGAGE Learning: Boston, 2016;

110. Lucklum, F.; Vellekoop, M.J. Bandgap engineering of three-dimensional phononic crystals in a simple cubic lattice. *Appl. Phys. Lett.* **2018**, *113*, 201902.

111. Warmuth, F.; Wormser, M.; Körner, C. Single phase 3D phononic band gap material. *Scienti* **2017**, 1–7.

112. Wormser, M.; Warmuth, F.; Körner, C. Evolution of full phononic band gaps in periodic cellular structures. *Appl. Phys. A* **2017**, *123*, 661.

113. Lucklum, F.; Vellekoop, M.J. Design and fabrication challenges for millimeter-scale three-dimensional phononic crystals. *Crystals* **2017**, *7*, 348.

114. Kruisová, A.; Ševčík, M.; Seiner, H.; Sedlák, P.; Román-Manso, B.; Miranzo, P.; Belmonte, M.; Landa, M. Ultrasonic bandgaps in 3D-printed periodic ceramic microlattices. *Ultrasonics* **2018**, *82*, 91–100.

115. Yoo, D.-J. Advanced porous scaffold design using multi-void triply periodic minimal surface models with high surface area to volume ratios. *Int. J. Precis. Eng. Manuf.* **2014**, *15*, 1657–1666.

116. Aremu, A.O.; Maskery, I.; Tuck, C.; Ashcroft, I.A.; Wildman, R.D.; Hague, R.I.M. A comparative finite element study of cubic unit cells for selective laser melting. In Proceedings of the Solid Freeform Symposium; 2014; pp. 1238–1249.

117. Sundén, B.; Fu, J. *Heat Transfer in Aerospace Applications*; Academic Press, 2016;

118. Daliri, A.; Zhang, J.; Wang, C.H. 6 - Hybrid polymer composites for high strain rate applications. In *Lightweight Composite Structures in Transport*; Njuguna, J., Ed.; Woodhead Publishing, 2016; pp. 121–163 ISBN 978-1-78242-325-6.

119. Leary, M.; Mazur, M.; Elambasseril, J.; McMillan, M.; Chirent, T.; Sun, Y.; Qian, M.; Easton, M.; Brandt, M. Selective laser melting (SLM) of AlSi12Mg lattice structures. *Mater. Des.* **2016**, *98*, 344–357.

120. Choi, J.-W.; Kim, H.-C.; Wicker, R. Multi-material stereolithography. *J. Mater. Process. Technol.* **2011**, *211*, 318–328.

121. Nouh, M.; Aldraihem, O.; Baz, A. Wave propagation in metamaterial plates with periodic local resonances. *J. Sound Vib.* **2015**, *341*, 53–73.

122. Wang, P.; Casadei, F.; Kang, S.H.; Bertoldi, K. Locally resonant band gaps in periodic beam lattices by tuning connectivity. *Phys. Rev. B* **2015**, *91*, 20103.

123. Bacigalupo, A.; Gambarotta, L. Simplified modelling of chiral lattice materials with local resonators. *Int. J. Solids Struct.* **2016**, *83*, 126–141.

124. Sharma, B.; Sun, C.T. Local resonance and Bragg bandgaps in sandwich beams containing periodically inserted resonators. *J. Sound Vib.* **2016**, *364*, 133–146.

125. Yilmaz, C.; Hulbert, G.M. Dynamics of locally resonant and inertially amplified lattice materials. In *Dynamics of lattice materials*; Phani, A.S., Hussein, M.I., Eds.; John Wiley and Sons, 2017; p. 233.

126. Liu; Zhang; Mao; Zhu; Yang; Chan; Sheng Locally resonant sonic materials. *Science* **2000**, *289*, 1734–1736.

127. Fang, N.; Xi, D.; Xu, J.; Ambati, M.; Srituravanich, W.; Sun, C.; Zhang, X. Ultrasonic metamaterials with negative modulus. *Nat. Mater.* **2006**, *5*, 452.

128. Qureshi, A.; Li, B.; Tan, K.T. Numerical investigation of band gaps in 3D printed cantilever-in-mass metamaterials. *Sci. Rep.* **2016**, *6*, 28314.

129. D'Alessandro, L.; Belloni, E.; Ardito, R.; Corigliano, A.; Braghin, F. Modeling and experimental verification of an ultra-wide bandgap in 3D phononic crystal. *Appl. Phys. Lett.* **2016**, *109*, 221907.

130. Zhang, H.; Xiao, Y.; Wen, J.; Yu, D.; Wen, X. Flexural wave band gaps in metamaterial beams with membrane-type resonators : theory and experiment. **2015**.

131. Bilal, O.R.; Hussein, M.I. Trampoline metamaterial: Local resonance enhancement by springboards. *Appl. Phys. Lett.* **2013**, *103*, 111901.

132. Kruisová, A.; Ševčík, M.; Seiner, H.; Sedlák, P.; Román-Manso, B.; Miranzo, P.; Belmonte, M.; Landa, M. Ultrasonic bandgaps in 3D-printed periodic ceramic microlattices. *Ultrasonics* **2018**, *82*, 91–100.

133. Lazcano, Z.; Meza, O.; Arriaga, J. Localization of acoustic modes in periodic porous silicon structures. *Nanoscale Res. Lett.* **2014**, *9*, 419–428.

134. Croënne, C.; Lee, E.J.S.; Hu, H.; Page, J.H. Band gaps in phononic crystals : Generation mechanisms and interaction effects Band gaps in phononic crystals : Generation mechanisms. *AIPAdvances* **2011**, *041401*.

135. Hsu, F.C.; Lee, C.I.; Hsu, J.C.; Huang, T.C.; Wang, C.H.; Chang, P. Acoustic band gaps in phononic crystal strip waveguides. *Appl. Phys. Lett.* **2010**, *96*, 3–6.

136. Wang, L.; Bertoldi, K. Mechanically tunable phononic band gaps in three-dimensional periodic elastomeric structures. *Int. J. Solids Struct.* **2012**, *49*, 2881–2885.

137. Zhizhong, Y.A.N.; Yuesheng, W. Wavelet-based method for computing elastic band gaps of one-dimensional phononic crystals. *Sci. China Ser. G Physics, Mech. Astron.* **2007**, *50*, 622–630.

138. Moore, M. Symmetrical Intersections of right circular cylinders. *Math. Gaz.* **1974**, *58*, 181–185.

139. Chen, S.-B.; Wen, J.-H.; Wang, G.; Han, X.-Y.; Wen, X.-S. Locally Resonant Gaps of Phononic Beams Induced by Periodic Arrays of Resonant Shunts. *Chinese Phys. Lett.* **2011**, *28*, 94301.

140. The Modal Shop 60 lbf Modal Shaker Available online: http://www.modalshop.com/filelibrary/60lbf-Modal-Shaker-Datasheet-(DS-0076).pdf (accessed on Feb 19, 2018).

141. The Modal Shop Modal Exciter 60 lbf: Model 2060E.

142. G., B.; G.T., H. A revolutionary 3-D interferometric vibrational mode display. In Proceedings of the Audio Engineering Society Convention 66; Audio Engineering Society, 1980.

143. Polytec PDV 100 laser vibrometer Available online: https://www.polytec.com/fileadmin/d/Vibrometrie/OM_DS_PDV-100_E_42474.pdf (accessed on Jan 1, 2018).

144. Jaffe, B. *Piezoelectric Ceramics (Vol. 3)*; Elsevier, 2012;

145. PCB Piezotronics MODEL: 288D01 Available online: https://www.pcb.com/products?model=288D01 (accessed on Jun 1, 2018).

146. Craft, G.; Nussbaum, J.; Crane, N.; Harmon, J.P. Impact of extended sintering

times on mechanical properties in PA-12 parts produced by powderbed fusion processes. *Addit. Manuf.* **2018**, *22*, 800–806.

147. Materialise PA 12 (SLS): Datasheet Available online: http://www.materialise.com/en/manufacturing/materials/pa-12-sls (accessed on Jan 31, 2018).

148. Yan, Z.; Wang, Y.; Zhang, C. Wavelet method for calculating the defect states of two-dimensional phononicx crystals. *Acta Mech. Solida Sin.* **2008**, *21*, 104–109.

149. Liu, Z.; Chan, C.T.; Sheng, P. Three-component elastic wave band-gap material. *Phys. Rev. B - Condens. Matter Mater. Phys.* **2002**, *65*, 1651161–1651166.

150. Marwaha, A.; Marwaha, S.; Hudiara, I.S. Analysis of Curved Boundaries by FDTD and FE Methods. *IETE J. Res.* **2001**, *47*, 301–310.

151. Maurin, F.; Claeys, C.; Deckers, E.; Desmet, W. Probability that a band-gap extremum is located on the irreducible Brillouin-zone contour for the 17 different plane crystallographic lattices. *Int. J. Solids Struct.* **2017**.

152. Ashcroft, N.; Mermin, N. *Solid state physics*; Holt, Rinhert and Winston, 1976;

153. Brillioun, L. *Wave propagation in periodic structures*; 2nd Editio.; Dover Publications, 1953;

154. D'Alessandro, L.; Zega, V.; Ardito, R.; Corigliano, A. 3D auxetic single material periodic structure with ultra-wide tunable bandgap. *Sci. Rep.* **2018**, *8*, 2262.

155. Van Belle, L.; Claeys, C.; Deckers, E.; Desmet, W. On the impact of damping on the dispersion curves of a locally resonant metamaterial: Modelling and experimental validation. *J. Sound Vib.* **2017**, *409*, 1–23.

156. Li, J.; Wang, Y.; Zhang, C. Finite element method for analysis of band structures of phononic crystal slabs with archimedean-like tilings. In Proceedings of the AIP Conference Proceedings; 2009; Vol. 1, pp. 1548–1551.

157. Ostachowicz, W.; Radzieński, M. Structural health monitoring by means of elastic wave propagation. *J. Phys. Conf. Ser.* **2012**, *382*, 12003.

158. Zhuge, J. Multi-resolution spectrum analysis Available online: https://www.crystalinstruments.com/multi-resolution-spectrum-analysis (accessed on May 7, 2019).

159. W. Elmadih, W.P. Syam, I. Maskery, D. Chornopoulos, R.K.L. Mechanical vibration bandgaps in surface-based lattices. *J. Addit. Manuf.* **2018**, *Submitted*.

160. Elmadih, W.; Syam, W.P.; Maskery, I.; Chronopoulos, D.; Leach, R. Multidimensional phononic bandgaps in three-dimensional lattices for additive manufacturing. *Mater. (Basel, Switzerland)* **2019**, *12*, 1878.

161. W. Elmadih, W.P. Syam, I. Maskery, R.K.L. Designing low frequency band gaps in additively manufactured parts using internal resonators. In Proceedings of the 33rd Annual Meeting of American Society for Precision Engineering November 4-9; 2018; pp. 162–167.

162. Elmadih, W.; Chronopoulos, D.; Syam, W.P.; Maskery, I.; Meng, H.; Leach, R.K.

Three-dimensional resonating metamaterials for low-frequency vibration attenuation. *Sci. Rep.* **2019**, *9*, 11503.

163. Elmadih, W.; Syam, W.; Maskery, I.; Leach, R. Additively manufactured lattice structures for precision engineering applications. In Proceedings of the 32nd Annual Meeting of American Society for Precision Engineering; In Press, 2018.

164. Instron - Illinios Tool Works Inc. Universal Testing Systems Available online: https://www.instron.co.uk/-/media/literature-library/products/2019/04/3400-series-universal-testing-systems.pdf#page=17 (accessed on Jul 1, 2019).

165. IDEERS at Bristol University Resistant buildings vibrating.

166. Leach, R.; Elmadih, W.; Piano, S.; Senin, N.; Sims-Waterhouse, D.; Syam, W.; Su, R.; Thomas, M. Enriching micro-scale metrology with an all- optical dimensional measuring system. In Proceedings of the Proc. euspen Micro/Nano Manufacturing Workshop; Strathclyde, 2017.

167. Karim, S.; Weber, U. Kinematic design. In *Basics of precision engineering*; Leach, R.K., Smith, S., Eds.; CRC Press, 2018; pp. 205–262.

168. Gandy, P.J.F.; Cvijović, D.; Mackay, A.L.; Klinowski, J. Exact computation of the triply periodic D (`diamond') minimal surface. *Chem. Phys. Lett.* **1999**, *314*, 543–551.

169. Zhuang, S.; Ravichandran, G.; Grady, D.E. An experimental investigation of shock wave propagation in periodically layered composites. *J. Mech. Phys. Solids* **2003**, *51*, 245–265.

170. Chen, Y.; Yao, H.; Wang, L. Acoustic band gaps of three-dimensional periodic polymer cellular solids with cubic symmetry. *J. Appl. Phys.* **2013**, *114*.

171. Tasch, D.; Mad, A.; Stadlbauer, R.; Schagerl, M. Thickness dependency of mechanical properties of laser-sintered polyamide lightweight structures. *Addit. Manuf.* **2018**, *23*, 25–33.

172. Erke Wang, Thomas Nelson, R.R. Back to Elements - Tetrahedra vs. Hexahedra.

173. Agius, D.; Kourousis, K.I.; Wallbrink, C. A Review of the As-Built SLM Ti-6Al-4V Mechanical Properties towards Achieving Fatigue Resistant Designs. *Metals (Basel).* **2018**, *8*.

174. D'Alessandro, L.; Belloni, E.; D'Alo, G.; Daniel, L.; Ardito, R.; Corigliano, A.; Braghin, F. Modelling and experimental verification of a single phase three-dimensional lightweight locally resonant elastic metamaterial with complete low frequency bandgap. In Proceedings of the 2017 11th International Congress on Engineered Materials Platforms for Novel Wave Phenomena (Metamaterials); 2017; pp. 70–72.

175. SAS IP Inc Mesh Generation Available online: https://www.ansys.com/products/platform/ansys-meshing (accessed on Apr 1, 2019).

176. Ampatzidis, T.; Leach, R.K.; Tuck, C.J.; Chronopoulos, D. Band gap behaviour of optimal one-dimensional composite structures with an additive manufactured stiffener. *Compos. Part B Eng.* **2018**, *153*, 26–35.